



HAL
open science

Dispersion in unsaturated porous media

Emma Ollivier-Triquet

► **To cite this version:**

Emma Ollivier-Triquet. Dispersion in unsaturated porous media. Fluid mechanics [physics.class-ph]. Université Paris-Saclay, 2023. English. NNT : 2023UPAST152 . tel-04577632

HAL Id: tel-04577632

<https://theses.hal.science/tel-04577632>

Submitted on 16 May 2024

HAL is a multi-disciplinary open access archive for the deposit and dissemination of scientific research documents, whether they are published or not. The documents may come from teaching and research institutions in France or abroad, or from public or private research centers.

L'archive ouverte pluridisciplinaire **HAL**, est destinée au dépôt et à la diffusion de documents scientifiques de niveau recherche, publiés ou non, émanant des établissements d'enseignement et de recherche français ou étrangers, des laboratoires publics ou privés.

Dispersion in unsaturated porous media

Dispersion dans les milieux poreux insaturés

Thèse de doctorat de l'université Paris-Saclay

Ecole doctorale n° 579, Sciences Mécaniques et Énergétiques, Matériaux
et Géosciences (SMEMaG)
Spécialité de doctorat: Mécanique des fluides
Graduate school: Sciences de l'Ingénierie et des systèmes. Référent: ENS
Paris-Saclay

Thèse préparée dans l'unité de recherche du **FAST** (Université Paris-Saclay, CNRS), sous
la direction de **Laurent TALON**, chargé de recherche au CNRS; de la tutrice **Daniela
BAUER**.

Thèse soutenue à Rueil-Malmaison, le 27 octobre 2023, par

Emma OLLIVIER-TRIQUET

Composition du Jury

Membres du jury avec voix délibérative

Sergio Chibbaro Professeur, LISN, Université Paris-Saclay	Président
Philippe Renard Professeur, Centre d'hydrogéologie, Université de Neuchâtel	Rapporteur
Yohan Davit Chargé de recherche, HDR, IMFT, Université Toulouse III	Rapporteur
Cyprien Soulaïne Chargé de recherche, Groupe de recherche des milieux poreux, ISTO	Examineur

Titre: Dispersion dans les milieux poreux insaturés

Mots clés: Transport anormal, zone vadose, milieux poreux insaturés, écoulements multiphasiques, micromodèle.

Résumé: L'activité humaine a un impact significatif sur la vadose, une zone située au-dessus des nappes phréatiques, qui n'est que partiellement saturée en eau. La vadose peut être polluée par les activités agricoles ou industrielles, ce qui constitue une menace pour les ressources en eau. De plus, la saturation varie considérablement, notamment en raison des sécheresses plus fréquentes dues au changement climatique. Prévoir le transport de contaminants en milieux insaturés est donc essentiel. Cependant, la compréhension de la dispersion dans les milieux poreux insaturés reste limitée, en raison de l'interaction complexe des flux multiphasiques non miscibles avec le milieu poreux. Les modèles traditionnels tels que le modèle Fickien, décrit par l'équation d'Advection-Diffusion, ne parviennent pas à rendre compte avec précision de la dispersion dans les milieux poreux insaturés. L'objectif est d'aborder la question du transport dans les milieux poreux insaturés en identifiant les propriétés pertinentes à l'échelle du pore pour comprendre la dispersion à plus grande échelle. Il s'agit notamment de déterminer si la dispersion est fickienne ou non-fickienne, ce qui est crucial pour prédire la propagation des polluants. Une double approche est adoptée : des expériences de transport à l'échelle du pore et des simulations de Lattice Boltzmann. La visualisation directe des fluides dans les milieux poreux est un défi. Nous utilisons donc des micromodèles, réseaux poreux transparents interconnectés, pour permettre la visualisation optique à l'échelle du pore. Tout d'abord, un dispositif expérimental micromodèle a été établi et optimisé pour étudier l'écoulement et le transport multiphasiques. Des méthodes d'analyse ont été développées, ainsi que des techniques de caractérisation de la dispersion par l'analyse des moments spatiaux. Une première série d'expériences mène à des résultats préliminaires, l'évolution de la saturation et des distributions de phases avec le nombre capillaire a été caractérisée. Les expéri-

ences de transport réalisées pour toute la gamme de saturation montrent que la dispersion augmente à mesure que la saturation diminue. Cependant, l'analyse des faibles saturations s'est avérée difficile en raison de l'augmentation significative de la dispersion et des limites imposées par la taille du micromodèle, empêchant l'étude de la dispersion à long terme. Pour surmonter cette limitation, des simulations Lattice-Boltzmann ont été utilisées pour l'écoulement et le transport, car elles sont flexibles en taille et seulement limitées par le temps de calcul. Toutefois, simuler la distribution de deux phases après un écoulement multiphasique dans un milieu poreux complexe reste un défi. Générer des images à grande échelle de milieux poreux insaturés à partir de données expérimentales s'est donc avéré nécessaire pour observer la dispersion à temps long. Un algorithme de statistique multipoints (MPS) a été utilisé pour générer à la fois des images de milieux poreux non saturés plus larges et un grand ensemble de d'images plus petites pour augmenter la signification statistique de l'étude. Des simulations d'écoulement et de transport ont été réalisées sur l'ensemble des images générées afin d'explorer l'influence de la saturation sur l'écoulement et le transport. Cette étude révèle que la diminution de la saturation augmente de manière significative l'hétérogénéité de l'écoulement, ce qui entraîne une dispersion accrue. Notamment, la nature non fickienne de l'écoulement tend à être plus prononcée à faible saturation. De plus, la transition d'un transport fickien à un transport non fickien dépend du nombre de Peclet. Il existe une compétition entre l'advection et la diffusion dans des conditions saturées, ce qui entraîne un régime Fickien diffusif pour les faibles nombres de Peclet. Cependant, le transport en conditions non saturées est principalement advectif, même à faible nombre de Peclet, et présente donc un comportement non Fickien.

Title: Dispersion in unsaturated porous media

Keywords: Non-Fickian dispersion, unsaturated porous media, vadose zone, multiphase flow, micromodels.

Abstract: Human activity has a significant impact on the vadose zone, an area located below the land surface and above the water tables, only partially saturated with water. The vadose is susceptible to pollution from agricultural or industrial activities, posing a threat to water resources. Plus, saturation levels vary greatly, especially with the increasing frequency of droughts due to climate change. Hence, predicting contaminant transport in unsaturated conditions is crucial. However, the understanding of dispersion in unsaturated porous media remains limited, due to the complex interaction of multiphase non-miscible flows with the porous medium. Traditional models such as the Fickian model, described by the Advection-Diffusion Equation, fail to accurately capture dispersion in unsaturated porous media.

The objective is to address the issue of transport in unsaturated porous media by identifying relevant properties at the pore scale to understand dispersion at a larger scale. One of the goals is to determine whether dispersion follows Fickian or non-Fickian behavior, as this understanding is crucial for predicting the spreading of pollutant in the vadose zone.

To investigate transport in unsaturated porous media, a dual approach is being employed: pore-scale transport experiments and Lattice Boltzmann simulations. Direct visualization of fluid structure in natural porous media is challenging. Thus, we use micromodels, transparent interconnected porous networks, to enable optical visualization at the pore scale. First, a micromodel experimental set-up was established and optimized to study multiphase flow and transport. Analysis methods were developed, along with techniques for characterizing dispersion through spatial moment analysis.

A series of experiments were conducted to obtain initial results on multiphase flow and dispersion. The evolution of saturation and phase distributions with the capillary number was characterized. Transport experiments were performed for the entire range

of saturations, showing that dispersion increases as saturation decreases. However, analyzing low saturations was challenging due to the significant increase in dispersion and limitations imposed by the micromodel size, preventing the study of long-term dispersion.

To overcome this limitation, Lattice Boltzmann simulations were used for flow and transport, as there is no size limitation except for computational time. However, simulating the distribution of two phases after a multiphase flow in a complex porous medium remains challenging. Generating large-scale images of unsaturated porous media based on experimental data was then crucial for observing late-time dispersion. Machine learning techniques, specifically the Multiple Point Statistic algorithm, were employed to generate images of wider unsaturated porous media and a large dataset of smaller images to increase the statistical significance of the study.

Flow and transport simulations were conducted using the generated image dataset to explore the influence of saturation on flow and transport. This involved examining flow properties under saturated and unsaturated conditions. The nature of transport, specifically whether it exhibited Fickian or non-Fickian behavior was investigated. Furthermore, the effect of the Peclet number (a measure of the balance between advection and diffusion) on dispersion for different saturation levels was analyzed.

This study revealed that decreasing saturation significantly increases flow heterogeneity, leading to increased dispersion. Notably, the non-Fickian nature of flow tends to be more pronounced with low saturations. Plus, the transition from Fickian to non-Fickian depends on the Peclet number. There is a competition between advection and diffusion in saturated conditions, resulting in a diffusive Fickian regime for low Peclet numbers. However, transport in unsaturated conditions is mainly advective, even at low Peclet, and thus displays a non-Fickian behavior.

Remerciements

Je remercie mes encadrants, Laurent, Benjamin, Daniela, Souhail. Désolée Souhail d'avoir mis de l'encre partout, et Benjamin merci de m'avoir aidé malgré toutes les bêtises que j'ai pu écrire dans les codes!

Je remercie Anne-So d'avoir supporté un petit dobby ronchon face à elle pendant 3 ans, et d'avoir apporté tant de cookies aux M&Ns. Ravie d'avoir autant ri pendant 3 ans, heureusement que le bureau est au fond du couloir.

Je remercie les thésards qui dépôtent pour les rires, les week-ends de folie, big-up pour Valentine, Camille, Jean-Lou, Alexis, Elliot, Carlos et les deux tours jumelles Théo et Ugo.

Je remercie Upstairs pour 3 années de musique, et François pour m'avoir invitée dans le groupe de rockeurs en partie pré-retraités mais avec plus d'énergie que je n'en aurais jamais.

Je remercie Mathieu d'avoir supporté mes messages teams stupides, les memes absurdes et mon sens du rythme douteux.

Je remercie tous les collègues de Myosotis pour les pauses en salle café même si j'ai pas mal raté celles de 9h sur la fin.

Je remercie Suzon pour être une sacré pote depuis 10 ans déjà, de me suivre dans mes lubies de voyage même quand c'est à plus de 4000 m d'altitude, et pas peu fière de finir en même temps qu'une physicienne de qualité.

Je remercie Clara Débila, docteur maintenant sauf que moi je soigne personne sauf des cailloux.

Je remercie tous mes amis, Nico, Apo, Bibi, Gaétan, Louise, Magzou, QR, Roro, Adèle, Céleste, Jacques, Cyp, Babtou, Louis, Brims, Jules, Nolwenn, Héloïse, Raphaël, Julie, Clara, Théophile, Carla, et tant d'autres!

Je remercie ma famille, les deux meilleurs frères du monde Maëlou et Toto, à mes parents même si vous n'avez pas encore compris ce que j'ai fait en thèse c'est pas grave.

Merci à tous!

Synthèse

La zone non saturée, ou zone vadose, située au-dessus des nappes phréatiques et partiellement saturée en eau, joue un rôle crucial en hydrogéologie, notamment dans la recharge des nappes d'eau. Les activités humaines, y compris les pratiques agricoles, contribuent à la pollution affectant la zone vadose. Avec différents niveaux de saturation, on s'attend à ce que la zone non saturée connaisse une augmentation significative de la variabilité de saturation, surtout dans le sud de la France en raison du changement climatique et des sécheresses de plus en plus fréquentes. Par conséquent, la compréhension du transport des contaminants dans les milieux poreux non saturés devient essentielle pour évaluer et gérer efficacement les ressources en eau.

Néanmoins, la compréhension de la dispersion dans les milieux poreux non saturés reste incomplète. Dans la littérature existante, il y a une disparité significative concernant l'impact de la saturation sur la dispersion. À mesure que la saturation diminue et que le milieu poreux devient plus hétérogène, le processus de transport devient de plus en plus complexe. Par conséquent, les modèles conventionnels de dispersion, tels que l'équation d'advection-diffusion, échouent souvent à capturer précisément le phénomène de dispersion dans de telles conditions.

À travers cette étude, notre objectif est de mieux comprendre la dispersion dans les milieux poreux non saturés en étudiant le transport à l'échelle des pores. Ce faisant, nous visons à évaluer les propriétés à une plus grande échelle et, en particulier, à comprendre comment la dispersion peut être caractérisée et modélisée dans les milieux poreux non saturés. Malgré un nombre substantiel d'études sur ce sujet, un consensus concernant l'impact de la saturation sur la dispersion reste insaisissable. En particulier, la relation entre le coefficient de dispersion et la saturation présente des divergences considérables. Alors que la majorité des études suggèrent une augmentation du coefficient de dispersion avec la diminution de la saturation en eau, certaines montrent une relation non monotone, et quelques-unes proposent même une diminution du coefficient de dispersion avec la diminution de la saturation. Pour comprendre les origines de ces disparités, nous devons explorer les mécanismes fondamentaux de la dispersion et l'interaction complexe entre l'écoulement multiphasique et les caractéristiques du milieu poreux.

Dans le modèle classique, la loi empirique de Fick énonce que le flux est directement proportionnel au gradient de concentration, donnant ainsi lieu à l'équation d'advection-diffusion (ADE). Le coefficient de dispersion est la constante de proportionnalité entre la variance de concentration (σ^2) et le temps dans le régime asymptotique $D = \frac{1}{2} \lim_{t \rightarrow \infty} \frac{d\sigma^2}{dt}$. Lorsque la dispersion suit la loi de Fick, elle est appelée dispersion fickienne. Pour obtenir l'ADE théoriquement, on considère le mouvement brownien, où les molécules subissent des déplacements aléatoires, conduisant finalement à l'ADE avec un coefficient de diffusion égal au coefficient de diffusion moléculaire. Dans les milieux poreux, la dispersion est influencée non seulement par la diffusion moléculaire mais aussi par l'advection due à l'hétérogénéité de l'écoulement, ce qui donne un coefficient de dispersion exprimé comme la somme de composantes de diffusion et d'advection.

Pour parvenir à une convergence vers un mouvement fickien, la variance des déplacements doit être finie. Une variance plus élevée conduit à une convergence plus lente vers une dispersion fickienne. Étant donné que les milieux poreux réels ont une largeur finie, la variance des déplacements doit également être finie. Par conséquent, la dispersion asymptotique devrait être théoriquement fickienne. En conséquence, la dispersion non-fickienne caractérise un comportement transitoire. Cependant, la convergence vers une dispersion fickienne peut être extrêmement lente, et dans certains cas, le régime fickien peut ne ja-

mais être observé. En fait, la dispersion non-fickienne est plutôt la norme que l'exception dans les milieux poreux.

Dans le contexte des milieux poreux non saturés, la présence d'une deuxième phase introduit une hétérogénéité supplémentaire, ce qui entraîne souvent une dispersion accrue. Une question fondamentale abordée dans cette thèse était de comprendre l'impact de la saturation sur la nature de la dispersion, qu'elle présente un comportement fickien ou non-fickien. Caractériser et modéliser correctement la dispersion revêt une importance capitale à cet égard. Pour comprendre la dispersion dans les milieux poreux non saturés, il était essentiel d'étudier les interactions entre l'écoulement multiphasique et le milieu poreux. Plus précisément, l'étude s'est concentrée sur la manière dont les propriétés structurales du milieu poreux changent avec la saturation. Par exemple, l'étude visait à comprendre comment l'hétérogénéité du milieu poreux varie avec les niveaux de saturation.

Afin de comprendre la dispersion dans les milieux poreux non saturés, nous avons réalisé une étude à l'échelle des pores pour identifier les mécanismes d'écoulement et de dispersion à l'échelle microscopique afin de mieux caractériser la dispersion à une plus grande échelle. Ce travail a été entrepris sur deux axes principaux, une étude expérimentale et un travail numérique pour compléter les résultats expérimentaux.

Pour notre étude, nous avons utilisé un micromodèle, un réseau poreux 2D transparent qui permet la visualisation à l'échelle des pores, couramment utilisé pour les études d'écoulement et de transport multiphasiques. Le micromodèle a été créé sur la base d'une tranche 2D d'une roche. Pour mener nos expériences, nous avons conçu un dispositif expérimental spécifique pour réaliser des expériences d'écoulement multiphasique air-eau suivies d'expériences de transport.

Notre objectif était d'étudier le transport dans les milieux poreux non saturés avec une phase piégée, ce qui signifie que des bulles étaient piégées dans le milieu, et nous n'avons pas délibérément examiné le transport lors du mouvement des bulles, car cela aurait introduit une complexité significative dans l'étude. Nous avons conçu un dispositif expérimental pour créer un milieu poreux non saturé avec des distributions de bulles uniformes et reproductibles. Pour cela, nous avons utilisé un système de co-injection, où l'eau et l'air étaient injectés simultanément, et nous avons arrêté l'injection une fois un état stable atteint. L'écoulement multiphasique résultant a conduit à un milieu poreux avec des bulles piégées, que nous avons utilisé pour nos expériences de transport.

Un défi dans la réalisation d'expériences de transport dans un micromodèle est d'établir une condition d'entrée claire. Avec un système d'entrée simple, le traceur se disperse dans le milieu même avant d'entrer dans le milieu poreux, ce qui rend difficile de quantifier précisément la dispersion. Pour résoudre ce problème, nous avons amélioré l'expérience de transport en développant un dispositif avec un système d'injection d'entrée bien défini.

De plus, nous avons développé des techniques spécifiques de traitement des données pour nos données expérimentales. Nous avons conçu des méthodes pour analyser la distribution des phases résultant de la co-injection, pour effectuer la segmentation des phases, calculer les valeurs de porosité et de saturation, ainsi que les distributions de taille de grains et de pores.

En outre, pour analyser quantitativement comment la dispersion change avec la saturation, nous nous sommes appuyés sur l'étude des moments spatiaux de la concentration. Un avantage de cette méthode est qu'elle ne nécessite pas de faire des hypothèses sur la nature de la dispersion, comme savoir si elle est fickienne ou non-fickienne. Au lieu de cela, en examinant l'évolution du deuxième moment avec le temps, nous pouvons caractériser si la dispersion est fickienne ou non-fickienne. Plus spécifiquement, si le deuxième mo-

ment σ^2 est proportionnel à t^α , et si α est égal à 1, cela indique une dispersion fickienne. Inversement, si α diffère de 1, cela indique une dispersion non-fickienne. Pour calculer les moments spatiaux, nous avons utilisé l'intégration par parties, une technique qui nous permet de calculer les moments même pour des distributions affectées par du bruit, ce qui est courant dans des conditions non saturées.

L'ensemble du dispositif expérimental a fourni des résultats expérimentaux de qualité sur la dispersion dans les milieux poreux non saturés. Initialement, nous avons caractérisé l'interaction entre l'écoulement multiphasique et le milieu poreux et identifié les propriétés du milieu poreux non saturé résultant.

Plus précisément, nous avons observé que la saturation augmente avec le nombre capillaire (Ca), défini en fonction de la viscosité dynamique μ , de la vitesse d'écoulement (v) et de la tension superficielle (γ) comme $Ca = \frac{\mu v}{\gamma}$. Cette relation suit une loi de puissance, et la saturation approche 1 pour des valeurs de Ca suffisamment élevées. Cependant, nous n'avons pas pu explorer l'ensemble de la plage de saturation car, en dessous de $S_w = 0.5$, la phase aqueuse ne percole pas. Par conséquent, notre étude de la dispersion était limitée à la plage $[0.5 - 1]$ pour la saturation. La distribution des bulles dépendait principalement du nombre capillaire maximal imposé dans le système. Nos résultats correspondent étroitement aux découvertes antérieures dans la littérature, notamment en ce qui concerne la distribution des tailles de bulles. Aux grandes tailles de bulles, i.e. les bulles plus grandes que la taille moyenne d'une pore, les distributions de tailles de bulles suivent une décroissance en loi de puissance avec une coupure dépendant du nombre capillaire. À mesure que les débits augmentent, les plus grosses bulles sont chassées, ce qui entraîne une diminution de la taille maximale des bulles. Notamment, en dessous de la taille des pores, le nombre capillaire avait peu d'impact sur la distribution des bulles.

De plus, à l'échelle des pores dans des conditions non saturées, nous avons observé que les pores étaient soit presque complètement remplis d'air, ne contenant qu'un mince film d'eau avec une saturation locale en eau ($S_{w,local}$) d'environ 0.2, soit complètement saturés d'eau. Avec la diminution de la saturation, le nombre de pores remplis d'air a augmenté, et les gros pores étaient préférentiellement occupés par des bulles par rapport à des conditions plus saturées.

Après avoir caractérisé le milieu poreux non saturé, nous avons ensuite étudié l'effet de la saturation sur la dispersion. Nos résultats ont révélé une augmentation globale de la dispersion à mesure que la saturation diminuait. Dans des conditions saturées, le front de concentration semble relativement plat et uniforme. Cependant, à mesure que la saturation diminue, le front de concentration présente plus de distorsion, avec l'émergence de chemins préférentiels et de zones stagnantes. Par conséquent, l'hétérogénéité dans le processus de dispersion augmente significativement. Pour quantifier la dispersion, nous avons calculé des moments spatiaux. Dans l'ensemble, nous avons observé une augmentation de la dispersivité¹ à mesure que la saturation diminuait. Néanmoins, caractériser la nature de la dispersion, qu'elle soit fickienne ou non-fickienne, s'est révélé difficile, en particulier dans des conditions non saturées. Plusieurs facteurs ont contribué à cette difficulté. Premièrement, la taille limitée du micromodèle a restreint notre étude à de courtes périodes de temps, en particulier dans des conditions non saturées où le traceur sort rapidement du micromodèle. Deuxièmement, le bruit expérimental et l'incertitude ont rendu difficile la quantification précise des moments spatiaux, surtout pour les saturations les plus basses. Par conséquent, il n'était pas possible d'observer une dispersion à long terme. De plus, notre étude était limitée en termes de débits, ce qui nous a empêchés d'analyser

1. Rapport du coefficient de dispersion et de la vitesse d'écoulement moyenne

expérimentalement la dispersion sur une large plage de nombres de Péclet.

Pour surmonter les limitations expérimentales de la configuration du micromodèle, nous nous sommes tournés vers les simulations numériques. Plus précisément, nous avons utilisé des simulations de Boltzmann sur réseau (LBM), une méthode largement adoptée pour simuler l'écoulement et le transport dans des milieux poreux complexes. LBM offre une grande précision et peut être parallélisé de manière efficace, ce qui permet des temps de calcul relativement courts.

Dans nos simulations numériques, nous avons réalisé des calculs séparés pour l'écoulement dans le milieu non saturé, puis pour le transport. Cette approche présente plusieurs avantages. Notamment, elle donne accès aux champs de vitesse, ce qui est difficile expérimentalement. Pour la simulation de transport, elle nous permet d'obtenir des conditions d'entrée parfaitement nettes pour les injections de traceurs, ce qui est difficile à réaliser dans les configurations expérimentales. Par conséquent, les données générées par les simulations numériques sont moins bruitées et plus faciles à quantifier. C'est particulièrement avantageux lors du calcul du deuxième moment spatial, qui joue un rôle crucial dans la détermination de la nature de la dispersion.

Actuellement, simuler le résultat d'un écoulement multiphasique immiscible dans un milieu poreux complexe à l'aide de méthodes numériques, telles que les simulations de Lattice-Boltzmann, reste un défi. Par conséquent, nous nous appuyons sur les distributions de phases expérimentales comme entrées pour les simulations LBM afin d'étudier l'écoulement et le transport dans de tels milieux. Cependant, cette approche nécessite de faire plusieurs hypothèses fortes et des simplifications par rapport aux conditions expérimentales réelles. Reproduire avec précision les conditions complexes à l'interface entre le ménisque d'air et l'eau n'est pas réalisable dans les simulations LBM. Par conséquent, nous avons dû considérer la phase gazeuse comme une phase solide additive et imposer une condition de non-glissement pour tous les obstacles dans la simulation. De plus, en raison des contraintes informatiques, les simulations LBM sont généralement réalisées en 2D, alors que le micromodèle a une profondeur (L_z). Pour prendre en compte la profondeur de la cellule de Hele-Shaw, nous incorporons le modèle de Darcy-Brinkman pour l'écoulement. Cependant, cette approche néglige le profil de profondeur des bulles, qui est présent dans la configuration expérimentale réelle. Pour valider l'exactitude du flux de travail LBM dans la simulation du transport dans des conditions non saturées dans le micromodèle, nous comparons les résultats des simulations de transport avec des données expérimentales pour trois valeurs de saturation différentes. De manière remarquable, les simulations LBM produisent des résultats proches des données expérimentales de transport, ce qui indique que l'approche LBM capture avec succès la physique de l'écoulement et du transport dans le micromodèle non saturé, malgré les hypothèses et simplifications faites. Ce processus de validation offre une confiance dans l'utilisation des simulations LBM pour étudier les phénomènes de transport dans les milieux poreux non saturés, compensant les limitations des configurations expérimentales et fournissant des informations précieuses sur la dynamique du transport dans ces conditions.

Étant donné que la méthode LBM nécessite toujours des distributions de phases expérimentales en entrée, l'étude est intrinsèquement limitée à la taille des images du micromodèle. À mesure que la saturation diminue et que l'hétérogénéité augmente, la taille du micromodèle devient de plus en plus petite par rapport au Volume Élémentaire Représentatif (VER) du milieu poreux non saturé. Par conséquent, pour garantir la pertinence de notre étude sur la dispersion, nous avons besoin soit d'images plus longues du micromodèle pour prendre en compte une dispersion temporelle plus longue, soit d'un grand nombre de configurations à deux phases. Malheureusement, obtenir de telles données expérimentales

peut être difficile et coûteux en temps.

Pour répondre à ces contraintes et élargir la portée de notre étude, nous avons envisagé l'utilisation d'algorithmes de type machine learning. Nous visons à créer des modèles de milieux poreux non saturés à partir de nos données expérimentales. Cette approche promet de surmonter les limitations de taille et de nombre d'échantillons.

Nous avons utilisé l'algorithme Multiple Point Statistics (MPS), développé à l'origine pour des applications statistiques mais de plus en plus utilisé dans les études sur les milieux poreux, en particulier par Jimenez-Martinez [31] pour générer des milieux poreux non saturés. Dans leur travail, ils ont simulé la phase piégée en utilisant des données expérimentales avec une grille régulière comme milieu poreux. Notre approche est similaire, mais nous allons plus loin en générant à la fois un nouveau milieu poreux et la distribution de phase associée pour une saturation donnée. Pour valider l'efficacité de la méthode MPS, nous avons comparé les propriétés structurales des milieux générés avec les images expérimentales utilisées comme données d'entraînement. Notamment, nous avons comparé les valeurs de porosité et de saturation, ainsi que les distributions de bulles et de grains. La comparaison a montré que les propriétés structurales étaient très comparables entre les milieux générés et les images expérimentales. Pour valider davantage la méthode, nous avons réalisé des simulations d'écoulement et de transport à la fois dans les images expérimentales et générées en utilisant la méthode Lattice-Boltzmann. Les résultats ont démontré que les milieux poreux générés par MPS reproduisaient efficacement les propriétés d'écoulement et de transport observées dans les images expérimentales. Les distributions de vitesse de l'écoulement ont été reproduites avec précision, et les propriétés de transport ont montré une bonne concordance entre les images expérimentales et générées.

Dans l'ensemble, nous avons réussi à valider avec succès la méthode MPS pour la génération de milieux poreux non saturés à partir d'images expérimentales, qui permettent l'étude de l'écoulement et du transport avec des propriétés similaires du milieu d'origine. La force de cette approche réside dans sa généralité, ce qui la rend applicable à toute distribution bidimensionnelle à deux phases non saturée. En utilisant l'algorithme MPS, nous pouvons surmonter les limitations de taille expérimentale et de nombre d'échantillons, nous permettant d'explorer les phénomènes de dispersion et de transport dans les milieux poreux non saturés à une plus grande échelle et avec une précision accrue.

Une fois que l'ensemble du workflow développé, nous avons poursuivi deux stratégies différentes pour étudier la dispersion dans les milieux poreux non saturés. La première stratégie consistait à générer de longues images pour étudier le comportement de dispersion à long terme. Cependant, cela entraînait un coût de calcul significatif associé aux simulations Lattice-Boltzmann, car il est quadratique avec la taille de l'image. De plus, la plage de Péclet que nous pouvions explorer était limitée en raison de la stabilité numérique ou des contraintes computationnelles. Pour pallier cette limitation, nous avons adopté une deuxième stratégie, qui consistait à générer un grand ensemble de données d'images de milieux poreux générées par MPS à la taille du micromodèle. Cet ensemble de données couvrait l'ensemble de la plage de valeurs de saturation, permettant une étude statistique de la dispersion dans les milieux poreux non saturés. Contrairement aux longues images, les courtes images de cet ensemble de données nous ont permis d'explorer une large gamme de valeurs de Péclet. En employant ces deux stratégies, nous avons pu obtenir des informations sur le comportement de dispersion à long terme à travers les longues images et sur les tendances statistiques de la dispersion avec des valeurs de saturation et de Péclet variables à travers le grand ensemble de données de courtes images.

Tout d'abord, en ce qui concerne les propriétés d'écoulement, nous nous sommes concentrés sur la perméabilité apparente, la tortuosité et l'hétérogénéité dans des conditions

saturées pour les petites réalisations. La perméabilité apparente a montré une diminution significative à mesure que la saturation diminuait, approchant zéro près de la saturation en gaz résiduel. Comme le gaz agissait comme une matrice solide supplémentaire dans notre système, nous avons comparé nos résultats avec des relations perméabilité-porosité en utilisant le concept de porosité apparente $\phi_{app} = \phi S_w$. Les données de perméabilité étaient en accord avec la relation de puissance couramment trouvée dans la littérature, suivant la forme $K_{app} \propto (\phi_{app} - \phi_0)^c$. De même, la tortuosité a considérablement augmenté avec la diminution de la saturation. Nous avons de nouveau comparé nos résultats avec des relations tortuosité-porosité, en incorporant le concept de porosité apparente, et avons trouvé un bon ajustement avec une fonction logarithmique, $\tau = 1 - p \ln \phi_{app}$ communément utilisée dans la littérature. Cela suggère que la porosité apparente représente assez bien les caractéristiques de l'écoulement, indiquant que la nature gazeuse de la phase piégée n'impacte pas significativement les propriétés d'écoulement.

De plus, nous avons quantifié l'hétérogénéité de l'écoulement en examinant l'écart-type normalisé de la vitesse σ_u . Ce paramètre a montré une augmentation significative à mesure que la saturation diminuait, entraînée par l'émergence de zones stagnantes et de chemins préférentiels. À mesure que la saturation diminuait, les zones stagnantes s'élargissent de manière exponentielle, caractérisées par des vitesses très faibles, tandis que les chemins d'écoulement préférentiels présentent des vitesses très élevées.

Sur la base de notre analyse des petites réalisations, nous avons constaté que l'évolution des seconds moments dans le temps indiquait un comportement de transport non-fickien sur une large plage de valeurs de Péclet, tant dans des conditions saturées que non saturées. Par conséquent, nous n'observerions pas de dispersion asymptotique pour la longueur moyenne et le Pe considérés, et nous avons caractérisé un régime transitoire. La valeur moyenne de l'indice de la loi de puissance α dans le second moment a été estimée à 1,5, mais il y avait une variance statistique considérable parmi les données. Étant donné que le transport était non-fickien, nous avons caractérisé quantitativement la dispersion en utilisant le coefficient de dispersion fractionnaire D_α^{frac} associé à $\alpha = 1,5$. Cette analyse a révélé une augmentation significative de la dispersion à mesure que la saturation diminuait, ce qui confirmait les résultats expérimentaux.

De manière intéressante, pour des milieux poreux saturés et modérément non saturés, la dispersion est devenue fickienne à mesure que le nombre de Péclet diminuait. De plus, la transition du comportement non-fickien au comportement fickien était plutôt nette. La dépendance du coefficient de dispersion normalisé par rapport au nombre de Péclet indiquait que la transition se produisait lorsque la diffusion devenait plus efficace dans le processus de dispersion. De plus, nous avons observé que la plage de nombres de Péclet pour lesquels la dispersion était non-fickienne augmentait avec la diminution de la saturation. En d'autres termes, à faible saturation, le transport était principalement advectif, ce qui conduisait à une dispersion non-fickienne plus prononcée. En revanche, à saturation élevée, la diffusion est devenue plus dominante, ce qui a conduit à une transition vers une dispersion fickienne.

Dans les longues réalisations temporelles, nous avons observé que l'indice de la loi de puissance α augmentait à mesure que la saturation diminuait, ce qui confirmait les résultats des petites réalisations. Cette tendance suggère qu'à mesure que la saturation diminue, le comportement non-fickien devient plus prononcé, avec des effets de dispersion plus forts. De plus, malgré la plage limitée de valeurs de Péclet que nous avons pu explorer dans les longues simulations, nous avons quand même observé le même effet de Péclet que celui trouvé dans les courtes images. Cette cohérence entre les simulations courtes et longues souligne la robustesse de nos conclusions.

Pour résumer, cette étude a permis des avancées significatives sur la compréhension du transport dans les milieux poreux non saturés. Nous avons développé un dispositif expérimental nous permettant d'étudier à la fois l'écoulement multiphase et le transport dans un micromodèle, ainsi que le développement de techniques de traitement des données appropriées. À travers ces expériences, nous avons caractérisé l'interaction entre l'écoulement multiphase et le milieu poreux et étudié les propriétés structurales du milieu poreux non saturé. Les expériences de transport ont indiqué une augmentation de la dispersion avec la diminution de la saturation, bien que l'analyse quantitative soit limitée en raison de contraintes expérimentales. Pour surmonter ces limitations, nous avons utilisé des simulations Lattice-Boltzmann (LBM) après avoir validé leur aptitude à modéliser l'écoulement et le transport dans des conditions non saturées dans le micromodèle. De plus, nous avons développé une méthode basée sur le machine learning utilisant l'algorithme des statistiques multipoints (MPS) pour générer des images avec des données expérimentales, permettant une production d'échantillons à grande échelle sans limitations de taille. L'utilisation de simulations LBM dans les images générées par MPS a permis d'obtenir de nombreux résultats sur les propriétés d'écoulement et de dispersion. Notamment, nous avons constaté qu'à mesure que l'hétérogénéité de l'écoulement augmente et que les chemins d'écoulement deviennent plus tortueux, avec une présence accrue de zones stagnantes, la dispersion dans les milieux poreux non saturés présente un comportement plus advectif. En conséquence, nous avons constaté que la dispersion non-fickienne devient plus prononcée dans des conditions non saturées. En revanche, dans des conditions saturées, la dispersion a tendance à être fickienne à mesure que le nombre de Péclet diminue, car la diffusion devient plus efficace dans le processus de dispersion. Dans l'ensemble, cette approche globale combinant des expériences, la génération d'images basée sur le machine learning et des simulations LBM a considérablement fait progresser notre compréhension des phénomènes de transport dans les milieux poreux non saturés. Les résultats éclairent l'interaction complexe entre l'écoulement et la dispersion, ce qui a des implications pour un large éventail d'applications, notamment la gestion des eaux souterraines, la remédiation environnementale et le transport des contaminants dans les milieux poreux.

Ce travail pose les bases de futures avancées potentielles, notamment la modélisation de la dispersion non-fickienne dans les milieux poreux non saturés. Par exemple, il serait intéressant d'appliquer l'approche de la marche aléatoire en temps continu (CTRW) dans les milieux non saturés pour prédire les comportements de transport sur de plus longues périodes dans des conditions non saturées. De plus, il convient de noter que notre étude actuelle s'est concentrée sur la dispersion dans des milieux non saturés avec une phase piégée immobile. Élargir notre étude pour inclure le transport impliquant deux phases immiscibles mobiles fournirait une compréhension plus complète de la dynamique de transport dans des conditions non saturées. À l'avenir, il est possible d'étendre la méthodologie de cette étude à des conditions tridimensionnelles, ce qui permettrait une représentation plus proche des milieux poreux du monde réel. Cependant, il est important de reconnaître que de telles applications numériques exigeraient des ressources computationnelles substantielles en raison de la complexité accrue et des exigences computationnelles associées aux simulations 3D.

Nomenclature

	Porous medium
ϕ	Porosity
ϕ_{app}	Apparent porosity
S_w	Water saturation
τ	Tortuosity
K	Permeability
K_{app}	Apparent permeability
Q	Flow rate
R_{pore}^{eq}	Pore equivalent radius
d	Pore diameter
d_{pore}	Mean pore diameter
s_{bubble}^m	Mean bubble surface
s_{pore}^m	Mean bubble surface
L_x	Length of the micromodel
L_y	Width of the micromodel
L_z	Depth of the micromodel
	Dimensionless numbers
Ca	Capillary number
Kn	Knudsen number
Pe	Peclet number
Re	Reynolds number
	Flow
γ	Air-Water surface tension
ν	Fluid cinematic viscosity
ρ	Fluid density
P	Pressure
Q_{air}	Air flow rate
Q_{water}	Water flow rate
\mathbf{u}	Velocity field
σ_u	Normalized standard deviation of the velocity field
u_x	Velocity along the flow direction (x)
u_y	Velocity along the transverse direction of the flow (y)
$\langle \ \mathbf{u}\ \rangle$	Mean of the norm interstitial velocity
$\langle u_x \rangle$	Mean interstitial velocity along the direction of the flow
$\langle u_y \rangle$	Mean absolute interstitial velocity along the transverse direction of the flow
U_{Darcy}	Darcy velocity $\phi \langle u_x \rangle$
$u_{norm}(x,y)$	Normalized velocity $u_{norm}(x,y) = \frac{\ \mathbf{u}(x,y)\ }{\langle \ \mathbf{u}\ \rangle}$
L_{border}	Characteristic length of the border influence on the flow
$\xi_{y=0}$	Correlation function in the flow direction
$\xi_{x=0}$	Correlation function in the transverse direction of the flow
$\zeta_{y=0}$	Correlation length in the flow direction
$\zeta_{x=0}$	Correlation length in the transverse direction of the flow

	Lattice-Boltzmann Methods
λ^+	Symmetric relaxation rate
λ^-	Anti-symmetric relaxation rate
Ω	Collision operator
D_{LB}	Diffusion coefficient
	Multiple Point Statistics algorithm
\mathcal{W}	Rectangular window to form the patterns of the database from the TI
w	Size of \mathcal{W}
\mathcal{T}	Patterns of the database
\mathcal{P}	Patch selected from the patterns of the database
p	Size of \mathcal{P} with $p < w$
\mathcal{W}_c	Window to browse the coarse Training Image (multi-scale algorithm)
w_c	Size of \mathcal{W}_c
\mathcal{W}_f	Window to browse the fine Training Image (multi-scale algorithm)
w_f	Size of \mathcal{W}_f
p_c	Size of \mathcal{P} in the coarse simulation
p_f	Size of \mathcal{P} in the fine simulation
Ups	Size ratio between the fine and coarse scale image
	Transport
c	Concentration
\tilde{c}	Normalized averaged concentration over the transverse direction
\tilde{c}_{in}	Injected tracer concentration
D	Dispersion coefficient
v	Flow velocity
D_m	Molecular dispersion coefficient
D^*	Normalized dispersion coefficient $\frac{D}{D^*}$
μ	First moment of the concentration profile
σ^2	Centered second moment- Variance of the concentration profile
γ	Skewness
m_r	Centered moment of the order r
λ	Dispersivity
α	Second moment power law index
D_α^{frac}	Fractional dispersion coefficient associated to the power law index α
	Abbreviations
ADE	Advection-Diffusion Equation
BTC	Breakthrough curves
CTRW	Continuous Time Random Walk
LBM	Lattice Boltzmann Methods
MIM	Mobile Immobile Model
MPS	Multiple Point Statistic algorithm
REV	Representative Elementary Volume
TI	Training Image

Contents

1	Introduction	1
2	State of the art	5
2.1	Introduction: generalities on flow and dispersion in porous media	6
2.1.1	Porous media: from the microscopic to the macroscopic scale	6
2.1.2	Flow in porous media, from the microscopic to the macroscopic scales	6
2.1.3	Dispersion in porous media	7
2.2	Non-Fickian dispersion in porous media	13
2.2.1	Observation of non-Fickian dispersion in porous media	13
2.2.2	Random walk and non-Fickian dispersion	16
2.2.3	Modelling non-Fickian dispersion	19
2.3	Properties of a two-phase flow in porous media	24
2.3.1	Generalities: physics at the interface	24
2.3.2	Two phase flow in porous media: quasi-static conditions	25
2.3.3	Dynamics of a two phase flow in porous media	26
2.3.4	Flow with a trapped phase	27
2.4	Saturation effects on dispersion in porous media	31
2.4.1	Effect of saturation: discrepancy of results	32
2.4.2	Description of the dispersion: ambiguities	32
2.4.3	Different trends	33
2.4.4	Influence of the two phase flow topology on the dispersion	36
2.5	Micromodels for porous media studies	38
2.5.1	Generalities	38
2.5.2	Micromodels for the characterization of non miscible two-phase flows in porous media	41
2.5.3	Micromodels to study dispersion in porous media	42
2.6	Synthetic image reconstruction in porous media	44
2.6.1	Introduction	44
2.6.2	Multiple-Point statistics algorithm	45
2.6.3	MPS application to porous media	46
2.7	Conclusion	47
3	Experimental methods and data processing	49
3.1	Multi-phase flow and transport experiments	50
3.1.1	Experimental set-up	50
3.1.2	Experimental protocols	53
3.2	Data processing	55
3.2.1	Data analysis of the non miscible fluid distribution: image processing	55
3.2.2	Data analysis of the concentration fields: methods of moments	58

3.2.3	Further Data Processing	66
3.3	Validation of the transport protocol	67
3.3.1	Repeatability of the injection	67
3.4	Conclusion	68
4	Numerical strategy	71
4.1	Numerical methods for flow and transport simulations	71
4.2	Lattice Boltzmann method	73
4.2.1	Introduction	73
4.2.2	Boltzmann equation	73
4.2.3	Lattice-Boltzmann method	74
4.2.4	Macroscopic flow behavior	75
4.2.5	Numerical resolution	75
4.2.6	Selecting a collision operator	76
4.2.7	TRT collision operator	77
4.2.8	Lattice units	78
4.2.9	D2Q9 Velocity set	78
4.3	Lattice-Boltzmann method for porous media	79
4.3.1	Flow simulations	79
4.3.2	Transport simulation	81
4.4	Illustration of LBM simulation	82
4.5	Conclusion	82
5	Experimental results on dispersion in unsaturated porous media	85
5.1	Introduction	85
5.2	Multiphase flow in porous media	86
5.2.1	Co-injection experiments	86
5.2.2	Macroscopic scale: evolution of the saturation with the flow rate	86
5.2.3	Microscopic scale: bubble's distribution	88
5.2.4	Microscopic scale: structural properties at the pore scale	91
5.2.5	Conclusion: insight on multiphase flow interaction in porous media	93
5.3	Dispersion in unsaturated porous media	94
5.3.1	Dispersion dependence with saturation	94
5.3.2	Influence of bubbles distributions	98
5.4	Experimental validation of Lattice-Boltzmann simulation in the micromodel	100
5.4.1	Experimental and simulation conditions	100
5.4.2	Results	101
5.4.3	Validation of LBM simulation to compute transport in saturated and unsaturated micromodel	103
5.5	Conclusion on preliminary results	104
6	Generating synthetic images of unsaturated porous media with a multi- scale multipoint statistics approach	105
6.1	Motivation	105
6.2	Multiple-point statistics algorithm	107
6.2.1	MPS algorithm	107
6.2.2	Multi-scale algorithm	109
6.2.3	Application of MPS to unsaturated porous media images	109
6.3	Method validation	112
6.3.1	Generated images	113

6.3.2	Structural properties	113
6.3.3	Flow and transport properties	115
6.4	Conclusions	118
7	Numerical results on flow and dispersion in unsaturated porous media	121
7.1	Introduction	121
7.2	Data set	122
7.2.1	Experimental Dataset: training images	122
7.2.2	Generated images: two data sets	123
7.3	Effect of saturation on the flow	124
7.3.1	Introduction	124
7.3.2	Apparent permeability	124
7.3.3	Velocity field distributions	126
7.3.4	Spatial evolution of the flow	128
7.3.5	Conclusion	132
7.4	Dispersion in unsaturated porous media	134
7.4.1	Introduction	134
7.4.2	Methodology	135
7.4.3	Qualitative observations	136
7.4.4	Short time dispersion: spatial moments of the dispersion	138
7.4.5	Short time dispersion: Effect of the Peclet number	143
7.4.6	Long time dispersion	146
7.4.7	Conclusion	148
7.5	Quantification of the boundary effect on flow and transport	149
7.5.1	Motivation	149
7.5.2	Effect of the medium width on the flow properties	150
7.5.3	Effect of the medium width on transport properties	152
7.5.4	Influence of saturation on the boundary effect	154
7.5.5	Conclusion	155
8	Conclusion	157
9	Appendices	165
9.1	Bibliography appendix: Non Fickian dispersion modelling	165
9.1.1	Modeling with the Mobile-Immobile concept	165
9.1.2	Modelling with random walk concepts: Continuous Time Random Walk	166
9.1.3	Generalization of the Fokker-Planck equation: fractional advection-diffusion equations	168
9.1.4	Comparison of dispersion models	173
9.1.5	Micromodels bibliography appendix	173
9.2	Method appendix	175
9.2.1	Taylor dispersion in the tubing	175
9.3	Experimental results appendix	175
9.3.1	Phase distribution resulting from a two-phase flow	175
9.3.2	Structural properties of the unsaturated porous medium	177
	Bibliography	181

Chapter 1

Introduction

The vadose zone, also known as the unsaturated zone, is a critical component of the subsurface environment that plays an essential role in the transport and fate of contaminants. Fig. 1.1 depicts the vadose zone. Unlike the saturated zone, where the pore spaces are completely filled with water, the vadose zone consists of partially saturated porous media, with both air and water occupying the pore spaces. This unique characteristic gives rise to complex and dynamic flow and transport processes that significantly influence the movement and behavior of contaminants in the subsurface.

Understanding contaminant transport in unsaturated porous media is of paramount importance due to its relevance in various fields, such as environmental science, hydrogeology, soil and groundwater remediation. Contaminants can enter the subsurface through a multitude of sources, including industrial activities, agricultural practices, and accidental spills. Once in the vadose zone, they can migrate downward, potentially reaching the saturated zone and causing groundwater contamination. Additionally, the vadose zone acts as a critical buffer, regulating the transport of contaminants before they reach sensitive areas such as surface water bodies or drinking water wells. The study of transport in unsaturated porous media presents unique challenges and opportunities. Unlike saturated flow, where the physics of fluid movement are relatively well understood, the presence of both air and water phases in the vadose zone introduces complexities that demand further investigation. Capillary forces, interfacial interactions, and preferential flow paths are among the factors that influence the behavior of contaminants in unsaturated porous media.

Furthermore, the vadose zone serves as an interface between the atmosphere and the saturated zone, making it susceptible to climate change impacts and land-use activities. Changes in precipitation patterns, temperature, and vegetation cover can have profound effects on the hydraulic properties and flow dynamics in unsaturated porous media, thereby altering the fate and transport of contaminants. Notably, the level of saturation depends directly on precipitations, hence periods of drought or floods directly affect the vadose zone. With climate change, periods of drought in places such as in the south of France will become increasingly more frequent. As a result, the level of saturation of the vadose zones will vary significantly more compared to previous conditions. The ability to predict contaminant transport for various degrees of saturation is, therefore, of vital importance. Understanding dispersion in unsaturated porous media, the subject of this thesis, is thus becoming an environmental issue as well.

However, the understanding of how saturation affects dispersion in porous media remains limited. Classical models, such as advection-diffusion equations, are not always applicable in unsaturated porous media, and there is disagreement among authors regard-

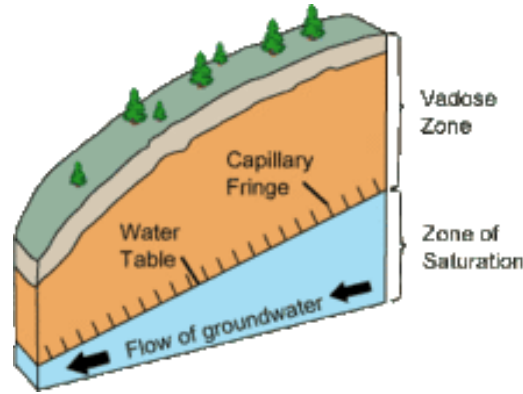


Figure 1.1 – Vadose zone, illustration from wikipedia

ing the influence of saturation on dispersion [91, 93, 121, 161].

The challenge arises from the fact that the volume of accessible pores depends on the interaction of multiphase non-miscible flows (water/air) with the porous medium. The presence of gas bubbles introduces greater heterogeneity into the system, with stagnant zones exhibiting very low velocities and preferential paths displaying high velocities. As a result, both flow and dispersion are influenced by the saturation level and the medium's heterogeneity.

In stagnant zones, dispersion is primarily controlled by diffusion, resulting in slow transport. On the other hand, dispersion in preferential paths is predominantly advective, leading to rapid solute displacements. Consequently, transport in unsaturated porous media is significantly more complex compared to saturated media. As an example, Fig. 1.2 illustrates the stagnant zones (dead ends) and preferential paths observed in a transport experiment using a micromodel 2D porous medium.

However, the effect of saturation on dispersion in porous media remains incompletely understood, and further research is necessary. Classical models, such as advection-diffusion equations, cannot always be applied in unsaturated porous media, and authors have differing opinions on the influence of saturation on dispersion.

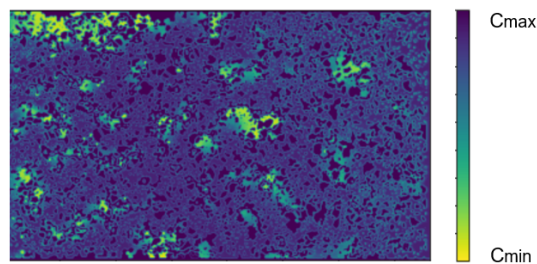


Figure 1.2 – Illustration of dead-ends in transport in the unsaturated micromodel: concentration field in a porous media shortly after a tracer injection. The dead-ends are represented by green areas with low concentration, signifying zones of low velocity where transport is predominantly controlled by diffusion.

In this study, our primary objective is to examine transport phenomena at the microscopic scale. This involves identifying key structural properties within the porous medium that influence dispersion, such as saturation and connectivity. As previously mentioned, the advection-dispersion equation does not always accurately depict transport in unsatu-

rated media. In other words, transport may not necessarily follow Fick's law. Therefore, one of our objectives is to determine whether dispersion exhibits Fickian or non-Fickian behavior, as this understanding is crucial for selecting appropriate models to describe transport in unsaturated porous media. Ultimately, our goal is to enhance our understanding of dispersion processes on larger scales.

This thesis is structured around two main axes: an experimental aspect involving transport experiments conducted using micromodels, which are essential for comprehending the multiphase nature of our system, and a numerical aspect that complements the experimental data through Lattice Boltzmann simulations of flow and transport in micromodels. The simulations allow for the study of larger media compared to the experimental setup, resulting in a longer dispersion time, which is crucial for investigating late-stage dispersion behavior.

Initially, our focus was on the experimental aspect. We employed micromodel technology, which utilizes transparent interconnected porous networks, allowing for direct visualization of fluid structure at the pore scale. Our efforts were dedicated to developing a micromodel setup for conducting transport experiments in unsaturated porous media, as well as establishing methods for analyzing the acquired data. As a result, we obtained preliminary experimental findings that shed light on the impact of saturation on phase distribution and transport within the porous media under multiphase flow conditions.

However, due to the limited size of the micromodel, it does not permit the observation of late-time dispersion in experiments, notably under low saturation conditions. Furthermore, due to experimental uncertainty, a precise quantitative analysis of dispersion was constrained. The determination of the transport nature, whether it followed a Fickian or non-Fickian behavior, was challenging. To overcome these limitations, we utilized Lattice-Boltzmann simulations for flow and transport, which offer the advantage of scalability and allow to explore a large Peclet range, with the primary constraint being computational time.

Although the methods for flow and transport simulations have been established, simulating the resulting distribution of two phases (air/water) after multiphase flow in a complex porous medium remains a challenging task. Plus, it is crucial to generate large-scale images of unsaturated porous media based on experimental data to observe pore-scale late-time dispersion. To accomplish this, we employed a machine learning approach using our experimental data (i.e., two-phase distributions in the micromodel resulting from multiphase flow experiments) as training images. By utilizing a Multi-scale Multiple Point algorithm (MPS), commonly employed in geostatistics, we generated images that replicated unsaturated porous media, incorporating a significant number of realizations to enhance the statistical significance of our study.

Consequently, we constructed a dataset of training images derived from our experimental data, enabling the creation of an artificial image dataset encompassing various saturations and configurations. Additionally, we generated representations of longer media with different saturations to investigate long-term dispersion phenomena.

Finally, we conducted flow and transport simulations using our dataset to explore the influence of saturation on flow and transport processes. Specifically, we examined the properties of flow under both saturated and unsaturated conditions, including permeability, tortuosity, and flow heterogeneity. We also investigated the nature of transport, focusing on whether it exhibited Fickian or non-Fickian behavior. This was accomplished by studying the evolution of the second moment of the concentration front in transport simulations and calculating the power index α , which represents the relationship between the variance (σ^2) and time (t) as $\sigma^2 \propto t^\alpha$. Non-Fickian dispersion occurs when α is differ-

ent from 1. Thus, we aimed to investigate whether the nature of transport changed with saturation as the complexity of transport increased.

Additionally, we examined the effect of the Peclet number on dispersion for different saturation levels to understand how the balance between advection and diffusion influences dispersion in both saturated and unsaturated conditions. Another aspect we focused on was quantifying the impact of flow boundaries on transport. Since the media used in our simulations have limited widths, transport is affected by borders and is not entirely analogous to a medium with infinite width. We quantified the typical length of the borders effect and explored how it varied with saturation.

This thesis is structured as follows.

Chapter 2 provides an literature review conducted to establish a solid understanding of dispersion in unsaturated media, covering essential concepts and theories.

Chapter 3 details the experimental methods employed in this study, including data analysis techniques.

Chapter 4 presents the numerical method, that complements the experimental ones. It explains the use of Lattice Boltzmann methods to compute flow and transport within the micromodel.

Chapter 5 presents the preliminary experimental results pertaining to multiphase flow and dispersion in unsaturated porous media. Additionally, it discusses the experimental validation of the Lattice Boltzmann methods employed for studying transport in unsaturated porous media.

Chapter 6 focuses on the workflow developed for the Multi-scale Multiple Point algorithm (MPS), which enables the creation of unsaturated images using our experimental data. This chapter also proposes a validation of the method based on flow and transport properties.

Chapter 7 encompasses the numerical results obtained from the LBM simulations of flow and transport in our data set, and notably results on long time dispersion.

Finally, in Chapter 8, a conclusion is provided, highlighting the insights obtained through this study concerning dispersion in unsaturated porous media.

By organizing the thesis in this manner, a systematic exploration of the research objectives, methods, experimental findings, and validation processes is presented, leading to comprehensive and conclusive results

Chapter 2

State of the art

To begin with, it is essential to establish some fundamental aspects of physics related to porous media. A quick review of the literature reveals that the physics of dispersion in unsaturated porous media lies at the intersection of various disciplines, including hydrology, fluid mechanics, and applied mathematics. Therefore, it becomes necessary to cover multiple aspects of this subject, starting with the basics of fluid mechanics in a porous medium and understanding dispersion in porous media.

When exploring dispersion in unsaturated porous media, numerous concepts from porous media physics come into play, leading to several questions:

- What is dispersion, precisely? We will introduce generalities about flow and dispersion in porous media in a first section (2.1).
- How do we characterize and model dispersion in porous media? We detail the nature of transient and asymptotic dispersion in a section about non-Fickian dispersion (section 2.2).
- What are the main multiphase flow mechanisms in porous media? The interactions between immiscible air-water flow and a porous medium are introduced in a third section (2.3).
- What have we learned so far from the results on dispersion in unsaturated porous media, and what insights do they provide? An overview on dispersion in unsaturated porous media is provided section 2.4.
- How micromodels can be a powerful device to study dispersion in unsaturated porous media? Section 2.5 details how micromodels can be used to study transport in unsaturated porous media.
- Is there a way to tackle the limited amount of experimental data by creating synthetic porous media? The generation of artificial porous media from experimental images is presented section 2.6.

In this study, we aim to address these questions to gain a deeper understanding of dispersion in unsaturated porous media.

2.1 Introduction: generalities on flow and dispersion in porous media

In this section, we will introduce few notions on porous media necessary to understand the following sections.

2.1.1 Porous media: from the microscopic to the macroscopic scale

In this study, we are interested in how we can relate the dispersion properties at the microscopic scale, resulting from the medium interaction with a two phase flow, to a general behavior at the macroscopic scale.

To understand any property of a porous medium, it is essential to look into each scale of the porous media. We go from the microscopic scale or the pore scale, where Stokes law governs the flow, to the mesoscopic and the macroscopic scale, for which the porous media can be characterized by averaged properties like its porosity, permeability, or an average pressure gradient. A very large amount of studies in porous media aim to create a link between the properties at the microscopic scales and the properties at a greater scale, depending on the statistical properties of the porous medium [36, 50, 56].

In the porous medium, we will need to work with averaged quantities, such as the mean flow velocity or porosity, that are defined at the mesoscopic scale. For an average quantity to be representative, it needs to be averaged over a Representative Equivalent Volume (REV) (see Fig 2.1) such that the averaged value does not vary significantly if this volume increases.

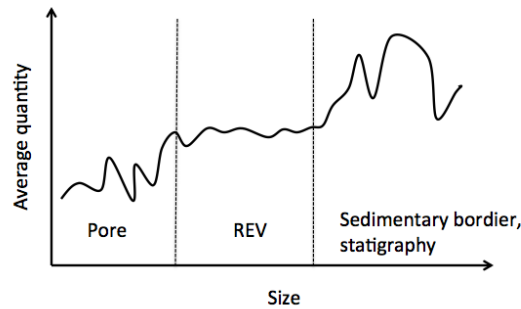


Figure 2.1 – Representative Elementary Volume (REV)

The porous media structural properties will be described mainly by the pore statistical characteristics, such as the pore size distribution, the mean pore size, the connectivity of the pores, or other properties characterizing the pore and throat shapes.

2.1.2 Flow in porous media, from the microscopic to the macroscopic scales

Microscopic and mesoscopic scales

At the pore scale, the flow is characterized by low Reynolds¹ numbers, it is therefore well described by the Stokes equation

$$\eta \Delta \mathbf{u}_{\text{micro}} = \nabla P_{\text{micro}}, \quad (2.1.1)$$

1. The Reynolds number characterizes the ratio between inertial and viscous forces

where $\mathbf{u}_{\text{micro}}$ and P_{micro} are respectively the velocity vector and the pressure at the pore scale and η is the dynamic viscosity of the fluid.

At the mesoscopic scale, the flow can usually be described by Darcy's law, that gives a relation between the mean flow rate and the mean pressure gradient [168] through the permeability coefficient K that can be a function of space for heterogeneous media

$$\eta \mathbf{u} = -K \nabla P, \quad (2.1.2)$$

where \mathbf{u} and ∇P denotes respectively the velocity and the pressure gradient at the mesoscopic scale. The Darcy velocity and pressure are averaged over a representative volume denoted V such as follows

$$\mathbf{u} = \frac{1}{V} \iiint_V \mathbf{u}_{\text{micro}} dv \quad (2.1.3)$$

Generalization of Darcy's law, Darcy Brinkmann

In a medium for which the permeability field exhibits discontinuities, the Darcy equation is no longer adequate to describe the flow. Indeed, a discontinuity of the permeability would imply a discontinuity of the Darcy velocity field, which is not physically acceptable. Hence, a dissipative term is introduced to the Stokes equation 2.1.2, leading to the Darcy-Brinkmann equation [24].

$$\eta \mathbf{u} = -K \nabla P + \eta \Delta \mathbf{u}.$$

The validity limit of the Darcy's law and the necessity to use the Darcy-Brinkmann equation is deduced from the scale of the permeability fluctuations. If there are some heterogeneity which vary on a smaller scale than the pore scale, then the Darcy-Brinkmann equation becomes necessary. In other words, for λ the correlation length of the permeability field and K the medium permeability, the Darcy-Brinkmann equation becomes necessary when $\lambda < \sqrt{K}$. Indeed, the pore scale can be estimated by \sqrt{K} .

Particularly, Darcy-Brinkmann models flow in Hele-Shaw cells (two parallel flat plates separated by a very small gap) with obstacles, which is the same concept than micromodels [179].

2.1.3 Dispersion in porous media

In the following, we consider two miscible fluids, one of them containing a tracer which can diffuse in the other one.

Fick's law and advection-diffusion equation

Historically, the diffusion has been first described empirically by Adolf Fick in 1855. The first Fick's law relates the diffusive flux to the concentration gradient. It states that the flux J_{diff} goes from high concentration zones to low concentration zones, with a magnitude proportional to the concentration gradient ∇c . The proportionality coefficient is called the diffusion coefficient D .

$$J_{\text{diff}} = -D \nabla c. \quad (2.1.4)$$

The mass conservation combined with the first Fick law leads to the second Fick law or the Diffusion Equation

$$\frac{\partial c}{\partial t} = D \nabla^2 c. \quad (2.1.5)$$

Considering an advective flux $J_{\text{adv}} = vC$ as well as a diffusive flux, with the mean velocity v , we end up with the Advection-Diffusion Equation (ADE)

$$\frac{\partial c}{\partial t} + v\nabla c = D\nabla^2 c. \quad (2.1.6)$$

For a Dirac initial condition initially located at $x = 0$ and a one dimensional problem without boundaries, the solution for the concentration $C(x,t)$ is given by a Gaussian

$$c(x,t) = \frac{1}{\sqrt{4\pi Dt}} e^{-\frac{(x-vt)^2}{4Dt}}. \quad (2.1.7)$$

When the solute concentration follows the ADE, the transport is qualified of Fickian transport, otherwise the transport is qualified as non-Fickian or anomalous.

In a porous media, the transport is not necessarily Fickian [18]. In order to understand transport at the different scales of the porous media, it is necessary to know the nature of the dispersion. Therefore, it is essential to have tools to characterize the dispersion, such as spatial moments.

Characterization of the dispersion: spatial moments of the concentration distribution

In this section, we will introduce the definition of the moments and how they characterize dispersion, typically how they distinguish Fickian transport from anomalous transport. To go further, we introduce the operator $\langle \cdot \rangle$ which defines the overall average over a large number of realizations and a 1D concentration profile $c(x,t)$ for a Dirac injection. The probability distribution for the particle is $p(x) = \frac{c(x,t)}{c_0}$ with $c_0 = \int c(x)dx$ the mean concentration. An example of concentration profile at different times is given by Fig. 2.2.

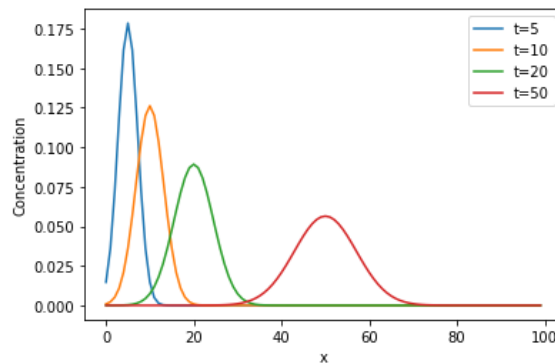


Figure 2.2 – Concentration profiles $c(x,t)$ at different times

A moment of the order r is given by

$$m_r = \langle x^r \rangle = \int_x p(x)x^r dx.$$

The first moment corresponds to the mean position, which coincides with the peak position for a symmetric distribution

$$\mu = m_1 = \langle x \rangle = \int_x p(x)x dx.$$

In Fickian dispersion, the mean flow velocity will be given by $\frac{d\mu}{dt}$.

The centered² second moment corresponds to the variance, it is the square of the standard deviation. It characterizes the spread of the plume, and that is the most common indicator to describe the dispersion

$$\mu_2 = V(x) = \sigma^2 = \int_x p(x)(x - \langle x \rangle)^2 dx = \int_x p(x)(x - \mu)^2 dx.$$

For a Fickian dispersion, the variance is proportional to time $\sigma^2 \propto t$, and the dispersion coefficient is defined as

$$D = \frac{1}{2} \lim_{t \rightarrow \infty} \frac{d\sigma^2}{dt}.$$

For example, with the ADE solution to a Dirac injection given equation 2.1.7, the variance calculus gives indeed

$$\sigma^2 = 2Dt.$$

The third moment of the reduced and centered variable, the skewness, is defined as

$$\gamma = \left\langle \left(\frac{x - \mu}{\sigma} \right)^3 \right\rangle = \int_x p(x) \left(\frac{x - \mu}{\sigma} \right)^3 dx.$$

The skewness γ characterizes the symmetry of the distribution. Negative values of skewness indicate that the mean is shifted from the median to the right, which indicates a tail of distribution spread to the left. Conversely, positive values of skewness indicate that the mean is shifted from the median to the left, which indicates a tail of distribution spread to the right, as shown Fig. 2.3. The skewness is equal to zero for symmetric curves. For a Fickian dispersion, the skewness equals zero.

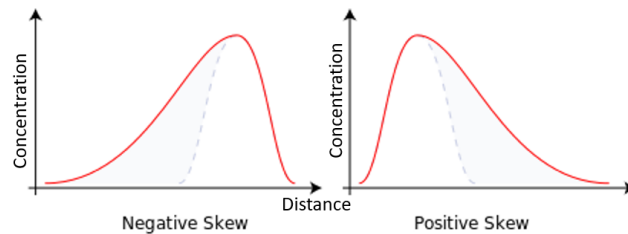


Figure 2.3 – Negative and positive skewness

Multi-scale dispersion in porous media

To study transport process in porous media, it is necessary to consider all dispersive processes involved at each scale of the porous medium. For instance, if the dispersion is assumed to be Fickian at the microscopic scale or pore scale, it does not necessarily imply that the dispersion will be Fickian at a greater scale.

From the microscopic scale to the mesoscopic scale: example of the Taylor dispersion

2. Centering is the process of subtracting the variable mean (average) from each of the values of that same variable

The main idea is to get the dispersion law of the mesoscopic scale from the dispersion at the microscopic scale, governed by the ADE given by Eq. 2.2.4. Let first define the velocity \mathbf{u} and c the concentration at the mesoscopic scale from their counterparts at the microscopic scale \mathbf{u}_{micro} and c_m .

$$\mathbf{u} = \frac{1}{|V|} \int_V \mathbf{u}_{micro} dv \quad \text{and} \quad c = \frac{1}{|V_f|} \int_{V_f} c_m dv, \quad (2.1.8)$$

where the volume of integration V stands for an REV and the concentration is averaged on the fluid volume V_f .

They are numerous laws that can describe the transport for these averaged quantities. In the simplest cases, we also get the advection-diffusion equation

$$\boxed{\frac{\partial c}{\partial t} + \frac{1}{\phi} \mathbf{u} \cdot \nabla c = D \Delta c}, \quad (2.1.9)$$

where D is the mesoscopic dispersion coefficient.

D is usually different from the molecular diffusion coefficient, because the dispersion has different sources than the molecular diffusion; indeed, the fluctuations of the velocity field will be new sources of dispersion,

$$\boxed{D = D_m + D_{disp}}, \quad (2.1.10)$$

where the term D_{disp} stands for the dispersion.

As an illustration, we can mention the simple case of Taylor dispersion [154], obtained by derivation of tracer transport laws in a infinite tube. This illustration makes sense in our study of diffusion in porous media as the tube can be assimilated to a pore, in which there is a mean flow \mathbf{u}_0 .

We now demonstrate that we can get an ADE from the advection-diffusion equation at the microscopic scale, through a perturbation method.



Figure 2.4 – Taylor dispersion

We consider an infinite tube of radius R with a flow of mean velocity \mathbf{u}_0 in the z direction (cf Fig. 2.4). A tracer is injected at the tube entrance, and we suppose that the advection-diffusion law 2.1.9 controls the transport at the microscopic scale. Moreover, the flow follows the Poiseuille's law

$$u_{micro}(r, \theta, z) = u_{max} \left(1 - \frac{r^2}{R^2} \right)$$

with $u_{max} = 2u_0$.

We use a small perturbation method, the concentration and the velocity are expressed as a sum of their cross mean value (\bar{c}, u_0) and a small fluctuation (c', u')

$$c_m(r, \theta, z) = \bar{c}_m(z) + c'_m(r, \theta, z) \quad \text{and} \quad \mathbf{u}_{\text{micro}}(r, \theta, z) = u_0 \mathbf{e}_z + u'(r, \theta, z) \mathbf{e}_z.$$

By replacing the latter expression in equation 2.1.9 we obtain

$$\frac{\partial(\bar{c}_m + c'_m)}{\partial t} + (\mathbf{u}_0 + \mathbf{u}') \cdot \nabla(\bar{c}_m + c'_m) = D_m \Delta c_m + D_m \Delta c'_m.$$

Averaging this equation in the transverse direction, it comes

$$\frac{\partial \bar{c}_m}{\partial t} + u_0 \frac{\partial \bar{c}_m}{\partial z} + \frac{1}{\pi R^2} \frac{\partial}{\partial z} \int u' c'_m r dr d\theta = D_m \frac{\partial^2}{\partial z^2} \bar{c}_m.$$

Except for the integral term, the mean concentration follows the classical law of advection-diffusion. However, this term depending on the correlation between the fluctuation of velocity and concentration can have a significant impact on the transport.

In the frame moving at the velocity \mathbf{u}_0 , we suppose that the concentration field is stationary. Then, at the first order of the ADE, we get

$$u' \frac{\partial \bar{c}_m}{\partial z} = D_m \Delta c'_m.$$

Then, we can calculate c' as a function of the mean gradient and derive the integral term

$$\frac{1}{\pi R^2} \frac{\partial}{\partial z} \int u' c'_m r dr d\theta = -\frac{R^2 u_0^2}{48 D_m} \frac{\partial^2 \bar{c}_m}{\partial z^2}.$$

We deduce that the mean concentration follows an ADE, for which the diffusion coefficient as well as the Taylor dispersion coefficient depends on the heterogeneity of the velocity fields

$$\frac{\partial \bar{c}_m}{\partial t} + u_0 \frac{\partial \bar{c}_m}{\partial z} = (D_m + D_{\text{Taylor}}) \frac{\partial^2 \bar{c}_m}{\partial z^2}, \quad (2.1.11)$$

with $D_{\text{Taylor}} = \frac{R^2 u_0^2}{48 D_m}$.

The example of Taylor dispersion is a typical approach adopted for porous media study: from the ADE law at the microscopic scale, we derive the transport law at the mesoscopic scale. With the same kind of approach, it is possible to derive transport laws at the macroscopic scale.

Effect of the Peclet number on dispersion in porous media

The Peclet number is defined to be the ratio of the rate of advection to the rate of diffusion, it can be written as

$$Pe = \frac{uL}{D_m} \quad (2.1.12)$$

with L the characteristic length, u the mean velocity of the flow and D_m the diffusion coefficient.

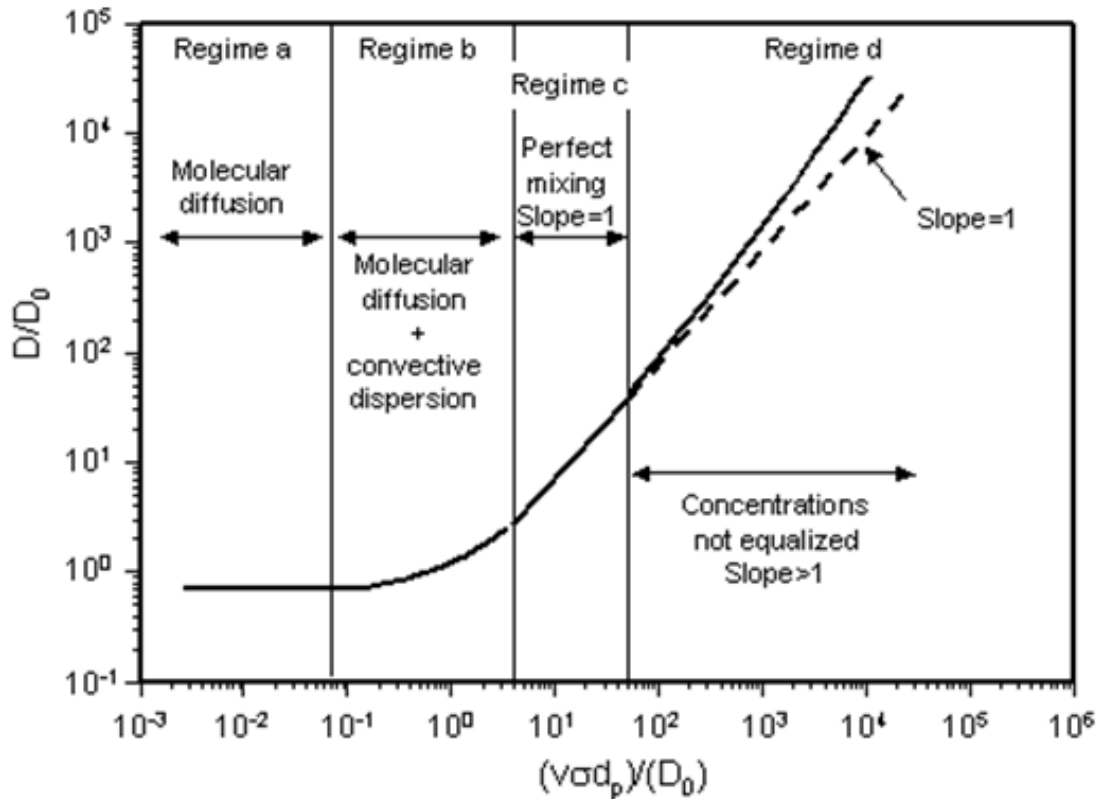


Figure 2.5 – Dependence of dispersion coefficient on Peclet number in different flow regimes. The curve shown approximates longitudinal dispersion in unconsolidated random packs (Adapted from Perkins and Johnston (1963) [124]).

For very low Peclet number, transport is purely diffusive and the dispersion coefficient is of the same order of magnitude of the molecular diffusion coefficient, depending of the medium tortuosity. When the Peclet number increases, dispersion depends in both diffusion and advection, leading to an increase of dispersion. The dependence of the dispersion coefficient according to the Peclet number (see Fig. 2.5) has been thoroughly studied, starting from Perkins and Johnston (1963) [124], and confirmed by a large number of experimental and numerical studies [115]. It highlights several flow regimes for dispersion according to the Peclet number. The first regime (a) shows that at low velocities or high molecular diffusion coefficients, molecular diffusion predominantly governs dispersion, resulting in a constant dispersion coefficient equivalent to the apparent molecular diffusion coefficient, somewhat lower than the true molecular diffusion coefficient due to the tortuosity of the porous medium. The second regime (b) shows that as advective dispersion becomes more effective, both molecular diffusion and convection contribute to the overall dispersion. In the regime (c), the porous medium can be likened to an efficient mixer. For the regime (d), as the Peclet number escalates significantly, the equilibrium between the concentrations within the pores can't be easily achieved, causing the slope to be larger than 1. In the regime (c) and (d), diffusion is often neglected and the coefficient of dispersion is expressed as $D = \lambda u$ with λ the dispersivity and u the mean flow velocity.

Fickian regime and anomalous dispersion

At the mesoscopic or macroscopic scale, a Fickian regime can present a dispersion coefficient different from the molecular diffusion coefficient, as a result of coupling velocity and concentration fluctuations. The origin of the dispersion lies in the fluctuations of the velocity field, that tends to deform the concentration front and produce a spreading at the macroscopic scale.

Velocity fluctuations can have different sources, such as viscosity or surface tension. For passive transport, i.e the concentration does not affect the flow, the velocity field fluctuations are caused mainly by the heterogeneity of the porous structure.

Plus, as we said, mesoscopic or macroscopic dispersion are not necessarily Fickian. Anomalous dispersion can be observed as a transient, before the Fickian regime can be observed, but also as an asymptotic regime, in cases of highly heterogeneous media for example. Nonetheless, as we will discuss later, in theory, dispersion should converge toward a Fickian regime for a finite medium, but the convergence might be so slow that it never occurs. Anomalous dispersion will be thoroughly described in the following section.

2.2 Non-Fickian dispersion in porous media

In porous media, the dispersion can not always be described by the advection-diffusion equation. In particular, the width of the plume following a tracer injection will not necessarily spread at the square root of the time. In other words, the standard deviation of the distribution of concentration doesn't necessarily grow as \sqrt{Dt} [108] [97] [158].

There are numerous sources of non-Fickian dispersion, such as the presence of fractures in the porous media [12], or heterogeneity at the mesoscopic or macroscopic scale [131] that can induce great differences in the velocity fields, and extreme displacement of particles. Notably, unsaturated porous media has recently shown non-Fickian behavior [81].

In the previous section, we described Fickian dispersion as an empirical result deriving from the first Fick law. However, the other classic approach to describe diffusion is the statistical mechanics: the Brownian motion, based on the a random walk model. It leads to the same results as Fick's law, and notably the ADE equation. However, the random walk concept can be more general than Brownian motion, and can be used to describe anomalous dispersion.

In this section, we will describe the conditions for dispersion to converge toward Fickian dispersion by considering the random walk process. Subsequently, we will present some models that have been developed to predict non-Fickian dispersion in porous media and how they can be used. The next section will be devoted to the dispersion in the specific case of unsaturated porous media.

2.2.1 Observation of non-Fickian dispersion in porous media

Context for non-Fickian dispersion in porous media

Non-Fickian dispersion has been observed a great number of times when studying dispersion in porous media, whether it is in laboratory studies, or in natural porous media [18]. This has also been observed for experiments of different scales, from a few centimeters (micromodels) [93], a few meters in laboratory experiments with columns of soil [121], sand or glass beads [33], to wider scales in hydrology experiments in the field [71].

Whereas non-Fickian dispersion is usually noticed for media with particular features, such as strong heterogeneity, fractures [12], fractal designs [132] or unsaturated medium [81], it also has been reported for macroscopically homogeneous media [183]. Hence, non-Fickian dispersion is rather common in porous media [18].

Manifestation of non-Fickian dispersion

Usually, dispersion at field scale is studied through Breakthrough Curves (BTC) [138] [105]. A tracer is injected in the medium at one side and the concentration is measured at another side as a function of time. BTC are also used in laboratory experiments through columns of medium (at a smaller scale), and even in simulation works. An example of BTC is given Fig. 2.6.

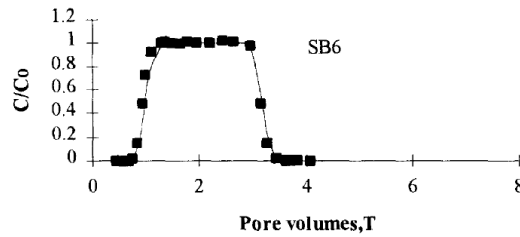


Figure 2.6 – Example of a symmetric Breakthrough Curve (BTC) for a pulse injection. From Maroqa *et al* (1997) [107]

The non-Fickian nature of the dispersion may be observed from the BTC curves. If the dispersion is strongly anomalous, the BTC curves will show asymmetry, a long tailing at long times, as well as an early arrivals of concentration. In Fig. 2.7, we see that for low heterogeneity the BTC curve is rather symmetrical, and with increasing the porous medium heterogeneity, the non-Fickian character can be observed with an increased asymmetry of the curves.

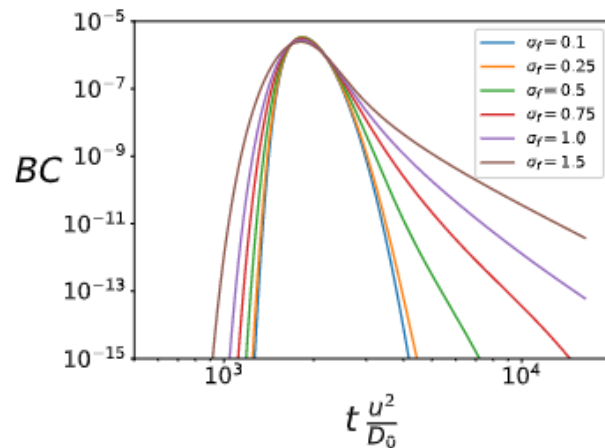


Figure 2.7 – Simulations of breakthrough curves (BC) as a function of dimensionless time $t \frac{u^2}{D_0}$ with different levels of permeability fluctuations σ_f . From Talon, Ollivier-Triquet *et al.* 2023 [151].

However, the BTC shape will not necessarily reveal anomalous dispersion, especially when the dispersion is not too anomalous. Indeed, the BTC can have a regular shape even when the dispersion is not Fickian. However, several BTC at different depths of penetration of the concentration in the medium allow to determine non-Fickian behavior [26] [118] (Fig. 2.8). Indeed, the BTC fitted with an ADE model will give a coefficient of dispersion different for each depth of the medium, typically a coefficient of dispersion that grows with time. Some authors conclude in a coefficient of dispersion non constant in space (or in time, given that $t_{\text{exp}} = x_{\text{exp}}/u_{\text{mean}}$), such as in Silliman *et al.* (1987) [138], or Bromly *et al.* (2004) [26].

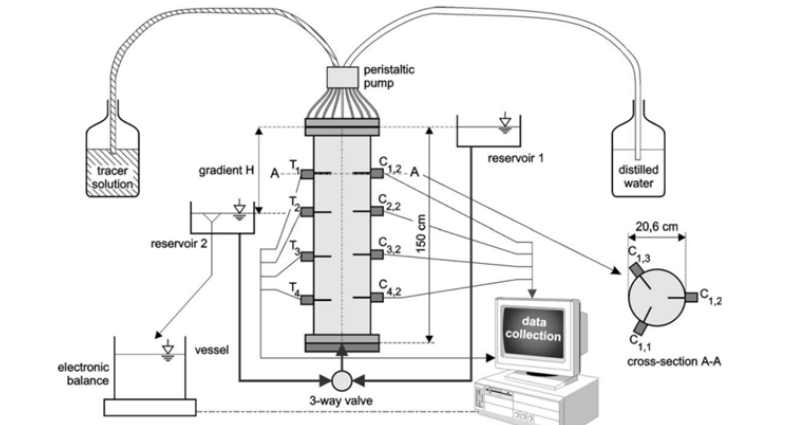


Figure 2.8 – Experimental conditions with concentration measurement at different depths, from Nützmann *et al.* (2002)

Actually, the changing dispersion coefficient accounts for the anomalous dispersion: the standard deviation is not proportional to the square root of the time and we can not rigorously define a dispersion coefficient properly in this case. Indeed, the dispersion coefficient is defined as a constant in the Fickian model, during the asymptotic regime.

$$D = \lim_{t \rightarrow \infty} \frac{1}{2} \frac{d\sigma^2}{dt}$$

Hence, one should be careful employing the term dispersion coefficient when there is evidence of non-Fickian dispersion. Furthermore, one should be cautious when fitting ADE solutions to BTC curves when indications of non Fickian dispersion are present. Indeed the fit might be good but if the model is not adequate, the results might be misleading.

The non-Fickian nature of dispersion is more obvious with the concentration distribution in the medium. However, it is not always accessible, particularly in field or laboratory experiments. Consequently, concentration profiles or concentration fields are less commonly used than BTC to study dispersion even though they contain more information.

Nonetheless, concentration fields can be obtained in some cases, typically simulation work where the concentration can be derived everywhere in the medium for each time step (for example with pore-network modeling or Lattice-Boltzmann simulations) [106], but also for some experimental work where it is possible to have access to concentration profiles. This is the case of micromodels for example [93] [104]. Then, if the concentration profile is not Gaussian, and/or the standard deviation is not proportional to the square root of t , the dispersion is non-Fickian.

Need for a model for non-Fickian dispersion

As explained earlier, non-Fickian dispersion is rather common in porous media, which is why numerous authors have developed concepts and innovative models to predict anomalous dispersion, especially in the last decades [105] [18] [139] [8] [15]. Particularly, it avoids the ambiguity behind the use of coefficient of dispersion or dispersivity alone to characterize the dispersion, which is not truly adequate.

The increased heterogeneity in an unsaturated porous medium can lead to non-Fickian dispersion. Yet, many authors dealing with the subject use the ADE model to fit their data, and run their analysis on the evolution of the dispersion coefficient with saturation. If the tendencies they observe are still valuable information, the use of a model accounting for the anomalous dispersion would be more appropriate and would avoid ambiguities as well as bad interpretations of the data.

The models developed for non-Fickian dispersion can be quite complex and are not necessarily well understood, especially in experimental fields. However, some experimenters used non-Fickian models to process their data [121] [107].

2.2.2 Random walk and non-Fickian dispersion

Before we can understand what lies behind these models, first we need to come back at the roots of the dispersion, the Brownian motion or the random walk, and what hypotheses have been made to derive the ADE. Indeed, we will see how the advection-diffusion equation can be a particular case of dispersion under less restrictive hypothesis [15] [14].

Brownian motion: consequence of random walk for finite variance processes

Before introducing the Brownian motion and the random walk concept, let first recall the Central Limit Theorem which will be useful in the following. We consider X_1, X_2, \dots, X_n a random sample of n random variables, independent and identically distributed that follows a distribution characterized by a mean μ and a finite variance σ^2 . Denoting $S_n = \frac{1}{n} \sum_{k=1}^n X_k$ the mean of these samples, we have the following convergence for distribution p of the random variable

$$\frac{\sqrt{n}}{\sigma}(S_n - \mu) \xrightarrow[n \rightarrow \infty]{\text{law}} \mathcal{N}(0,1),$$

with $\mathcal{N}(0,1)$ the normal distribution with the probability density function given by

$$\varphi(t) = \frac{1}{\sqrt{2\pi}} e^{-\frac{t^2}{2}}.$$

In 1908, Einstein theorised the Brownian motion as the consequence of the random walk [40]. The simplest consideration of the random walk consists in this: for each step of time, which is constant, the particle moves from a distance L , also constant, in a random direction of space, as can be seen Fig. 2.9.

In a more general approach, the particle displacements follow a probability distribution of mean length of displacement μ . We can apply the Central Limit theorem with X_i the displacement of the particle, the time step i , and nS_n the position of the particle. Assuming that the X_i are independent and identically distributed, and follow a distribution characterized by a mean μ and a finite variance σ_0 , the random serie $\sqrt{n}(S_n - \mu)/\sigma_0$ converges towards $\mathcal{N}(0,1)$.

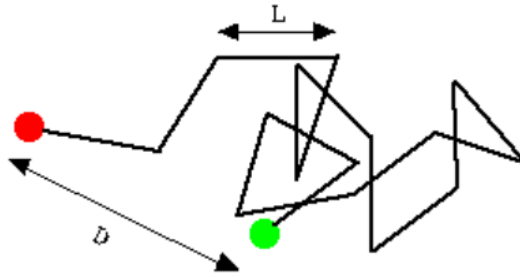


Figure 2.9 – Schematic of a random walk. Red dot: starting point. Green dot: End point. The steps length is L , and the final distance between the starting point and the end point is noted D .

With $n = t/T_0$ and t the time since the the start of the random walk, T_0 the time step, $x(t)$ the particle position at time t is given by $S_n n$. Hence, the mean position is $\mu n = \mu t/T_0 = vt$ with $v = \mu/T_0$ the drift. The standard deviation is given by $\sigma = \sigma_0 \sqrt{n}$ or $\sigma(t) = \frac{\sigma_0}{\sqrt{T_0}} \sqrt{t} = \sqrt{2Dt}$ with $D = \frac{\sigma_0^2}{2T_0}$ the diffusion coefficient.

The large time limit probability of a particle position is given by

$$p(x,t) = \frac{1}{\sqrt{2\pi Dt}} e^{-\frac{(x-vt)^2}{2Dt}}, \quad (2.2.1)$$

with v the drift.

The distribution mean position and variance give the traditional results of the Brownian motion, the particle position $x(t)$ at the time t is given by

$$\langle x(t) - x_0 \rangle = vt,$$

and

$$\langle (x(t) - x_0 - vt)^2 \rangle = 2Dt.$$

Assuming no drift ($\mu = 0$ or $v = 0$), the latter equations becomes

$$\langle x(t) - x_0 \rangle = 0, \quad (2.2.2)$$

and

$$\langle (x(t) - x_0)^2 \rangle = 2Dt, \quad (2.2.3)$$

The variance is proportional to time, with a diffusion coefficient D . We see that we find the same results for the evolution of the first and second moments as for the solution of the ADE equation as described section 2.1.3.

The limit distribution of a particle position $p(x,t)$ (equation 2.2.1) fully describes the result of the random walk. Furthermore, the distribution $p(x,t)$ is the fundamental solution of the Fokker-Plank equation, with v the drift

$$\frac{\partial p}{\partial t} + \nabla(vp) = \Delta(Dp). \quad (2.2.4)$$

It comes that the particle position probability follows the Fokker-Plank equation. Plus, for a great number of particles, the density of particles or concentration $c(x,t)$ follows the advection-diffusion equation and the molecular diffusion coefficient is noted D_m

$$\frac{\partial c}{\partial t} + v \cdot \nabla c = D_m \Delta c. \quad (2.2.5)$$

For a Dirac initial condition initially located at $x = 0$ and a one dimensional problem, the solution for the concentration $c(x,t)$ is given by a Gaussian

$$c(x,t) = \frac{1}{\sqrt{4\pi D_m t}} e^{-\frac{(x-vt)^2}{4D_m t}}. \quad (2.2.6)$$

Finally, we see here that Brownian motion is obtained if the distribution of probability of particle displacement are identical, independent and characterized by a finite variance. At the microscopic scale, we are in the classical situation of two miscible fluids in contact and the microscopic velocity and concentration follow the ADE.

Actually, the convergence toward Brownian motion needs less strict hypotheses [20] [15] [14]. Indeed, in the late 20th century, mathematicians came with some generalizations of the Central Limit Theorem, such as the Lyapunov extension, that states that under some conditions, the distributions of the X_i do not need to be identical, but independent and with finite variance to obtain a convergence to the normal distribution.

In conclusion, the main condition to converge toward the Brownian motion, i.e, normal dispersion, is to have finite variance for the particles velocities [18]. Consequently, anomalous dispersion, in the asymptotic regime, can occur only if the displacement of particles shows infinite variance. Since this is quite unlikely, it is reasonable to think that at later times, dispersion is Fickian.

Link between transient regime and non-Fickian regime

As we stated in the preceding section, the asymptotic nature of the dispersion is anomalous only if the displacement of particle have infinite variance. However, in the case of finite but high values of variances, the convergence toward the ADE might be extremely long, and the transient regime will show features of non-Fickian dispersion.

In the case of porous media, the displacements of particles can take extreme values due to zones of really weak velocities and mean paths with greater velocities. Thus, the distribution variance can be extremely large. Nonetheless, infinite variance in a finite medium is not physically possible (the integral is finite). Consequently, the theory states that the dispersion should converge toward normal dispersion after a very long time [18] [17] [16].

However, in the case of porous media dispersion experiments, the duration of the experiment and the size of the medium is limited, which is why it is possible not to observe the convergence toward normal dispersion. Several dispersion experiments show anomalous dispersion even after a year of experiment [15]. Hence, the anomalous dispersion in porous media corresponds to a transient regime, but that transient can be so long that the asymptotic regime is never observed.

If the variance is sufficiently high, we might consider that the dispersion is anomalous nonetheless, especially for prediction purposes, but it is important to keep in mind that if what we observed is a transient or pre-asymptotic regime, it might evolve at longer times.

2.2.3 Modelling non-Fickian dispersion

A great diversity of models

There is abundant literature about modeling anomalous dispersion in porous media. Indeed, a great diversity of models has been developed in the last decades, but it is a bit difficult to find consistency between all these different models at first glance [139]. We can mention the most common ones, such as the Mobile-Immobile model, the Multirate mass transfer model, the Continuous Random Walk model (CTRW), the fractional (fADE), Lévy flights, dual porosity models, ADE with non constant coefficients.

Most of these models are non-local formulations in time, which means that they allow non equilibrium in the porous media, for example delayed storage mobilization or delayed drainage for the concentration, it is usually referenced as a memory effect.

The great diversity of models is a consequence of the different scientific fields involved in the research in dispersion in porous media. Theoreticians and researchers in applied mathematics developed very general models around the generalization of the random walk. This is the case of CTRW ([18]) and fractional ADE [15]. However, those models are rarely used by experimenters in hydrology, notably because they require a lot of parameters. On the other hand, the MIM model (Mobile Immobile) is widely used by experimenters [118] [121] [107], next to the ADE, because it is easy to implement.

The CTRW, fractional ADE and MRMT allow distributions with infinite variance, i.e, an asymptotic non-Fickian regime. The MIM, however, does not allow such a feature, and then can only model transient non-Fickian regime. However, as explained in the previous section, the non-Fickian behavior of dispersion observed in real condition is a transient, so this model could still be adequate to model non-Fickian regime.

We will only describe the MIM model and CTRW because they are commonly used by researchers studying anomalous transport, even if these models are not a primal interest of this thesis. However, for interested readers, a thorough description of the models can be found in Appendix chapter 9 9.1.

Modeling with the Mobile-Immobile concept

In this section, we will present the MIM model, how it can be applied to estimate parameters of the dispersion and used in the prediction of non-Fickian dispersion in porous media. Then, we will discuss briefly the advantages and the limits of such methods.

MIM model

Observations in porous media show that there are often great difference of velocity flow in the medium, with preferential flow paths and stagnant zones with nearly no flow. In Fig. 2.10 showing the concentration field in a micromodel with a continuous injection, we can see that there are some green zones of low concentration left behind. The concentration in these zones reaches the tracer concentration much later because the flow there is almost stagnant and the mass transfer is mostly diffusive. Fig. 2.11 shows the case of an unsaturated flow in a porous media (micromodel) for which the velocity field has been estimated, the blue zones correspond to stagnant flow or immobile region with nearly zero velocity.

These discrepancies in the flow field are held responsible for the long tailing in the distributions of concentration in dispersion experiments. The dispersion in the stagnant

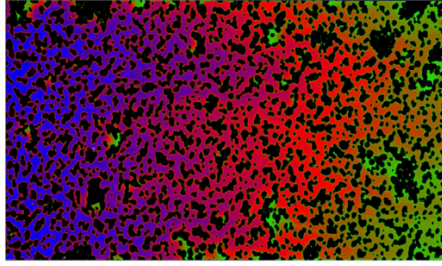


Figure 2.10 – Concentration field in a porous media (micromodel), blue for high concentration and green for low concentration, from [104].

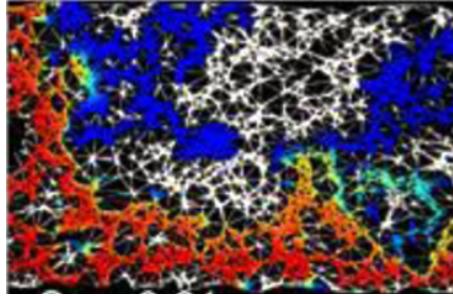


Figure 2.11 – Velocity field in a porous media (micromodel), blue for low velocity and red for high velocity, from [93].

zones is controlled mainly by diffusion (low Peclet number), and the dispersion in the main flow paths is rather controlled by advection (high Peclet) [81].

The MIM model is based on these observations, and presumes that the porous medium is divided into a mobile zone and an immobile zone, where the flow is stagnant. The model allows a state of non equilibrium between the immobile zone characterized by the concentration C_{im} and the mobile zone characterized by the concentration C_m and a mean flow velocity v . The solute transfer between these regions is modeled by a diffusive exchange rate. The equations of the model (1D) are given by

$$S_m \frac{\partial C_m}{\partial t} = -v S_m \nabla C_m + S_m D_m \Delta C_m - \frac{\alpha}{\phi} (C_m - C_{im}), \quad (2.2.7a)$$

$$S_{im} \phi \frac{\partial C_{im}}{\partial t} = \alpha (C_{im} - C_m), \quad (2.2.7b)$$

$$SC = S_m C_m + S_{im} C_{im}, \quad (2.2.7c)$$

with α the transfer coefficient from the mobile to the immobile zone, ϕ the porosity, D_m the hydrodynamic dispersion coefficient and v the effective flow velocity in the flowing region. S_m is the water saturation of the mobile zone and S_{im} the water saturation of the immobile zone, and $S_m + S_{im} = S$ the total saturation. C_m the mean concentration in the mobile zone and C_{im} the concentration in the immobile zone.

The concentration in the mobile zone is controlled by the classical advection-diffusion, except for a sink term related to the diffusion to the immobile zone. This transfer of concentration is linear, proportional to the difference of concentration between the zones. Consequently, the evolution of concentration in the immobile zone is completely determined by diffusion from the mobile zone, through the transfer of concentration as a source term.

In the asymptotic regime for which a dispersion coefficient can be defined, a correction to the diffusion coefficient in the ADE, taking into account the transfer to the immobile zones is given by [93] [141]

$$D = \phi D_m + (1 - \phi)^2 \frac{v^2}{\phi \alpha S},$$

with ϕ the proportion of mobile zone ($\phi = S_m/S$). The first term represents the dispersion in the mobile region (D_m), and the second term corresponds to the apparent dispersion resulting of solute exchange between the mobile and immobile regions.

The MIM model is defined through four fitting parameters, ϕ , α , D_m and v , the two first parameters define the interaction between the mobile and immobile zone. They are obtained through curve fitting. They are supposed to be constant in the medium and in time.

Applications of the MIM model, limitations

The MIM has been widely used to fit and predict anomalous dispersion, especially for unsaturated porous media, because it is rather easy to implement. The MIM model is often compared to the standard ADE [121] [107] [81] [93], the results of the fits are often far better than the fits with ADE solutions, especially for long tailed and asymmetric BTC that can not be well described by ADE solutions, since they are exhibiting anomalous behavior.

However, whereas the fits are rather good with experimental data, the predictions of the MIM model often show discrepancies. For example, in Bromly and Hinz, 2004 [26], the MIM model fits well with the BTC showing anomalous characteristics. However, the predictions in the depths of the column are not good, and better predictions are found with other models such as CTRW. Plus, some authors such as Hasan, 2019 [81], brought to light that the coefficients of the MIM, constant in the model, would vary in time when fitted with experimental data, which questions the adequacy of the model. In the case of unsaturated porous media, one issue is that it does not take into account the topology of the phase distribution [93], [81].

Generalization of the random walk: Continuous Time Random Walk model (CTRW)

Asymptotic non-Fickian dispersion

As explained in the preceding section, asymptotic non-Fickian dispersion implies infinite variance of the displacement. Even if this kind of dispersion is not physically possible, at least in porous media, it can be used to model dispersion with extreme values of variance.

Generalizations of random walk were introduced to model anomalous dispersion, allowing distributions of displacement or transition times with infinite variances. This concept allowed the development of models such as the Continuous Time Random Walk (CTRW) [18], the modeling of dispersion with fractional ADE or Levy flight [15]. These models will be explained in details in the following section.

Remark concerning the CLT:

In cases of infinite variances for the random walk, whether it is in time transition or displacements, the Central Limit Theorem is no longer valid. Gnedenko and Kolmogorov (1854) [67] proposed a generalization of the theorem for infinite variances under certain

restrictive conditions. Instead of converging toward a Gaussian, there is a positive integer α such that the density converges to an α -stable Levy density.

If $(X_k)_{k \in \mathbb{N}}$ are random variables identically distributed, complying with the restrictive conditions, characterized by their mean μ , then the sum of these converges in distribution to an α -stable random variable Y

$$\frac{1}{\sigma n^{\frac{1}{\alpha}}} \left(\sum_{k=1}^n X_k - n\mu \right) \xrightarrow[n \rightarrow \infty]{\text{law}} Y,$$

with σ a constant.

Many infinite variance random variables such as Pareto or power law converge toward a Levy α -stable random variable. Particularly, for power-law tail distribution decreasing a $x^{-\alpha-1}$, where $0 < \alpha < 2$ (if $\alpha \geq 2$), then the variance is finite according to Riemann criteria), they converge toward an α -stable random variable Y_α .

The stable variables are different from the normal variable because the tails of the distributions decay as a power-law. If Y is a stable variable, then the probability p for large y values is given by

$$p(Y > y) \propto y^{-\alpha} \quad (2.2.8)$$

This generalized version of the central limit theorem can be used to describe anomalous dispersion, notably for fractional advection-dispersion equations [15]. A generalisation of the random walk consists on a random walk with fixed time steps continuous in space (Levy flights), for which the displacement follows any probability distribution, as seen Fig. 2.12, then the particle distribution can be described by an α -stable random variable.

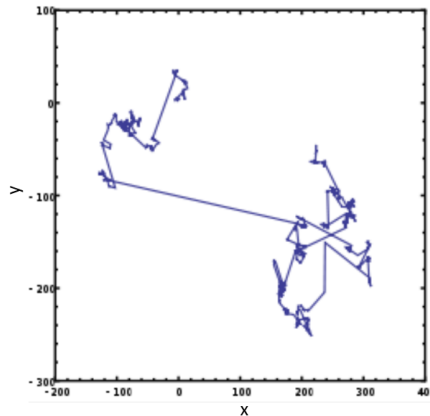


Figure 2.12 – Illustration of a random walk continuous in space: Levy Flight

Principle of the CTRW

The random walk with constant time and displacement steps converges to Brownian motion, hence Fickian dispersion. The principle of the CTRW is to generalize the random walk to any time transition distribution, each step of the random walk can occur with a waiting time that follows any given probability distribution [18] [17] [16]. This is why it is called Continuous Time Random Walk. An illustration of such a random walk is given Fig. 2.13.

The model is by essence extremely general, and almost all others models can be formulated as particular cases of the CTRW. We will see later that those formulations are formally equivalent.

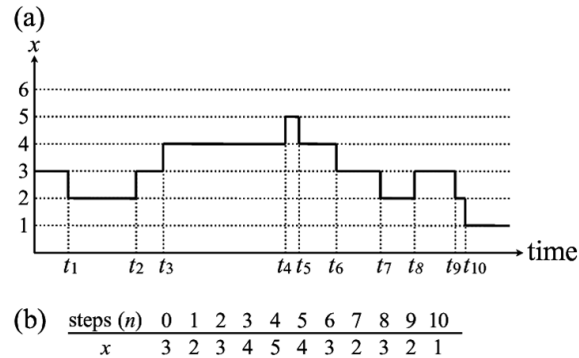


Figure 2.13 – Illustration of a Continuous Time Random Walk

As we explained in the previous section 2.2.2, the random walk will eventually converge toward Brownian motion, unless the probability distribution of transition time has infinite variance. In other words, the CTRW will model pre-asymptotic anomalous transport, converging toward ADE if the chosen distribution has finite variance, and conversely, asymptotic anomalous transport will be obtained for distributions with infinite variance. The CTRW formulation can be found in the appendix Chapter 9, section 9.1.

Application of the CTRW

The CTRW has been successfully applied to a diversity of situations, for highly heterogeneous and fractured media [17] but also macroscopically homogeneous media [18]. Even though it is not widely used yet by experimenters, maybe because the mathematical concepts are a bit complex at first glance, some examples of CTRW model used in the study of dispersion in unsaturated media can be found [26].

Equivalence between models

Common principle

Even though the models described in this section can be based on different concepts, they share some basic principles. If we restrict these models to a non locality in the time, which means that the mobilization of the concentration does not depend uniquely of the time but also of the historic (memory function), those formulations can be equivalent [139].

Indeed, they all consist on the expression of a linear mass transfer between the mobile and immobile regions, and whether this transfer is characterized by a residence time distribution, a memory function or fractional derivative is not critical.

Equivalences between models

Berkowitz *et al.* (2001) [17] demonstrated the equivalence between the fractional ADE and CTRW. They highlight that fractional ADE are not different models from the CTRW; rather they are asymptotic cases of the CTRW theory. They explicit the equivalence for fractional ADE and CTRW in term of probability of transition distribution in Laplace space, for both time fADE and space fADE (Lévy flights).

However, the diversity of approaches makes more difficult a global comprehension, this is why Silva *et al.* (2004) [140] tried to unify the formulations through an Multi-Rate Mass Transfer formulation, on the basis of the work undertaken by several other authors ([16], [23], [77]). They give the equivalence between the MRMT models parameters and the other model formulations (cf the appendix Chapter 9, section 9.1). An overview of the non-Fickian dispersion model is also given in the appendix.

2.3 Properties of a two-phase flow in porous media

2.3.1 Generalities: physics at the interface

To gain a deeper comprehension of dispersion within unsaturated porous materials, it is imperative to grasp the interplay between multiphase fluid flow and the porous medium itself. This entails examining the dynamics occurring at the fluid interface, as it dictates the dynamics of flow at the pore scale.

Therefore, to characterize two phase flow in a porous media, we will introduce the physics arising at the interface between fluids [27] [86] [173].

Surface tension

At the interface between two phases, there is a surface tension. The strength dF arising from the surface tension γ is given by $dF = \gamma dl$. From each side of the interface, the pressure difference is given by Laplace's law

$$\Delta P = \gamma \left(\frac{1}{R_1} + \frac{1}{R_2} \right),$$

with R_1 and R_2 the curvature radii of the interface (Fig. 2.14). Their sign depends of the convexity of the interface.

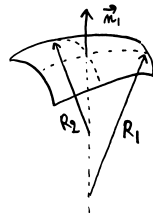


Figure 2.14 – Definition of the curvature radii

One of the most remarkable consequences of surface tension in porous media is the Jurin's law, which will govern the water rise in a capillary, and consequently in a pore, as shown in Fig. 2.15. In capillary of radius r_0 immersed in a liquid, the fluid rises up the

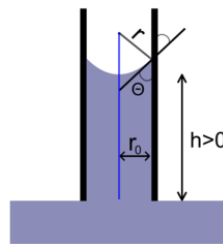


Figure 2.15 – Schematic of Jurin's law

height given by

$$h = \frac{2\gamma \cos \theta}{\rho g r_0},$$

with θ the contact angle, ρ the density. For a wetting fluid ($\cos \theta > 0$), Jurin's law predicts a capillary rise. For a non wetting fluid ($\cos \theta < 0$), Jurin's law predicts a capillary drop.

Capillary number

The capillary number, denoted Ca , is a dimensionless quantity representing the relative effect of the viscous drag forces versus the surface tension:

$$Ca = \frac{\mu v}{\gamma},$$

where μ is the dynamic viscosity of the liquid, v is a characteristic velocity and γ the surface tension.

2.3.2 Two phase flow in porous media: quasi-static conditions

Imbibition

Imbibition is the injection of a wetting fluid in a porous media saturated with a non wetting fluid, typically the infiltration of water in a wall by capillarity.

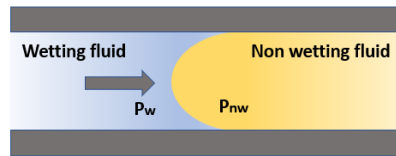


Figure 2.16 – Imbibition at the pore scale.

At the pore scale, $\Delta P = P_{nw} - P_w = \frac{4\gamma \cos \theta}{d} > 0$, with d the pore diameter, P_{nw} the pressure in the non wetting fluid, P_w the pressure in the wetting fluid, and θ the contact angle. Hence, the surface tension favors the displacement of fluid, which means that this is a spontaneous invasion (Fig. 2.16). Plus, the smaller the pore, the more efficient the imbibition will be.

Drainage

Drainage is when a non-wetting fluid displaces a wetting-fluid. In this case, capillary

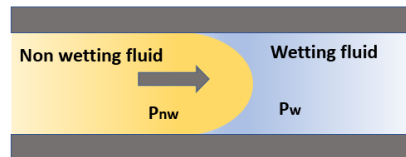


Figure 2.17 – Drainage at the pore scale.

forces oppose the displacement (Fig 2.17). Thus, there must be an excess of pressure to impose the drainage. The pressure must be particularly high to fill the small pores. Indeed, invasion is possible in a pore if $\Delta P > \frac{4\gamma \cos \theta}{d}$. In other words, if a pressure ΔP is imposed, only pores for which $d > \frac{4\gamma \cos \theta}{\Delta P} = d_{\min}$ will be invaded.

2.3.3 Dynamics of a two phase flow in porous media

In the previous section, we were considering events of drainage and imbibition in quasi-static conditions. In these cases, the pressure for the non wetting fluid P_{nw} and the pressure for the wetting fluid P_w are uniformly distributed. In this configuration, small pores would be invaded in priority during imbibition, and a pore whose diameters is superior to the threshold value ($d = \frac{4\gamma \cos \theta}{\Delta P}$) would be filled during drainage.

Now, we consider a flow in the porous medium. There will be a pressure loss in the medium, due to viscous forces. There is now a competition between capillary forces and viscous forces. The capillary forces, illustrated with Figure 2.18, can be written as

$$dF_\gamma = \gamma dx,$$

and the viscous forces as

$$F_\nu = \mu v L, \quad (2.3.1)$$

with v the mean velocity, dx the distance travelled by the fluid and L the height of the domain.

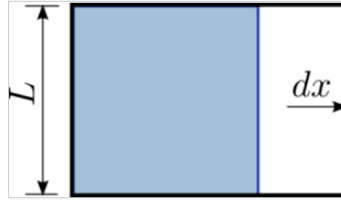


Figure 2.18 – Illustration of the force necessary to increase the surface area. $dF = \gamma dx$
 $F = \gamma L$ for one interface.

Therefore, capillarity favors the filling of small pores when viscosity penalizes long paths. This competition is characterized by the capillary number $Ca = \mu U_0 / \gamma$. This competition between capillary and viscous forces is the origin of the capillary fingering phenomena. For low Ca , capillary forces are dominant and capillary fingering can be observed, since pores are filled as a function of their radius (Fig. 2.19). If the capillary number is high, viscous forces are dominant and the front of imbibition will be rather flat.

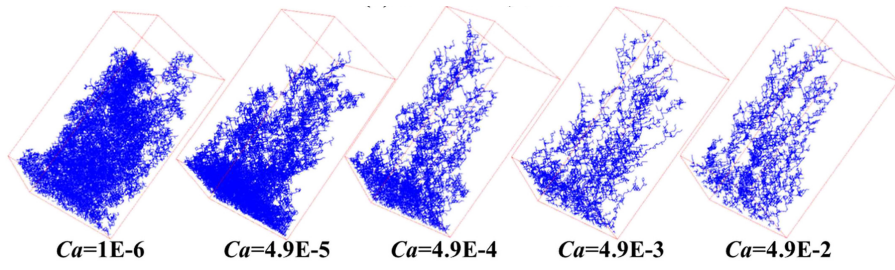


Figure 2.19 – Capillary fingering: effect of increasing Ca from left to right. Adapted from Tang (2020) [153]

However, even for high values of the capillary numbers, fingering can be observed when the two fluids have a different viscosity. This is called the Saffman-Taylor instability, or viscous fingering. A difference of density between the fluids can also lead to fingering, this is called the Rayleigh-Taylor instability or density fingering.

Generalised Darcy equations: relative permeability

In the previous sections, we only considered a fluid pushing another fluid. Now, we consider a simultaneous injection of two fluids, a wetting fluid (denoted w) and a non-wetting fluid (denoted nw). For each phase, we define a velocity rate³ (\vec{u}_w and \vec{u}_{nw}) and a pressure (P_w and P_{nw}). The saturation of each phase are noted S_w and $S_{nw}(= 1 - S_w)$ respectively. The generalized Darcy equations writes

$$\vec{u}_w = -K \frac{kr_w(S_w)}{\mu_w} (\nabla P_w - \rho_w \vec{g}) \quad \text{and} \quad \vec{u}_{nw} = -K \frac{kr_{nw}(S_w)}{\mu_{nw}} (\nabla P_{nw} - \rho_{nw} \vec{g}),$$

where K is the medium permeability. kr_w and kr_{nw} are the relative permeabilities, μ_w and μ_{nw} are the viscosities of the wetting and the non-wetting phases respectively. The phases pressure P_w and P_{nw} are not equal, but are related with the equation

$$P_{nw}(S_w) - P_w(S_w) = P_c(S_w),$$

where P_c is the capillary pressure, a function of the saturation.

Omitting source terms and phase compressibility, the mass conservation of the phases are given by

$$\frac{\partial}{\partial t}(\phi S_w) + \nabla \cdot \vec{u}_w = 0, \tag{2.3.2a}$$

$$\frac{\partial}{\partial t}(\phi S_{nw}) + \nabla \cdot \vec{u}_{nw} = 0. \tag{2.3.2b}$$

The relative permeabilities kr_w and kr_{nw} and the capillary pressure P_c are functions of the wetting phase saturation S_w to determine. There can be different kinds of models, experimental or numerical [51, 84].

2.3.4 Flow with a trapped phase

In a natural porous medium, many events can lead to the trapping of gas in the medium, such as a combination of drainage, imbibition and drying. Hence, the distribution of gas clusters in the system results from the hydrological history of the porous media. Many phenomena are involved in the trapping, and lead to the fragmentation of gas by the porous medium.

Bubble creation mechanisms

We will describe a few processes that lead to bubble creation at the pore level, in the case of drainage in a porous medium [135] [127] [130]. Bubble creation during drainage can follow three main mechanisms.

Snap-off

The snap-off occurs when gas penetrates through a constriction filled with liquid. Then, the sudden decrease in local capillary pressure in the constriction leads to the refill of liquid in the constriction. Consequently, a discontinuous gas bubble is formed and a lamella is created in the constriction perpendicular to the flow direction (Fig. 2.20).

The decrease in capillary pressure necessary to induce the snap-off depends on the geometry of the constriction. For instance, in the case of straight cylindrical throats, the capillary pressure must decrease to half of the one capillary pressure at the entrance. Basically, smaller pore throats lead more easily to snap-off events.

3. volumetric mean

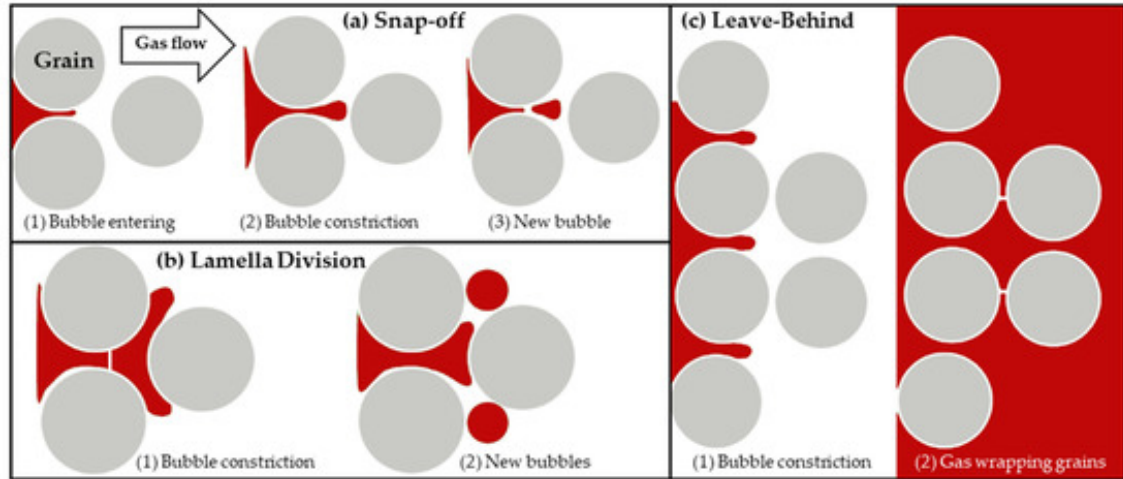


Figure 2.20 – Illustration of bubble creation mechanisms, from Haggerty (2023) [78]

Lamella division

It occurs when a pre-existing liquid lamella goes through a bifurcation in the porous medium, and simultaneously invades both passages, dividing into two. It results in the creation of a net new lamella (Fig 2.20).

Leave behind

When a gas phase invades two adjacent pore bodies, it leaves a liquid filled constriction intact and isolated as a new lamella (Fig 2.20). Those different mechanisms depend strongly on the capillary number. We observe high fragmentation of gas at high capillary numbers (hence smaller clusters) [175].

Residual saturation resulting from a two phase flow

For a simultaneous air-water injection, in an artificial porous medium initially saturated in water, authors found that a steady state can be reached ([150] [35]), for which the air is transported in disconnected bubbles. The bubbles are either mobile or trapped, and sometimes trapped bubbles can coalesce with mobile ones and leave the medium.

The saturation at steady state after stopping the air injection depends on the flow history. For different initial conditions, the resulting trapped phase might not be the same, and it will be mainly determined by the maximal value of the capillary number reached during the flow history. In other words, for a air-water co-injection, the saturation at the steady state will depend mainly of the maximal flow-rate that has been imposed during the flow history. Indeed, in the figure 2.21, we see that at lower Ca values, when capillary forces are dominant, the saturation value depends significantly on the initial phase configuration or on the flow history. However, at higher Ca , the saturation becomes independent of the initial configuration and it follows a master curve converging toward an asymptotic residual value.

Distribution of ganglia resulting from a two-phase flow

We consider two non miscible fluids injected in a porous media, whether it is a co-injection of fluids, cycles of drainage and imbibitions, or even more complex two phase

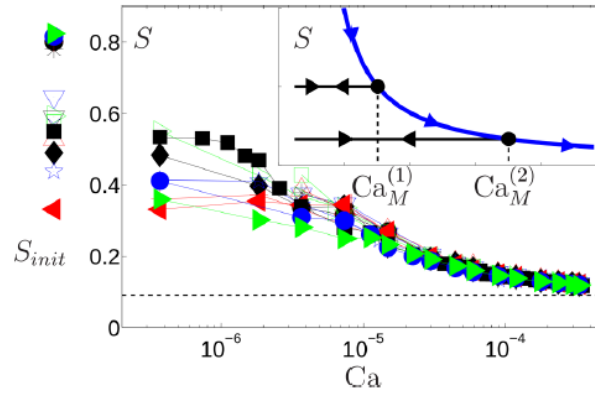


Figure 2.21 – Residual saturation of non wetting fluid VS Ca for different initial conditions, from Chevalier *et al.* (2015).

flow. When the saturation of the wetting phase becomes large enough, ganglia of the non-wetting phase ends up disconnected. It results in the trapping of the non wetting phase. Then, at a steady state, how will the non wetting phase be trapped in the medium, and particularly, what kind of distribution will the ganglia adopt?

Authors generally agree in a power law distribution for the ganglia size, with a cut-off at large sizes (compared to the mean pore throat).

Two phase flow air-water: gas bubbles distributions

For a simultaneous injection of air and water, at the steady state, Chevalier *et al.* (2015) [35] and Tallakstad *et al.* (2009) [150] show that the distribution of the trapped phase is given by a power law with cut-off [150], [35], [91] such as:

$$p(l) = l^{-\phi} h\left(\frac{l}{l^*}\right),$$

with p the probability distribution of the ganglia size, h the cut-off function, and l^* the cut-off size. The probability distributions of bubbles size is represented in Fig 2.22.

In Tallakstad [150], they find a power law coefficient $\phi = 2.07$ and they choose an exponential cut-off function $h(l/l^*) = e^{-l/l^*}$. They also note a cut-off for small sizes. Chevalier *et al.* [35] find a power law coefficient close to 2 for large sizes and $\frac{1}{2}$ for smaller sizes. They show that the cut-off size is inversely proportional to the capillary number:

$$l^* \propto \frac{1}{Ca}.$$

In other words, the maximal bubble size depends on the maximal flow rate that has been injected in the system.

Trapping of bubbles in the porous medium

When disconnected, air bubbles are transported in the porous medium, some of them will follow mean flow paths and others will get stuck in zones of low velocity flow, or dead ends. The trapping results from an interaction between the porous medium structural properties and the flow history. Indeed, the pore sizes distribution, as well as the pore throat sizes will influence the snap-off mechanism, and the fragmentation of the non-wetting phase, and the gas bubbles will get stuck preferentially in zones of low flow velocity

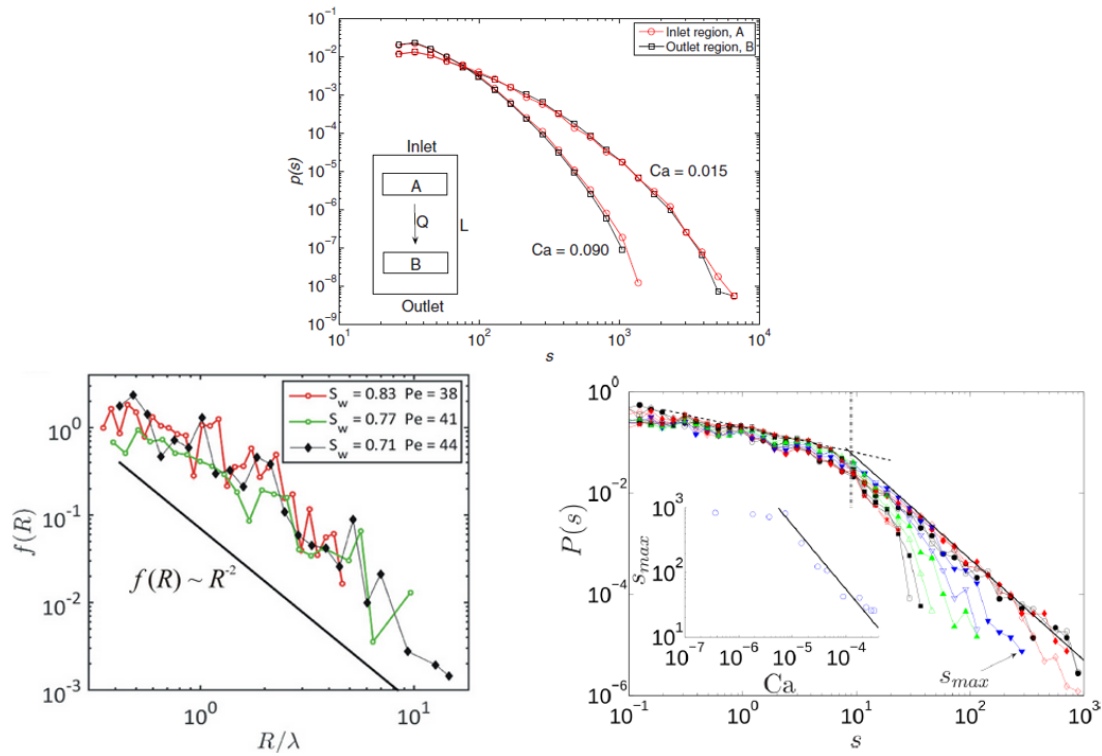


Figure 2.22 – Distribution of air bubbles in porous media after a air-water co-injection, From Jimenez-Martinez *et al.* [91] (left), Chevalier *et al.* [35] (Right), Tallakstad *et al.* [150] (top).

or dead-ends. Thus, the distribution of trapping sites is an intrinsic property of the medium.

Hence, structural characteristics such as the porous medium heterogeneity will influence the trapping pattern. Indeed, a more heterogeneous medium will usually lead to a more heterogeneous pattern of the trapped phase [53]. Moreover, according to Chevalier *et al.* [35], the position of the clusters becomes deterministic for high capillary numbers. Indeed, in Fig 2.23, the spatial distribution maps between different realizations for the probability of trapping get more and more contrasted as the capillary number grows. This means that the localisation for the trapping becomes more deterministic. Furthermore, trapping sites for low Ca numbers often include the trapping sites of high Ca numbers.

Topology of the flow with a trapped phase

The presence of bubble leads to new zones of low velocity, or dead ends, as well as preferential paths. Even though dead zones and preferential flow paths may have existed in the medium without the trapped phase, they will not be the same with the presence of bubbles.

Furthermore, the trapped phase increases the spread of the velocity distribution, as there are bubble blocking the way to certain parts of the medium, in addition to the dead ends already present in the saturated case. This reorganization of the flow is marked by a deep change of the velocity probability distribution function (pdf), with a strong increase of the low velocity probability. According to Velasquez *et al.* (2021), [122], the low velocity exhibits a power-law trend and the high velocity follows an exponential trend.

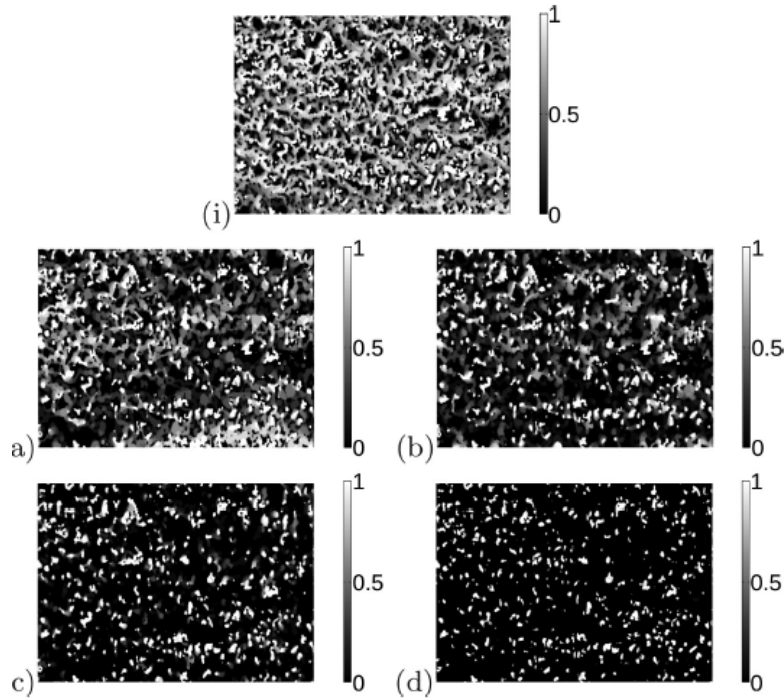


Figure 2.23 – Probability maps of trapping for different Ca numbers: $Ca = 3.7 \cdot 10^{-7}$ (a), $7.4 \cdot 10^{-6}$ (b), $3.0 \cdot 10^{-5}$ (c), and $3.3 \cdot 10^{-4}$ (d).

Thus, to characterize the flow field, it is possible to define a backbone, that is constituted of the main flow paths, to which are connected dead zones of low velocity [91] [122]. In Velasquez *et al.*, 2021, the threshold to do so is chosen as the change of trend between the power law and the exponential trend. This allows the authors to decompose the velocity pdf in the sum of the velocity pdf in the backbone and the velocity pdf in the dead-ends

$$p(q) = (1 - f)p^B(q) + fp^D(q),$$

with f the ratio of the dead-end area to the total area, $p^B(q)$ the backbone flow rate pdf and $p^D(q)$ the dead-ends pdf. Under some hypothesis not detailed here, the authors model the velocity pdf for low velocity as

$$p_E(v) = \frac{2\gamma f}{v(1 + 2\gamma)} \ln \left(\frac{v}{v_c} \right)^{-1-2\gamma},$$

and the velocity pdf for high velocity as

$$p_E(v) = \left(\frac{2\gamma f}{1 + 2\gamma} \sqrt{\frac{\alpha v_c}{v}} + (1 - f) \sqrt{\frac{v}{\alpha v_c}} \right) \frac{C_*}{\alpha v_c} e^{-\frac{v}{\alpha v_c}},$$

with γ a power law coefficient, v_c the characteristic velocity which is saturation dependant and C_* and α geometric coefficients depending on the throats width and the channel size.

2.4 Saturation effects on dispersion in porous media

In nature, dispersion in unsaturated media is rather common. Indeed, the soils are not necessarily saturated in water and they may contain air bubbles. However, the effect of

saturation on dispersion in porous media is still not well known at the moment. Indeed, even though numerous authors have worked on the subject, there is a large discrepancy in the results. The nature of the dispersion in unsaturated porous media is difficult to characterize because it is necessary to understand first the non miscible air-water flow and its interaction with the porous media topology; and how the dispersion will arise according to this flow history.

In this section, we will give an overview of the different results on unsaturated porous media, and give a few keys of interpretation to explain the discrepancy of the results.

2.4.1 Effect of saturation: discrepancy of results

At first stance, there is a large discrepancy in the results concerning the effect of saturation in porous media. This is partly due to the different background of the authors who study the dispersion in unsaturated porous media, and consequently the different approaches that are used to characterize the dispersion.

Indeed, hydrologists, petrophysicists, geologists, experimental or theoretical physicist do not have an uniform understanding of the problem, which leads to different approaches to characterize the dispersion, and different models to describe the nature of dispersion. Therefore, this diversity of methods and models to describe the dispersion leads to ambiguities in the interpretation and the comparison of certain results.

2.4.2 Description of the dispersion: ambiguities

Given the different backgrounds of the authors studying the dispersion in porous media, there are somehow ambiguities that lie in the description of the dispersion, typically with the use of the dispersion coefficient, even in presence of anomalous dispersion.

Anomalous dispersion: inadequacy of the dispersion coefficient

A number of authors characterize the effect of saturation on dispersion with the value of the dispersion coefficient. Notably, authors do not necessarily make a clear distinction between anomalous and Fickian regime. In some cases they use the dispersion coefficient with clear signs of anomalous dispersion [118], without considering that they are characterizing a transient. Indeed, it can result from a pre-asymptotic regime that can converge toward Fickian dispersion. Plus, the anomalous signature is shown to be greater in multiphase flows [157]. Indeed, many experiments in unsaturated conditions show signs of anomalous dispersion. Therefore, the dispersion coefficient is not rigorously defined, and it is biased to describe the dispersion only using the dispersion coefficient. Therefore, authors often choose to describe the dispersion with other parameters as well, such as the transfer coefficient for the MIM model. However, since the models used are often different, it can be difficult to compare accurately the results of different studies.

Peclet number

When experimentally studying the effect of saturation in the dispersion, numerous authors change the flow rate to adapt the degree of saturation and study transport with different flow rates. Indeed, increasing the water flow rate tends to reduce the quantity of air in the medium.

However, the Peclet number depends directly of the flow rate, and it is an essential parameter for the dispersion. Typically, for a Fickian dispersion, the dispersion coefficient increases with the Pe number, this is illustrated by the expression of the Taylor dispersion coefficient in a tube

$$D_{\text{Taylor}} = D_m \left(1 + \frac{Pe^2}{48}\right).$$

To characterize the dispersion and take into account the change of Pe , some authors use the empiric law depending of the mean flow velocity

$$D_{\text{disp}} = D_m \tau^2 + \lambda v,$$

or eventually

$$D_{\text{disp}} = D_m \tau^2 + \lambda v^\theta,$$

with τ the diffusive tortuosity, λ the dispersivity and θ an empirical exponent. They give values of the dispersivity instead of values of dispersion coefficient. However, this does not necessarily mean that all the influence of the Pe number is taken into account with this formulation of the dispersion coefficient, especially if the dispersion is anomalous. Notably, it was demonstrated [116] that high Pe numbers usually favor anomalous dispersion.

For example, for a porous medium with immobile zones, if the flow rate is increased, the stagnant zones are still characterized by low local Pe number, but the main flow paths will be characterized by a higher Pe number. Hence, when changing the flow rate to change the saturation and study transport, we observe the coupling of two opposing effects. If the flow rate decreases and the air saturation increases, on the one hand, the diminution of the Pe number tends to decrease the dispersion. On the other hand, the increase of air bubbles in the medium tends to create more stagnant zones in the medium and preferential paths, leading to an increased flow heterogeneity, increasing advective dispersion. This coupling effect exists whether the resulting dispersion is anomalous or not, therefore it is complicated to interpret results for which there is a variation of both saturation and Peclet number. Triadis *et al.*(2018) [157] show that the Pe numbers increases the anomalous nature of the dispersion in multiphase flows, typically with a transient time towards a Fickian regime longer with high Pe numbers, or no Fickian regime observed even at large times. Therefore, if possible, it is better to compare experiments with the same Pe number.

2.4.3 Different trends

Increase of the dispersion with a decreasing water saturation

A large number of authors note an increase of the dispersion in unsaturated porous media, compared to saturated conditions, as shown Fig. 2.24. Among them, Bromly and Hinz (2004) [26] noted an increase of dispersivity for low water content, compared to high water content, for experiment of tracer injection in sand columns (cf Fig. a). Maraqa *et al.* (1997) [107] noted that the dispersivity was multiplied by a factor two in unsaturated conditions, for BTC experiments in various soil samples (cf Fig. b). Furthermore, Nützman *et al.* (2002) [118] gave a monotone decreasing relation between the dispersivity and the water content. Haga *et al.* (1999) [76] also noted an increase of the dispersion under unsaturated conditions, highlighted by the BTC at different saturation conditions, that are widening when the saturation decreases in the sub-figure (d) of 2.24.

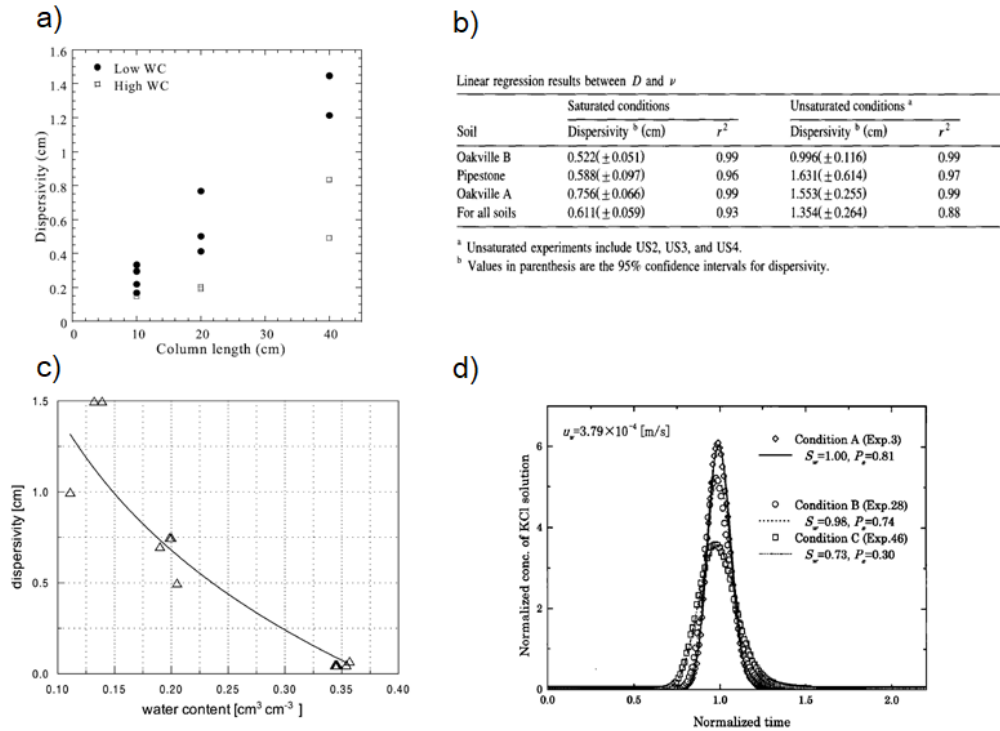


Figure 2.24 – Figures illustrating the increase of dispersion under unsaturated condition. a) From Bromly and Hinz (2004): Dispersivity calculated from BTC curves, tracer injection in columns of sand. The measurements are made at different column lengths and for low and high water content (WC) b) From Maraqa *et al.* (1997): Dispersivity values calculated from BTC curves for different natural samples, under saturated and unsaturated conditions c) From Nützman *et al.* (2002): Dispersivity values as a function of the water content, calculated from BTC, for a tracer injection in soil columns d) From Haga *et al.* (1999): BTC of dispersion experiments in packed beds, for different conditions of saturation.

Non monotonic tendencies

Some articles tends to highlight non monotone relations between the saturation and the dispersivity, or the dispersion coefficient, as shown Fig. 2.25. Particularly, Padilla *et al.* (1999) [121] measured a dispersion coefficient that increases with water content until it reaches a maximum, then decreases to a minimum level in saturated condition (cf Fig. 2.25 a)), for a dispersion coefficient calculated with the ADE model and the MIM model.

Karadimitriou [93] also noted a non monotonic relation between the dispersion coefficient and the water saturation, the dispersion coefficient increases with water saturation and reaches a maximum for medium values of water saturation, and decreases when the water saturation gets closer to full saturation. This tendency is verified for different flow rates, or in other words Peclet numbers.

This tendency is also brought to light by Raouf et Hassanizadey (2013) [128] with poreflow network simulations. Their results suggest that there could be a link between the water saturation for which the dispersion is maximal and the fraction of percolating saturated pores.

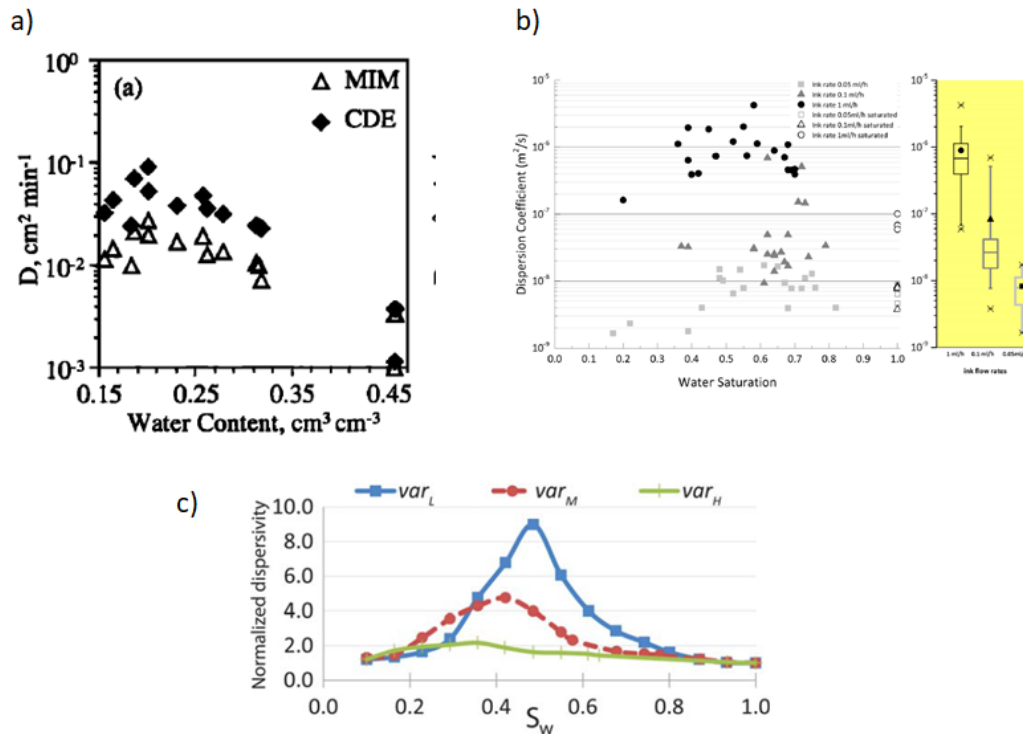


Figure 2.25 – Illustrations of the non monotonic relation of dispersion with water content or saturation. a) Dispersion coefficient as a function of water content, for BTC experiments in soil columns from Padilla *et al.* (1999) b) Dispersion coefficient as a function of water saturation, calculated from BTC experiments in 2D micromodels from Karadamitriou *et al.*(2016). c) Dispersivity as a function of saturation. Results of simulations using a pore flow network model, for three generic networks. The pore-body size distributions have different variances: high (var_H), medium(var_M), low(var_L). From Raouf et Hassanizadey *et al.* (2013).

Other tendencies

A minority of articles show different tendencies for the dispersion from what we have mentioned in the preceding sections, as shown in Fig. 2.26. That is the case of Vanderborght *et al.* (2007) [161], which collects data to analyse dispersion properties. However, the influence of saturation is difficult to interpret here, because a great number of parameters change with the saturation.

Birkholzer *et al.* (1997) [21] investigated on channeling effects in porous media through unsaturated highly heterogeneous media through numerical simulations, and found dispersivity that tends to decrease with saturation, although the tendency is not clear. In both cases, the water saturation is modified through the flow rate, so the Peclet number also changes, which makes the interpretation for the influence of the saturation hazardous.

Conclusion

There is a divergence in the results concerning the effect of saturation on dispersion, mainly because of the multiplicity of the approaches, and the different parameters that can be changed during the experiments. Nonetheless, the decrease of saturation from the

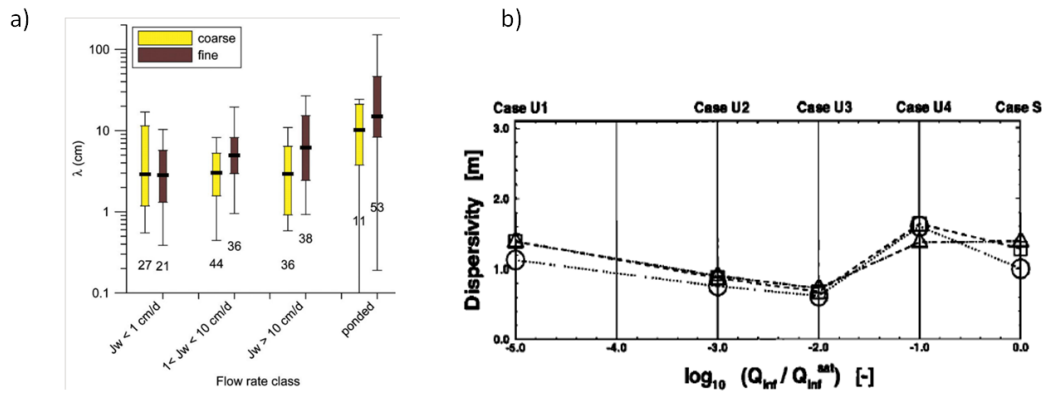


Figure 2.26 – a) Dispersivity as a function of the flow rate. From Vanderborgh *et al.* (2007). b) Dispersivity as a function of the flow rate. From Birkholzer *et al.* (1997).

fully saturated porous medium tends to increase the dispersion, at least for a range of saturation values close to the full saturation.

Thus, the increasing dispersion is linked to an expansion of the velocity field. The unsaturated medium favors extreme velocity values in stagnant zones and preferential flow paths leading to an increased dispersion and often anomalous dispersion. For example, in Triadis *et al.*, 2018 [157], the dispersion for saturated medium quickly converges towards Fickian dispersion, when the dispersion in unsaturated porous medium is anomalous for a long period of time, until eventually converging to Fickian dispersion, as shown in the Fig. 2.27.

However, non monotonic relations observed by several authors suggest that the effect of the decrease of saturation is much more complex and can not be reduced to an increase of the dispersion coefficient. Then, to understand how the unsaturated porous media affects the flow field, it is essential to characterize the interaction between the porous media structural properties and the non-miscible two-phase flow.

2.4.4 Influence of the two phase flow topology on the dispersion

Role of heterogeneity

The anomalous character of the dispersion is known to increase with more complex geometry for porous media. Quite intuitively, the presence of a trapped phase in the porous medium increases the flow heterogeneity, it also affects the connectivity and the complexity of the possible paths. According to the way the trapped phase is distributed in the medium, it can lead to a greater number of dead-ends and preferential paths, both resulting in an increased spreading [157].

Velocity probability density function

With a trapped phase, the reorganization of the flow is marked with a deep change of the velocity probability density function, with a strong increase of the low velocities probability (see subsection 2.3.4), due to the formation of dead-ends. A. V. Parra *et al.*

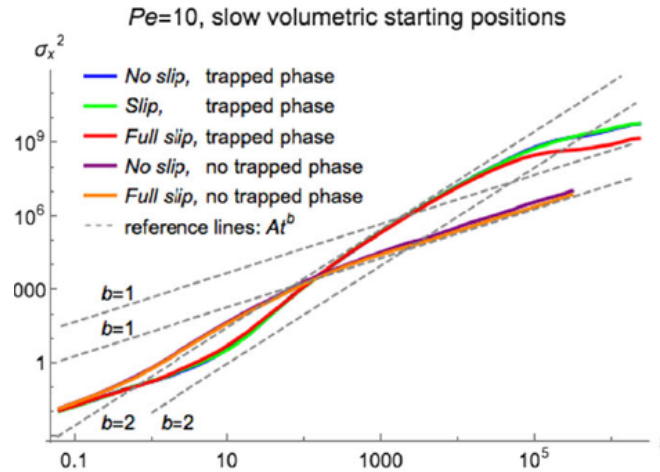


Figure 2.27 – Pore scale simulations of dispersion in saturated (no trapped phase) and unsaturated media (trapped phase). Variance as function of time, for different slip conditions. The lines $b = 1$ correspond to Fickian dispersion while the lines $b = 2$ correspond to ballistic dispersion (non Fickian). From Triadis *et al.* (2018) [157].

(2021) [122] showed the effect of the saturation on the transition to strong anomalous transport in unsaturated conditions by modelling the velocity probability distribution function, decomposed in the preferential flow path and the dead end zones. Fig. 2.28

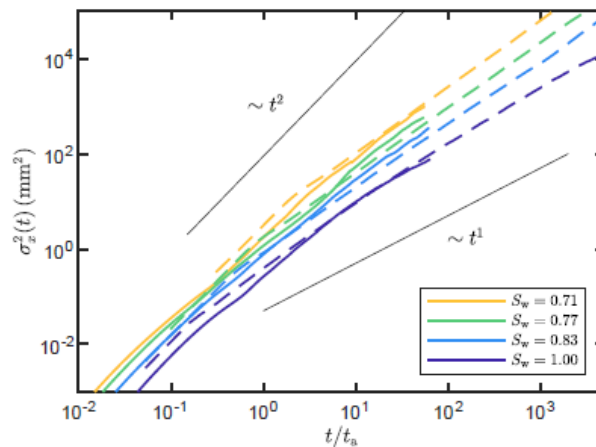


Figure 2.28 – Simulation of advective dispersion in time for four saturation values. The plot compares σ_x^2 using the particle tracking analysis (continuous lines) with σ_x^2 from a CTRW approach computed using the predicted velocity PDF $p_E(v)$ (dashed lines). From A.V Parra *et al.* (2021).

from Velasquez *et al.* shows that for unsaturated media, the dispersion tends to get closer to a ballistic behavior ($\sigma \propto t$) whereas it reaches a diffusive behavior in saturated conditions ($\sigma^2 \propto t$).

Nature of the trapped phase

Once the trapped phase is distributed, and that the preferential paths and the dead ends are created, does the gas nature of trapped phase influences significantly the dispersion, or the air bubbles are acting as an additive solid matrix in the medium?

The answer lies at the phase interface. In the case of CO₂ and water injection in a micromodel, Kazemifar *et al.* (2016) [95] noted shear induced circulation zones, i.e, vortices near the interface thanks to micro-PIV techniques. Thus, the trapped water ganglia are not entirely stagnant as they are near the fluid-fluid interface. Therefore, water films could have an impact on the unsaturated porous media transport properties.

2.5 Micromodels for porous media studies

In this section, we will describe micromodels and their utility to study dispersion in unsaturated porous media. More particularly, we want to show how they are relevant to study both multi phase flow and dispersion in porous media. This experimental device consists of microfluidic interconnected channels in a transparent material, with an inlet and an outlet that allow to introduce and extract the different phases. It allows the visualization of fluid dynamics and transport in a porous medium. We will comment briefly micromodels fabrication methods and the visualization techniques associated to understand how micromodels can be used. Then, we will report some of the results obtained through micromodels on multiphase flows and dispersion that highlight the contribution of micromodels in porous media during these last decades.

2.5.1 Generalities

Complex flow and transport in porous media can be difficult to characterize experimentally. Visualization techniques are particularly helpful to identify some key elements in the studied phenomenon. To allow direct visualization of the fluid structure and dispersion patterns, micromodels have been developed since 1950. They consist of a transparent interconnected porous network that enables optical visualization at the pore scale [92], [1]. Although there are other techniques of visualization in non-transparent porous media, they are not quite adapted to study pore scale dynamics. Focused ion beam scanning electron microscopy (FIB/SEM) or X-Ray micro-computed tomography (micro-CT) requires long scanning times, therefore it has a poor temporal resolution. An alternative is the NMR, but is still limited in spatial resolution.

Micromodels allow a pore scale observation of the flow and fluid structure under transient condition with a camera and eventually a microscope. According to the fabrication method, they can be in 2D or 3D. Whereas 3D micromodels better mimic the physics, they imply more complex visualization techniques, and a close match of refractive indexes for both solid matrix and fluids, whereas the flow in a 2D micromodel can be easily observed with a camera. It is constituted of a single layer of microfluidic channels with an arbitrary porous structure, but consequently, it does not capture the physics associated with 3D porous connections [1].

There are different kind of micromodels, according to the pattern of pores chosen. They can be perfectly regular, with the same geometry for all pores; partially regular, for example with pores shaped like square or crosses but with pore sizes chosen according to a statistical distribution, correlated or uncorrelated. The pattern can also be fractal, or

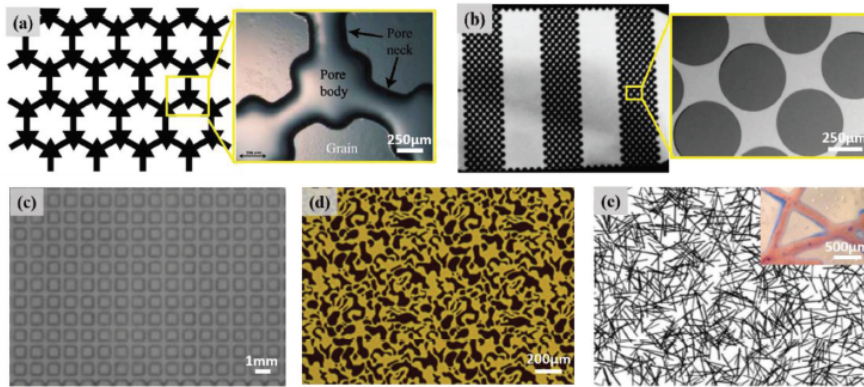


Figure 2.29 – Different geometry of micromodels, from [1].

irregular: there is no spatial correlation, the pores are placed randomly in the network and their size is chosen according to a given spatial distribution. The diversity of micromodels patterns is illustrated in Fig. 2.29.

Fabrication

Different methods of fabrication are possible depending on the kind of transparent material that is used, or the quality required for the micromodel. Hard material can be used, such as glass and silicon: glass micromodels are of good quality although they are fragile; silicon micromodels are quite close to glass except that the silicon is translucent and not water-wet. Soft materials, such as PDMS (poly-dimethyl-siloxane) or PMMA (poly-méthyl-méthacrylate) are really cheap but they present several drawbacks, among them the reactivity with some fluids and chemical products, that can induce a swelling of the micromodel [92]. There are two main categories of fabrication: non additive or additive manufacturing (and eventually micro-particles packing for 3D porous media) [1], [92]. The non additive manufacturing consists in several steps: first, the lithography. It is the transfer of the pre-designed geometric pattern from a mask to a photo-resist layer on the substrate. The second step is the shaping, which allows to give the particular shape to the micromodel. It can be done by etching, replica molding, etc.

For the lithography, the most common technique is photo-lithography (Fig. 2.30). A photo-resisting layer is exposed to UV light through a mask to create the porous pattern [1], [92].

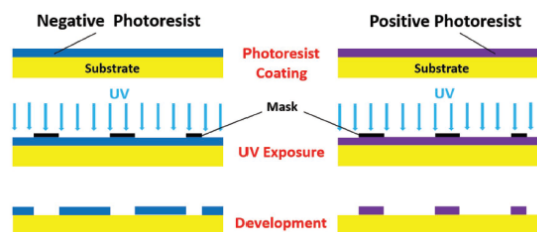


Figure 2.30 – Illustration of photo-lithography, from Anbari, 2018 [1]

As for the shaping, several methods are possible (Fig. 2.31). The dry-etching uses a reactive ion beam to attack the substrate. The replica molding uses a model with a negative shape of the micro-pattern, therefore the structure can be copied a dozen time

with the same mold. Laser engraving is also used for etching with all variety of materials. For the latter method, the problem is often the resolution [1]. The Fig. 9.9 in the appendix (Chapter 9, section 9.1.5) summarizes the fabrication methods, their advantages and disadvantages.

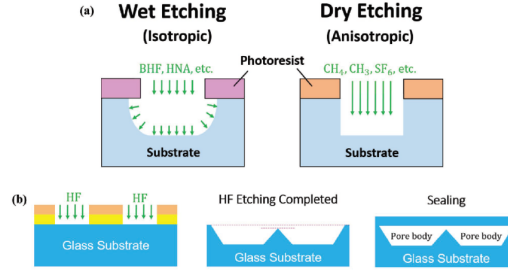


Figure 2.31 – Schematic of the etching technique, from Anbari, 2018

Visualization techniques

For 2D micromodels, visualization techniques simply consist in camera observation, with a microscope if needed. For 3D micromodels, the pore space and the fluid flow structure is visualized by confocal microscopy. Fig. 9.10 in the appendix Chapter 9, section 9.1.5 sums up the different visualization methods, their suitability and their limits.

Limitations of micromodels

Although micromodels have become really interesting tools to investigate mechanisms at the pore scale, there are still limitations to the use of micromodels that one should keep in mind. Indeed, one primordial limitation for 2D micromodels, that are the most commonly used, is the difficulty to relate quantitatively the behavior observed in the micromodel in 2D to the behavior in a real medium in 3D. Typically, it might be difficult to upscale parameters obtained from micromodels studies to 3D porous media.

Another limitation is that 2D micromodels are not rigorously two-dimensional: the depth can have an effect on the observation. Indeed, experiments observation in micromodels often relate to depth-average quantities [143]. Typically, experiments using camera observation to measure concentration profiles in micromodels provide values that are averaged along the depth L_z and no information about the depth profile is available. For example, the average concentration is computed as

$$\langle c(x,y) \rangle = \frac{1}{L_z} \int_0^{L_z} c(x,y,z) dz. \quad (2.5.1)$$

The depth of the micromodel can be really significant when it comes to the comparison of 2D simulations and micromodel experiments. Indeed, 2D Navier-Stokes simulations or 2D Darcy simulations do not capture fully the behavior of 2.5 D micromodels, as Soulaïne *et al.* (2021) showed [143] (Fig. 2.32). According to the ratio of the micromodel depth over the pore throat, it might be relevant to use a depth integrated model, which is equivalent to a Darcy-Brinkmann model, to take into account the effect of depth on the flow.

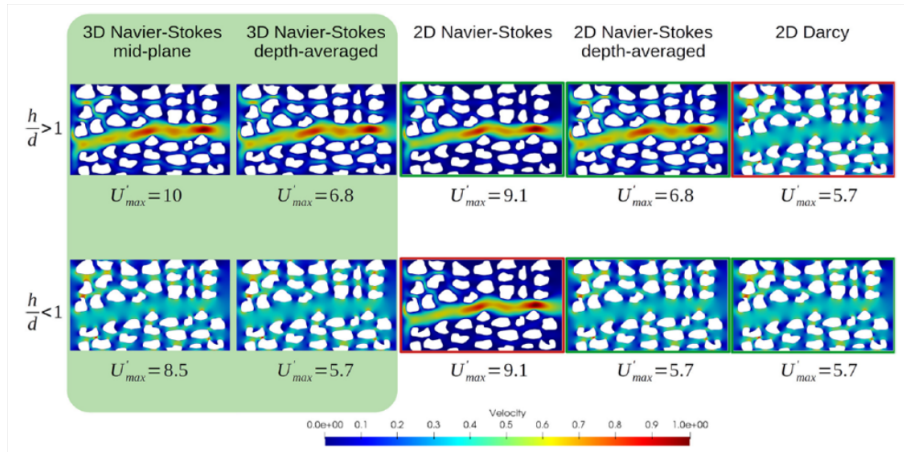


Figure 2.32 – Comparison of different models to model flow in a micromodel. Single phase flow simulation using 3D, 2D and 2D depth averaged for different aspect ratio between the micromodel thickness and the pore-throat. From Soulaine *et al.* (2021) [143].

2.5.2 Micromodels for the characterization of non miscible two-phase flows in porous media

Micromodels are frequently used to study multiphase flow in porous media, indeed, they allow to assess the volume fraction of each phase, assuming that the cross section on the image reflects exactly the volume occupation [1]. The distribution of the phases can be obtained at any time.

Non miscible multiphase flows

Notably, non miscible multiphase flow processes have been thoroughly studied through micromodel experiments [35] [94] [79] [180]. Indeed, during non miscible multiphase flow processes, there are multiple possible configurations for the phase distributions of the wetting fluid (typically water if the micromodel is waterwet) and non wetting fluid (typically air or oil), that depend on the capillary number, on each phase saturation and on the flow history.

The previous section (2.3.4 and 2.3.4) described the work of several authors that studies two-phase flow with micromodels, notably Tallakstad [150] and Chevalier [35]. Chevalier *et al.* (2015) [35] use a micromodel with random flow obstacle that mimics a fractured rock sample to study the distribution of ganglia during a co-injection process, as seen Fig. 2.33.

In order to study the multi-phase flow, several authors assessed the velocity map in the micromodel using micro-PIV (Particle Image Velocimetry) techniques [79] [22]. Indeed, in Haques *et al.*, 2021 [79], the velocity distribution obtained for a two-phase flow had distinct characteristics that are completely different from the single phase flow. Particularly, those peculiarities create instabilities that lead to preferential flow paths near stagnant fluid ganglia.

Velasquez *et al.* (2021) [122] decomposed the medium in a back-bone and dead ends from flow simulations in the micromodel, as seen in the Fig. 2.34. It is possible to map the preferential flow-paths as well as the dead ends to characterize the structure of the flow and the effect of crucial parameters, such as the saturation value.

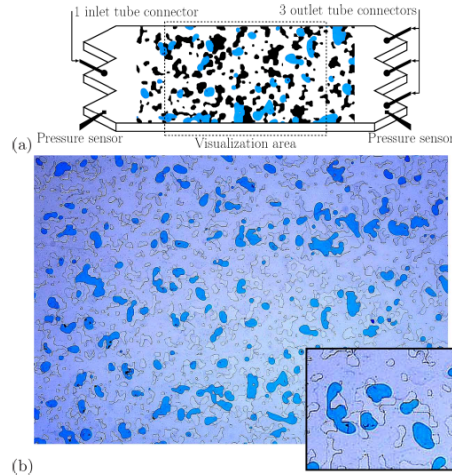


Figure 2.33 – Micromodel device to study two phase flow process. Blue: oil. Grey: solid. light purple: water. From Chevalier *et al.*, 2015 [35].

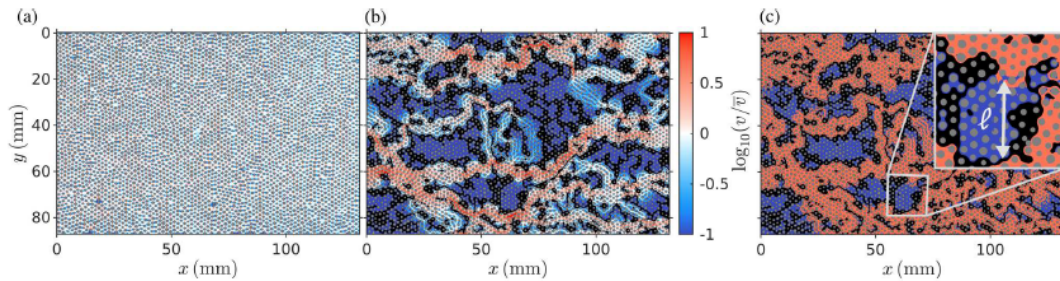


Figure 2.34 – Decomposition of the medium into a back-bone (red) and dead-ends (blue) from the velocity field in the unsaturated micromodel. Obstacle are shown in grey, air clusters in black, the velocity in the water phase is indicated with the color bar. From Velasquez *et al.* (2021) [122].

Influence of the pattern for multi-phase flow in micromodels

The pattern, defined amongst other things by the pore distributions and the pore depths, can be designed to mimic as closely as possible the natural porous media of interest. For example, it can be useful to model multi-scale pore sizes, that are common in carbonate rocks, and eventually pores of different depths [177] [172], that are involved in multi-phase flow mechanisms. Indeed, the capillary snap-off mechanism is an important characteristic for oil and bubble break-up. It only occurs when the size of the throats are smaller than the pore bodies in both perpendicular directions of the flow. Therefore, a limitation of 2D micromodels is that the unique depth does not allow the snap-off mechanism and therefore does not fully capture the 3D physics of multiphase flows [37].

2.5.3 Micromodels to study dispersion in porous media

Saturated conditions

Micromodels have been widely used to study transport in porous media, they allow to visualize and quantify solute transport in porous media [38] [88]. In saturated condi-

tions, they also can be used to study dispersion of complex objects such as colloids [5], suspensions [13] or even micro-organisms, as illustrated in Fig. 2.35.

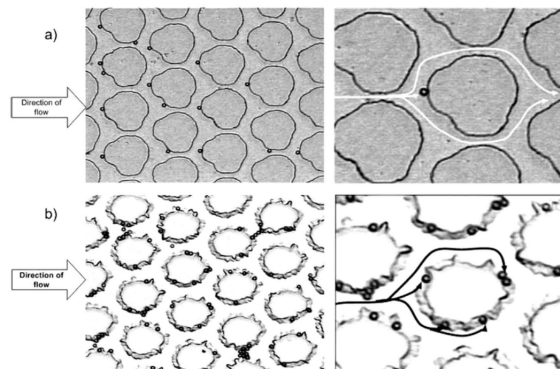


Figure 2.35 – Pore scale visualization of colloids straining in saturated porous media using micromodels. From Auset, 2006 [4].

Unlike rock samples or columns experiments, they provide a concentration map of the tracer, which gives significantly more information on the transport mechanism than BTC curves for example. Particularly, it gives insight on the interaction between the nature of the porous media (pore sizes distribution, connectivity, roughness, etc) and the transport, i.e., how some characteristics of the network will influence the dispersion, and for instance lead to preferential paths or stagnant zones in the porous medium.

Unsaturated conditions

Micromodels are ideal tools to study transport in unsaturated porous media since they provide both non miscible phases configurations and concentration fields. Therefore, they have been widely used in several fields of research, such as biology, to study the influence of the water-air interface on transport of micro-organisms [166], or colloid transport [165] [96] [133] or to quantify liquid volatilization in unsaturated porous media or vapor transport [169] [136]. In the last decade, there has been a growing interest about transport in unsaturated conditions, particularly in the vadose zone and how micromodels can be used to study the dispersion [165] [92] [93] [81]. Leontidis *et al.* (2020) [104] studied the influence of saturation on the dispersion using micromodels, as well as Kadamitriou *et al.* (2016) [93] (cf Fig. 2.36 and Fig. 2.37), who investigated the influence of the immobile zones in the transport, as well as the mixing at the pore scale. Jimenez *et al.* (2020) [90] studied the impact of phase distributions on mixing and reactions in unsaturated porous media.

When studying transport with a micromodel, an experimental difficulty is to create a neat front of concentration at the entrance of the device; particularly because of the dispersion in the tubing connecting the fluid and the inlet of the micromodel. To improve the tracer injection, Jimenez-Martinez [91] developed a photo-bleaching method that allows to create a rather neat Dirac injection of the tracer, as can be seen in Fig. 2.38.

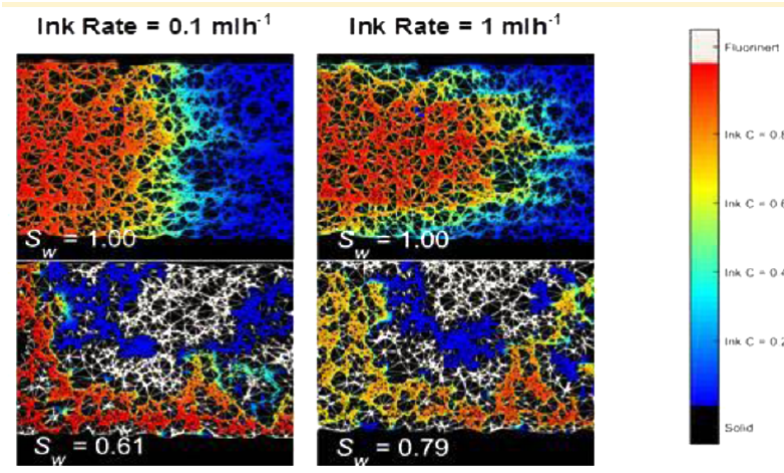


Figure 2.36 – Micromodel experiment of dispersion in unsaturated porous media, from Kadamitriou *et al.*, 2016 [93].

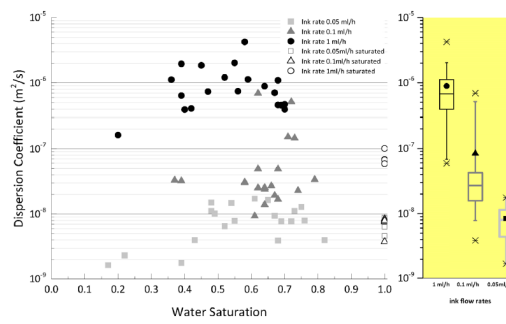


Figure 2.37 – Dispersion coefficients computed from micromodel experiments, from Kadamitriou *et al.*, 2016 [93].

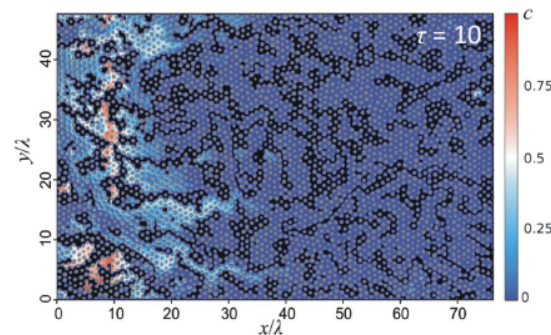


Figure 2.38 – Dirac injection in an unsaturated porous media, from Jimenez-Martinez, 2017 [91]

2.6 Synthetic image reconstruction in porous media

2.6.1 Introduction

Earth science studies can be restricted by the amount of experimental data available, either because of the limited sample sizes or the finite number of data samples. To overcome this issue, it can be advantageous to generate artificial media from experimental

images through numerical methods, such as multiple-point statistics algorithms (MPS) or deep learning methods [167].

Multiple-Point statistics algorithms are commonly used in pore scale imaging and geostatistics. They allow to generate images with complex shapes and structures. Their leading idea is to retrieve information about the desired shape, spatial distribution and connection of the objects from a training image (TI), that represents a conceptual model of the expected structure. This information is then used to fill iteratively the simulation grid, resulting in a synthetic medium with spatial distribution consistent with the training image [59, 148].

MPS algorithms are based on minimization problems, and as such are not technically machine learning algorithms. Deep learning methods, based on neural networks, have become more and more common in Earth sciences and particularly pore scale modelling and imaging [167]. They have been used to replace or accelerate traditional methods with neural networks. As an illustration, Conventional Neural Networks (CNN) have been used for pore space segmentation [117, 162, 167], to identify different types of minerals from gray scales images with minimal human supervision. Generative Adversarial Networks (GANs), along with CNNs have been used for image quality enhancement, and image generation. GANs for image generation are based on two neural networks, a discriminator, that is trained to identify fake data, and a generator that creates data close enough from the database to deceive the discriminator [70].

Deep learning is used either for reconstruction of 3D images from 2D slices of a rotating sample, or for generation of synthetic images. Mosser et al. (2017) [114] have trained a GANs network to create synthetic images from a data set consisting on subsets of a rock CT-scan, allowing a large number of training images (between 2000 and 10000 according to the rocks studied). The synthetic images give satisfying results, notably for average values such as porosity and permeability. However, neural networks ask for a very large amount of data with equivalent statistic properties, that is not always easy to obtain in experimental conditions. Databases in Earth science are still in a early stage of development, even though the recent years have shown a great improvement in that matter [167]. Moreover, they still fail to fully capture complex geometry pattern and the different scales of the porous structure. The main advantage of deep learning methods is that once the neural network is trained, the time to produce sample is very short, which allows to create large samples while maintaining computational efficiency. GANs have also been used to accelerate MPS algorithm for image generation.

In the following, we will focus on MPS algorithms as they are still the most commonly used for porous media generation, and have the advantage to allow image generation with a single training image.

2.6.2 Multiple-Point statistics algorithm

MPS approaches were initially developed for geological modeling to generate new distributions of complex geometry patterns from a training image that represents the expected structure. Originally, geostatistics would rely on correlations between two points of the reservoir. It did not allow to model complex objects such as curvilinear channels. Therefore, the leading idea was to rely on more than 2 points and use a training image as a conceptual representation of the spatial structure to analyse the geological statistics and to reproduce it in a simulation. The first idea was formalised in 1993 by Guardiana et al [72], but the first efficient algorithm was created in 2000 [145].

Simultaneously, significant developments occurred in infography, notably for texture mapping. Texture mapping was introduced by Catmull in 1974 [29] to cover 3D objects with 2D images. Issues about image distortion in 3D and pixelisation when the image is stretched led to a new idea: to generate a texture similar to the original sample directly on the 3D object (Heeger Berger [82]). In 1999, a texture mapping algorithm for image reparation with very good results was proposed by Efros and Leung [49]. Since then, numerous methods were developed, for instance the generation through neighbourhood prospecting: a pixel with similar neighbourhood than the pixel to be simulated is identified in the original texture. A similar method is developed with patch instead of pixels [59].

In 2007, Multiple-point statistics and texture mapping are combined with Arpat and Caers work [2]. They replace the probabilistic approach (i.e the reproduction of statistics) by the reproduction of patterns used in infography, using a database of extracted pattern from the training image. Since then, MPS algorithms have been increasingly used, as the occurrences of publication mentioning MPS highlights (see Fig. 2.39). Furthermore, the range of application of multiple-point statistics has widened, and notably they have been applied to porous media image generation.

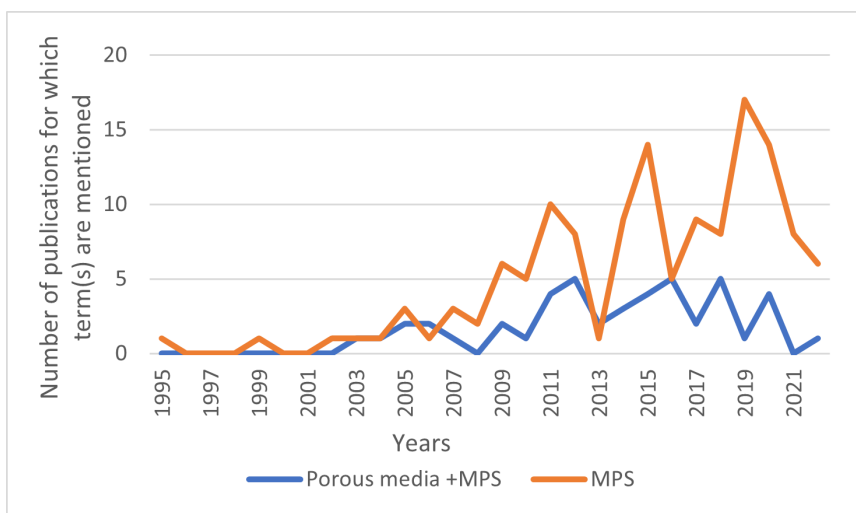


Figure 2.39 – Evolution of the importance of MPS algorithm and its applications to porous media in the recent decades.

2.6.3 MPS application to porous media

MPS were first applied to porous for 3D reconstruction from 2D images in 2004 by Okabe and Blunt [119]. They managed to recover permeability from Lattice Boltzmann simulation of flow in the 3D porous medium synthesised by MPS. In a similar vein, Zhang et al (2012) [181] proposed a method using MPS to reconstruct 3D porous media from a 2D thin section of a porous media, tested on three sandstones samples. Multiple-point statistics is used to reconstruct the image of the next layer, that becomes the new training image. The 3D medium is obtained by stacking all the reconstructed layers. Numerous authors developed the reconstruction of 3D images with 2D thin sections in the following years ([41, 52, 171, 182]).

Another application of MPS to porous media was proposed by Jimenez *et al* in 2020 [90]. They used an MPS algorithm to generate unsaturated porous media from

experimental data that share similar statistics in term of saturation and trapped fluid distribution.

2.7 Conclusion

The second chapter of this thesis aimed to provide an overview of the state of the art in transport phenomena in unsaturated porous media. We introduced notions about physics on porous media for better comprehension. Afterwards, the following key findings and insights were obtained:

On one hand, we focused on the multiphase flow phenomena in porous media. Immiscible two-phase flow in quasi-static and dynamic conditions were studied, as well as mechanisms of bubbles creation in the porous medium during two-phase flow. We particularly detailed the behavior of a flow with a trapped phase, and how the trapped phase depends on the history of the two-phase flow, and notably on the maximal capillary number reached during the flow.

On the other hand, the chapter highlighted how dispersion arises in porous media and how it can be modeled. Indeed, dispersion cannot always be described with advection-dispersion equation in porous media, notably in heterogeneous and unsaturated porous media. Hence, we detailed what determines the nature of dispersion, Fickian or non-Fickian. In theory, asymptotic dispersion should be Fickian no matter how heterogeneous the medium is, however the time to reach this dispersion might never be too long to be observed. Therefore, models for non-Fickian dispersion have been developed to describe more accurately dispersion in porous media.

Furthermore, a thorough review of the existing literature revealed various simulation and experimental approaches that have been employed to study transport processes in unsaturated porous media. These studies do not agree on the effect of saturation on dispersion. The majority finds a dispersion coefficient that increases when the saturation decreases, but non-monotonic relations were also observed, and a minority find an increase of the dispersion coefficient with decreasing saturation. These discrepancies can be explained partially by the variability in the approach, the different kind of flow and model considered while studying the dispersion in unsaturated porous media. Furthermore, the impact of various factors, including soil heterogeneity, capillary forces, and boundary conditions, on transport behavior in unsaturated porous media was examined. The findings indicated that these factors can significantly influence flow patterns, transport rates, and the spreading of contaminants in the subsurface.

Finally, we detailed some specific methodology that impact research in flow and transport, notably we highlighted the importance of micromodels in the study of multi-phase flow and transport in porous media, and machine learning methods that can be used to tackle the experimental lack of data in porous media studies.

The next chapter of this thesis will build upon the foundation established in this state-of-the-art review. It will delve into the experimental methodology used to investigate transport phenomena in unsaturated porous media, including the setup, measurements, and data analysis techniques employed.

Chapter 3

Experimental methods and data processing

Having established the key concepts for understanding the mechanisms involved in dispersion in unsaturated porous media, this chapter focuses on the experimental setup employed to study dispersion in an unsaturated porous medium using a micromodel.

The challenge was twofold: first, we needed to design a transport experiment using the micromodel that would ensure a neat injection front at the inlet. Conventional tracer injection methods, where the tracer is introduced through a single inlet, do not yield such a precise concentration front. Second, we had to devise a method to create unsaturated porous media with a relatively uniform distribution of bubbles at the scale of the micromodel, and this needed to be reproducible. Finally, we used these two methods to perform transport experiments in unsaturated porous media, and with the aim to monitor concentration fields evolution with time, for various degrees of saturation.

Furthermore, we will detail the analytical methods we developed to analyze transport experiment images, i.e., how we analyse the concentration fields and their evolution in time to characterize the dispersion. Indeed, we developed a method based on spatial moments computation to characterize dispersion. This method is rather straightforward, and avoids to use a model to fit the data, which often implies hypothesis on the nature of dispersion. This is typically the case when the breakthrough curves are fitted with ADE solutions. We will also present how we can analyze the unsaturated porous media, notably the partition of the phases, and what kind of statistics we can extract from the images.

3.1 Multi-phase flow and transport experiments

3.1.1 Experimental set-up

Micromodel

We use a glass micromodel of inner etched network dimensions of 10 mm wide by 17 mm long. The micromodel is wet-etched with fabrication depth L_z of 40 μm . The interior model network is based on an image of a 2D slice of Bentheimer rock, obtained from X-Ray tomography. It was modified to force percolation in 2D leading to a higher final porosity than the original rock. The mask is presented Fig. 3.1.

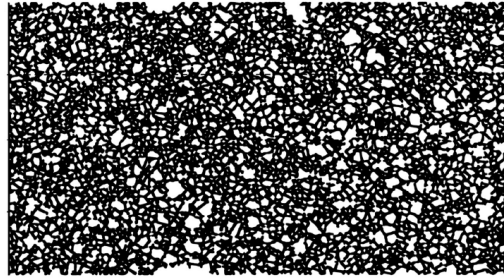


Figure 3.1 – Binarized mask of the inner micromodel network

The inner porous media is characterized by a total number of grains of 2602; the average porosity is $\phi = 0.66$ and the permeability K of the micromodel (including connectors) is 4.7 Darcy. Plus, the micromodel can be considered as strongly water-wet as it is entirely made of glass.

Each longitudinal side of the inner porous network comprises a rectangular reservoir followed by a flow diverting system of larger canals that bring the different fluids into the micromodel, as shown in Fig. 3.2. This micromodel has the particularity to have three inlets and three outlets as well as inlet and outlet tanks. The central inlet (or outlet) undergoes successive bifurcations, it splits into two branches, that split into two branches as well, resulting in eight branches evenly distributed and connected with the model entrance.

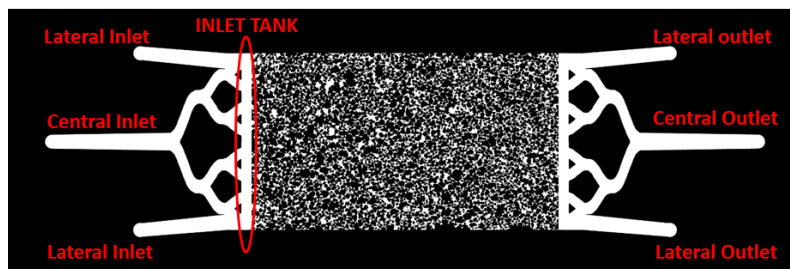


Figure 3.2 – Micromodel connectors configuration: three inlets and three outlets, an inlet and outlet tank

The analysis of the micromodel structure with ImageJ watershed algorithms gives the distribution of pores as well as the pore equivalent radius, as shown in Fig. 3.3. The pores size distribution shows a long tail towards large pores, and the dashed line indicates the mean equivalent pore radius, estimated to 0.1 mm.

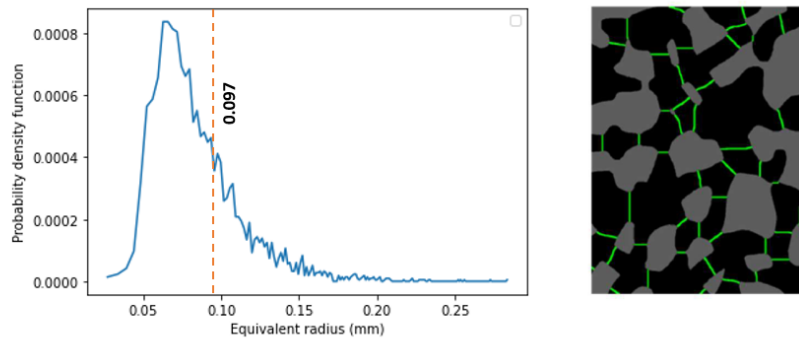


Figure 3.3 – Micromodel network characteristics, with mean values shown as dashed line. A sample of the pore network decomposition is shown on the right, throats are shown in green separating the black pores.

Fluids and injection system

The gas used is ambient air, the liquid is MilliQ and the tracer is Parker Quink blue-black ink, diluted at 40% in mass with MilliQ water. We chose the ink as a tracer and the percentage after Leontidis, 2020 [104], that tested different tracer and concentrations to improve the contrast.

Water and ink are injected with a Vinduum pump, delivering a continuous flow rate that can be chosen for our system between approximately $0.1 \mu\text{l}/\text{min}$ and $1 \text{ ml}/\text{min}$. As the flow rate is too low to be accurately assessed by a flow meter, the pump was pre-calibrated by weighting produced water. We observed a 2% error margin for flow rates superior to $0.001 \text{ ml}/\text{min}$. Below this flow rate, the error increases, up to 35% for flow rates around $0.1 \mu\text{L}/\text{min}$. Air is injected with a Harvard syringe pump, with a range of flow rate similar to the Vinduum pump. The exact air flow rate was not significant for our measures so no calibration was done.

Visualisation techniques

The micromodel is inserted in a holder and it is placed horizontally on the optical bench, above a flat dome red light with adjustable intensity. A high speed camera with a lens is placed above the system to visualize the concentration field or the two phase flow (Fig. 3.4). The camera JAI (SP-12000M-CXP4 model) provides 12-megapixel monochrome resolution (4096×3072 pixel) and full-field framerate of 189 frames per second (fps). The software Hiris realizes the connection with the camera for the image acquisition.

Microfluidic set-up

The micromodel is connected to the pump and/or the syringe pump at the inlet through different tubings and connectors, as seen in Fig. 3.5. The outlet is connected to the pressure and flow rate sensors.

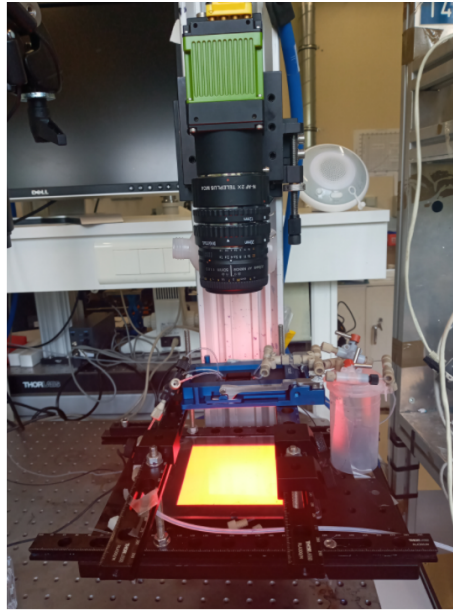


Figure 3.4 – Experimental set-up

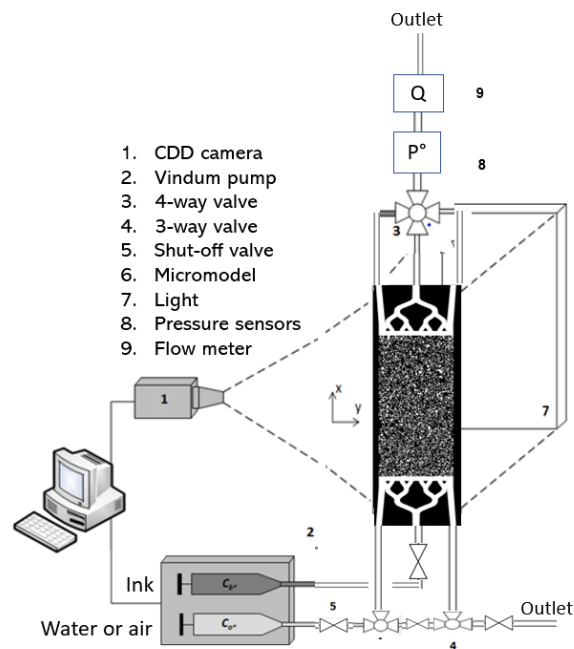


Figure 3.5 – Microfluidic set-up

Data acquisition

Data acquisition is done thanks to the Hiris software. We choose the fps value for transport or co-injection experiment as a function of the flow rate. The fps is chosen from a range of 10 to 100 fps. For each experiment, it is essential to capture an image of the saturated porous medium (with or without tracer) so it can be used as a mask later on the image processing.

3.1.2 Experimental protocols

Fluid injections methods

To study the dispersion in unsaturated conditions, the first step is to set a steady-state two phase fluid distribution, for which the gas is distributed rather uniformly in the system. To this goal, we choose to co-inject air and water simultaneously in the system at different fractional flow ratio. The air is injected with the syringe pump at a given flow rate Q_{air} through the central inlet while water is injected on the lateral sides with a flow rate Q_{water} , as it can be seen in Fig. 3.6.

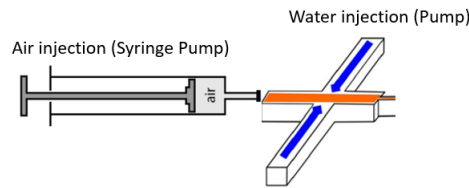


Figure 3.6 – Co-injection set-up

The air and water are injected simultaneously, but in the micromodel we observe alternating passages of water and air. By adjusting the water and air flow rates, we get successive sequences of air and water injections. During the air passage, there are both mobile and trapped air clusters, whereas during the water passage there are only the trapped air clusters. After a few cycles, the air distribution during the water passages becomes stable (saturation and air clusters distribution). As shown Fig. 3.7, the mean image gray level (which is monotonically proportional to the mean saturation as we will see later) linked to the saturation of the medium, reaches stable values for each part of the co-injection cycle. The injection can be stopped when a steady-state is reached. This method allows to obtain unsaturated porous media with a spatially uniform phase distribution in the porous medium.

Transport experiment

To be able to characterize the dispersion, we need a neat concentration front, with the maximal and minimal concentration of the tracer in the same considered concentration field. However, with a simple injection system (i.e., a system with one inlet for the ink injection and one outlet), and as the dispersion begins inside the tubing connecting to the micromodel, the concentration profile inside the micromodel is already very dispersed at the beginning of the injection. The dispersion in the tubing can be slightly reduced, notably with the flow rate, but not sufficiently because of the length of the tubing, so that the concentration front is already dispersed when entering the micromodel [104] (cf Appendix Chapter 9, 9.2).

To tackle this issue, we take advantage of the multi-inlet configuration of the micromodel to set a new injection protocol that allows a neat concentration front at the entrance of the micromodel, so that the concentration profiles can be analysed by the methods of moments.

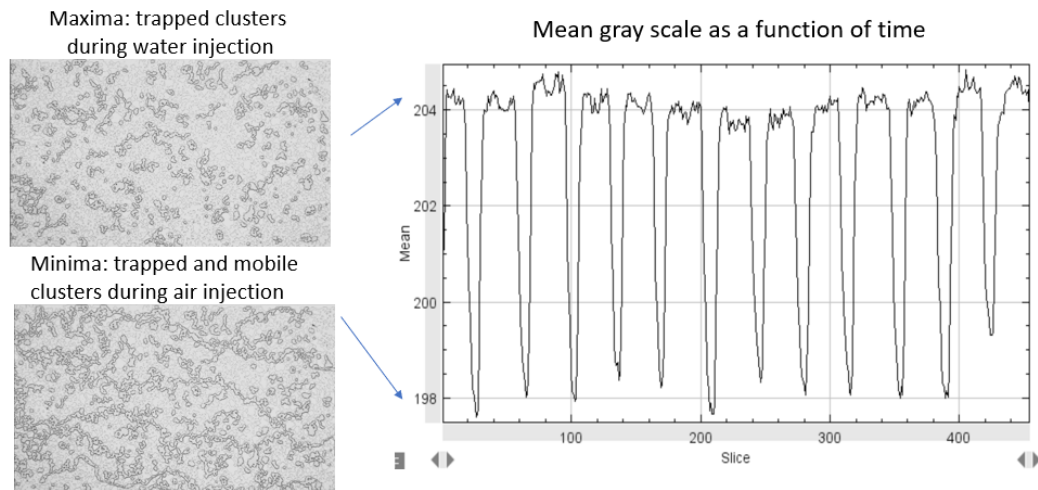


Figure 3.7 – Co-injection dynamics. (Left) unsaturated porous media during water injection with trapped air clusters (up) and during air injection with trapped and mobile air clusters (bottom). The bubbles are in darker gray. (Right) Mean gray level of the image, showing cycling behavior linked to the alternating between the water injection (trapped air clusters only) and the air injection (trapped and mobile air clusters).

Injection protocol for a neat boundary condition

The objective of the new protocol is to saturate the inlet tank with 100% ink solution before entering the micromodel porous region.

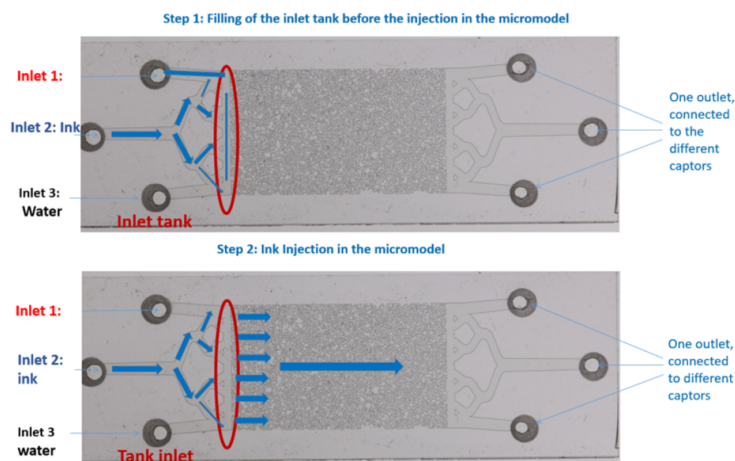


Figure 3.8 – Schematic of the injection configuration: first step

The injection configuration is achieved in two steps (Fig. 3.8): first ink solution is injected from the central inlet while inlet 1 is opened to the atmosphere. At this step, the ink will fill preferentially the lateral inlets and the inlet tank without entering the porous medium because of the greater pressure (due to the water column at the end of the microfluidic set-up). When the inlets and the inlet tank are filled with the tracer, the lateral inlet 1 is closed and the injection in the porous medium begins.

This new configuration allows to get a concentration front particularly neat as it is

shown in the comparison with the dispersion experiment in a one inlet micromodel (Fig. 3.9). The concentration profiles are now fully contained in the micromodel, which makes possible the measure of spatial moments. It is particularly useful for dispersion experiments in unsaturated porous media as the dispersion usually increases and the concentration front is more spread.

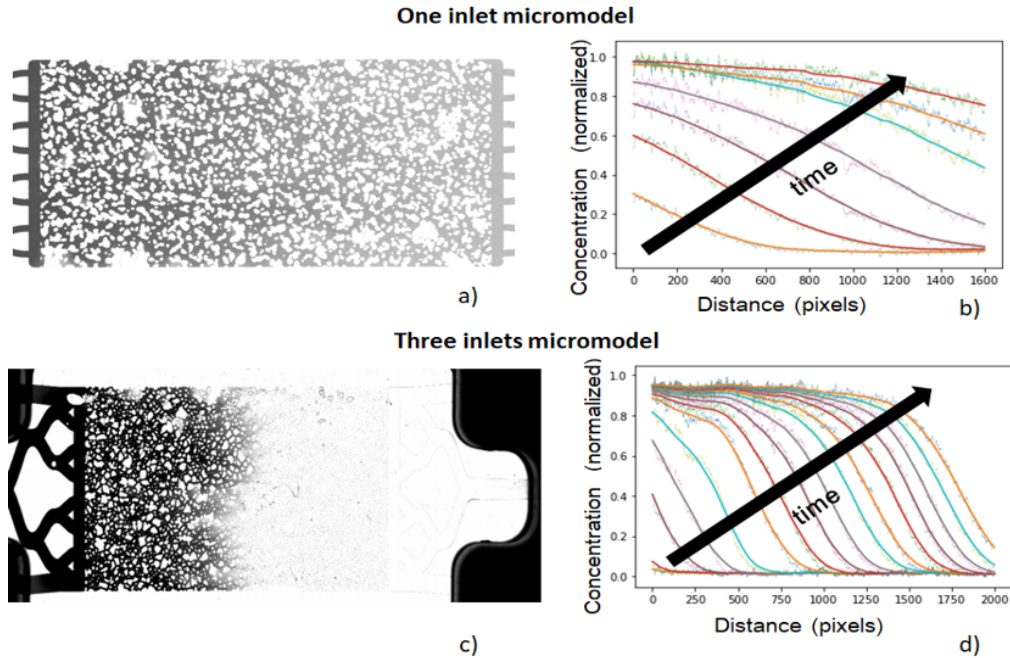


Figure 3.9 – Illustration of the new method efficiency: Transport experiment with the one inlet micromodel, from Leontidis, 2020 [104] VS transport experiment in the three inlets micromodel. The micromodel image a) concentration profile is represented by the purple curve on the Fig.b). The micromodel image c) corresponds to the purple curve in the center from the image d). The images have not been edited to show the difference of contrast regarding the concentration front between the two methods.

3.2 Data processing

3.2.1 Data analysis of the non miscible fluid distribution: image processing

All image processing is done using Fiji software [134].

Image segmentation

In a first step we identified the different phases (air, solid and water) in the images. The camera settings (light intensity and the objective aperture) were optimised in order to produce the largest possible difference between the gray levels of each phase.

For a saturated micromodel (only solid and water), a gray level threshold is chosen at the minimum between the two peaks of the gray level histogram to differentiate the solid and the water phase. The image is binarized according to this threshold value, with a

gray level value for the solid phase (0) and a gray level value for the aqueous phase (255) as shown Fig. 3.10.

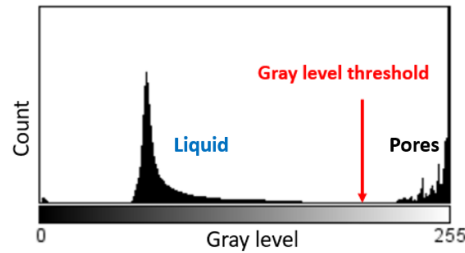


Figure 3.10 – Histogram of saturated image: choice of the threshold value for binarization.

For unsaturated conditions (solid, water and air), the segmentation is difficult to perform when using only the image of the unsaturated micromodel. Indeed, there is no clear contrast difference between air clusters and the other phases, except for the air clusters interface. An ink solution is injected in the unsaturated media to obtain a clear contrast between air clusters and the water phase.

To identify the different phases in unsaturated conditions, we developed the following image processing workflow (see Fig. 3.11) :

1. Subtraction of the saturated image from the unsaturated image to obtain the image of the air clusters (Fig. 3.11).
2. Binarization of the air clusters image, the gray-scale of the air is set to 55.
3. Binarization of the saturated micromodel to obtain a mask of the porous structure.
4. Add the image of the air clusters to the mask. This results in an image with three specific gray levels, each one corresponding to a different phase (Fig. 3.12).

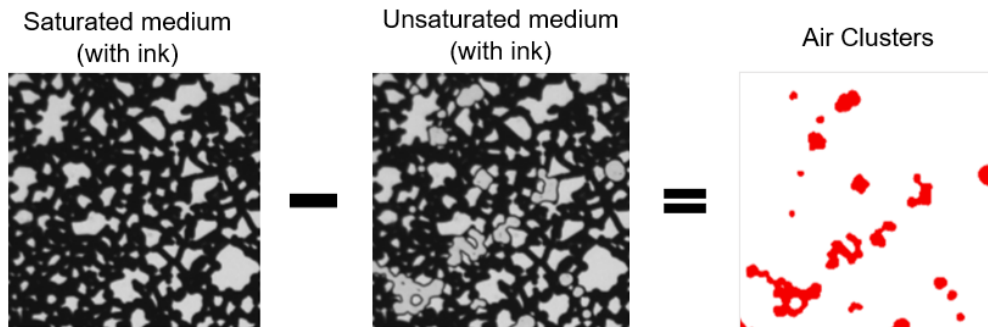


Figure 3.11 – Subtraction of the saturated image from the unsaturated image to obtain the image of the air clusters

Gray scale and concentration calibration

To relate the gray scale of the image and the concentration, it is necessary to calibrate. This work has been done before by Leontidis, 2020 [104] (cf Fig. 3.13). The calibration method consists in saturating the porous medium with solutions at different ink concentrations between 0 and 40 percent in mass and measuring the gray scale for the different concentrations.

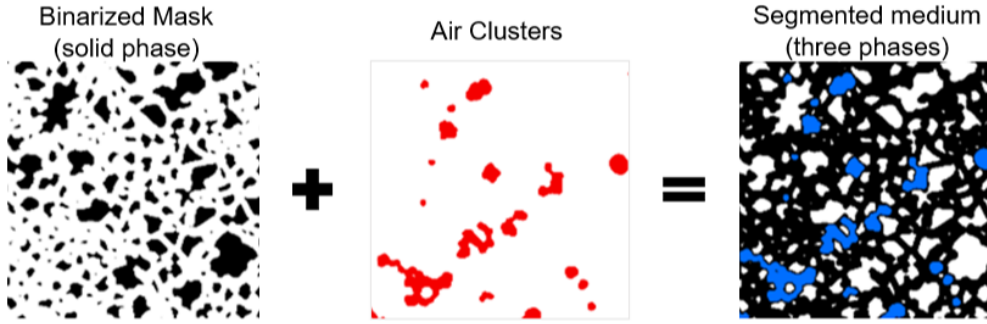


Figure 3.12 – Addition of the image of the air clusters to the mask. This results in an image with three specific gray levels, each one corresponding to a different phase

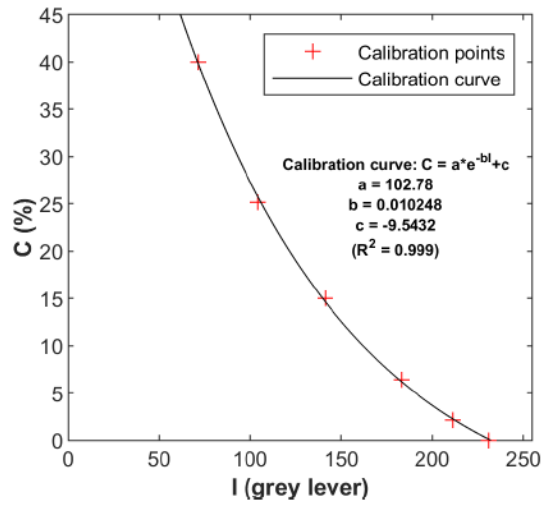


Figure 3.13 – Calibration curve for the image technique, from Leontidis 2020 ([104])

Concentration profiles

To get the concentration profiles, we average on the transverse direction the pixel grayscales $G(x,y)$, excluding pixels that do not belong to the flow zone (for which the grayscale is zero)

$$\bar{G}(x) = \frac{\sum_{y_i/G(x,y_i) \neq 0} G(x,y_i)}{\sum_{y_i/G(x,y_i) \neq 0} 1}.$$

Then, we convert the mean grayscale in a mean concentration. For an affine relation between the grayscale $\bar{G}(x)$ and the concentration, we get

$$c(x) = c_{\min} + (c_{\max} - c_{\min}) \frac{G_{\min} - \bar{G}(x)}{G_{\min} - G_{\max}}.$$

Concentration profiles can be noisy, particularly for experimental data. Therefore, we can use a filter to smooth the curve, such as the Savgol filter present in Python library, as shown Fig. 3.14.

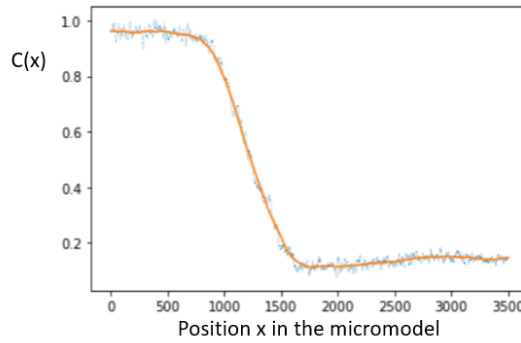


Figure 3.14 – Concentration profile for a continuous injection and smoothed curve with the Savitsky-Golay algorithm (Savgol filter).

Quantitative analysis on phases distribution

With binary images for each phase of the system, we can compute the area occupied by each phase with ImageJ measuring tools. Indeed, the histogram gives the number of pixels for each gray level (i.e for each phase), namely n_{solid} , n_{air} and n_{water} . Notably, it gives access to the saturation denoted S_w

$$S_w = \frac{n_{\text{water}}}{n_{\text{air}} + n_{\text{water}}},$$

and the porosity denoted ϕ

$$\phi = \frac{n_{\text{air}} + n_{\text{water}}}{n_{\text{air}} + n_{\text{water}} + n_{\text{solid}}}.$$

The analyse particle tool from the ImageJ toolbox allows to identify each particle on a binarized image, with selection parameters such as the minimal area and the circularity. The characteristics of each identified object are measured (area, perimeter, shape factors, etc). It allows us to get statistical data on the bubbles and solid particle distributions.

These data serve as a base to extract different statistical properties, such as the area distribution of the bubbles (maximal area, mean area, etc). It is possible to use them to perform more complex analysis and/or operations on the image stack.

3.2.2 Data analysis of the concentration fields: methods of moments

Introduction

The spatial moments method is a straightforward method to characterize dispersion, which does not require any hypothesis on the nature of dispersion, contrary to fitting breakthrough curves with models such as ADE solutions. The method can be applied to experimental or simulation data (Fig. 3.15), for continuous or Dirac injections. Notably, it can be applied to 2D Lattice-Boltzmann transport simulations in porous media, that will be detailed in a later chapter.

In this section, we will present the method of spatial moments for analysing the dispersion in the medium. To this goal, we consider a 2D flow characterized by a mean flow in the x direction, and with an injection of tracer at the entrance of the medium ($x = 0$). We aim at quantifying dispersion by deriving the moments of the concentration profiles. The computations are realized with the Python software.

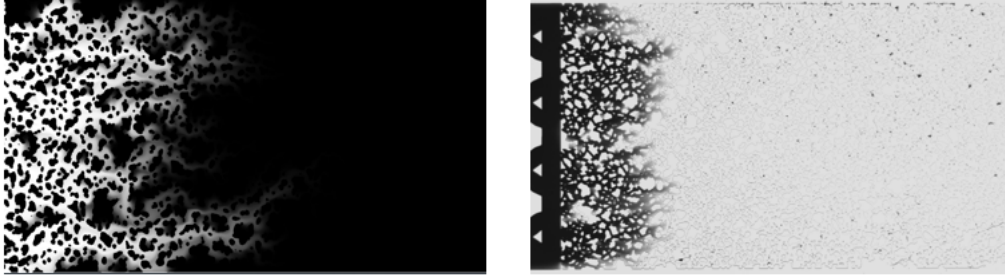


Figure 3.15 – Example of concentration fields. (Left) LBM transport simulation in saturated porous media. (Right) Laboratory experiment of dispersion in saturated porous media.

We work with a set of images of concentration fields as a function of time, for which concentration is quantified by the pixel gray level. Images should have been modified beforehand so that the part where there is no water (solid or gas) has a zero gray scale level. In order to test the validity of the method, we take the example of dispersion in a 2D channel (2D Taylor dispersion), for which analytical solutions are well known. We run dispersion simulations on a 2D channel and use the moments methods to see if it fits with the theory.

General principle

Spatial moments of the concentration fields are frequently used to characterize dispersion, notably because they enable to distinguish Fickian transport from anomalous transport. In particular, we study the temporal evolution of the concentration field along the flow direction via time dependent second moments. First, we average the concentration over the width of the medium to have one dimensional normalized concentration profiles defined as $\tilde{c}(x,t) = \frac{1}{c^{\text{in}} L_y} \int_0^{L_y} c(x,y,t) dy$ with c^{in} being the injection concentration. Then, the dispersion analysis is done by characterizing the statistical properties of the distribution over time through the computation of spatial moments, as shown Fig. 3.17.

The first moment leads to the mean position of the concentration front for a given time. Its time evolution allows to know the effective velocity of the concentration front in the medium. The second moment characterizes the width of the distribution, consequently, its evolution with time allows to assess the concentration front spreading. Notably, in the context of normal dispersion it allows to derive the dispersion coefficient.

If the injection is a pulse, we can characterize directly the distributions of the concentration profiles. On the other hand, if the injection is continuous (Fig. 3.16, (Left)), then we need to characterize the distributions of the profile derivatives (Right). Then, for continuous injection, 1D distributions $p(x,t)$ are generally obtained from the normalized derivatives of the concentration profiles such that $p(x,t) = -\frac{\partial \tilde{c}(x,t)}{\partial x}$. The moment of order r is defined as

$$m_r(t) = \int_0^{L_x} p(x,t) x^r dx = - \int_0^{L_x} \frac{\partial \tilde{c}(x,t)}{\partial x} x^r dx. \quad (3.2.1)$$

For $r \geq 1$, this formula requires the computation of the average concentration derivative, however it leads to noisy results in practice. To improve the quality of the analysis and decrease the noise, we can resort to integration by part in Eq. 3.2.1. In the following,

we detail the alternative method of calculation and compare it to the classical integrative method.

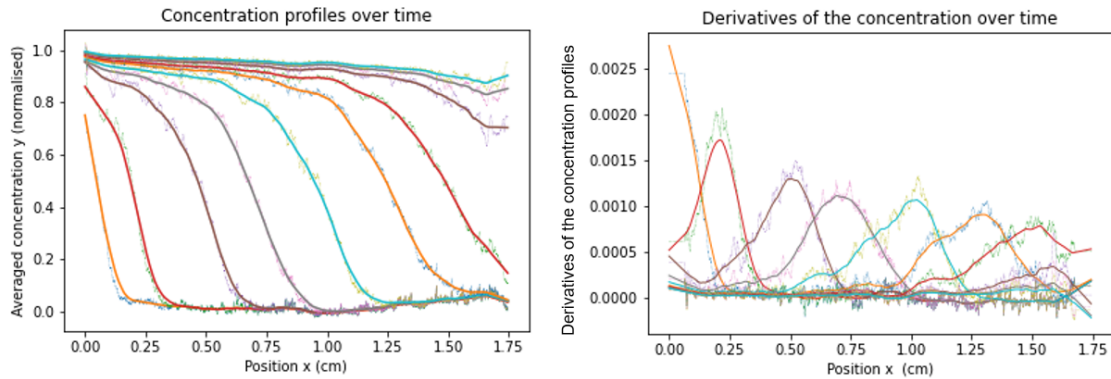


Figure 3.16 – Example of concentration profiles for a continuous injection (Left) and derivatives of the concentration profiles for a continuous injection (Right)

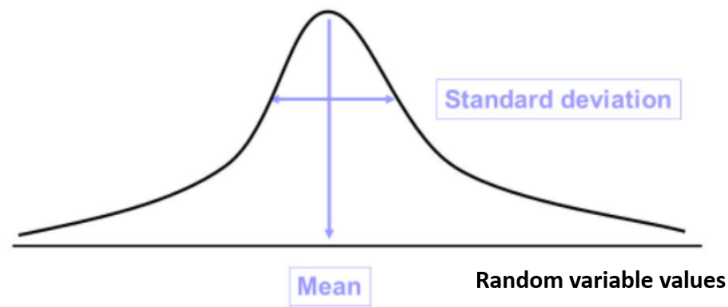


Figure 3.17 – Illustration of the first and second moment: mean position and width of the distribution

Calculation methods

Spatial moments calculation: classical method

The derivatives of the concentration profiles are computed numerically and can be smoothed with the Savgol filter as shown 3.18. Then, moments expression are computed according to Eq. 3.2.1.

Remarks

In the preceding chapter, the expression of moments is presented using integrals. However, since concentration profiles are discrete, calculating the moments numerically requires summation instead of integration. When dealing with experimental images, it is common to encounter noisy distributions. To address this issue, we adopt specific measures to ensure the reliability of our calculations:

- Exclusion of negative values: Since noise can lead to occasional negative values in the distribution, which are not physically meaningful, we exclude such values from our analysis.

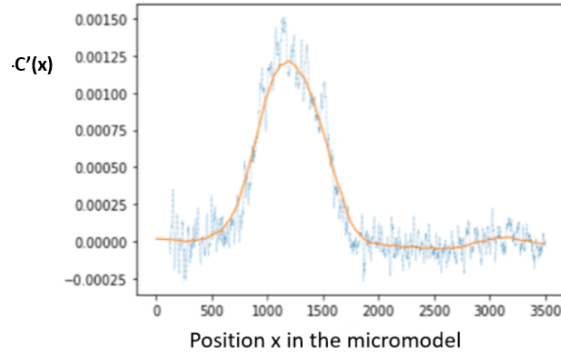


Figure 3.18 – Concentration profile derivative and smoothed curve with the Savitsky-Golay algorithm

- Limiting the interval for variance calculation: To mitigate the influence of noise at the extremities of the distributions, we set appropriate limits for calculating the variance around the mean position $[x_{\text{moy}} - r\sigma; x_{\text{moy}} + r\sigma]$, with $r > 3$, to avoid the noise at the extremities of the distributions. For a Gaussian distribution, it means that values below $c_{in} e^{-(r\sigma)^2/\sigma^2} = c_{in} e^{-r^2} = 10^{-4} c_{in}$ are neglected for $r = 3$.

Spatial moments calculation: integrative method

To avoid the computation of the derivatives, we resort to integration by part in Eq. 3.2.1, for $r > 0$. With the boundary conditions $\tilde{c}(x = 0, t) = 1$ and $\tilde{c}(x = L_x, t) = 0$, we have

$$m_r(t) = - \left([\tilde{c}(x)x^r]_0^{L_x} - r \int_0^{L_x} \tilde{c}(x,t)x^{r-1} dx \right), \quad (3.2.2)$$

considering the boundary conditions, it simplifies as

$$m_r(t) = r \int_0^{L_x} \tilde{c}(x,t)x^{r-1} dx. \quad (3.2.3)$$

We obtain moments of the order r . We now detail the formula for $r = 1, 2, 3$ as they are the most useful to characterize dispersion. The first moment ($r = 1$) is given by

$$m_1(t) = \mu(t) = \int_0^{L_x} \tilde{c}(x,t) dx. \quad (3.2.4)$$

Furthermore, the variance defined as

$$\sigma^2(t) = \int_0^{L_x} p(x,t)(x - m_1(t))^2 dx, \quad (3.2.5)$$

recasts

$$\sigma^2(t) = m_2(t) - m_1^2(t) \quad (3.2.6)$$

with

$$m_2(t) = 2 \int_0^{L_x} \tilde{c}(x,t)x dx. \quad (3.2.7)$$

Finally, the skewness is given by

$$\gamma(t) = E \left[\left(\frac{x(t) - \mu(t)}{\sigma(t)} \right)^3 \right] = \frac{m_3(t) - 3\mu(t)\sigma(t)^2 - \mu(t)^3}{\sigma(t)^3}$$

with

$$m_3(t) = 3 \int_0^{L_x} \tilde{c}(x,t)x^2 dx. \quad (3.2.8)$$

For a discrete set of concentration $(\tilde{c}_i)_{i \in 1, \dots, n}$ over the domain $(\tilde{x}_i)_{i \in 1, \dots, n}$, the first moment writes

$$\mu = \frac{L_x}{n} \sum_{i=1}^n \tilde{c}_i,$$

the variance

$$\sigma^2 = -\mu^2 + 2 \frac{L_x}{n} \sum_{i=1}^n \tilde{c}_i x_i,$$

and the skewness

$$\gamma = \frac{3 \frac{L_x}{n} \sum_{i=1}^n \tilde{c}_i x_i^2 - 3\mu\sigma^2 - \mu^3}{\sigma^3}.$$

Remarks

The values obtained using this method are highly sensitive to the boundary conditions applied. Therefore, it is crucial to carefully set and define appropriate boundary conditions to ensure accurate results. One common adjustment involves subtracting an offset from the data so that the concentration at the right side of the profile equals zero. For datasets with minimal noise, such as simulation results in a channel, both the integrative and derivative methods will yield similar outcomes. However, when dealing with data containing a substantial amount of noise, the integrative method proves to be more advantageous. In such cases, the derivative curve can become extremely noisy, making the derivative approach less reliable, while the integrative method remains robust and suitable for analyzing the noisy data accurately.

Dispersion characterization

Moments verification

To check the accuracy of the calculated first and second moments, we can compare the concentration distribution with a Gaussian function that has the same first and second moments. For Fickian dispersion, the Gaussian function should fit the data quite well. This comparison provides a means to ensure that the moments we calculated are correct, as illustrated in Fig. 3.19. Once the spatial moments have been computed, we can characterize the dispersion.

First moment: front velocity

The front velocity can be determined by examining the slope of the first moment as a function of time. The first moment provides the mean position of the concentration front over time. In the case of a constant flow rate, the front velocity typically reaches a steady value after an initial transient period. To obtain the final value of the front velocity, a linear regression analysis is performed on the data to estimate the slope of the first moment versus time during the steady-state phase.

Second moment: nature of the dispersion

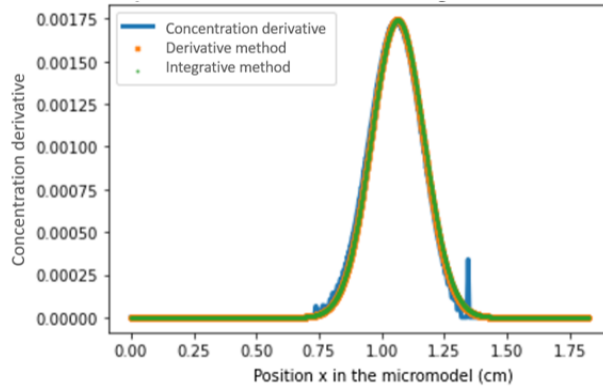


Figure 3.19 – From simulation data. Comparison of the distribution (derivative) with a Gaussian taking the moments calculated as parameters.

The variation of the second moment with time provides valuable insights into the nature of dispersion. If the second moment becomes proportional to time, it indicates Fickian dispersion behavior. In the Fickian case, a dispersion coefficient can be calculated by performing a linear regression analysis on the second moment versus time data.

$$\sigma^2 \propto 2Dt. \quad (3.2.9)$$

Validation of the method with an example: Taylor dispersion simulations in a bi-dimensional channel

To validate the derivative and integrative method, we take the well-known example of Taylor dispersion (in 2D), for which the coefficient of dispersion is given by

$$D = D_m \left(1 + \frac{Pe^2}{210} \right) = D_m + \frac{v^2 L^2}{210 D_m},$$

with D_m being the microscopic diffusion coefficient, L the channel length and v the flow velocity.

We conducted a series of simulations to explore dispersion within the channel at various velocity levels. The primary objectives were to analyze the dispersion outcomes and verify the accuracy of our methodology. We chose a configuration of a channel that is 10000 pixels long and 46 wide, with 3 solid pixels (i.e pixels with a 0 value) on each side to mark the limits of the channel.

Simulations: generation of the flow field with Stokes and dispersion with ADE equations

We used a Lattice-Boltzmann code developed at IFPEN to simulate flow and transport in porous media. It is a TRT-LBM method and it will be described more thoroughly in the numerical section. We performed the Lattice-Boltzmann simulation in two steps. First, we simulated the flow with a Stokes law in the channel. Then, once the flow was stable, we simulated the injection of a tracer at the inlet, the microscopic diffusion being controlled by the advection-diffusion equation with the diffusion coefficient D_m . We realized two types of injection: Dirac injection (Fig. 3.21) and continuous injections 3.20.

Simulations parameters

Figure 3.20 – Concentration field for a continuous injection in the channel

Figure 3.21 – Concentration field for a Dirac injection in the channel

We realized those simulations for different values of the flow velocity and for the two types of injection. Thus, we could derive the spatial moments and particularly the second moment and its evolution with time, for each value of the flow velocity. From the dispersion coefficient expression, there must be a linear dependency between the dispersion coefficient and the square of the Peclet number.

Derivation of the moments

We compute the moments with the derivative and integrative method. As shown in Fig. 3.19, the computed moments fit really well with the simulation data, for both methods. We took a simple example of bi-dimensional channel, and it is simulation data, therefore there is very little noise. Hence, there is almost no difference between the two methods results. The moments computed being quasi identical for the two methods, for simplicity, only one curve or set of data is shown in the following discussion, that is representative of both methods results.

Analysis of the dispersion

We analysed the simulations with the methods previously described. The first moment and the variance are linear with time, so we could derive the effective velocity and the dispersion coefficient. As shown in Fig. 3.22, effective velocity obtained from the calculations corresponds to the fluid velocity imposed in the simulation, which validates the method to characterize the front velocity with the first moment.

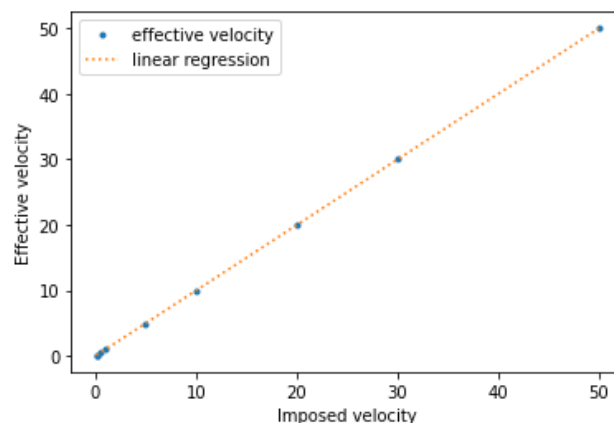


Figure 3.22 – Effective velocity as a function of the velocity imposed in the simulation.

Then, we derived the dispersion coefficients from the simulation as well as the theoretical values (cf Tab. 3.1). As shown Fig. 3.23, we found a linear dependence between

the dispersion coefficient and the velocity squared as predicted by the Taylor formula in a channel. Plus, the dispersion coefficient computed fits well with the theoretical coefficients, as Tab. 3.1 highlights.

Table 3.1 – Theoretical coefficient dispersion values and computed values. The error is computed as the relative difference with the theoretical value. For Pe values for which no Dirac injection simulation was realized, the table indicates \emptyset .

D_{theory}	Pe	$D_{\text{continuous}}$	D_{Dirac}	$\text{Error}_{\text{continuous}}$
0.00346	4.8	0.00347	0.00344	0.2 %
0.00399	7.6	0.00404	\emptyset	1 %
0.0121	24.4	0.125	0.0120	3 %
0.0388	49.0	0.0401	\emptyset	3 %
0.144	97.3	0.141	\emptyset	2 %
0.88	242.0	0.83	0.86	5 %
3.52	486	3.45	3.52	2 %
14.1	975	13.6	13.5	4 %

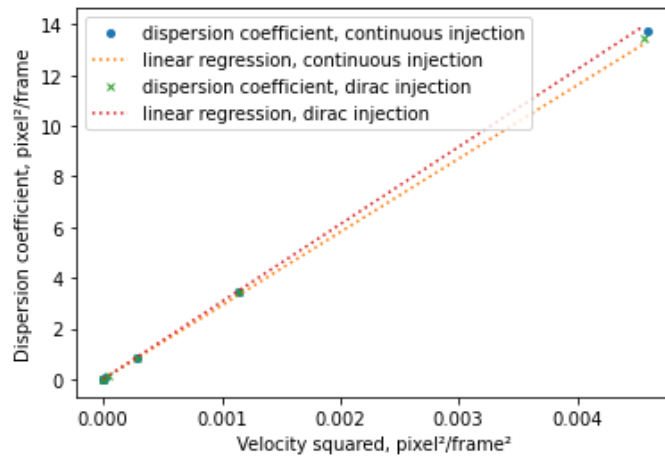


Figure 3.23 – Dispersion coefficient as a function of the mean flow velocity

Therefore, the method is accurate to characterize the dispersion whether it is a Dirac or continuous injection. However, simulations with high Pe involved larger numerical errors and were less accurate than simulations at low velocity: the problem probably comes from the size of the channel, using a wider channel instead would decrease the error.

Comparison of the integrative and derivative methods

The integrative and derivative method have been validated with the channel simulations, for which they give similar results. However, in the case of experimental data, typically in the case of unsaturated porous media, the derivative method is not adapted because the concentration profiles are too noisy. In such cases, the integrative method is more accurate and can be used to analyse the data, as it can be seen in Fig. 3.24.

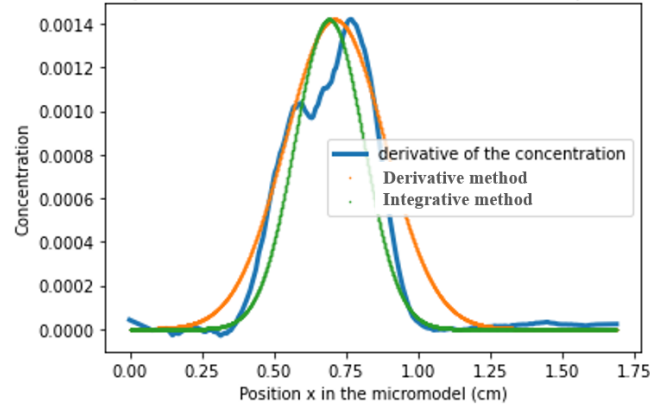


Figure 3.24 – Moments computation for experimental data in unsaturated condition

Conclusion

In this section, we have provided a detailed explanation of the method used to study dispersion by computing spatial moments. To validate the effectiveness of this method, we applied it to a well-known example of Taylor dispersion, which served as a benchmark.

Moreover, we have introduced an alternative approach that overcomes the limitations of the traditional method, specifically when dealing with noisy experimental distributions, which are common in unsaturated conditions. This alternative method allows us to calculate spatial moments more reliably and accurately even in the presence of significant noise in the experimental data.

3.2.3 Further Data Processing

Porous media analysis

REV (Representative Elementary Volume)

It can be useful to compute a Representative Elementary volume (REV) of the porous medium, typically to ensure that the medium is sufficiently large to be statistically representative.

The process of calculating the REV involves taking windows of increasing size within the image of the porous medium. For each window, a statistical analysis is performed to determine specific properties, such as porosity value or mean grain area. The goal is to identify the window size at which the statistical properties stabilize, indicating that the medium is sufficiently large to be considered statistically representative. The REV is defined for a specific property, the porosity value for example, or the mean grain area. As we can see in Fig. 3.25, the porosity is not constant when computed in a small window, but it reaches a constant value when the window is sufficiently large, for a size that can be defined as the REV_{porosity} . The same behavior is observed with the grain area, and we can define another REV, the REV_{grains} . The REV computed after different criteria can be different, here for example the REV_{porosity} is larger than the REV_{grains} .

Furthermore, we can define a REV for unsaturated media. For example by taking the saturation or the bubble mean size as a REV criteria (REV_{sat} and REV_{bubble}). It allows us to assess the minimal size we need to have statistically representative properties. Still, if we want to study dispersion, having a porous media that has a REV for porosity does

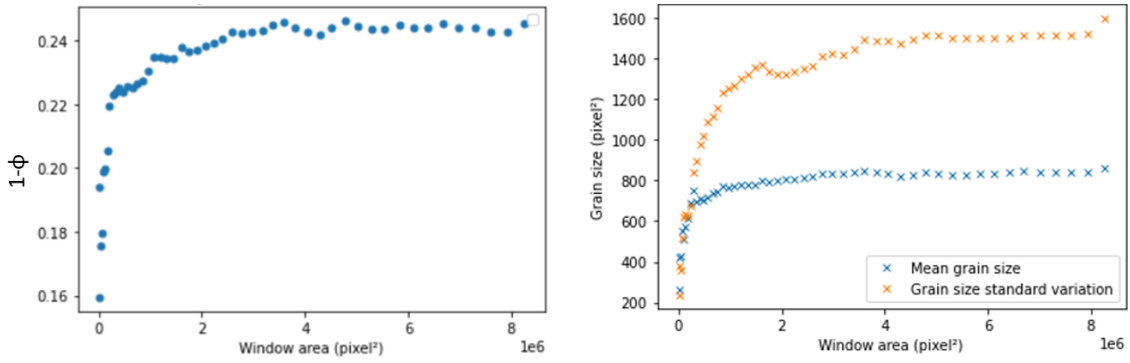


Figure 3.25 – REV of the porous media. (Left) Porosity ϕ as a function of the window’s size. (Right) Mean grain size and grain size standard deviation as a function of the window’s size.

not mean that it is statistically representative for the dispersion. Indeed, the REV for dispersion (computed for the dispersion coefficient for example) is often a lot larger than the $\text{REV}_{\text{porosity}}$, and particularly so in unsaturated conditions [39].

3.3 Validation of the transport protocol

3.3.1 Repeatability of the injection

The repeatability of the injection has been investigated. To this end, we repeated the injection for different flow rates and computed the moments in order to see if the results were comparable, and especially if the front velocity was constant (non interruption of the injection) and the velocity value similar for all injections. The front velocity can be computed with the first moment. The front velocity corresponds to the slope of the first moment.

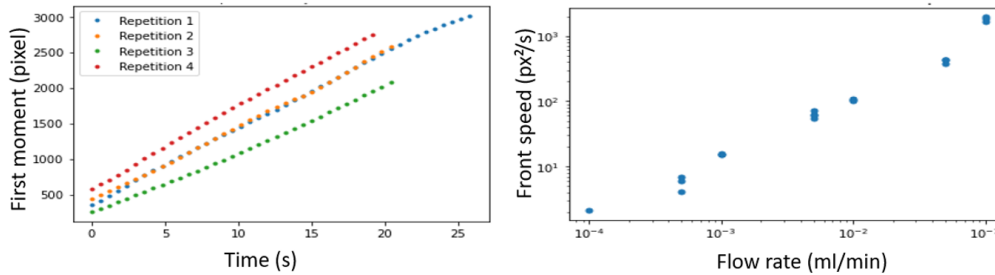


Figure 3.26 – Repeatability of the injection in saturated conditions: First moment evolution with time for a given flow rate ($Q=0.01\text{mL}/\text{min}$), for 4 repetitions (left); Front velocity as function of flow rate (right)

We see in Fig. 3.26 (left) that the slopes of the first moment represented as a function of time are really similar, which means the front velocity is the same for all injections. There is a slight transient regime where the slopes are different at the beginning of the injection, which might be linked to the fact that the initial conditions are not exactly identical when we open and close the valves.

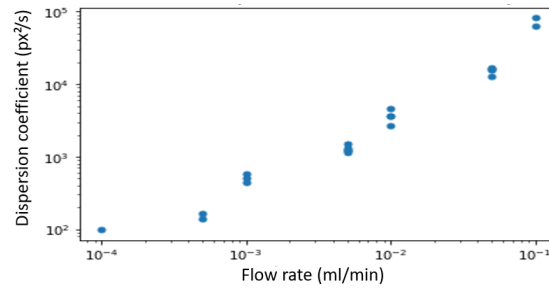


Figure 3.27 – Repeatability of the dispersion experiment in saturated conditions: Dispersion coefficient as a function of flow rate.

The dispersion experiment is also repeatable in terms of dispersion coefficients as we can see in Fig. 3.27. We computed the dispersion coefficient from the slopes of the second spatial moment, for a wide range of flow rates and under saturated conditions. As expected, the dispersion coefficient increases with the flow rate. The repeatability of the injection has also been investigated under unsaturated conditions for different flow rates and saturation values. It gives similar results as shown in Fig. 3.28. Indeed, the slope of the moments are also similar. There is a slight inflexion of the curves at the beginning of the experiment in some cases, as the configuration of injection is complex, there is a little delay before the flow velocity becomes constant.

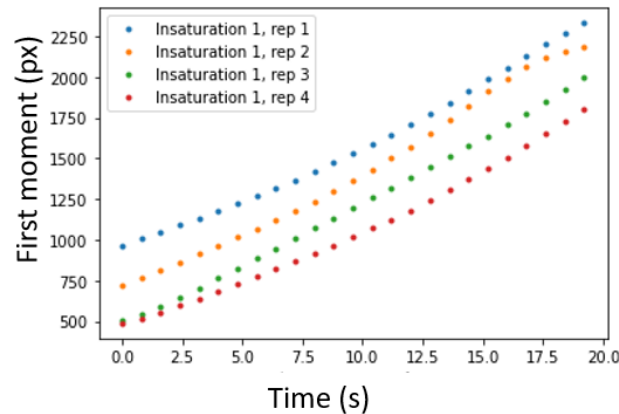


Figure 3.28 – Repeatability of the injection: First moment evolution with time for a given flow rate ($Q=0.01\text{mL}/\text{min}$), for 4 repetitions in unsaturated conditions.

3.4 Conclusion

In this chapter, we provided a comprehensive description of the experimental and data processing methods developed for this research. To study flow in unsaturated porous media, we developed a micromodel experimental setup. This micromodel enables the capture of the multiphase structure and allows access to the concentration field at any point during the experiment. Firstly, we outline the co-injection setup and the procedure for creating unsaturated conditions in the micromodel. Specifically, we described how water and air are simultaneously injected into a cross tubing, resulting in a cyclic process of air and water injections within the micromodel. The co-injection process is halted when the trapped phase reaches a steady state, thereby preserving the unsaturated medium with immobile

air clusters for subsequent transport experiments. Additionally, we provide details on the tracer injection configuration, which ensures a clear boundary condition at the entrance of the micromodel. This modified configuration allows for the filling of the reservoir and the inlets of the micromodel with the tracer before starting the injection within the micromodel itself. This approach effectively prevents dispersion in the upstream tubing. Furthermore, we presented the data processing developed to analyze the concentration fields resulting from transport experiments. Notably, we characterize transport properties by computing moments of the concentration profiles.

However, the experimental methods we developed have intrinsic limitations, first we do not have direct access to the flow and the velocity field with experiments, and the range of Peclet or flow rates we can achieve is rather limited. Despite, perfectly determined boundary condition is impossible to achieve. This is why we complemented experimental techniques with flow and transport simulation using the Lattice Boltzmann method (LBM), a class of Computational Fluid Dynamics method commonly used for its high computational efficiency and its ability to deal with complex geometry such as porous media.

Chapter 4

Numerical strategy

4.1 Numerical methods for flow and transport simulations

Regarding the experimental limitations in a micromodel, we propose to complement our experimental work with numerical simulations. In fact, flow experiments in a micro-model do not provide direct access to the flow, whereas numerical simulations can easily compute the velocity field at any point. In addition, the experimental device does not have a perfectly neat ink inlet condition. Although complex conditions at the interface between the different phases cannot be accurately reproduced in simulations, transport simulations can guarantee a clear boundary condition and a more accurate analysis. Finally, changing the micro-model structure is a time consuming and complicated task in experiments whereas it can be done easily with numerical models.

Many approach and numerical methods can be considered to simulate our physical system. In this work, we seek for a fast, robust and accurate numerical method. Also, we want this method efficient on large domain while keeping a micro pore-scale (micro, meso) resolution. On one side, we have the conventional numerical methods, where a macroscopic description of the fluid dynamic is characterized by a set of equations. To solve these equations, we could resort to classical methods such as finite difference (FD) methods for which derivatives are computed numerically. The FD methods do not conserve mass, momentum and energy. Their order of accuracy can be significantly upgraded but their robustness is irretrievably reduced. They are barely used for complex geometry because they are based on regular grid most of the time. Finite volume (FV) methods rely on a decomposition of the geometry (called mesh) in non overlapping small volumes (called cells). The equation are integrated on each cell so that fluxes need to be computed at each cell boundary. FV methods are robust, conservative and can resolve complex geometry. However the mesh construction might not be easy for complex/large geometries and the mesh orientation can have a deep impact on the solution accuracy [103, 129]. Also, FV methods generate numerical diffusion which can prevail over the real physics. Their accuracy improvement is generally limited to second order (theoretically) [160] and is effectively less for complex problem involving non-linearly or rheology [45]. Finite element methods (FEM) requires a gridding of the geometry to define an associated basis of polynomial function. A variational formulation of the problem is then deduced and solved. FEM can deal with complex geometry and can have a high order accuracy. However, they do not preserve conservation and generally generates instabilities. FEM, and also FD and FV methods when associated with an implicit numerical scheme, require to solve very large sparse linear systems. The resolution of these sparse linear systems is a key point for the methods efficiency [89] which is generally degraded when the number of unknowns increases. On the other side,

we have the kinetic methods which model distributions of particles in coordinates and velocity spaces. Integration of these particle distributions yields moments (mass, momentum, energy, etc.) to recover information of the flow. Kinetics methods requires a collision operator which is designed to recover the desired physics. Among others, let cite the lattice gas models [57, 80], the smoothed-particle hydrodynamics (SPH) methods [164] and the Lattice Boltzman methods (LBM) [99]. These methods can deal with complex geometry. The LBM are natively second order accuracy and are very efficient on huge mesh with massive parallel computations. For these reasons, LBM are becoming increasingly popular in the scientific community as illustrated in Fig. 4.1.

In [174], Yang *et al* performed a comparison of numerical methods for 3D pore-scale flow with solute transport. They reviewed FV methods with the codes TETHYS (The Transient Energy Transport Hydrodynamics Simulator [126]) and STAR-CCM [137] (associated with a multigrid solver), LBM methods [61, 62], SPH methods [156] with the library LAMMPS [125] and the pore network model (PNM) with code UT-PNM from University of Texas at Austin [110]. Their simulation models are composed of about 53 million nodes and 3.7 million nodes. They concluded that all the methods provide similar results in term of accuracy. The UT-PNM was very efficient but it needed a geometry simplification and the local flow velocity was no more available for precise analysis. They noticed that the LBM were very efficient, especially when used on GPU. For these reasons, we choose to use LBM to simulate our physical systems. The first reason is the simplicity of use, especially because we do not need to generate a mesh. Keep also in mind that we will use the method for very large domains while keeping the pore scale resolution. To be clear, in the chapter 7, we performed simulations with more than 350 million nodes. It was possible thanks to the parallel computing ability of the LBM method; 9000 processors were used. In comparison, the efficiency of classical numerical methods would have dropped drastically because processor communications become a bottleneck and the data size is limited.

To reduce our computational costs and times, we choose to proceed the simulation methodology in two sequential steps. We first resolve a steady "base flow" in the porous media, without any tracer. A pressure gradient is imposed between the inlet and the outlet of the domain and we let the simulations converge through a steady state, up to a well tuned criterion. From this first computational step, we retrieve the local velocity field. Then, we solve the advection diffusion of a passive tracer, its advection velocity being the velocity obtained from our first step. The tracer is numerically injected at the entrance of the domain and we simulate until its breakthrough at the outlet. With this simulation methodology, we suppose that the tracer is effectively passive: it has no influence on the 'base flow'. Even if this assumption might look restrictive, it is perfectly appropriate to our physical problem. Thus, we used two separate codes, each one devoted to its physics. This has another great advantage on the numerical efficiency; we can optimize the numerical parameters (time steps for example) separately. To finish with, to further reduce computational times, we will restrict our simulation on 2D numerical models. The Darcy-Brinkman equation is used to compute the depth-average velocity. This allows to describe a 3D velocity field with a 2D equation as demonstrated by [178]. Then, the ADE flow is solved in 2D also by using the depth-average velocity. The numerical simulations have been performed with the waLBerla Framework [11] [68].

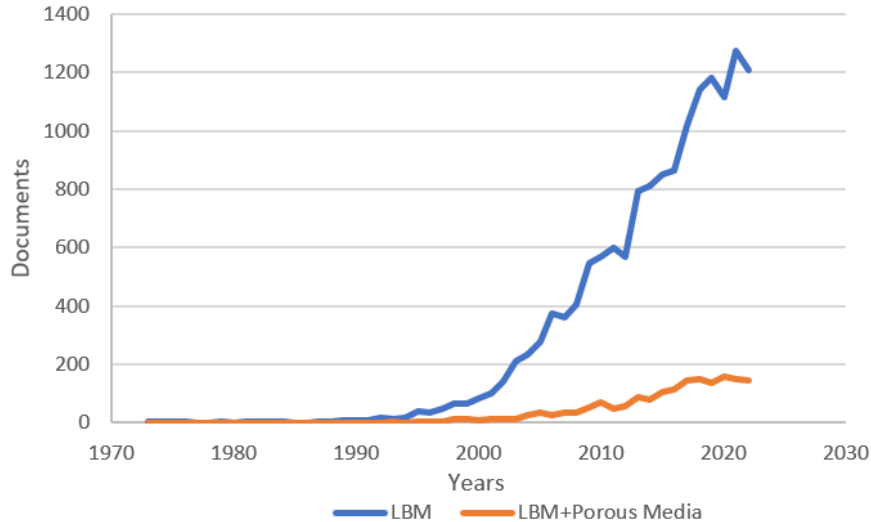


Figure 4.1 – Increasing popularity of Lattice Boltzmann Method: occurrences of "Lattice Boltzmann Method" and "LBM + porous media" in research papers

4.2 Lattice Boltzmann method

4.2.1 Introduction

With the growth of computer power, CFD methods for numerical resolution of governing equations of fluid mechanics have been increasingly used and developed. Indeed, a great number of model equations do not have analytical solutions, such as Navier-Stokes equation [142]. It motivates the development of methods for numerical resolution. Over the last two decades, LBM, an alternative approach to simulate flow, transport and heat transfer gained in popularity [34]. In this approach, instead of solving directly the governing equations, the kinetic equation is solved to obtain the particle distribution function. Then, one obtains the macroscopic variables by evaluating the hydrodynamic moments of the particle distribution function. The main idea behind the LBM approach is that the collective behaviour of many microscopic particles defines the macroscopic dynamics of a fluid. Moreover, the individual behavior of an individual particle does not impact the macroscopic behavior. Therefore, the LBM finds the solution of a minimal Boltzmann kinetic equation instead of discretizing the fluid governing equation.

In this section, we describe the Lattice-Boltzmann method in its general framework; we start by the description of the Boltzmann equation (BE) and then the Lattice-Boltzmann Method (LBM) which corresponds to a discretization of the BE in space and velocity. We review some classical collision operator and start to focus on our problems: flow in unsaturated porous media. Then, we select the best operator in line with our objectives and our means. Most of the classical concepts of LBM presented in this section have been inspired by [99] and [123].

4.2.2 Boltzmann equation

Kinetic models describe the particle distribution function $f(\mathbf{r}, \mathbf{v}, t)$ which represent the density of particles at position \mathbf{r} , velocity \mathbf{v} and time t . f is connected to macroscopic

variables like the density, the momentum and the total energy with the relations

$$\begin{aligned} \rho(\mathbf{r}, t) &= \int f(\mathbf{r}, \mathbf{v}, t) d\mathbf{v}, & \rho \mathbf{u}(\mathbf{r}, t) &= \int f(\mathbf{r}, \mathbf{v}, t) \mathbf{v} d\mathbf{v}, \\ \text{and } \rho \mathbf{E}(\mathbf{r}, t) &= \int f(\mathbf{r}, \mathbf{v}, t) |\mathbf{v}|^2 d\mathbf{v}. \end{aligned} \quad (4.2.1)$$

When the fluid is left at rest, it is admitted that the particle distribution tends towards an equilibrium with an isotropic velocity denoted here \mathbf{u}^∞ . The equilibrium is given by the Maxwell-Boltzmann distribution [69]

$$f^{\text{eq}}(\mathbf{r}, |\mathbf{v} - \mathbf{u}^\infty|, t) = \rho \left(\frac{1}{2\pi RT} \right)^{\frac{3}{2}} \exp \left(-\frac{|\mathbf{v} - \mathbf{u}^\infty|^2}{2RT} \right), \quad (4.2.2)$$

where R is the ideal gas constant and T the fluid temperature.

The particle distribution is governed by the Boltzmann equation

$$\frac{\partial f}{\partial t} + \mathbf{v} \cdot \nabla_{\mathbf{r}} f + \mathbf{F} \cdot \nabla_{\mathbf{v}} f = \Omega(f), \quad (4.2.3)$$

where \mathbf{F} is the force field acting on the particles in the fluid. For simplicity, it will be omitted in the following. $\Omega(f)$ is the collision operator. In order to preserve mass, momentum and energy conservation, the collision operator must satisfy

$$\int \Omega(f) d\mathbf{v} = 0, \quad \int \Omega(f) \mathbf{v} d\mathbf{v} = \mathbf{0} \quad \text{and} \quad \int \Omega(f) |\mathbf{v}|^2 d\mathbf{v} = 0. \quad (4.2.4)$$

The original collision operator of Boltzmann is far too complex to be applied in practical cases. Generally, we consider simplified operator that are sufficient to reproduce correctly the physics. Several approximations of collision operators will be detailed later on in subsection 4.2.6. Here we just give the example of the Bhatnagar-Gross-Krook (BGK) collision model [19]

$$\Omega(f) = -\frac{1}{\tau} (f - f^{\text{eq}}), \quad (4.2.5)$$

where τ is the relaxation time.

To finish with, the Boltzmann equation admit an entropy

$$\mathcal{H} = \int \int f \ln(f) d\mathbf{r} d\mathbf{v}, \quad (4.2.6)$$

which can only decrease ($\frac{\partial \mathcal{H}}{\partial t} \leq 0$) and reaches its minimum value when $f \rightarrow f^{\text{eq}}$.

4.2.3 Lattice-Boltzmann method

LBM is a discretization method of the Boltzmann equation using a regular grid of spacing Δx and a discrete set of velocities \mathbf{c}_q . Many velocity sets have been experimented, most frequently in the framework of Navier-Stokes equations. Denoting these velocity sets as $DnQm$ with $n \in \{1, 2, 3\}$ the dimension of the domain and m the number of velocities, we can cite the classical D1Q3, D2Q9, D3Q15, D3Q19 and D3Q27 discretizations. Usually, increasing the dimension m of the velocity set increases the accuracy but also the computational costs. In addition to the velocity set chosen, we have to consider an associated set of positive weight w_q which must satisfy consistency relations to recover the moment conservation [99]. The first 3 consistency relations are given by

$$\sum_q w_q = 1, \quad \sum_q w_q \mathbf{c}_q = \mathbf{0}, \quad \text{and} \quad \sum_q w_q \mathbf{c}_q \otimes \mathbf{c}_q = c_s^2 \mathcal{I}_n, \quad (4.2.7)$$

Then we consider a discrete velocity distribution function $f_q(\mathbf{r}, t)$ which approximates the continuous distribution by using Hermite series expansions (see [99] for more details). This discrete velocity distribution function $f_q(\mathbf{r}, t)$ satisfies the Boltzmann equation in discretized velocity space

$$\frac{\partial f_q}{\partial t} + \mathbf{c}_q \cdot \nabla f_q = \Omega_q \quad (4.2.8)$$

From the discrete velocity function and with the consistency relations 4.2.7, we recover the macroscopic moments

$$\begin{aligned} \rho(\mathbf{r}, t) &= \sum_q f_q(\mathbf{r}, t), & \rho \mathbf{u}(\mathbf{r}, t) &= \sum_q \mathbf{c}_q f_q(\mathbf{r}, t), \\ \text{and } \rho E(\mathbf{r}, t) &= \sum_q |\mathbf{c}_q|^2 f_q(\mathbf{r}, t). \end{aligned} \quad (4.2.9)$$

As space and velocity are discretized such that nodes are connected by the velocity vectors \mathbf{c}_q up to a certain time increment Δt , the equation 4.2.3 can be integrated along the characteristics which yields the lattice Boltzmann equation

$$f_q(\mathbf{r} + \mathbf{c}_q \Delta t, t + \Delta t) - f_q(\mathbf{r}, t) = \int_0^{\Delta t} \Omega_q(\mathbf{r} + s \mathbf{c}_q, t + s) ds \quad (4.2.10)$$

where the integral term for the collision operator have to be approximated. When approximated explicitly and at first order $\int_0^{\Delta t} \Omega_q(\mathbf{r} + s \mathbf{c}_q, t + s) ds \approx \Delta t \Omega_q(\mathbf{r}, t)$ we recover the Lattice Boltzmann equation. It is possible to use the Crank-Nicolson method [159] for the integration of this collision operator, to obtain a second order in space and time method. This second order method can be reformulated as the first order Lattice Boltzmann method thanks to a clever change variable [42].

4.2.4 Macroscopic flow behavior

It is possible to prove that the Boltzmann equation with the BGK collision operator 4.2.5 describes the macroscopic behaviour of a fluid when certain conditions are satisfied. For example, it is possible to recover the Navier Stokes equations. Introducing the Knudsen number $Kn = l/L$ with l the particle mean free path and L the macroscopic length scale, we consider a Chapman-Enskog expansion [32] of the particle distribution from the Maxwell-Boltzmann distribution

$$f = f^{\text{eq}} + \epsilon f^{(1)} + \epsilon^2 f^{(2)} + \dots \quad (4.2.11)$$

where $\epsilon = O(Kn)$. By inserting this development in the Boltzmann equation, computing the moments (mass, momentum and energy) and identifying the term with respect to their order in ϵ , we find

$$p = \rho c_s^2 \quad \text{and} \quad \eta = \rho c_s^2 \left(\tau - \frac{\Delta t}{2} \right), \quad (4.2.12)$$

where $c_s = \sqrt{\frac{1}{3} \frac{\Delta x}{\Delta t}}$ is defined as the isothermal sound of speed of the Lattice.

4.2.5 Numerical resolution

The numerical resolution of LBE is made with two sequential steps:

1. the **collision step** consist in resolving

$$\tilde{f}_q(\mathbf{r}, t) = f_q(\mathbf{r}, t) + \Delta t \Omega_q(\mathbf{r}, t) \quad (4.2.13)$$

where $\tilde{f}_q(\mathbf{r}, t)$ is the particle distribution after collision. This step requires computation of the moments and the equilibrium distribution;

2. the **propagation step** is devoted to the integration of the transport operator along the characteristics

$$f_q(\mathbf{r} + \mathbf{c}_q \Delta t, t + \Delta t) = \tilde{f}_q(\mathbf{r}, t) \quad (4.2.14)$$

After this step, one obtain the update discrete particle distribution (*i.e.* f_q at time $t + \Delta t$).

Decomposing the numerical resolution of the LBE in two steps is a crucial feature of the LBM. The first step is said local and non-linear: the computation of $\tilde{f}_q(\mathbf{r}, t)$ do not require values from neighbouring nodes, despite it is non-linear because moments are required to evaluate the equilibrium distribution. The second step is said linear and non-local: discrete particle distribution are exchanged between the neighbouring nodes relatively to their discrete velocity. This makes the LBM a very appropriate and powerful tool for high-performance computing and very large data simulations. This property of the LBM is usually summarized as “non-linearity is local, non-locality is linear” [57].

Regarding the equilibrium distribution, the Maxwell-Boltzmann distribution 4.2.2 involve an exponential function that is time consuming. In order to increase the computer efficiency, it is generally admitted that computing the first three terms of the Hermite series expansion is sufficient in our macroscopic framework [99]. So, in the numerical implementation, we consider (under isothermal assumption)

$$f_q^{\text{eq}} = w_q \rho \left(1 + \frac{\mathbf{u} \cdot \mathbf{c}_q}{c_S^2} + \frac{(\mathbf{u} \cdot \mathbf{c}_q)^2}{2c_S^4} - \frac{|\mathbf{u}|^2}{2c_S^2} \right). \quad (4.2.15)$$

To finish with, with the consistency relations 4.2.7, we recover the moments

$$\begin{aligned} \rho &= \sum_q f_q^{\text{eq}} = \sum_q f_q, & \rho \mathbf{u} &= \sum_q f_q^{\text{eq}} \mathbf{c}_q = \sum_q f_q \mathbf{c}_q, \\ \text{and } \rho E &= \sum_q f_q^{\text{eq}} |\mathbf{c}_q|^2 = \sum_q f_q |\mathbf{c}_q|^2. \end{aligned} \quad (4.2.16)$$

About boundary condition, they can be solved numerically following different strategies. In our work, it will be necessary to model a wall boundary condition. We choose the half way bounce back algorithm [101] as it preserve mass conservation and is formally second order accurate.

4.2.6 Selecting a collision operator

The main differences between all the variety of LBM methods come mainly from the collision operator Ω_q (and the boundary condition) implementation strategies. Here, we propose a brief review of the classical operators and justify the operator chosen in our work. The goal here is not to perform a complete review of all the existing collision operators but to list the most used to justify our choice.

The first example of collision operator is the discrete version of the BGK operator [19] (see Eq. 4.2.5) which writes

$$\Omega_q = \frac{1}{\tau} (f_q^{\text{eq}} - f_q). \quad (4.2.17)$$

For this collision operator, all the discrete particle distribution relaxes to their equilibrium with the same relaxation time τ . The BGK collision operator was the first used in numerical simulations, in particular to solve the Navier-Stokes equations. Nevertheless, it has been shown that this operator lack of stability and accuracy [63, 100, 147].

To increase the stability and accuracy of the LBM, collision operators with more relaxation times were considered. Among the classical methods with more than one relaxation time, we propose to cite the two relaxation time (TRT) method [63, 65], the multiple relaxation time (MRT) method [48] operators, the cascaded method [3, 61] and the cumulant methods [3]. With these operators, it is not possible to determine all the relaxation times from the identification with the macroscopic equation with a Chapman-Enskog's like expansion. In fact, there is no doubt that these unconstrained relaxation times add potential stability to these methods. Despite, when the number of relaxation times is superior to two strictly, it is generally a difficult task to properly set these parameters and elaborate clear relations on the stability improvement [43, 47, 102]. In addition, the relaxation is not directly based on the particle distributions, but on some "moments" obtained by a linear or non-linear transformation of the f_q which generates inevitably additional computational cost. The latter is generally reduced by resorting to smart formulation and implementation of the methods.

Focusing on the ADE, we refer to [85] for a complete review. In comparison with the Navier-Stokes equation, fewer collision operators have been used. The BGK operator has been used in [54, 170] but stability and accuracy are limited [146, 147]. Chopard et al. [7] proposed an elegant improvement of the BGK, introducing a fictional volume force to reduce errors. The TRT collision operator [63, 66] has two relaxation time, the first enables to correctly capture the advection and diffusion physics accurately, the second enables to reduce instabilities and residual errors. The MRT [31, 176] and central moments [174] collision operators have also been experimented. The authors [174] admits that only the first relaxation parameter is determined with physical constraints, the other coefficients are "arbitrarily" set to 1. They recommend users of this collision operators to experiment other values than 1 to increase the accuracy or reduces numerical instabilities specifically for their application. As the goal of this thesis was not to evaluate collision operators, we choose to focus on the TRT operators described bellow. For similar reason and to reduce the implementation effort, the TRT operator will be used to solve the Darcy-Brinkman equation also.

4.2.7 TRT collision operator

In our work, we use the LBM-TRT (Two-Relaxation-Time) scheme [63]. The TRT collision operator is designed with two relaxation rates, λ^+ and λ^- . They govern respectively the relaxation of the symmetric and the anti-symmetric parts of the discrete distribution toward their equilibrium.

For convenience, let assume the vectors are order from $q = 0$ to $m - 1$ such that $\mathbf{c}_0 = \mathbf{0}$. Then, for each velocity index $q \in \{1, \dots, m - 1\}$, let note \bar{q} the associated index such that $\mathbf{c}_q = -\mathbf{c}_{\bar{q}}$. We can now define respectively the symmetric part f^+ and the unsymmetrical part f^- of the discrete distribution function as

$$f_q^+ = \frac{1}{2}(f_q + f_{\bar{q}}), \quad f_q^- = \frac{1}{2}(f_q - f_{\bar{q}}) \quad \text{for } q \geq 1 \quad \text{and} \quad f_0^+ = f_0, \quad f_0^- = 0. \quad (4.2.18)$$

In the same manner, we introduce the symmetric part $(f^{\text{eq}})^+$ and the unsymmetrical part $(f^{\text{eq}})^-$ of the discrete equilibrium distribution function f_q^{eq} .

For the TRT model, the collision step 4.2.13 writes as

$$\begin{aligned} \tilde{f}_q(\mathbf{r}, t) &= f_q(\mathbf{r}, t) - \Delta t \lambda^+ \left(f_q^+ - (f_q^{\text{eq}})^+ \right) - \Delta t \lambda^- \left(f_q^- - (f_q^{\text{eq}})^- \right) \quad \text{for } q \geq 1, \\ \text{and } \tilde{f}_0(\mathbf{r}, t) &= (1 - \Delta t \lambda^+) f_0(\mathbf{r}, t) + \Delta t \lambda^- f_0^{\text{eq}}. \end{aligned} \quad (4.2.19)$$

Let recall that \tilde{f}_q design the discrete particle distribution after the collision step.

For the TRT collision operator, we usually introduce the magic number Λ to tune the method accuracy and stability. The magic number is given by

$$\Lambda = \Lambda^+ \Lambda^- \quad \text{with} \quad \Lambda^+ = \left(\frac{1}{\Delta t \lambda^+} - \frac{1}{2} \right) \quad \text{and} \quad \Lambda^- = \left(\frac{1}{\Delta t \lambda^-} - \frac{1}{2} \right) \quad (4.2.20)$$

The parameters Λ^+ and Λ^- have to be positive [63] such that λ^+ and λ^- must satisfy

$$0 < \Delta t \lambda^\pm < 2. \quad (4.2.21)$$

With the TRT collision operator, the LBM can reproduce multiple flow physics. To do so, the numerical parameters Λ^+ and Λ^- (or λ^+ and λ^-) and the equilibrium distribution f^{eq} must be adapted to recover the desired physics. Once again, this adaptation are made by using Chapmann-Enskog expansion. In the next section 4.3, we explain how the TRT-LBM can reproduce Darcy Brinkam equation and ADE.

4.2.8 Lattice units

To improve the LBM efficiency, the simulation is usually performed in Lattice units. In fact, the physical systems are not resolve directly by the LBM, they are first converted in a non-dimensional problem where $\Delta t = 1$ and $\Delta x = 1$, which simplifies the relations 4.2.13, 4.2.14 4.2.19, 4.2.20 and 4.2.21. Denoting z a quantity in the physical units and z^* the same quantity in the lattice units, one can obtained the useful following conversion relations

$$t^* = \frac{t}{\Delta t}, \quad x^* = \frac{x}{\Delta x}, \quad \mathbf{u}^* = \frac{\Delta x}{\Delta t} \mathbf{u}, \quad \mu^* = \frac{\Delta t}{\Delta x^2} \mu, \quad D^* = \frac{\Delta t}{\Delta x^2} D. \quad (4.2.22)$$

Of course, the discrete set of vector \mathbf{c}_q have to be reshape accordingly to the Lattice unit system. Bellow, we detail the D2Q9 velocity set in Lattice units.

4.2.9 D2Q9 Velocity set

The numerical study of this work aims at reproducing 3D micromodels. As the micromodels width is small, we will focus on 2D numerical methods, the width effects being reproduced by using an appropriate physical model (see subsection 4.3.1). We will use the D2Q9 velocity set given by

$$\begin{aligned} \mathbf{c}_0 &= \mathbf{0}, \\ \mathbf{c}_1 &= \begin{pmatrix} 1 \\ 0 \end{pmatrix}, \quad \mathbf{c}_2 = \begin{pmatrix} 0 \\ 1 \end{pmatrix}, \quad \mathbf{c}_3 = \begin{pmatrix} -1 \\ 0 \end{pmatrix}, \quad \mathbf{c}_4 = \begin{pmatrix} 0 \\ -1 \end{pmatrix}, \\ \mathbf{c}_5 &= \begin{pmatrix} 1 \\ 1 \end{pmatrix}, \quad \mathbf{c}_6 = \begin{pmatrix} -1 \\ 1 \end{pmatrix}, \quad \mathbf{c}_7 = \begin{pmatrix} -1 \\ -1 \end{pmatrix}, \quad \mathbf{c}_8 = \begin{pmatrix} 1 \\ -1 \end{pmatrix}. \end{aligned} \quad (4.2.23)$$

For usual applications (Navier-Stokes equations for example), the weight are set to

$$w_0 = \frac{4}{9}, \quad w_q = \frac{1}{9} \quad \text{for } 1 \leq q \leq 4, \quad \text{and} \quad w_q = \frac{1}{36} \quad \text{for } 5 \leq q \leq 8. \quad (4.2.24)$$

4.3 Lattice-Boltzmann method for porous media

We aim to apply LBM method to compute flow and transport in porous media. We want to retrieve the velocity field at the equilibrium state solving flow equations with LBM, and then simulate a tracer injection solving the Advection-Diffusion equation in the computed flow. More precisely, we want to compute 2D flow field and concentration fields in experimental images of the micromodel, after segmentation between different phases. The micromodel has a depth L_z so we use a depth-average model to compute simulation in 2D. In our two-fluid-phase system, air clusters are immobile so in the following we consider flow and transport in the water phase only. In the following, we detail the flow and transport equations considered in order to obtain the velocity and concentration field specific to each saturation. We also describe the boundary conditions and the choice of parameters.

4.3.1 Flow simulations

Darcy-Brinkman equation

The Darcy-Brinkman equation [25] is used to compute the depth-average velocity. This allows to describe a 3D velocity field with a 2D equation as demonstrated by [178]. The velocity field \mathbf{u} in the fluid phase is thus governed by the Darcy-Brinkman equation [25]

$$-\rho\nu_{\text{eff}}\Delta\mathbf{u} + \frac{\rho\nu}{K}\mathbf{u} = \mathbf{g} - \nabla P \quad (4.3.1)$$

where ρ is the density of the fluid, ν represents the kinematic viscosity and P is the pressure, \mathbf{g} the gravity and ν_{eff} an effective viscosity accounting here for the length average. The permeability K is computed from the depth with the relation $K = L_z^2/12$. Physically, the Laplacian term models the transverse diffusion of momentum. It allows to describe the boundary layer induced by the no-slip wall boundary conditions. According to [178], ν_{eff} should be slightly different from ν . However, in our case, the permeability is low enough so that the boundary layer is small and thus its impact on the dispersion is limited [87, 143]. Thus, the gap between ν_{eff} and ν being small, it can be neglected in our study. For this reason, we set the effective viscosity as $\nu_{\text{eff}} = \nu$.

To solve the Darcy-Brinkman equation 4.3.1 with the LBM, we apply the strategy of Guo and Zhao [74] or also Ginzburg and Talon [64]. The Darcy-Brinkman equation is reformulated as a Stokes equation with a source terms that corresponds to the drag force due to the porous medium and the gravity

$$\nabla P = \rho\nu_{\text{eff}}\Delta\mathbf{u} + \mathbf{F}, \quad (4.3.2)$$

where the source term is given by

$$\mathbf{F} = -\frac{\rho\nu}{K}\mathbf{u} + \mathbf{g}. \quad (4.3.3)$$

The TRT method adaptation is presented in the next paragraph.

TRT collision operator for Darcy-Brinkman

The Two-Relaxation-Time Lattice (TRT) was used to compute the flow field at steady state. For this, we aim to solve solved Eq. 4.3.2 and 4.3.3 in the water phase to obtain the velocity field. To do so, the TRT collision operators described 4.2.7 has to be adapted. The propagation step 4.2.14 is left unchanged. Whereas the fluid density is still defined

from the particle distribution function as usual $\rho = \sum f_q$, the velocity is no more defined directly from the second moment $\mathbf{J} = \sum f_q \mathbf{c}_q$. In fact the collision step has to take into account of the external force (here the gravity and Darcy Brinkman drag force). For this we use the force model of Guo *et al.* [75]. First the velocity \mathbf{u} has to be shifted by the external force such that

$$\mathbf{u} = \frac{1}{\rho} \mathbf{J} + \frac{1}{2} \mathbf{F}. \quad (4.3.4)$$

Unfortunately, in our particular case, the former relation is not explicit in \mathbf{u} because the force \mathbf{F} given Eq. 4.3.3 includes the drag force which is linear relatively to \mathbf{u} . After [64,74], the velocity can be defined explicitly by defining a fictitious velocity

$$\mathbf{v} = \frac{1}{\rho} \mathbf{J} + \frac{1}{2} \mathbf{g} \quad (4.3.5)$$

which is used to deduced the fluid velocity

$$\mathbf{u} = \frac{1}{1 + 2\nu/K} \mathbf{v}. \quad (4.3.6)$$

Then the collision step must also be adapted to take account of the force. The relation 4.2.19 thus becomes

$$\tilde{f}_q(\mathbf{r}, t) = f_q(\mathbf{r}, t) - \lambda^+ \left(f_q^+ - (f_q^{\text{eq}})^+ \right) - \lambda^- \left(f_q^- - (f_q^{\text{eq}})^- \right) + S_q, \quad (4.3.7)$$

where the external force contribution S_q is adapted from [74]

$$S_q = \rho w_q \left(\mathbf{c}_q \cdot \mathbf{F} + \frac{\mathbf{u} \mathbf{F} : (\mathbf{c}_q \mathbf{c}_q - c_s^2 \mathcal{I}_n)}{c_s^2} \right). \quad (4.3.8)$$

The equilibrium distribution relation 4.2.15 is also formally the same but the velocity given by 4.3.6.

The scheme requires to calculate the two relaxation parameters λ^+ and λ^- . However, for numerical reasons (precision, stability), we fix the numerical parameter $\Lambda = \Lambda_+ \Lambda_-$ and the viscosity ν . Λ rules the numerical error of the scheme (see [64,65]), here we use $\Lambda = 0.1875$. λ^+ and λ^- are then deduced from

$$\lambda^+ = \frac{2}{6\nu + 1} \quad \text{and} \quad \lambda^- = \frac{2}{\frac{2\Lambda}{3\nu} + 1}. \quad (4.3.9)$$

Boundary conditions

We suppose that the gas phase is not modified by the actual flow and that there is no flow in the gas phase. No-slip boundary conditions are applied at the water-solid but also at the water-air interface. The latter assumption is thus equivalent to consider the gas phase as solid.

We apply the so-called bounce back rule corresponding to a no-slip condition at the solid/fluid interface given by:

$$f_{\bar{q}}(\mathbf{r}, t + \Delta t) = \tilde{f}_q(\mathbf{r}, t). \quad (4.3.10)$$

The fluid is driven by applying an inlet and outlet imposed pressure.

Simulation parameters

In order to obtain the velocity field by solving the Darcy-Brinkman equation, for images with the same length L_x than the micromodel, unless otherwise specified, we adopt the following parameters:

Convergence criteria	K	ΔP	ν	Λ
$2 \cdot 10^{-9}$	7.9	0.3	0.11	0.1875

As we apply pressure boundary conditions, the mean velocities depend on the saturation. Consequently, the velocity fields will be rescaled to preserve the Pechlet number in the ADE simulation.

4.3.2 Transport simulation

Advection-Diffusion-Equation

Transport of a passive tracer is governed by the advection-diffusion

$$\frac{\partial c}{\partial t} + \mathbf{u} \cdot \nabla c - D_m \Delta c = 0, \quad (4.3.11)$$

where c is the solute concentration in the fluid, \mathbf{u} the local velocity vector obtained from the resolution of the Darcy-Brinkman equation given by Eq. 4.3.1 in subsection 4.3.1 and D_m the molecular self-diffusion coefficient.

Lattice Boltzmann simulations

Here we detail the adaptation of the TRT LBM needed to simulated the ADE equation 4.3.11. For clarity, the discrete distribution functions for ADE are denoted g_q in the subsection to avoid confusion with the Darcy-Brinkman resolution.

In the case of the ADE, only the first moment has to be considered, and it gives the tracer concentration

$$c(\mathbf{r}, t) = \sum_q g_q(\mathbf{r}, t). \quad (4.3.12)$$

Then the equilibrium function involved in the collision operator has to be modified accordingly to [10, 63]

$$\left\{ \begin{array}{l} (f_q^{\text{eq}})^+(\mathbf{r}, t) = c(\mathbf{r}, t) E_q^+, \\ (f_q^{\text{eq}})^-(\mathbf{r}, t) = c(\mathbf{r}, t) E_q^-, \\ (f_0^{\text{eq}})^+(\mathbf{r}, t) = c(\mathbf{r}, t) E_0, \\ (f_0^{\text{eq}})^-(\mathbf{r}, t) = 0, \end{array} \right. \quad (4.3.13)$$

where

$$\left\{ \begin{array}{l} E_q^+ = w_q D_{LB} + \frac{w_q}{2} [3(\mathbf{u} \cdot \mathbf{c}_q)^2 - |\mathbf{u}|^2], \\ E_q^- = w_q (\mathbf{u} \cdot \mathbf{c}_q), \\ E_0 = 1 - \sum_{q=1}^{m-1} E_q^+(\mathbf{r}, t). \end{array} \right. \quad (4.3.14)$$

where the weight are given by

$$w_q = \frac{1}{3} \quad \text{for } 1 \leq q \leq 4, \quad \text{and} \quad w_q = \frac{1}{12} \quad \text{for } 5 \leq q \leq 8. \quad (4.3.15)$$

with w_0 unused. Beware this set of weight do not fulfill the consistency relation 4.2.7 anymore. In fact, only the first moment is used to compute the tracer concentration. \mathbf{u} is the advection velocity given from the Darcy Brinkman simulation with Eq. 4.3.1. The diffusion coefficient D_{LB} is deduced from the molecular diffusion coefficient.

$$D_{LB} = \frac{D_m}{\Lambda^-}. \quad (4.3.16)$$

Regarding the numerical parameters, we set

$$\Lambda^+ = 4 \quad \text{and} \quad \Lambda^- = \frac{1}{16}. \quad (4.3.17)$$

which gives the Mach number $\Lambda = 1/4$.

Boundary conditions

No-slip boundary conditions at the solid/fluid interfaces were applied by using the bounce-back condition

$$g_{\bar{q}}(\mathbf{r}, t + \Delta t) = \tilde{g}_q(\mathbf{r}, t). \quad (4.3.18)$$

We consider continuous tracer injection starting as a specific time $t = 0$, where molecules are injected from the top of the images. Tracers are thus injected continuously at the inlet slice (x_0, y) . In practice, this is done as follows

$$\forall \mathbf{r}_0 = (x_0, y) \quad \text{and} \quad \forall t \in (0, t_{\max}) \quad \begin{cases} g_0(\mathbf{r}_0, t) = c_0, \\ g_q(\mathbf{r}_0, t) = 0 \quad \text{for } q \geq 1, \end{cases} \quad (4.3.19)$$

with c_0 the concentration of the tracer injected at position \mathbf{r}_0 .

Simulation parameters

Let remark first, the velocity fields obtained from the Darcy-Brinkman simulation are not equal because we impose pressure boundary conditions and different water saturation. Consequently, so set the Pe number in the transport simulations, we rescale the velocity field with a prefactor $C_{\|\mathbf{u}\|}$. The other parameters are set such as follow

D_m	D_{LB}	Λ^+	Λ^-	Λ
$3.125 \cdot 10^{-4}, 6.25 \cdot 10^{-2}$	$5 \cdot 10^{-3}, 1$	4	0.0625	0.25

4.4 Illustration of LBM simulation

Fig. 4.2 shows an image of the micromodel containing the three phases (water, air, solid), the porous structure on which simulations are performed (supposing that the gas behaves as the solid), the velocity field in the fluid phase and the concentration field.

4.5 Conclusion

To complement the experimental methods, we incorporate Lattice-Boltzmann simulations using two-dimensional images of unsaturated porous media with trapped phases. These simulations enable the computation of the velocity field at equilibrium and facilitate the simulation of tracer injection in complex media. The Lattice-Boltzmann Method

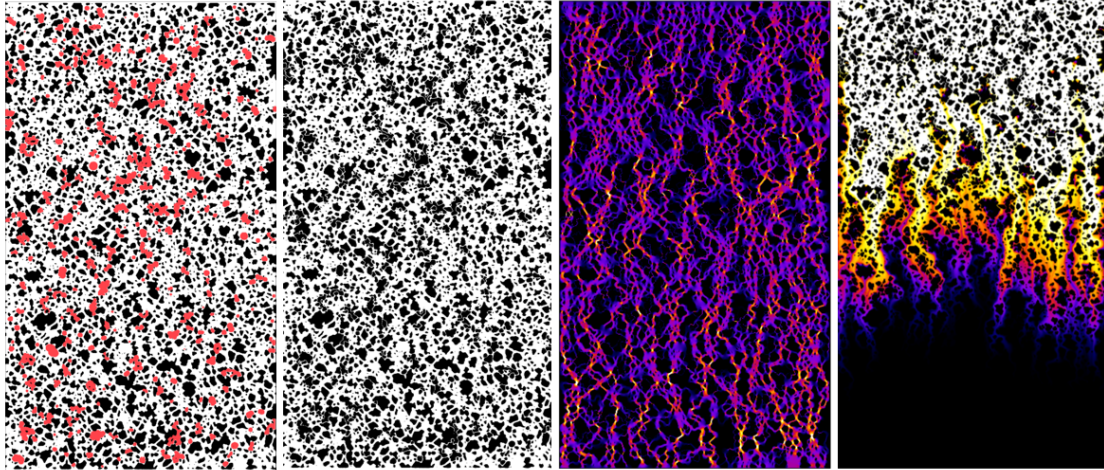


Figure 4.2 – (Left) Three phase segmented image (red: air, black: solid, white: water). [Middle left] Binary image with air clusters as solid (black) used for the velocity field simulation. [Middle right] Velocity magnitude. (Right) Concentration field for continuous injection from the top.

(LBM) is employed, which simulates fluid density on a lattice through streaming and collision processes, instead of directly solving the flow equations. For flow simulations, we utilized the LBM-TRT scheme for the Darcy-Brinkman equation within the two-dimensional images of the unsaturated micromodel. We applied the same boundary conditions for the gas phase as for the solid phase. Subsequently, for transport simulations, we solved the Advection-Diffusion Equation (ADE). The assumptions, boundary conditions, and parameter choices for these simulations are meticulously described in this chapter.

Chapter 5

Experimental results on dispersion in unsaturated porous media

5.1 Introduction

Throughout this thesis, extensive efforts were made to develop experimental methods and conduct data analysis to acquire essential experimental data, as described in Chapter 3. The micromodel setup was meticulously optimized to facilitate two-fluid flow experiments, followed by tracer transport experiments within the resulting unsaturated micromodel. This comprehensive experimental setup enabled the collection of valuable data concerning the dynamics of multiphase flow within the micromodel, as well as the transport behavior in an unsaturated micromodel featuring static air clusters. In this section, we present the preliminary findings obtained through these experiments, focusing specifically on dispersion phenomena in unsaturated porous media. Initially, we examine the outcomes of the interaction between air-water fluids and the micromodel, studying the resulting phase distributions achieved through co-injection experiments. Furthermore, we compare our results with existing literature to validate and reinforce the significance of our findings. Subsequently, for each phase distribution resulting from the two-fluid phase injection, a series of transport experiments are performed. These experiments provide initial insights into the influence of saturation on dispersion in porous media, particularly concerning the evolution of dispersivity with varying levels of saturation. However, as anticipated, the investigation of dispersion in low water cases saturation necessitates complementary methods, such as simulations. Due to the limitations imposed by the micromodel size, it becomes challenging to study dispersion over sufficiently long durations to obtain satisfactory results, particularly in assessing the Fickian or non-Fickian nature of dispersion. Nonetheless, important tendencies have been identified, guiding the subsequent stages of research.

Consequently, our objective is to complement the experimental data with Lattice Boltzmann simulations that replicate the experimental conditions within the micromodel. However, several strong hypotheses are needed to perform the LBM simulations, such as how we consider the micromodel depth and the nature of the interfaces between the water and the air phase. Therefore, we provide an experimental validation of the Lattice Boltzmann methodology, described in the previous chapter.

The following chapter is structured as follows: the first part presents the results regarding non-miscible multiphase flow in the micromodel, followed by the presentation of preliminary results on dispersion in the second part. Finally, we propose an experimental validation of Lattice-Boltzmann simulations in the micromodel to consolidate the findings

of our study.

5.2 Multiphase flow in porous media

Before we could address the subject of dispersion in unsaturated porous media, it was necessary to understand the interaction between the micromodel and the non-miscible multiphase flow, more specifically what kind of phase distribution we would obtain after a non-miscible multiphase flow.

5.2.1 Co-injection experiments

We conducted air water co-injection experiments for a large range of flow rates (according to the method described in the Chapter 3, section 3.1.2). At the end of the co-injection, we stopped the experiment to get the trapped phase distributions. An example of phases distribution after image processing is given Fig. 5.1. We can see a disconnected phase in blue (air bubble) in the percolating wetting phase (water). The distribution seems rather homogeneous.

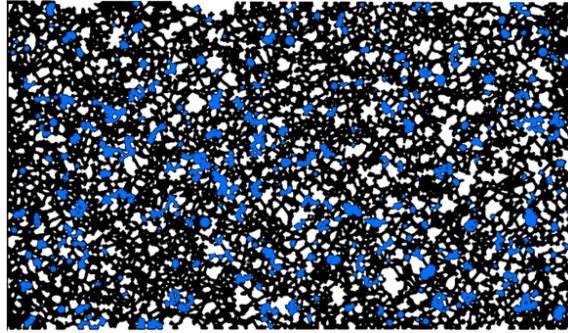


Figure 5.1 – Example of distribution after a co-injection experiment, $Q_{water} = 0.25\text{mL}/\text{min}$, $Q_{air} = 1\text{mL}/\text{min}$. Black: water, white: solid, blue: air.

By adjusting the flow rates Q_{water} and Q_{air} , it is possible to change the final saturation in the medium (computed according to the method described in the Chapter 3, 3.2.1). The values of flow rates, Ca numbers and saturation for the different experiments are given in table 5.1.

The Ca number defined for the water flow is computed as follow:

$$Ca = \frac{\mu Q_{water}}{\phi S \gamma},$$

with

$$\begin{cases} \mu = 1.005 \cdot 10^{-3} \text{ Pa.s at } 20^\circ\text{C}, \\ \phi = 0.70 \text{ (computed from the binarized mask)}, \\ \gamma = 72.8 \cdot 10^{-3} \text{ N/m at } 20^\circ\text{C}. \end{cases}$$

5.2.2 Macroscopic scale: evolution of the saturation with the flow rate

The saturation range we could obtain was from $S_w = 0.55$ at the lowest to the full saturation $S_w = 1$. In other word, there is a maximal threshold of $S_g \simeq 0.45$ for the air saturation, which corresponds to the residual gas saturation S_{gr} . When the air saturation

Table 5.1 – Table of the chosen flow rates Q_{water} and Q_{air} for each experiment, the corresponding Ca number and the resulting saturation S_w .

Q_{water} (mL/min)	Q_{air} (mL/min)	$Ca \times 10^{-4}$	S_w
0.025	0.025	0.23	0.55
0.025	0.025	0.23	0.58
0.03	0.03	0.27	0.59
0.03	0.03	0.27	0.59
0.03	0.03	0.27	0.59
0.05	0.05	0.46	0.62
0.05	0.05	0.46	0.60
0.05	0.05	0.46	0.61
0.07	0.07	0.64	0.69
0.07	0.07	0.64	0.66
0.07	0.07	0.64	0.68
0.10	0.10	0.91	0.68
0.15	0.15	1.37	0.74
0.15	0.15	1.37	0.76
0.15	0.15	1.37	0.73
0.25	1.00	2.28	0.78
0.25	1.00	2.28	0.81
0.70	5.00	6.37	0.90
0.70	5.00	6.37	0.84
0.70	5.00	6.37	0.87
1.70	6.00	15.47	0.95
1.70	6.00	15.47	0.95

exceeds this threshold, the water comes back spontaneously in the medium by capillarity. We cannot maintain an air saturation above S_{gr} while having water percolation. Fig. 5.2 illustrates the range of saturation we obtain from the co-injection experiment.

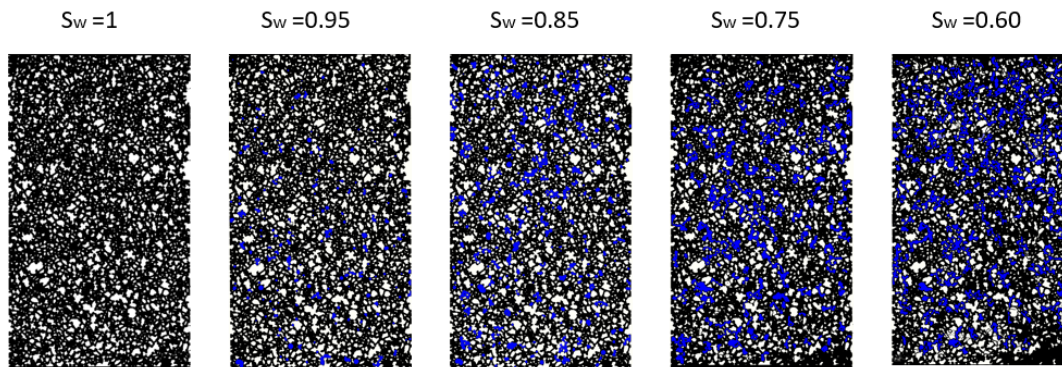


Figure 5.2 – Different saturation obtained with co-injection. Black: water; white: solid; Blue: air.

Fig. 5.3 shows the evolution of the saturation with the capillary number, for the range of saturation reachable with co-injection. The saturation values are rather repeatable between the different co-injection experiments. The water saturation increases with the

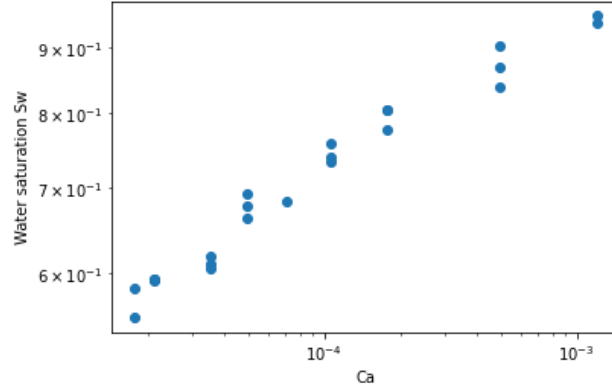


Figure 5.3 – Water saturation evolution with the Ca used during the co-injection

Ca number as a higher flow rate chases the air more efficiently. Data can be fitted with a power law with $S_w \in [0.55, 1]$. Thus, for our experimental conditions, we could derive an empirical law for the saturation as a function of the Ca number

$$S_w - S_{w0} = a Ca^b,$$

with $(a, b) = (0.12, 0.35)$ and $S_{w0} = 0.55$.

The results are consistent with the analysis of Chevalier *et al.* [35], for which the saturation at the steady state after a non miscible multiphase flow experiment depends essentially on the maximal capillary number (or flow rate) that has been imposed to the system.

5.2.3 Microscopic scale: bubble's distribution

The saturation value is not sufficient to describe the interaction between the porous medium and the multiphase flow at the pore scale, as it only gives a cumulative value of all the bubble area. Therefore, we analysed the bubbles area distribution for the same data set as the saturation analysis. From the distribution, we could extract information such as the mean or maximal bubble size. Then, in the following section we investigate the properties of the phase distribution.

Air bubble distributions

Mean bubble area

As we can see in Fig. 5.4, the mean bubble area decreases with increasing Ca number. Also, the mean bubble size is quite similar for all repetitions of co-injection experiments. Plus, the bubble area is maximum for the lowest Ca numbers, corresponding to the lowest water saturation values. It decreases similarly to a power law when the flow rate increases.

According to the analysis described in the Chapter 3, the pore equivalent radius of our micromodel is given by

$$R_{\text{pore}}^{eq} = 97 \mu\text{m}. \quad (5.2.1)$$

Thus, the mean pore surface is given by

$$s_{\text{pore}}^m = \pi R_{\text{pore}}^{eq 2} = 3.0 \cdot 10^{-2} \text{ mm}^2. \quad (5.2.2)$$

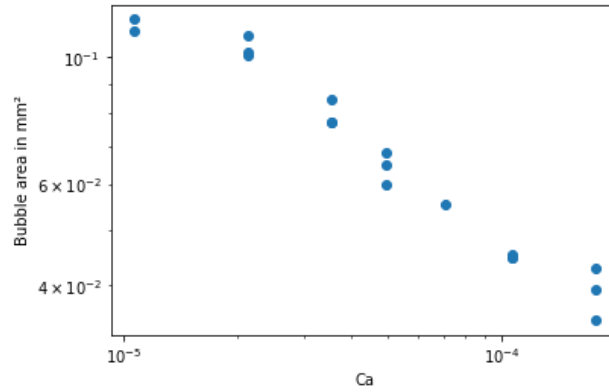


Figure 5.4 – Mean bubble area as a function of the capillary number

Denoting the mean bubble area s_{bubble}^m we see that for highest Ca number s_{bubble}^m is slightly superior to s_{pore}^m , which means that bubbles occupy a bit more than one pore on average. The area occupied by one bubble increases up to 4 pores average area for the lowest Ca numbers.

$$s_{\text{bubble}}^m \simeq 4s_{\text{pore}}^m.$$

Maximal area

The maximal bubble area follows the same trend than the mean area as it can be seen in Fig. 5.5, but the dispersion of the data is higher. This is expected, as the probability for extreme area values is small, so the data is based on low probability events (as it will be shown in the next section with the computation of the probability density function).

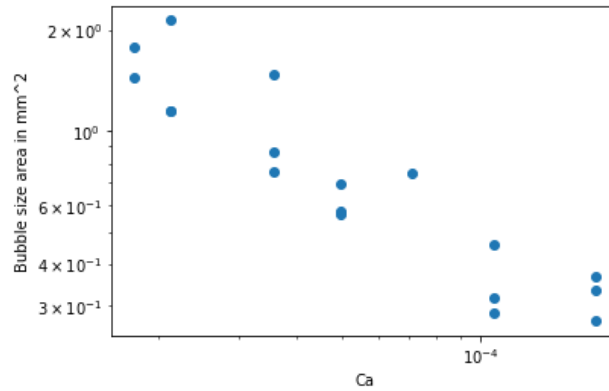


Figure 5.5 – Maximal bubble area as a function of the capillary number Ca

Nonetheless, the tendency is consistent with the relation of proportionality between the maximal bubble size s_{max} and the inverse of the Ca number mentioned by Chevalier [35]

$$s_{\text{max}} \propto \frac{1}{Ca}.$$

Indeed, the bubble size area decreases by approximately a decade for a decade of the capillary number. Therefore, the flow rate sets a maximal size of bubbles in the medium, the bubbles above this threshold are systematically chased away or fragmented.

Bubbles distributions: probability density function

To characterize the phase distribution, we can compute the probability density function (pdf) $p(s)$, with s the bubble area. The probability $p_{[s_a, s_b]}$ for a bubble to have an area in the interval $[s_a, s_b]$ is given by

$$p_{[s_a, s_b]} = \int_{s_a}^{s_b} p(s) ds. \quad (5.2.3)$$

As we are working with a logarithmic distribution, we compute the intervals of the distribution along a logarithmic scale. For $[s_1, s_2, \dots, s_N]$ the limits of the computation intervals, and N the number of intervals, for a logarithmic distribution, we have

$$\begin{cases} \log(s_{k+1}) - \log(s_k) = \alpha, \\ s_1 = s_{\min}, \\ s_N = s_{\max}, \end{cases}$$

with $\alpha = \frac{1}{N-1} \log(s_{\max}/s_{\min})$.

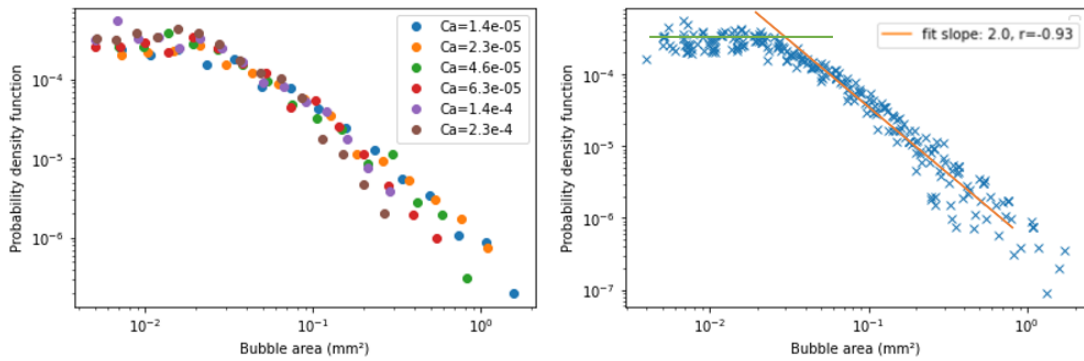


Figure 5.6 – Air bubbles probability density functions $p(s)$. (Left) pdf of the distributions for different values of capillary numbers. (Right) pdf of all the distributions and fit with a power law $p(s) \propto s^{-2}$.

Fig. 5.6 shows the probability density function $p(s)$ for different realisations and capillary numbers. Fig. 5.6 (left) shows a realisation by capillary number and the right sub-figure show all realisation regardless of the Ca . We observe a plateau for small bubble sizes, a power law decrease of the pdf from a threshold size, and a cut-off at large sizes. The slope break between the plateau and the power law slope happens for a bubble area s_{bubble}^m of 0.02 mm^2 , or $0.7 s_{\text{pore}}^m$. Thus, below the mean pore size, the bubble sizes are rather uniformly distributed. Above the pore size, the bubbles are fragmented by the porous network and the size pdf decreases with the bubble area.

The cut-off depends on the flow rate, the higher the flow rate the smaller the cut-off. This only means that the maximal size of the bubble is imposed by the capillary number, which we saw in the previous section. We find a power law decrease with a coefficient of 2.0, as shown in Fig. 5.6 (Right). This is consistent with the results of Tallakstad *et al.* [150] and Chevalier *et al.* [35], as Fig. 5.7 highlights. The distribution can be described by the following scaling

$$p(s) \propto s^2 f(sCa),$$

with $f(sCa)$ being a function cut-off of the capillary number. Indeed Chevalier *et al.* found the following scaling for $p(s)$

$$p(s) \propto s^2 e^{-sCa},$$

choosing $f(sCa) = e^{-sCa}$ as a cut-off function. Tallakstad [150] found a similar relation:

$$p(s) \propto s^\tau e^{-s/s_{\max}},$$

where $\tau = 2.07$; $e^{-s/s_{\max}}$ is another function cut-off, depending of Ca and assuming that $s_{\max} \propto 1/Ca$ as mentioned previously.

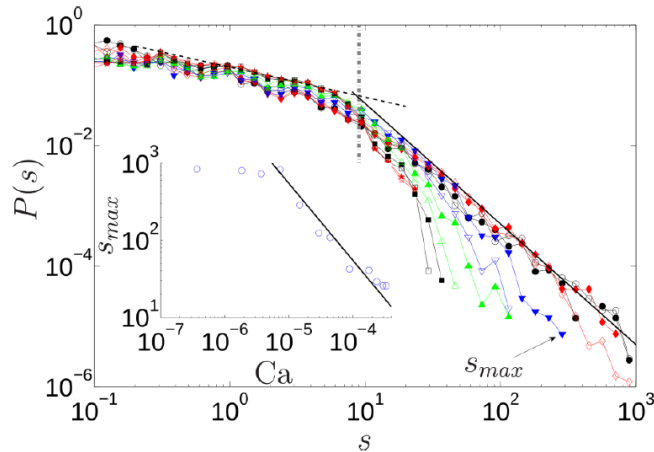


Figure 5.7 – From Chevalier *et al.* [35]. pdf of ganglia distribution resulting from a multiphase flow.

The Ca dependence of the cut-off functions highlights once again the fact that the bubble maximal size in the system is controlled by the flow rate imposed to the medium, when all other parameters about the fluids and the porous medium are fixed. Indeed, the maximal bubble size depends on the porous medium structure. In Oughanem *et al.* [120] they show that the oil ganglia size depends largely on the aspect ratio $\frac{R_{\text{pore}}}{R_{\text{throats}}}$, with R_{pore} the pore radius and R_{throats} the throat radius. In our experiment, the porous network properties such as the pore and throat distributions are fixed by the micromodel (cf Chapter 3). Complementary results about bubble preferential trapping sites can be found in the appendix, chapter 9, section 9.3.

5.2.4 Microscopic scale: structural properties at the pore scale

In this section, we want to analyze how the water saturation changes the medium properties at the pore scale, notably if certain pores are preferentially filled, and what effect the saturation has on the porous network structural properties. First, we consider the local saturation for each pore. The pore network of our micromodel is identified through a watershed operation (ImageJ software). It allows to define the pores and the throat of our medium, as well as their structural properties (size, shape). For our set of data, i.e. images of the micromodel in unsaturated conditions, we compute for each pore of the micromodel the local saturation (i.e. the fraction of the pore filled by water) using an ImageJ algorithm. For each mean saturation S_w , we can compute the local saturations $S_{w,i}$ for all pores i , and make the distinction between fully saturated and partially saturated pores populations (i.e. pores that only contain water VS pores that contain both air and water). The pore network and the local saturations are illustrated Fig. 5.8.

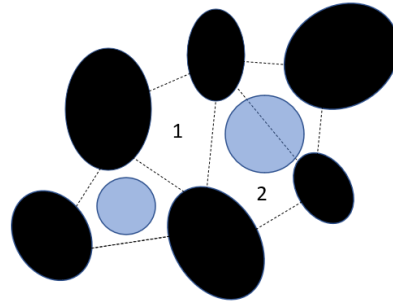


Figure 5.8 – Illustration of the unsaturated pore network. The solid grains are represented in black, the water phase in white and the air clusters in blue. The dashed lines shows the delimitation between the different pores. The pore 1 is fully saturated in water ($S_{w,1} = 1$, whereas the pore 2 is only partially saturated $S_{w,2} < 1$.

Saturated and unsaturated pores

To inquire on how the pores population evolve with saturation, we computed the size distribution of saturated and partially saturated pores for different mean saturation values (see Fig. 5.9).

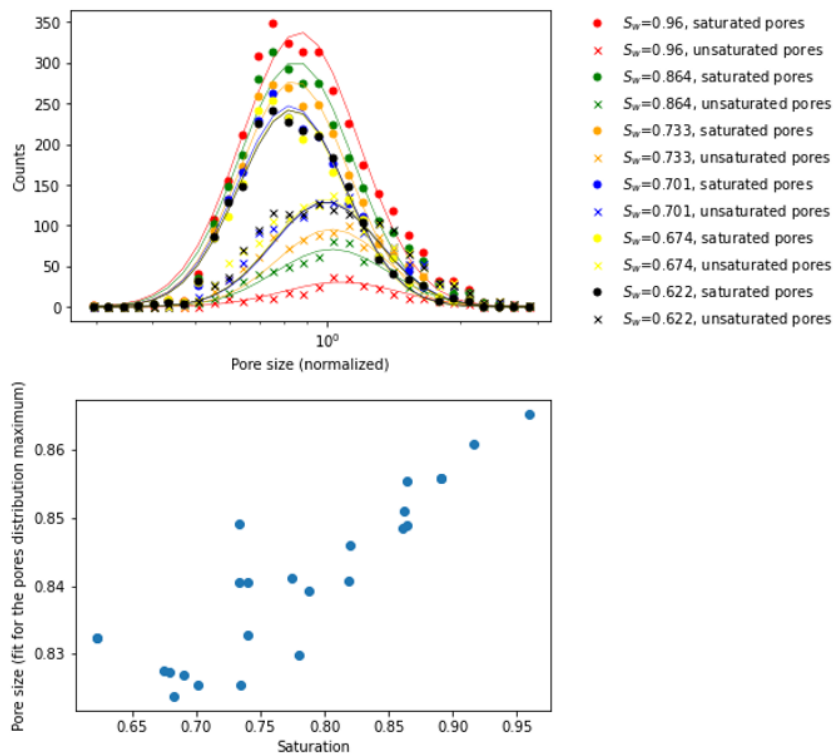


Figure 5.9 – [Top] Size distribution (log) of saturated and partially saturated pores for different mean saturation values. The distributions are fitted with log-normal distribution (in full lines). [Bottom] From the log-normal distribution fitted in the top figure: position of the maximum of the saturated pore size distribution as a function of the mean saturation.

The distributions show a good fit with log-normal distributions, displayed in Fig. 5.9 [Top]. First, the maximum of the peak for the saturated pores happens for smaller pore sizes than the partially saturated pores population. We can see that for the saturated pores, the peak of saturated pores is shifted toward the small pore sizes (and inversely the peak of unsaturated pores is shifted towards the large pore sizes) when the water saturation decreases. Fig. 5.9 [Bottom], showing the peak position of the maximum of the saturated pore distribution, highlights this tendency. In other words, as the saturation decreases, the bubbles fill preferentially large pores.

Local saturation

We computed the local saturation distribution for the unsaturated pores, i.e. the numbers of pores for a given local saturation. We can see Fig. 5.10 that there are two

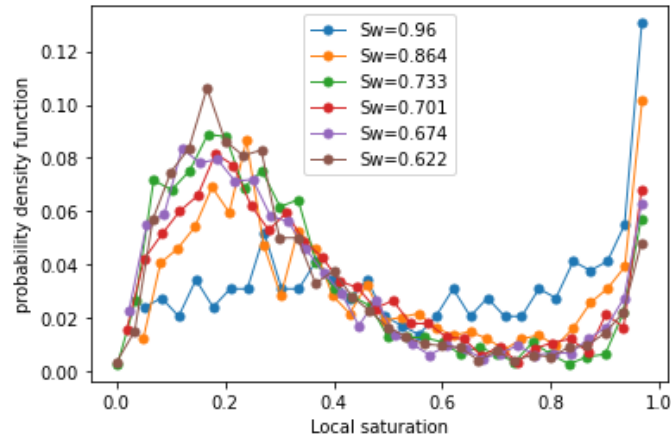


Figure 5.10 – Local water pore saturation distribution for different saturation values

principal water saturation values, a peak of water saturation around 0.2 and a peak near 1: i.e. a pore filled with air at 80% (a bubble fills more or less the whole pore, with water films) and pore almost saturated. The peaks intensity evolves with the global water saturation: when the saturation decreases, the ratio of pores with a local saturation of 0.2 increases. In conclusion, when the water saturation decreases, bubbles tends to fill more pores, they fill preferentially large pores and they fill them almost completely. Except for the water films, they form a global large structure with the solid grains around them.

Further analysis on the structural properties of the unsaturated porous medium can be found in the appendix Chapter 9, section 9.3.2.

5.2.5 Conclusion: insight on multiphase flow interaction in porous media

Our results and observations on multiphase flow in 2D micromodel are consistent with the literature results.

- The water saturation after a multiphase flow depends mainly on the water capillary number Ca imposed, the saturation increases with increasing Ca .
- The final air saturation is necessarily above the residual gas saturation S_{gr} due to capillary contact with the water phase.

- The order of magnitude for the mean bubble size and the pores mean radius is similar. The mean bubble size decreases with the capillary number.
- The maximal bubble size is determined by the Ca number.
- The probability density function for the bubble size follows a power law for sizes above the pore size, and a cut-off at large sizes.
- Locally, a pore is either completely saturated with water, almost fully unsaturated (i.e. filled by a bubble and the water film surrounding the bubble), or slightly unsaturated.
- As saturation decreases, larger bubbles occupy the porous network, and larger pores are unsaturated.

Furthermore, the properties of the unsaturated media and more particularly the properties of the phase distribution affect most likely the dispersion behavior. Thus, knowing how to characterize the interaction between the non-miscible two phase flow and the porous media will be useful in the following to describe dispersion mechanisms.

5.3 Dispersion in unsaturated porous media

5.3.1 Dispersion dependence with saturation

Data set

As we have shown before, we can obtain a range of water saturations from 0.55 to 1 through co-injection experiments. For a given saturation, the water miscible tracer is injected with the flow rate Q_t . In order to conserve the saturation of the porous medium, we need to use injection flow rates inferior to the co-injection flow rate Q_{water} . In practice, the gas phase is not completely stable even with flow rates inferior to the co-injection flow rates for long periods of time, so we use flow rates at least 10 times inferior to the injection flow rate. As high Peclet numbers tend to increase dispersion and that the dispersion is already greatly increased in unsaturated conditions, we work with the lowest flow rates available with the pump, from $0.1\mu\text{L}/\text{min}$ to $5\mu\text{L}/\text{min}$.

We conducted a large sequence of transport experiments for the whole range of saturation. For a given unsaturated porous medium, we usually performed several tracer injections when it was possible. Indeed, the gas phase can be destabilised easily and it is difficult to conserve the exact same configuration for a large series of transport experiments. For each transport experiment, we analyse the phase distribution as well.

Qualitative observations

For the same configuration as in section 5.2, we show in Fig. 5.11 the results of the tracer injection at different times. The first row gives the phase distribution of the medium, and the other columns show the concentration field at four different times. We can see that there is a clear change in the dispersion behavior with the saturation. Indeed, the concentration front (purple in the figure) is rather flat for saturated media or low saturations, but the more the saturation decreases, the more it is deformed, until it becomes difficult to visualise it. When the saturation decreases, the preferential flow paths appear as well as dead ends in the concentration field. The dead ends are particularly remarkable in the last column for low saturation, with orange zones (no tracer) completely surrounded by zones saturated with ink.

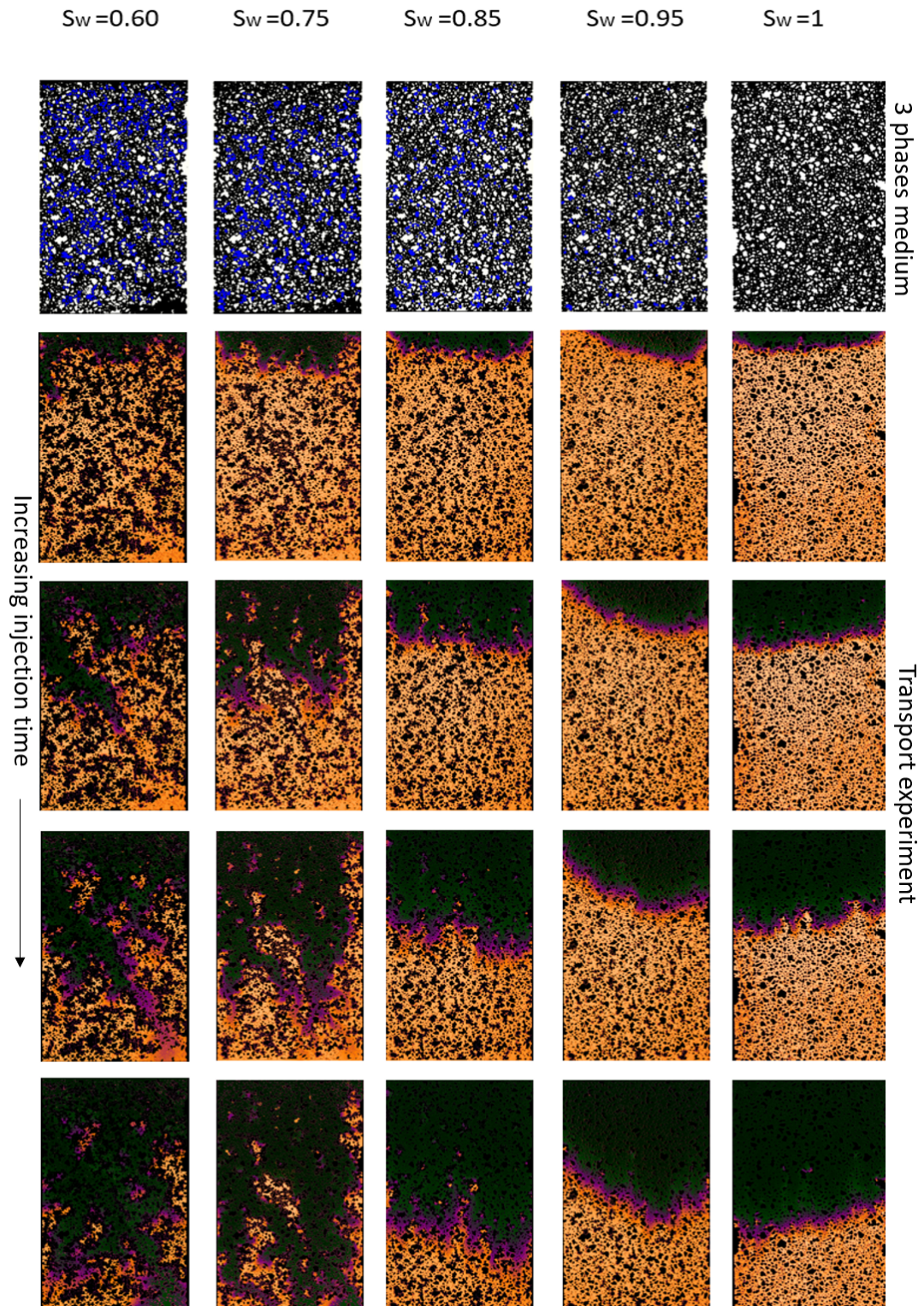


Figure 5.11 – Tracer injection experiments for 5 saturation values. First row: Phase distributions. Other columns: concentration fields. Dark green: tracer concentration. Light orange: no tracer.

Fig. 5.12 shows the concentration front for different values of saturation, the images have been binarized. Dispersion patterns change greatly with saturation. We observe a distortion of the concentration front which is enhanced when the water saturation is low. There seems to be some sort of threshold since water saturation around 0.85 and 0.7 show a distinctive pattern. Above 0.85, the concentration front is rather straight. On the other hand, we observe distinctive preferential flow paths features for saturation values around 0.7. This change of behavior might be related to the size of the obstacles, with the increase of the maximal bubble size when saturation decreases. However, quantitative analysis has yet to be done to evaluate how the concentration front extends for example, and see how it relates with saturation and the bubble sizes.

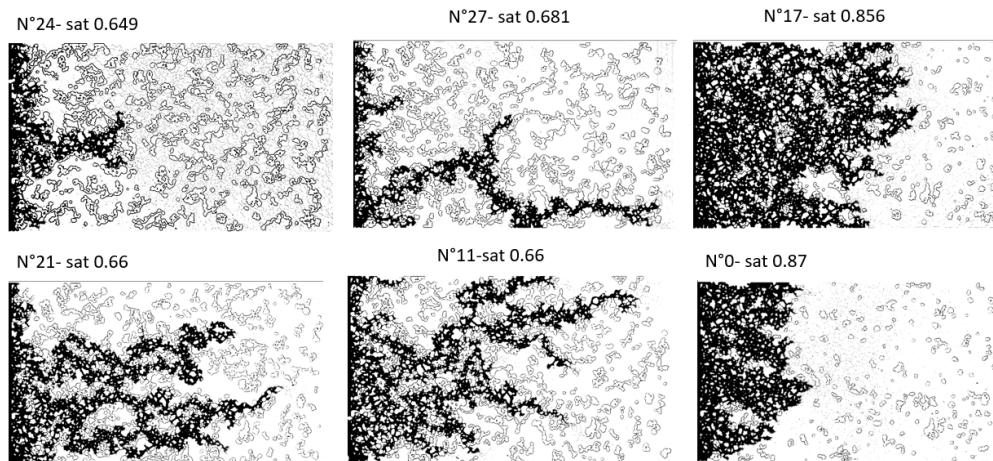


Figure 5.12 – Preferential flow paths for different saturation values. The experimental images have been binarized to emphasize on the tracer concentration flow paths.

Dispersion analysis

We calculated moments for each transport experiment. The moment computation is valid as long as the tracer has not left the micromodel. In Fig. 5.13, we computed the moments for the saturation values of Fig. 5.2. There is a clear influence of the saturation on the dispersion, the slope of the second moment increases when the saturation decreases. The slope of the second moment, computed by linear regression, gives an estimation of the dispersion coefficient.

Nature of the dispersion

We only observe short time dispersion here, so it is difficult to conclude on the Gaussian or non-Gaussian nature of dispersion, even when the moments computed are rather linear. Indeed, especially for low saturation, the micromodel exhibits strong front distortion patterns: we characterize very short time dispersion and the moments computation is often based on one or two preferential flowpaths (cf Fig. 5.11).

Furthermore, not all moments computed are as linear as in Fig. 5.13. Indeed, in the Fig. 5.14, we show the evolution of the second moment for three different phases configurations than the Fig. 5.13, including two different saturations, and two different realizations with a similar saturation. We see that if the evolution of the second moment can be linear, as seen in Fig. 5.14 (Left), it also can present a sort of initial transient, as seen in Fig. 5.14 (Center), and even show a non linear pattern as seen in Fig. 5.14 (Right).

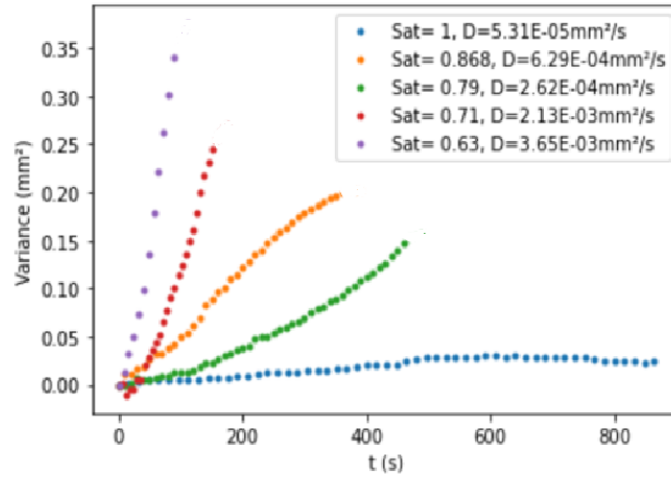


Figure 5.13 – Evolution of second moments with time for different saturation values. Linear regression of the second moment slopes allows to compute dispersion coefficient estimations for each saturation.

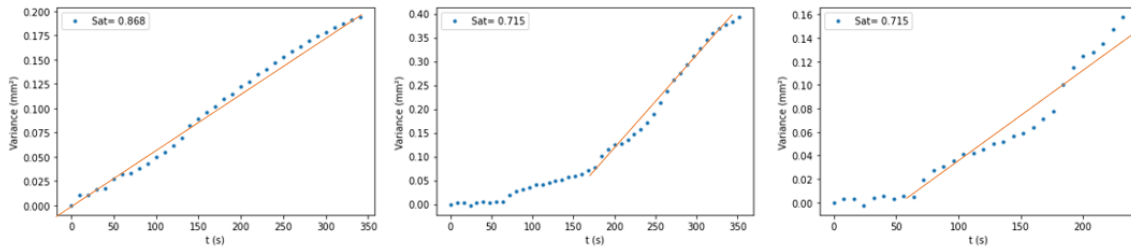


Figure 5.14 – Second moment evolution with time for different saturation values. (Left) Examples of linear second moment with time. (Center) and (Right) Examples of second moments non linear with time. The linear fits to estimate a dispersion coefficient are shown in orange.

The non linearity is more frequent when the water saturation is low. For high saturations, the moments are rather linear and the dispersion is probably Fickian. For lower saturations, the uncertainty is high and it is not possible to know whether the dispersion is Fickian or not. Therefore, characterizing transport with a dispersion coefficient might not be adequate. However, given the quality of experimental data, it is the only quantity that we can derive to compare the different transport experiments. Linear regressions realized to derive dispersion coefficient are shown in Fig. 5.14.

Dispersivity as a function of saturation: preliminary analysis

Keeping in mind the issues concerning the computation of the dispersion coefficient, we still derive the slopes of the second moments to get a first trend for the effect of saturation in dispersion. We used the moments computed to derive a value of the dispersivity λ . We compute the dispersivity rather than the dispersion coefficient because the effective velocity could be different between the different injections, and normalizing by the velocity gives better correlation with saturation.

$$\lambda = \frac{D}{v_{\text{eff}}} \quad (5.3.1)$$

Supposing that the moments evolve linearly with time, we computed the slopes for the first

and second moments, which gives respectively the effective velocity v_{eff} and the dispersion coefficient D . Then, the dispersivity can be computed. In Fig. 5.15, the shaded area highlights the range of saturation values for which the measured dispersivity is largely affected by errors. Still, the tendency is quite clear from the figure, the dispersivity tends to decrease as the water saturation increases.

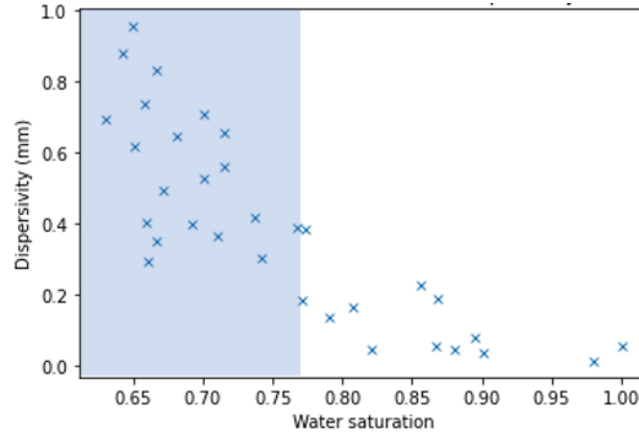


Figure 5.15 – Dispersivity values as a function of saturation. The shaded area shows the range of saturation for which there is a high uncertainty on the dispersion coefficient computation.

Limit of the analysis: need for simulation

Our analysis is limited by the length of the micromodel and by the uncertainty inherent to experimental data, we cannot conclude on the nature of dispersion and the results we obtain, such as Fig. 5.15 are not sufficient to describe properly the dispersion, notably at long times. This is why we will perform simulation in unsaturated porous media to improve our analysis, as we will detail in a later chapter.

5.3.2 Influence of bubbles distributions

We aim at understanding at the pore scale the mechanisms that induce the dispersion in unsaturated porous media, and see how the unsaturated porous media properties influence dispersion. As we characterize the bubbles distribution, we tried to see if some characteristics of the bubbles distribution (area, perimeter, Feret¹, etc) would show strong correlation with the dispersivity values. For each parameter, we would evaluate the mean, the standard deviation and the maximum of the distribution. Again, the values of dispersivity we computed are largely affected by errors for low saturation values.

The Fig. 5.16 shows the evolution of the dispersivity (calculated as described in the previous section) as a function of the bubble size characteristics of the bubble distributions, namely the bubble mean and maximal size, the perimeter and the mean Feret. As Fig. 5.16 highlights, there is a good correlation between the bubble characteristics such as the mean area or perimeter and the maximal size. The dispersivity increases with the bubble size. However, none of the parameter stands out particularly. We calculated Spearman correlation coefficients (correlation values based on the variables ranks) to assess if some

1. The Feret diameter (or caliper diameter) is a measure of an object size along a specified direction. In general, it can be defined as the distance between the two parallel planes restricting the object perpendicular to that direction. [111]

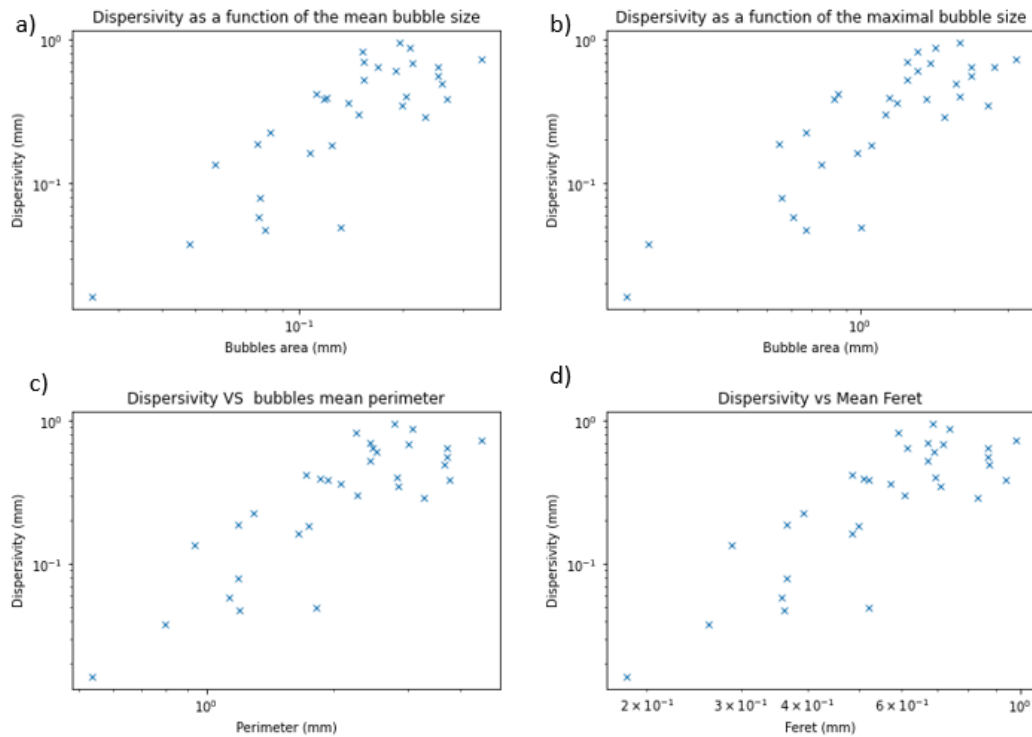


Figure 5.16 – Influence of the bubble characteristics on the dispersivity. Dispersivity as a function of: a) the bubbles mean size. b) the bubbles maximal size. c) the bubbles mean perimeter. d) the bubble mean Feret.

bubble parameters could be more relevant than others to influence the dispersivity (Fig. 5.17). Spearman correlation coefficients are between -1 and 1 . A negative value implies a negative correlation between the variable, and positive value implies a positive correlation. The closer the absolute value to 1 , the better correlation between the two variables.

	Saturation	Area			Perimeter			Feret			Width			Height		
		m	SD	M	m	SD	M	m	SD	M	m	SD	M	m	SD	M
Correlation coefficient	-0.85	0.74	0.78	0.80	0.76	0.80	0.80	0.74	0.77	0.80	0.74	0.62	0.81	0.71	0.76	0.76
p-value	3.10e-10	8.10e-7	1.10e-7	1.10e-7	4.10e-7	e-8	e-8	7.10e-7	2.10e-7	2.10e-8	7.10e-7	1.10e-4	7.10e-9	3.10e-6	3.10e-7	2.10e-7

Figure 5.17 – Correlation coefficient between the dispersivity and different bubble characteristics. m stands for mean, SD for Standard Deviation and M for maximum.

However, the correlation coefficient was always below the correlation coefficient between saturation and dispersivity (-0.85). The different parameters have similar correlation coefficients. Nonetheless, for each parameter, the maximum of the distribution has the best correlation coefficient (around 0.80). Therefore, the bigger bubbles in the unsaturated medium might have a greater influence in the dispersion.

However, our efforts involve dealing with data that contains noise, posing a challenge to deeper interpretation. It's conceivable that by using improved data, correlations might emerge between specific structural characteristics and dispersion. Notably, a parallel investigation employing numerical data was carried out later in this research, but it failed to

yield any additional insights into a potential correlation between structure and dispersion.

5.4 Experimental validation of Lattice-Boltzmann simulation in the micromodel

As mentioned earlier, the experimental system exhibits certain limitations, particularly in obtaining a well-defined entrance condition, resulting in significant variability in the dispersion experiment results. To overcome these experimental limitations, we aim to employ Lattice-Boltzmann simulations to compute flow and transport within the micromodel, considering both saturated and unsaturated conditions. Our goal with the simulations is to accurately reproduce the transport physics occurring in the micromodel. However, it is important to note that there are certain aspects of the experimental setup that Lattice-Boltzmann simulations cannot fully capture.

One such aspect is the exact conditions at the interfaces, such as air/solid and solid/air, which cannot be replicated in the simulation. In our case, where the immiscible gas phase is trapped and immobile, we treat it as an additional solid phase within the medium, applying the same boundary condition to all obstacles. Furthermore, our simulations are conducted in a 2D image of the micromodel, which has a limited depth, denoted as L_z . To account for the depth, we use a Darcy-Brinkmann (or depth average) model for the flow. However, we acknowledge that we still neglect the shape of air clusters and solid grains in the z direction.

Therefore, our objective is to assess the influence of these simulation assumptions on transport and evaluate the suitability of the method for studying transport in unsaturated micromodels. We achieve this by performing a comparative analysis between the experimental work and Lattice-Boltzmann simulations for three different saturations. Specifically, we conduct experiments for each saturation and, subsequently, for each phase configuration, we compute flow and transport using the simulations. After obtaining the concentration fields for both experiments and simulations, we proceed to compare the transport properties.

By conducting this thorough evaluation and comparison, we aim to gain insights into the adequacy of our simulation hypotheses for studying transport in unsaturated micromodels and understand the limitations and implications of our chosen approach.

5.4.1 Experimental and simulation conditions

Experimental conditions and simulation parameters

The injection is continuous for both simulation and experimental work. The inlet condition for simulation is perfectly neat ($\tilde{c}(x = 0) = 1$), while the experimental inlet condition is more diffuse and not completely symmetrical due to the complex injection set-up. Consequently, the concentration front in the experiments is already slightly diffuse and asymmetrical when the experiment starts, contrary to the simulation.

The experiments and simulation Pe number were computed from the front velocity values. Table 5.2 gives the Pe for simulation and experiments.

Hypotheses of comparison

As experimental and simulation conditions are not identical notably in term of Pe and inlet conditions, we formulate some hypotheses to be able to compare simulation and

Table 5.2 – Table of the Pe number for experiments and simulations, with $Pe = \frac{v d_{\text{pore}}}{D_m}$ and ($D_m^{\text{exp}} = 10^{-3}\text{mm/s}$, $D_m^{\text{sim}} = 0.003125$ (LBM units)).

S_w	Pe_{exp}	Pe_{sim}
1	15	10
0.87	4	10
0.70	2	10

experimental results. First, to take into account the inlet condition that is not exactly similar, we consider an offset in time to adjust experimental and simulation concentration fronts at the beginning.

Second, as the injection velocity is not the same for experiments and simulations, we suppose that the dispersion is invariant by normalization by v (at least, in our range of Pe). When considering the ADE equation, it is the same as considering only macroscopic diffusion coefficient.

Indeed, we assume that $D = D_m + D_{\text{macro}}$, with $D_{\text{macro}} \propto \lambda v$, λ being the dispersivity. If the microscopic dispersion can be neglected, $D_m \ll D_{\text{macro}}$, then, the ADE becomes

$$\frac{\partial \tilde{c}}{\partial t} + v \frac{\partial \tilde{c}}{\partial x} = \lambda v \Delta \tilde{c} \quad (5.4.1)$$

with $t' = \frac{tv}{L_x}$ the normalised time, it leads to

$$\frac{\partial \tilde{c}}{\partial t'} + L_x \frac{\partial \tilde{c}}{\partial x} = L_x \lambda \Delta \tilde{c} \quad (5.4.2)$$

Therefore, with these assumptions, the ADE is invariant by v . The concentration evolution can be compared for different Pe number with the relative time t' .

Considering the time offsets to take into account the inlet conditions, the relative time can be written as follow

$$t'_{S_w}{}^{\text{exp}} = \frac{t - t_{\text{offset}}^{\text{exp}}(S_w)}{\Delta t'_{S_w}{}^{\text{Exp}}} \quad (5.4.3)$$

with $\Delta t'_{S_w}{}^{\text{Exp}} = \frac{L_x}{v_{S_w}{}^{\text{exp}}}$, $v_{S_w}{}^{\text{exp}}$ is the mean flow velocity in the experiment at the saturation S_w .

$$t'_{S_w}{}^{\text{sim}} = \frac{t - t_{\text{offset}}^{\text{sim}}(S_w)}{\Delta t'_{S_w}{}^{\text{sim}}} \quad (5.4.4)$$

with $\Delta t'_{S_w}{}^{\text{sim}} = \frac{L_x}{v_{S_w}{}^{\text{sim}}}$, $v_{S_w}{}^{\text{sim}}$ is the mean flow velocity in the simulation at the saturation S_w .

5.4.2 Results

We consider three saturation values ($S_w = 1$, $S_w = 0.87$, $S_w = 0.7$) for which we performed transport experiments and simulations. We compute the concentration profiles, and find time offsets so that the beginning conditions are almost identical for the concentration profiles.

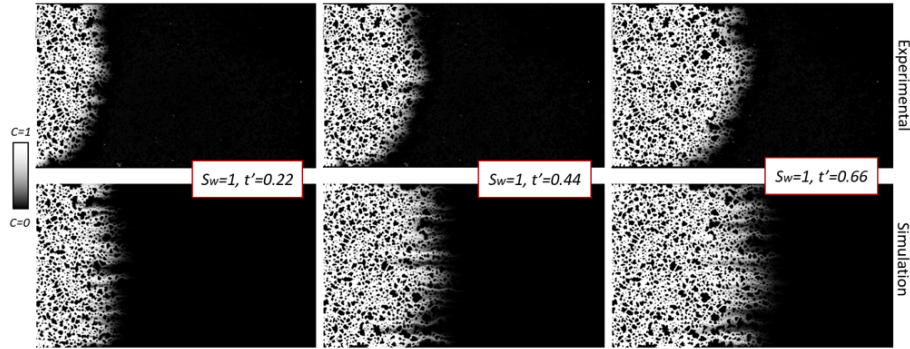


Figure 5.18 – Comparison of experimental and simulated concentration fields for three normalized times, $S_w = 1$.

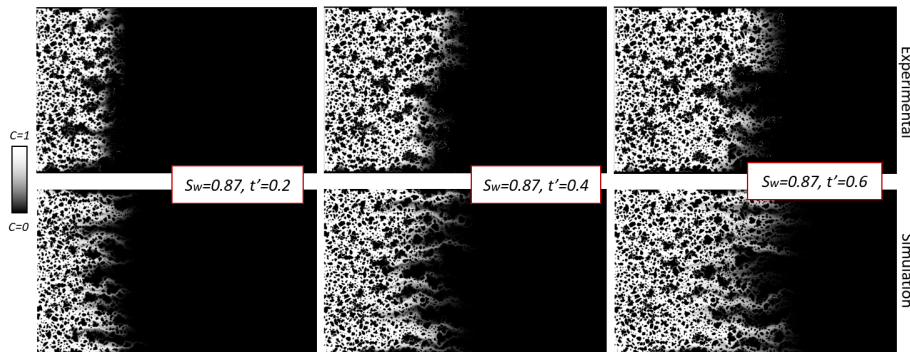


Figure 5.19 – Comparison of experimental and simulated concentration fields for three normalized times, $S_w = 0.87$.

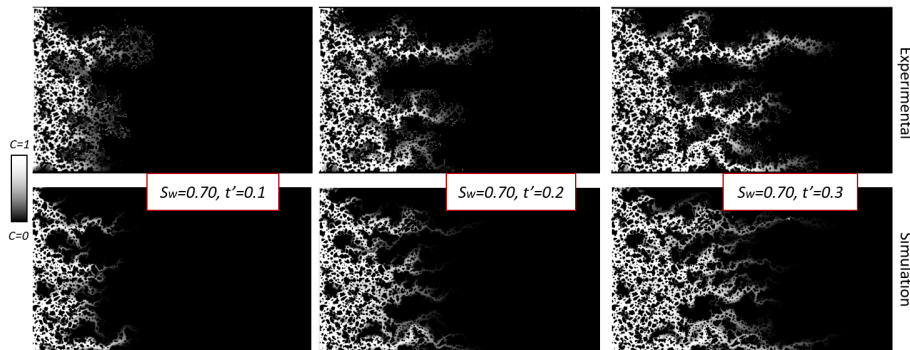


Figure 5.20 – Comparison of experimental and simulated concentration fields for three normalized times, $S_w = 0.70$.

Concentration fields

The concentration fields (Fig. 5.18, 5.19, and 5.20) show a good accordance between the experiments and the simulations. As we see in the saturated case (Fig. 5.18), there is more distortion of the concentration front in the simulation, which might be explained by the more diffuse inlet condition in the experiment. When the saturation decreases (Fig. 5.19), patterns such as preferential paths and dead ends appear and we can see that they match between simulation and experiments, even though some patterns can be more noticeable in the experiments and some other more noticeable in the simulation. The less

saturated case (Fig. 5.20) shows more discrepancies, as the system gains in complexity.

Dispersion analysis

By analyzing the concentration profiles depicted in Fig. 5.21, we can observe a satisfactory agreement between the experimental and simulation data, considering that the experimental profiles exhibit more pronounced noise, as anticipated. To further assess the dispersion behavior, we compute the second moment σ^2 for all simulations and experiments. The results reveal that experimental and simulation data share very similar dispersion characteristics, particularly in the case of higher saturation levels. However, as the saturation decreases, the concentration profiles become increasingly noisy. Consequently, due to the inherent noise in the experimental data, the computation of the second moment tends to be less precise. Nonetheless, despite the greater noise in the experimental data, the comparison between experiments and simulations provides valuable insights into the dispersion behavior within the system.

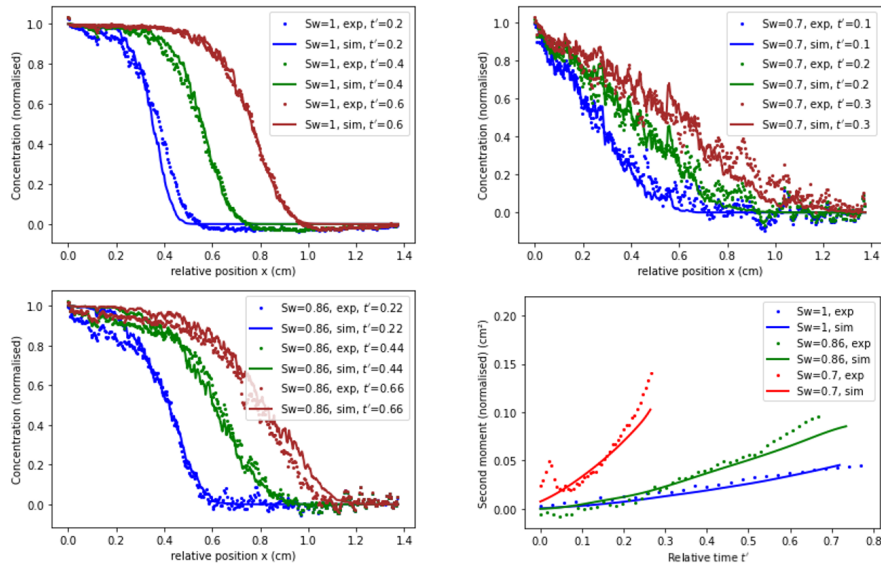


Figure 5.21 – [Top and bottom left] Comparison of experimental and simulated concentration profiles for three normalized times, and three saturation values respectively $S_w = 1$, $S_w = 0.87$ and $S_w = 70$. [Bottom right] Comparison of the second moment evolution with the normalised time t' for three saturations in simulation and experiments. An offset has been subtracted to the second moment for a better comparison of the slopes.

5.4.3 Validation of LBM simulation to compute transport in saturated and unsaturated micromodel

The comparison of transport properties between the experimental and simulation data demonstrates a high level of similarity, despite variations in Peclet numbers, inlet conditions, and the presence of significant experimental noise. This observation suggests that 2D Lattice-Boltzmann (LBM) simulations conducted within the micromodel are suitable for studying transport using experimental images. Notably, the impact of physical parameters that differ between the experiments and simulations, such as the dimensionality (3D vs. 2D) and physico-chemical interactions at the interfaces, is overshadowed by the noise inherent to experimental limitations. In other words, the experimental noise is more

pronounced than the discrepancies arising from these physical parameters. Thus, the utilization of 2D LBM simulations alongside experimental images provides an adequate approach for investigating transport phenomena within the micromodel, despite certain disparities between the experimental setup and the simulation framework.

5.5 Conclusion on preliminary results

Using the developed experimental setup, a series of experiments were conducted to acquire initial results on multiphase flow properties and preliminary findings on dispersion. The production of a wide range of saturations in the micromodel enabled the characterization of saturation evolution with the capillary number following multiphase flow. Notably, it was observed that saturation is primarily determined by the water capillary number, and it increases with increasing capillary number. The distribution of phases resulting from the co-injection was also analyzed, focusing on the size distribution of bubbles as a function of the capillary number. As indicated by existing literature, the bubbles size distribution for different capillary number differs mainly by the cut-off at large sizes, i.e. by the maximum bubble size in the medium.

Subsequently, transport experiments were conducted in the unsaturated micromodel across the entire range of saturations. These experiments facilitated a qualitative analysis of dispersion patterns, including dead-ends and preferential flows, as well as the computation of spatial moments to characterize dispersion. The findings indicated an increasing trend of dispersion as water saturation decreased. However, conclusive determination regarding the Gaussian nature of dispersion could not be made due to limitations imposed by the micromodel size and the increased dispersion observed in low saturation conditions.

Consequently, the second part of the thesis focuses on Lattice Boltzmann simulations, serving as a complementary numerical approach to the experimental investigations. These simulations are particularly valuable for studying non-miscible flow in porous media, which remains challenging to replicate experimentally. An experimental validation of Lattice Boltzmann simulations was proposed to investigate transport phenomena in both saturated and unsaturated micromodels.

Given the limitations of experimental images due to the micromodel size, an objective is to utilize the experimental images to generate larger unsaturated porous media through data training techniques. This approach would facilitate the study of long-term transport in unsaturated porous media and enable a statistical analysis of dispersion with various configurations for short porous media.

Chapter 6

Generating synthetic images of unsaturated porous media with a multiscale multipoint statistics approach

As we saw in the last chapter, transport experiments in a micromodel show significant limitations, notably the condition at the inlet is never completely neat and the size limit of the micromodel only allows to observe short time dispersion.

Although Lattice-Boltzmann simulations in unsaturated images of the micromodel allow to overcome the issue of the inlet condition, the size of the micromodel still limits the study to short term dispersion. Indeed, simulating the results of a multiphase flow in a complex porous media is still difficult. Plus, there is the question of representativity of the unsaturated porous medium: when the saturation decreases, the heterogeneity of the medium increases significantly and the size of the micromodel is not necessarily statistically representative. Therefore, it would be necessary to consider longer media, or realize experiments on a large number of samples which is rather time consuming.

Hence, creating artificial new images from experimental data would allow to overcome this issue. In this section, we designed a machine learning based method to produce artificial images of unsaturated porous media from our experimental data. The goal is to generate a large number of unsaturated images without limiting their size. We used a multiscale multi-point statistics algorithm, a methodology more commonly applied to geostatistics.

In this chapter, we detail the method developed and we propose a validation by comparing properties of the generated and experimental images, in term of structure, flow and transport.

6.1 Motivation

When conducting transport experiments in a micromodel, it is difficult to experimentally obtain a neat tracer injection condition due to the dispersion in the inlet tubing [91, 104]. To overcome this difficulty several authors simulated tracer transport in images of partially saturated porous media. These images were obtained either experi-

mentally or numerically (either by simulation of two-phase flow or machine learning methods) [6, 28, 46, 90, 163].

In both cases, creating new images for different saturations in various porous structures is time consuming. Moreover, further comprehension of the coupling between pore structure, immiscible two-fluid-phase distribution and transport requires a statistically relevant amount of data, i.e. two-fluid-phase distributions associated with their transport properties. Also, as the saturation decreases, the spatial heterogeneity of the system becomes more important, as air clusters size distributions widens. Therefore, it would be necessary to study larger sample sizes to ensure the relevance of the statistical analysis. The difficulty to obtain a sample size larger than the Representative Elementary Volume (REV) could explain partially the discrepancy in the literature about the effect of saturation in transport in porous media. One way to deal with the increased spatial heterogeneity is to increase the sample size, although it is often difficult experimentally. One alternative approach to address this issue is by conducting the experiment or simulation on multiple distinct samples. However, when it comes to experiments, it becomes exceedingly challenging and costly to carry them out in comparable mediums possessing identical properties. For simulations, it is thus necessary to generate a large number of different two-fluid-phase configurations having the same statistical properties.

To this goal, [90] considered multiple-point statistical simulations (MPS) [144] to generate two-fluid-phase distributions in a given two-dimensional porous structure consisting of irregularly arranged spheres. MPS approaches were initially developed for geological modeling to generate new distributions of complex geometry patterns from a training image that represents the expected structure (see for instance [149] for a review). In [90], the training images considered for simulation were obtained from immiscible two-fluid-phase experiments in their micromodel. The solid matrix was not modified during simulations and acted as a constraint in the algorithm. The approach was applied to three different saturations.

In the present work, we extend the previous approach to heterogeneous pore structures and consider a MPS algorithm to generate simultaneously a new solid structure and an air-water distribution. In this way, the coupling between saturation and pore topology can be easily studied for different structures. The MPS considered in our study [44, 58–60] introduces two levels of resolution for the training image in order to properly capture and reproduce the geometric features within limited simulation times. The training images consist of two-fluid-phase distributions (air/water) in porous media obtained experimentally, when a steady state is reached and air clusters are immobile. The resulting generated porous medium and the associated air clusters distribution share similar topological statistics with the training image. The proposed method thus appears as a generalisation of the one described in [90], notably because it simulates jointly the porous structure and the air clusters distribution for a complex porous medium geometry. Summarizing, the method is not specific to a given geometric structure of a porous medium and could be applied to any given 2D distribution, even with complex geometry patterns. The proposed approach presented here represents a significant novelty compared to the method outlined in [90]. It stands out as a generalization due to its ability to simultaneously simulate both the porous structure and the distribution of air clusters within a complex porous medium geometry. In essence, this method is not restricted to a particular geometric structure of a porous medium, making it applicable to any given 2D distribution, even those exhibiting intricate geometric patterns.

In the following, we detail the multi-scale MPS algorithm and explain how it is used

to create new images from experimental ones. We present images generated by the MPS algorithm for several saturations and analyze their statistical properties. Finally, results of flow and transport simulations are also provided and discussed to prove the relevance of our methodology.

6.2 Multiple-point statistics algorithm

In the following paragraphs, we first describe the principle of the MPS algorithm used in this work and then detail its multi-scale extension which is required to deal with large objects in restrained computational times. All the MPS algorithm notations can be found in the Nomenclature Table.

6.2.1 MPS algorithm

The first step of the approach consists in retrieving from the Training Image (TI) the information that will be used afterwards to generate new images. It consists more precisely in building a database of all the sub-images of a given size occurring in the Training Image. To do so, the Training Image is browsed with a rectangular window \mathcal{W} of size w pixels; all the sub-images of size w present in the Training Image are stored in the database. These images will be referred to as patterns in what follows and denoted \mathcal{T} .

The second step consists in generating a new image iteratively by complementing at each step the current (incomplete) generated image with a patch \mathcal{P} of size p pixels with $p < w$. This patch is selected from the pattern database to maximize the similarity with the incomplete image. The different steps of the algorithm are illustrated in **Fig. 6.1** and detailed below:

- Initialisation: we select randomly a pattern \mathcal{T} of the database, extract the patch \mathcal{P} located in its center and paste this patch in the center of the simulation grid (see **Fig. 6.1**).
- Until all pixels have been visited once:
 - Identify the set of non-simulated pixels that have at least one simulated neighbour.
 - Sort the pixels in descending order based on the number of simulated neighbors they have, from the pixel with the highest count of simulated neighbors to the pixel with the lowest count of simulated neighbors.
 - For each pixel i visited according to that order:
 - * Step 1: Extract from the partially generated image the sub-image $\mathcal{W}(i)$ of size w centered in i
 - * Step 2: Compare $\mathcal{W}(i)$ to the pattern database extracted from the TI and select the pattern $\mathcal{T}(i)$ the closest to $\mathcal{W}(i)$ in terms of Euclidean distance weighted by a Gaussian filter (to give more weight to the central pixels, see also [59, 60]).
 - * Step 3: Extract the central part of $\mathcal{T}(i)$ to obtain the patch $\mathcal{P}(i)$ and paste it on the simulated grid around pixel i while keeping the previously simulated pixels unchanged.

From a practical point of view, the main configuration parameters of the MPS are the Training Image size, the shape and size of the window \mathcal{W} used to browse the Training

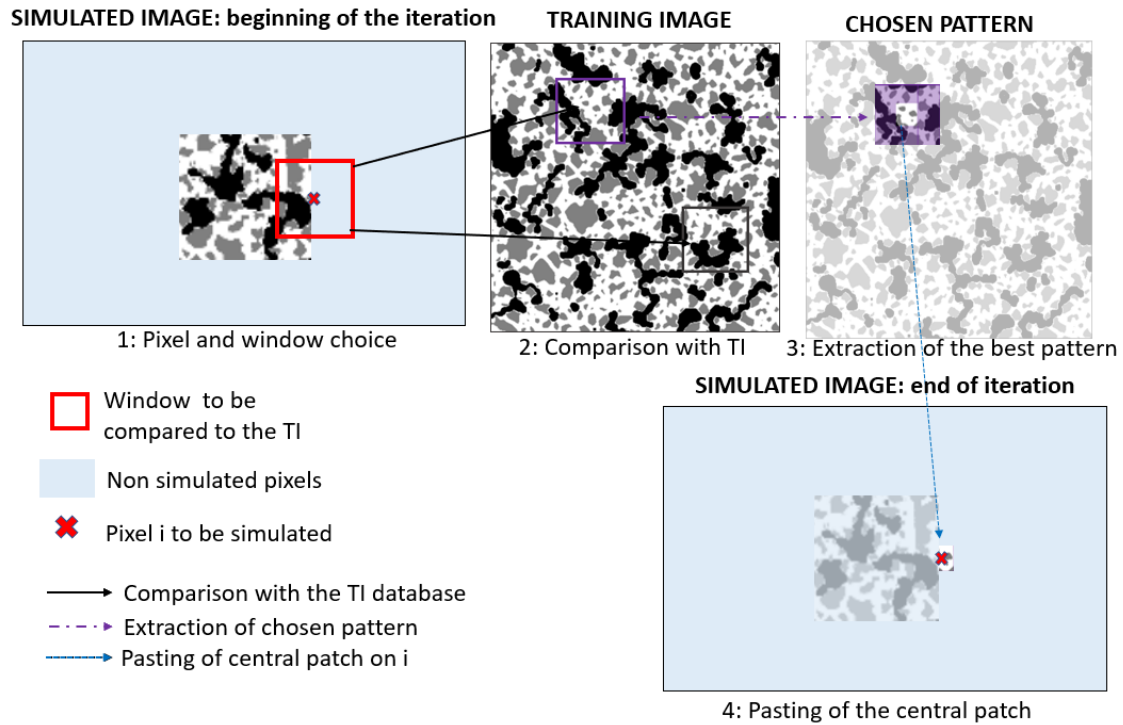


Figure 6.1 – Schematic for the simulation around pixel i . Step 1: At each iteration, pixels with at least one simulated neighbour are selected. Then, the pixel i with the most simulated neighbours is chosen for simulation (identified by a red cross). A window $\mathcal{W}(i)$ centered in i (indicated by a red square) defines the neighbourhood that will be compared to the Training Image (TI). Step 2: The pixels in the red square already simulated are compared to each pattern of size w in the TI (e.g black and purple square). Step 3: The closest pattern is extracted from the TI (here purple square). Step 4: A patch at the center of this chosen pattern is extracted and pasted on the generated image, centered on i while keeping the pixels already simulated unchanged.

Image, the shape and size of the patch \mathcal{P} used to fill progressively the generated image, the distance formulation for the comparison between the simulated, training patterns and in the search order in the database. As illustrated in [58–60], the window \mathcal{W} should be large enough to properly capture and reproduce the TI features. However, the larger the window is, the longer the simulation times becomes. On the contrary, the use of a larger patch \mathcal{P} reduces simulation times as the simulation grid is filled in less iterations, but this can also lead to a degradation of the results with occurrence of discontinuities for instance. Finally, a bigger Training Image allows to better capture the statistics of the medium but at the cost of longer simulation times induced by the larger size of the database. To overcome these limitations, we resort to the multi-scale MPS described in the following paragraph. Note that the MPS algorithm makes it possible to generate multiple realizations from the Training Image. The realization will be determined by the pattern selected in the database at the initialization step. Each initialization pattern leads to a new realization.

6.2.2 Multi-scale algorithm

To reduce the impact of the window and patch size on the generated image and the simulation time, the previous MPS algorithm was extended to a multi-scale framework [58,60]. For simplicity, this variant is presented here with two levels: a fine scale that corresponds to the initial Training Image, and a coarser scale used to speed up the computations. Nevertheless, it is important to note that the method remains applicable regardless of the number of scales employed, it can be extended to include multiple intermediate coarser images along with a fine image.

In a first step, the multi-scale algorithm consists in generating a coarse image. In this way, a coarse Training Image is generated by upscaling the initial fine one. Then we use the one-scale MPS algorithm described above: the coarse Training Image is browsed with a rectangular window \mathcal{W}_c of size w_c pixels to generate a database. The latter is used to produce a coarse realization. This coarse level simulation is generally fast, and provides a trend that is complemented with fine level details in the second step. This enables to reduce the size of the window \mathcal{W}_f used on the fine scale without degrading the results.

In the second step, the coarse and fine Training Images are considered to define a dual database consisting of pairs of fine and coarse patterns obtained by browsing the Training Images with fine and coarse windows \mathcal{W}_f and \mathcal{W}_c . The simulation on the fine scale then involves the joint comparison of the already simulated values on the fine and coarse scales with this dual database. At each pixel i to be simulated, the patched values $\mathcal{P}(i)$ thus depend on the values already simulated around i on both the fine and coarse scales. The approach is illustrated in **Fig. 6.2**. Further details on the MPS algorithm can be found in the aforementioned publications [44, 58–60].

The configuration parameters for this multiscale algorithm consist of the fine scale Training Image, the upscaling coefficient between the fine and coarse levels (Ups), and the window and patch sizes considered on the fine and coarse scales (w_f, p_f for the fine scale and w_c, p_c for the coarse scale).

6.2.3 Application of MPS to unsaturated porous media images

The following section details the application of MPS to unsaturated porous media images (consisting of three phases). It includes the choice and preparation of the Training Images from experimental data, the analysis of the configuration parameter influence on the resulting images and the post-processing procedure.

Preparation of Training Images

The MPS algorithm is applied to Training Images that should follow the subsequent criteria: to simulate a medium statistically representative, the Training Image size should be superior to the REV (Representative Elementary Volume) defined after statistical analysis of properties of interest (the medium porosity, saturation, grain and air cluster size distributions).

In addition, Training Images from experimental data are pre-processed. For example, some air clusters envelop grains entirely, and therefore they will not impact the flow or the transport. Thus, elements included in grains or air clusters that are not in contact with the percolating wetting phase are cleared. Also, elements of small size whose effects on the flow are negligible are suppressed as well. It allows to improve the MPS resulting images quality. The image processing is realized with the ImageJ software.

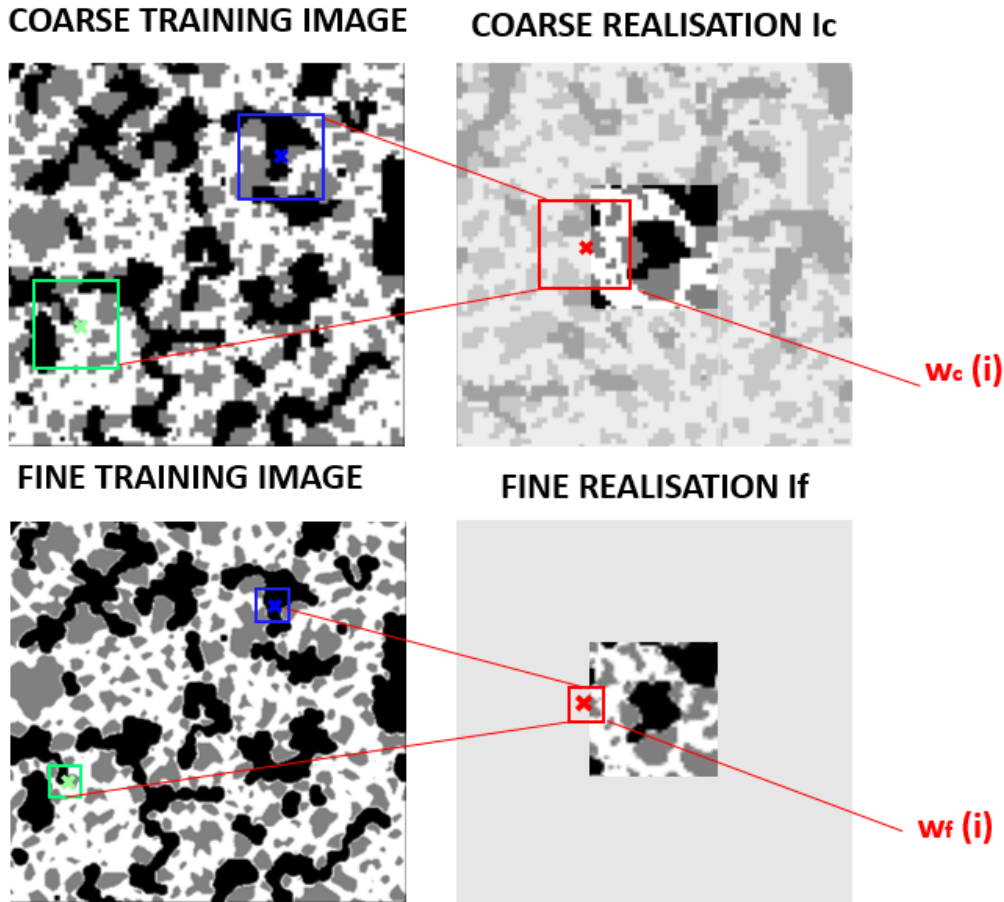


Figure 6.2 – Schematic for the attribution of the patch value for the multiscale algorithm. In what follows, square windows are considered. For a given pixel i to be simulated on the fine level, we extract the fine scale simulated sub-image $\mathcal{W}_f(i)$ of shape w_f centered in i , and the coarse simulated sub-image $\mathcal{W}_c(i)$ of shape w_c centered in i . Then, $\mathcal{W}_c(i)$ and $\mathcal{W}_f(i)$ are simultaneously compared to the patterns of the dual database, as shown by the green and blue rectangles.

Post-processing

Images obtained with MPS present small defects that are not physical: discontinuities of the different phases, absence of water film between grains and air clusters, inclusions in grains or air clusters. Such defects are shown in a zoom of a generated image in **Fig. 6.4** (Left). Note that they may be lessened with other configuration parameters for the MPS algorithm, but at the cost of longer simulation times. Here, we rather applied a post-processing algorithm to the generated images with the following features:

- Smoothing discontinuities and unnatural straight lines that appear in the generated images. Straight lines are due to the patch size. They are generated during the image simulation when patches are progressively added to the generated image.
- Suppression of inclusions in grains and air clusters, that do not participate to the flow
- Removal of grains and air clusters smaller than the minimal grain and air cluster size found in the Training Image

- Generation of the water film between air cluster and solid that is not always complete in the MPS image.

Post-processing algorithm methodology The post-processing algorithm is using ImageJ software. Fig. 6.3 shows the different steps of the post-processing algorithm. The

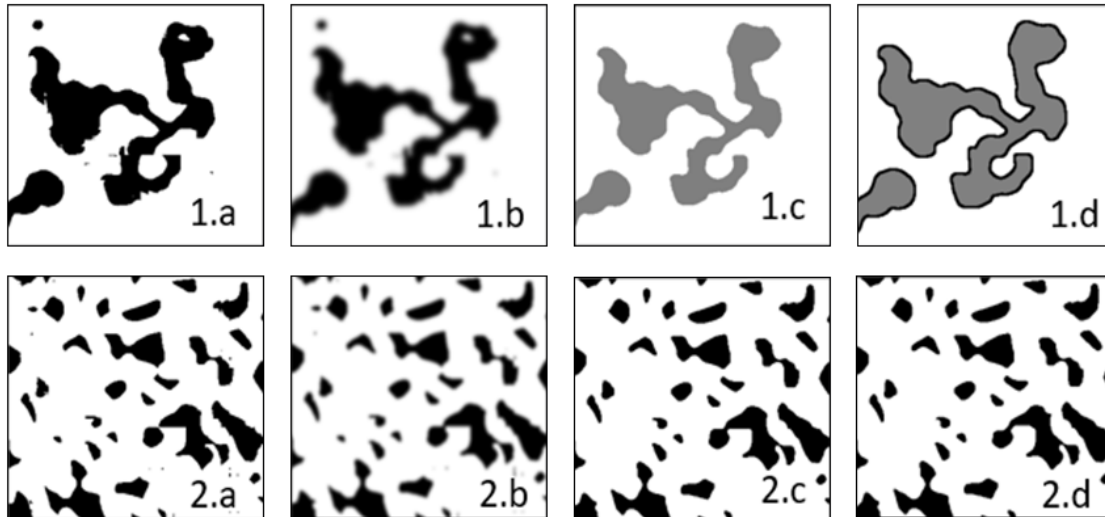


Figure 6.3 – MPS image post-processing. [Up] Air clusters processing. 1.a Air clusters before post-processing. 1.b Smoothed image of 1.a. 1.c Smoothed air clusters (binarized image of 1.b). 1.d Final air clusters image. Creation of the water film (black) around the air cluster. [Bottom] 2.a Solid grains before post-processing. 1.b Smoothed image of 2.a. 2.c Smoothed solid grains (binarized image of 2.b). 2.d Final solid grains image.

algorithm treats grains and air clusters separately, by isolating them and creating two distinct binarized images for air clusters (1.a) and grains (2.a). The post-processing consists in the following steps:

1. Air clusters: A blurred image (1.b) is created from the binarized air clusters image (1.a). Then, it is binarized with a threshold chosen to maintain the same air area percentage than the original image (1.a) to obtain (1.c). This allows smoothing of the air clusters outlines while conserving their general shape. Grains (2.a): The aim is similar but the method is slightly different, as the grains are not as circular as air clusters, and a strong blur would smooth the pointy grains. As we want to maintain shape characteristics, first a close operation is performed (it consists in a dilatation followed by a an erosion), then a light blur is applied (2.b). The image is then binarized (2.c).
2. Holes are filled for both grains and air clusters.
3. The particle grain sizes are analysed and particles whose size is smaller than the minimal grain size of the Training Image are erased. The same operation is performed for air clusters.
4. The air clusters image is dilated and subtracted from the grain image (2.c) to create a water film between solid and air cluster (2.d).

The final image is obtained by recomposing grains and air clusters. **Fig. 6.4** (Right) shows the image after post-processing.



Figure 6.4 – MPS image before (Left) and after (Right) post-processing, black: solid, red: air, white: water.

Choice of the configuration used for the MPS algorithm

Parameters of the MPS algorithm influence the resulting images. **Fig. 6.5** shows the statistics (porosity, saturation and grains/air clusters size distribution) obtained for different parameters of the multi-scale MPS algorithm. In order to select the best configuration, we compare statistics of the generated images to those of the Training Image. The studied parameters are the size of the window w_c and the patch p_c used for the coarse level simulation. The other parameters (w_f , p_f , Ups, and the seed used to initialize randomly this simulation) are kept constant.

Tab. 6.2.3 shows the different parameter settings of the MPS algorithm used to find suitable settings to reproduce experimental phase distributions (Fig. 6.5). Here, N_x and N_y are the dimensions in pixels of the Training Image, w_f and p_f the template and patch size at the fine scale, and w_c and p_c the template and patch size at the coarse scale. The random seed determines the choice of the first patch.

Fig. 6.5 shows that the configuration 5 shows the best agreement between generated and experimental image statistics, therefore we chose those parameters in the following.

Settings	N_x	N_y	w_f	p_f	w_c	p_c	Ups	seeds
n°1	1200	1200	39	29	49	29	10	5
n°2	1200	1200	39	29	59	29	10	5
n°3	1200	1200	39	29	9	6	10	5
n°4	1200	1200	39	29	29	9	10	5
n°5	1200	1200	39	29	9	3	10	5
n°6	1200	1200	39	29	49	19	10	5
n°7	1200	1200	39	29	39	29	10	5

Table 6.1 – MPS parameters for the choice of the best configuration.

6.3 Method validation

The study is based on three experimental images with different saturation levels ($S_w = 1$, $S_w = 0.87$ and $S_w = 0.70$). Saturation profiles were not constant along the micromodel axis, notably near the micromodel inlet and outlet due to capillary effects. In order to

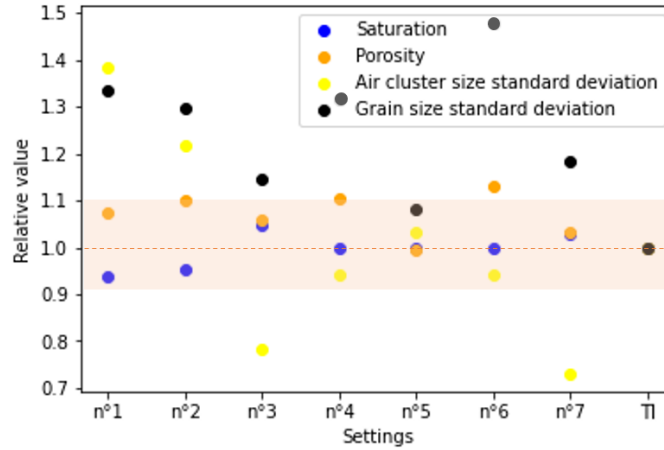


Figure 6.5 – Statistics of MPS generated image obtained with 7 parameter settings compared to the Training Image (TI) for saturation, porosity, grain and air clusters size distributions. The relative value is defined as the ratio between the MPS generated and experimental images value (for instance, for saturation the ratio is $S_w^{\text{MPS}}/S_w^{\text{Exp}}$). The shaded area indicates the tolerance zone for which the settings provide statistics close enough to the Training Image, for example settings n°5 ($w_f = 39$, $p_f = 29$, $w_c = 9$, $p_c = 3$, Ups = 10.)

work with rather homogeneous two-fluid-phase distributions, the experimental images have been slightly cropped to avoid boundary effects.

6.3.1 Generated images

Fig. 6.6 shows results of the MPS algorithm after post processing for both saturated and unsaturated cases. As a reminder, the parameters chosen for those images correspond to the best setting found **Fig. 6.5** (n°5). The training image TI, indicated on the experimental images in **Fig. 6.6**, is chosen to be as representative as possible of the whole image in terms of structure properties.

Visually, the generated images show good agreement with their respective training images. The saturated medium is reproduced with a similar porosity (0.66 *vs* 0.69 for the experimental and the generated image, respectively). The average values of saturation S_w are also very similar between the experimental images and their respective generated images (1 *vs* 1, 0.87 *vs* 0.85, 0.70 *vs* 0.65). Plus, fine structure elements such as water films around bubbles are reproduced as well, as it can be seen on the zooms of **Fig. 6.6**.

6.3.2 Structural properties

We analysed and compared the structural properties of the experimental images and MPS generated images, first focusing on the porous medium structure (i.e. the mask) and then on the two-fluid-phase distribution.

Statistical comparison of the porous structure

In the previous section, we analyzed four mean quantities (saturation, porosity, air and grains size standard deviation). To analyse further the structure of the generated porous medium and compare it to the experimental porous medium, grains, pores and throats

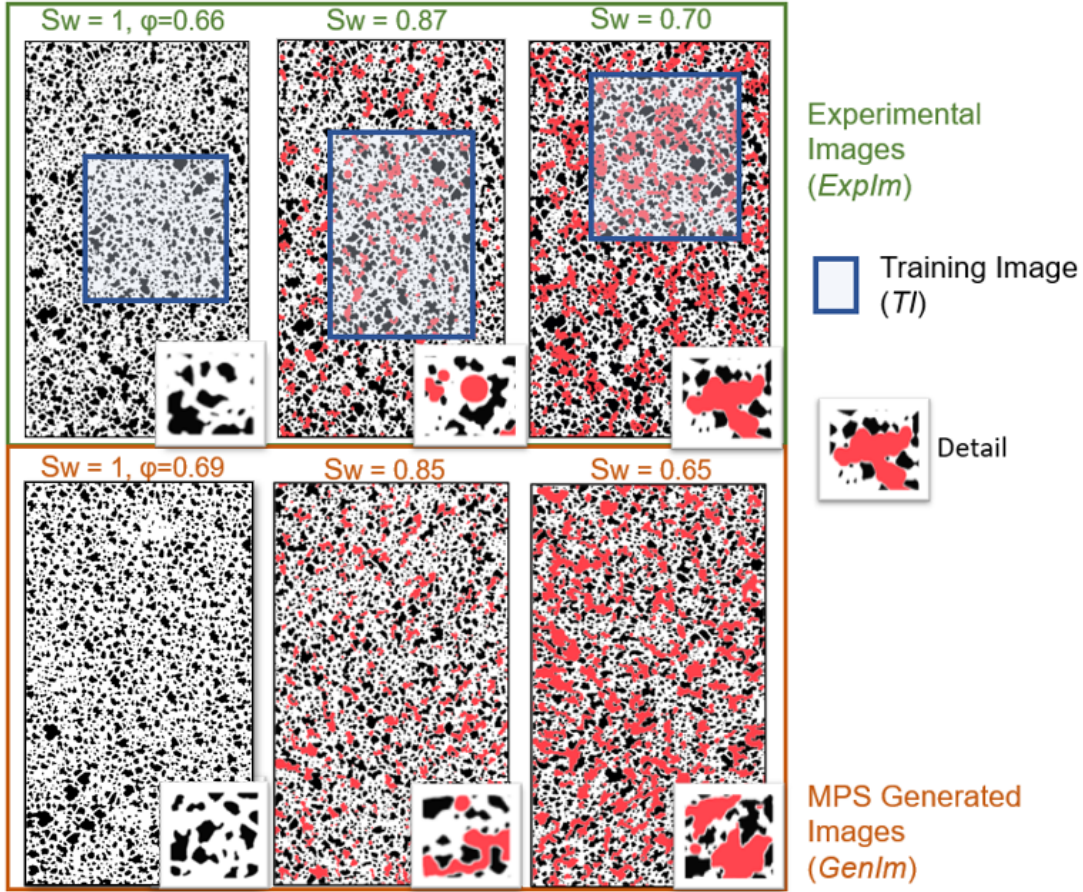


Figure 6.6 – [Top] Phase segmentation for saturated (Left) and unsaturated conditions [Middle and Right], respectively $ExpIm_{S_w=1}$, $ExpIm_{S_w=0.87}$ and $ExpIm_{S_w=0.70}$. The blue square indicates the window chosen as training image TI for the MPS algorithm. [Bottom] Simulation results, the MPS generated images are $GenIm_{S_w=1}$, $GenIm_{S_w=0.85}$ and $GenIm_{S_w=0.65}$ after post-processing. The algorithm settings are identical for these realizations ($w_f = 39$, $p_f = 29$, $w_c = 9$, $p_c = 3$, Ups = 10, as defined in section 6.2.3).

distributions in size (area) are computed. The analysis of pore and throats properties was performed with the imageJ software, as detailed in Chapter 3, 3.2.1. **Fig. 6.7** (Left) shows the cumulative distributions of grain, pore and throat sizes for the saturated experimental image $ExpIm_{S_w=1}$ and generated image $GenIm_{S_w=1}$. The distributions are all in good agreement.

Additionally, in order to assess if the grains shape was reproduced as well, we computed the distributions of several geometric factors such as the circularity and the solidity. The circularity of an object (grain or air cluster) is defined as $C = \frac{4\pi \text{Area}}{\text{Perimeter}^2}$, and the solidity $S = \frac{\text{Area}}{\text{Convex Area}}$ quantifies the objects convexity¹. **Fig. 6.7** (Right) shows the circularity and solidity distributions of the saturated experimental image $ExpIm_{S_w=1}$ and generated image $GenIm_{S_w=1}$, and they are in good agreement as well.

1. The convex area or convex hull of a shape is the smallest convex set that contains it.

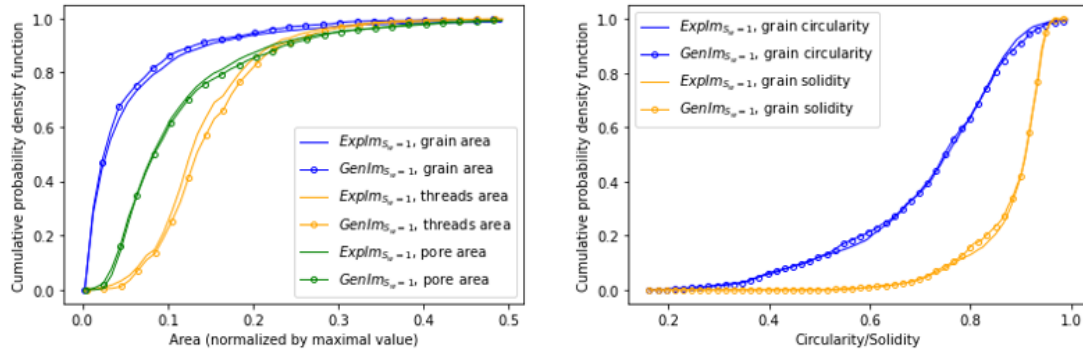


Figure 6.7 – (Left) Cumulative probability density function in size (area) of grains, pores and throats for the generated image ($GenIm_{sat}$) and the experimental image ($ExpIm_{sat}$) in the saturated case. To facilitate comparison across all saturations (ranging from 0 to 1), the area for each distribution has been normalized by its maximum value. It ensures that the sizes of the distributions are scaled within a common range of 0 to 1. (Right) Grains solidity and circularity cumulative probability density function for the generated image ($GenIm_{sat}$) and the experimental image ($ExpIm_{sat}$).

Statistical comparison of the two-fluid-phase distributions

We analysed and compared the two-fluid-phase topology of the unsaturated experimental images ($ExpIm_{S_w=0.87}$, $ExpIm_{S_w=0.70}$) and their respective generated image ($GenIm_{S_w=0.85}$, $GenIm_{S_w=0.65}$) for two saturation values. Air clusters are analysed in terms of size and geometry.

Fig. 6.8 shows the different distributions characterizing the air clusters of the experimental images and their respective generated images. The experimental air clusters distributions in size (**Fig. 6.8** (Left)) of both saturations are very well reproduced by the MPS algorithm. The size distribution for low saturation shows more large size clusters, for both generated and experimental images. In addition, the distributions of circularity and solidity (**Fig. 6.8** (Right)) show, that there is a rather good agreement between the air clusters shapes in the experimental images and the MPS generated ones, even though there is more discrepancy than for size distributions. Notably, air clusters circularity tends to be slightly superior for generated images than for the training images. This might be caused by the post-processing algorithm that tends to smooth the shapes and erases asperities, as well as by the size of the training image that might be slightly small.

6.3.3 Flow and transport properties

As the structures of the saturated and unsaturated porous media are correctly reproduced by MPS, we now investigate flow and transport properties of the generated images. To this goal, we simulate the velocity and concentration fields using Lattice Boltzmann method (LBM) in the MPS generated images $GenIm$ and in the experimental images $ExpIm$. We assume the bubbles to act as an extra solid matrix in the simulations.

Velocity fields comparison

Fig. 6.9 shows crops of the velocity field of the experimental images as well as the corresponding MPS generated images for the three saturation values. Specific patterns

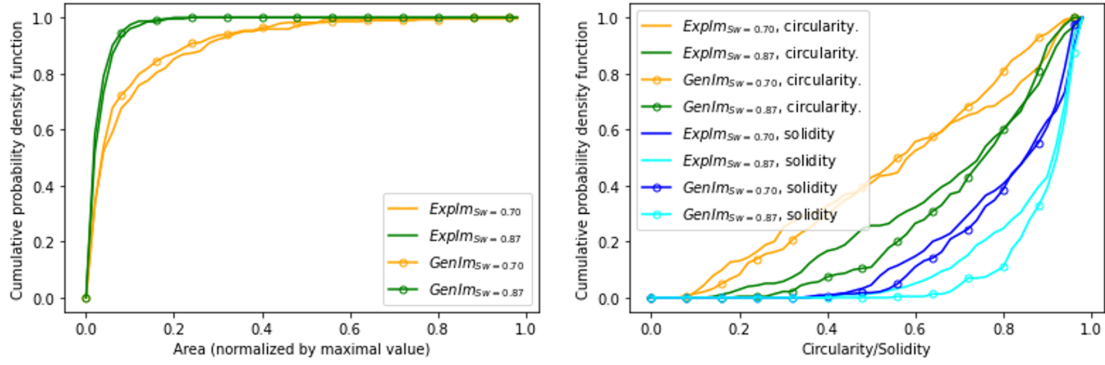


Figure 6.8 – Different distributions characterizing the shape of the air clusters for experimental images for two saturation values ($ExpIm_{S_w=0.70}$ and $ExpIm_{S_w=0.87}$) and their respective MPS generated images ($GenIm_{S_w=0.65}$ and $GenIm_{S_w=0.85}$). The distributions are described through cumulative probability distribution functions. (Left) Distribution in size. (Right) Distribution in solidity and circularity.

of the velocity field of each saturation are correctly reproduced in the generated images. Notably stagnant zones (corresponding to the black areas) and high velocity zones, that are characteristic for lower saturations, seem to be properly generated.

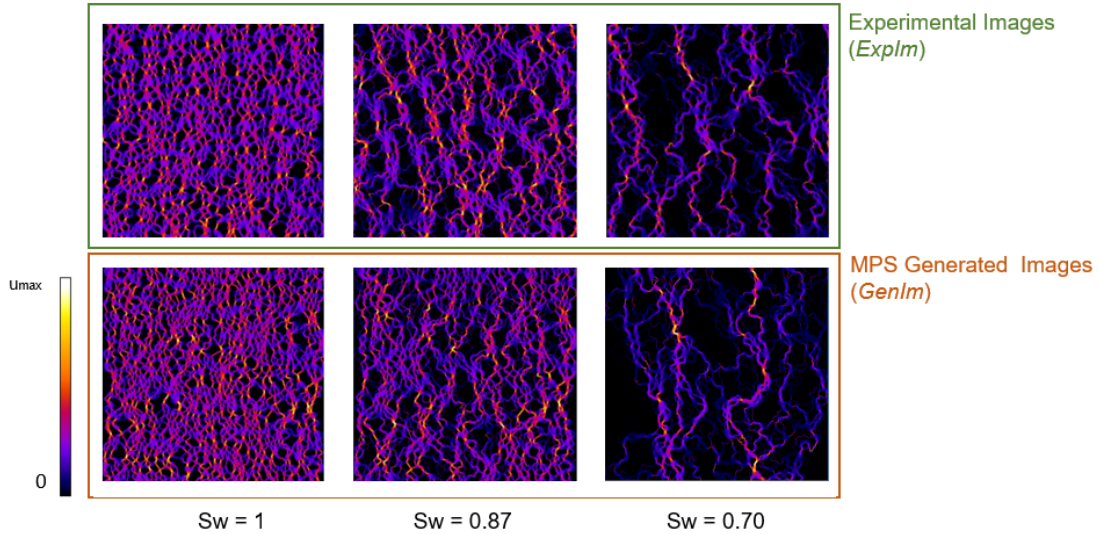


Figure 6.9 – Velocity magnitude computed with LBM (cropped images), in the experimental images [Top] and in the corresponding generated images [Bottom] for three saturation values ($S_w = 1$, $S_w = 0.87$, $S_w = 0.70$) $\langle \|\mathbf{u}\| \rangle_{max} = 0.06$ (LBM units).

More quantitatively, Table 6.2 shows the mean value of the velocity norm $\langle \|\mathbf{u}\| \rangle$ and its normalized standard deviation $\frac{\sigma_{\|\mathbf{u}\|}}{\langle \|\mathbf{u}\| \rangle}$ of the experimental and the generated images. The mean velocity in the generated images is rather well reproduced in the saturated case, but as water saturation decreases the gap between the mean velocity of the saturated and unsaturated porous medium widens. Nonetheless, the standard deviation is in rather good agreement for all saturation values. To be more quantitative, we computed the velocity

Image	$\langle \ \mathbf{u}\ \rangle$ (LB units)	$\frac{\sigma_{\ \mathbf{u}\ }}{\langle \ \mathbf{u}\ \rangle}$
<i>ExpIm</i> $_{S_w=1}$	$5.77 \cdot 10^{-3}$	0.62
<i>GenIm</i> $_{S_w=1}$	$5.41 \cdot 10^{-3}$	0.58
<i>ExpIm</i> $_{S_w=0.87}$	$5.06 \cdot 10^{-3}$	0.82
<i>GenIm</i> $_{S_w=0.85}$	$4.06 \cdot 10^{-3}$	0.87
<i>ExpIm</i> $_{S_w=0.70}$	$2.69 \cdot 10^{-3}$	1.05
<i>GenIm</i> $_{S_w=0.65}$	$1.70 \cdot 10^{-3}$	1.25

Table 6.2 – Comparison of the mean of velocity norm $\langle \|\mathbf{u}\| \rangle$ and its normalized standard deviation $\frac{\sigma_{\|\mathbf{u}\|}}{\langle \|\mathbf{u}\| \rangle}$ between experimental and generated images.

distribution shown in **Fig. 6.10**. Velocity distributions are also in very good agreement. The fact that the velocity fields of unsaturated porous media show more low velocity values is also correctly reproduced by the MPS images. Indeed, when the saturation decreases, the heterogeneity of the medium increases and it leads to stagnant zones, which accounts for very low velocities in the distribution, as well as water films. Consequently, the MPS algorithm allows properly reproducing the flow properties of saturated and unsaturated porous media.

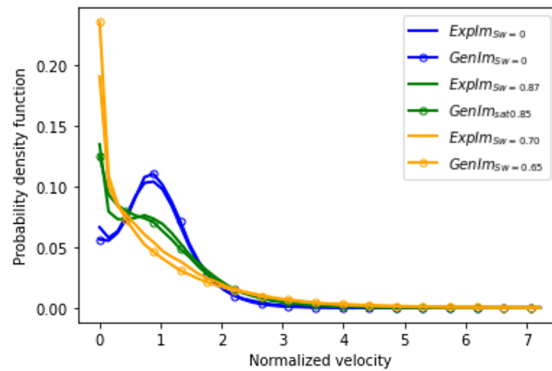


Figure 6.10 – Velocity distribution for the experimental images and their corresponding generated images. The velocity for each image has been normalized by its mean value.

Comparison of the concentration fields

As the flow properties are well conserved in the generated images, we computed the concentration fields using LBM. **Fig. 6.11** shows the resulting concentration fields of the experimental images as well as of the generated images, for identical simulation settings. Characteristic patterns of each saturation are qualitatively well reproduced by the MPS images. For the saturated porous medium a homogeneous tracer front can be observed in both images. Also, an increase in heterogeneity of the front with decreasing saturation can be seen in the experimental and the generated images. In addition, the appearance of low concentration zones (stagnant zones reached by the tracer only by diffusion) and high concentration zones (corresponding to preferential, high velocity paths in the velocity field) when the saturation decreases is well reproduced in the generated images. This is a consequence of the heterogeneity characterizing the velocity field. Furthermore, **Fig. 6.12** (Left) shows concentration profiles (average concentration in y -direction as a function of x)

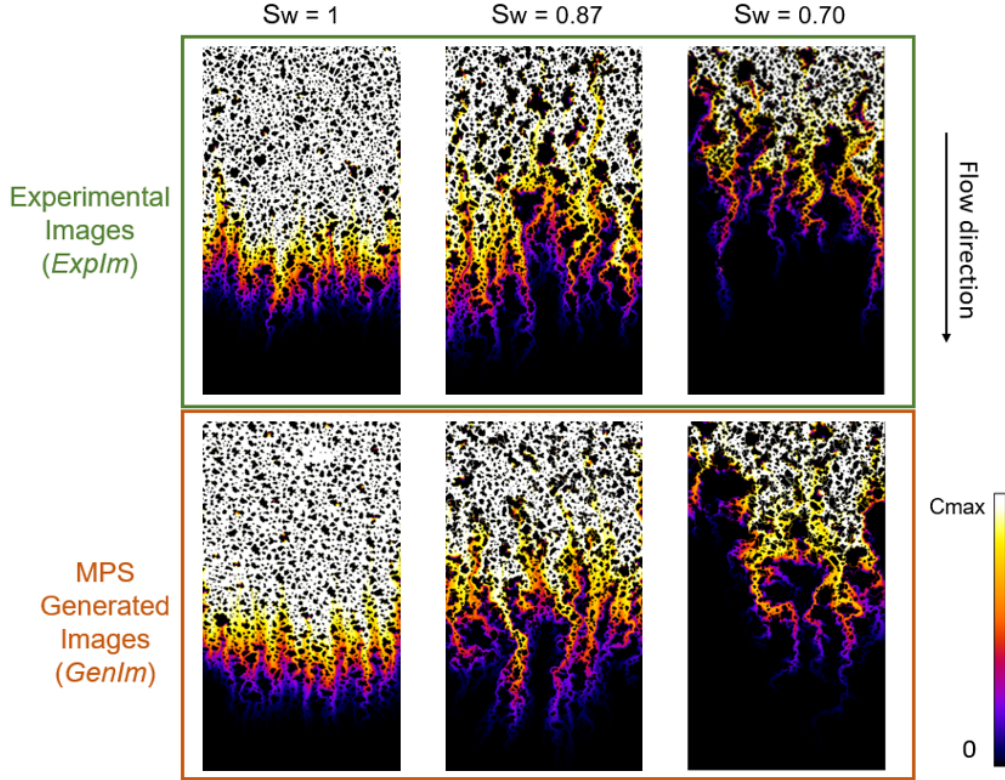


Figure 6.11 – Concentration fields simulated with Lattice Boltzmann for the three investigated saturation values for experimental images (Top) and their respective generated image (Bottom) at $t = 1.0 \cdot 10^5$ LB units, $c_{max} = 1$.

at a given time ($t = 1.2 \cdot 10^5$ LB units). The concentration profiles of the experimental and the generated images are very close. Second moments $\sigma^2(t)$ are computed as a function of time to quantify the spreading of the concentration front (see **Fig. 6.12** (Right)). Second moments in the unsaturated case show rather good agreement as well. However, we notice that the agreement is slightly weaker when we decrease the saturation. This is due to the fact that the saturation profile is increasingly noisy because the system becomes more heterogeneous. Increasing the training image size would probably improve the agreement.

In conclusion, dispersion behavior is similar in the generated and experimental porous media for all investigated saturations. Consequently, the methodology proposed here enables studying dispersion in unsaturated porous media in this whole range of saturation, for numerous phase configurations and porous media sizes.

6.4 Conclusions

In this chapter, we proposed a new workflow allowing further investigations of transport mechanisms in two-dimensional unsaturated porous media. From experimental images, we generated new images using a multi-scale MPS algorithm. We compared structural properties such as porosity, grain, pore and throat size distribution for the porous structure (saturated medium) and the saturation and air clusters distribution for the two-fluid-phase topology (unsaturated media). Using the proper parameters, there was an overall

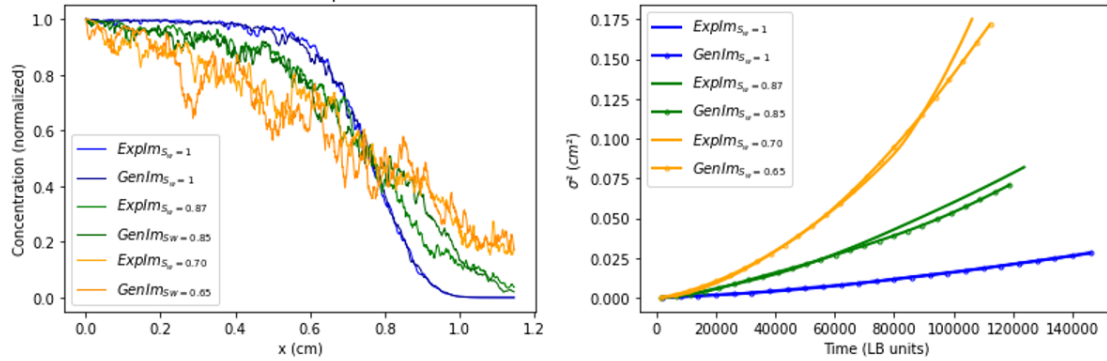


Figure 6.12 – (Left) Concentration profiles at $t = 1.2 \cdot 10^5$ LB units for the three saturation values for the experimental images *ExpIm* and their respective MPS generated images *GenIm*. (Right) Temporal evolution of the second spatial moments $\sigma^2(t)$ describing the spreading of the tracer front of the concentration fields given in **Fig. 6.11**. $\sigma^2(t)$ is given for the three saturation values for the experimental images *ExpIm* and their respective MPS generated images *GenIm*.

very good agreement between properties of the experimental images and MPS generated images. Using Lattice-Boltzmann method, we computed velocity and concentration fields in both experimental and generated images, for saturated and unsaturated conditions. We showed that the velocity distributions were very similar. Concentration profiles were also in very good agreement, and the variance points out that the dispersion properties of the experimental images are well reproduced by the MPS images. Consequently, it is possible to generate an unsaturated porous medium having a new topology but similar properties that will lead to the same transport behavior.

An interesting feature of this work is that the generated images are theoretically not limited in size, in contrast to experimental images. The only restrictions are the computational time and the computer’s memory. Therefore, it becomes possible to study long time dispersion, which is essential to grasp the asymptotic dispersion behavior in unsaturated porous media. Indeed, tracer diffusion into dead end pores is very slow and contributes to long tailed distributions. Consequently, the influence of dead ends can also be seen at larger time scales. Further on, for heterogeneous or unsaturated structures, asymptotic regimes only establish for large systems. Thus, the determination of the transport behavior (Gaussian or not) in unsaturated porous medium requires computations in large structures. The MPS algorithm also allows to generate a large number of different porous structures for a given saturation, leading to several statistical realisations when studying transport properties. Indeed, a statistical relevant data set allows further insights into the correlation between transport and saturation. In conclusion, the workflow proposed here provides the technical tools to gain valuable knowledge on transport in unsaturated porous media.

In the following, we use this new developed methodology for two main goals: study long time dispersion in long unsaturated porous media for different saturations, and realise a statistical analysis of short term dispersion by generating a large number of images with different configurations.

Chapter 7

Numerical results on flow and dispersion in unsaturated porous media

7.1 Introduction

In chapter 5, we conducted an experimental study on transport in unsaturated porous media using a micromodel. This allowed us to understand the nature of multiphase flow and observe phase configurations resulting from immiscible two-phase flow. Through transport experiments, we identified dispersion patterns such as dead ends and preferential flow paths in the medium, and we analyzed the influence of saturation on dispersivity.

However, we encountered several limitations in our experimental approach. Firstly, the micromodel's short length prevented us from studying long-time dispersion and determining whether the dispersion behavior in unsaturated porous media follows a Fickian or non-Fickian nature. Indeed, implementing precise initial conditions for transport is a challenging task, as the concentration front at the entrance of the micromodel is not perfectly neat at the beginning of experiments. Additionally, experimental noise posed challenges in interpreting the results accurately.

To overcome these limitations and complement our experimental findings, we used lattice Boltzmann methods (LBM) for flow and transport simulations within the image of the micromodel, making certain assumptions, notably considering gas as an additional solid phase. To validate the assumptions made in the Lattice Boltzmann Method (LBM) model, we conducted experimental tests using a micromodel. The micromodel served as a physical representation of the system under both saturated and unsaturated conditions. We compared experiments with simulations in the respective 2D images of the unsaturated medium. Thus, we could verify the accuracy of the LBM model against empirical observations. While we could not directly obtain phase distribution through simulations, we utilized a machine learning approach based on the multiple-point statistics (MPS) algorithm to generate images with similar structures to experimental unsaturated images used as training images. The MPS algorithm was presented in chapter 6. We conducted validation to ensure that the flow and transport properties in the generated images closely matched those observed in the experimental images. The results of the validation process confirmed that the properties in the generated images were indeed similar to those in the experimental images. This validation provides confidence in the use of the generated images for further analysis and study of flow and transport in unsaturated porous media.

With this workflow in place, our objective is to create a dataset of MPS-generated images to study transport in unsaturated porous media with statistical relevance. Additionally, we aim to investigate long-time dispersion using longer images generated by the MPS algorithm. Considering the quadratic increase in computation time with image length in LBM simulations, we employ two strategies. Firstly, we create a dataset of generated images that match the size of the micromodel to study many different realizations and enable statistical analysis of short-time dispersion. Simultaneously, we perform long time dispersion transport simulations in long images on a selected range of saturations.

The chapter is structured as follows:

- Presentation of the datasets used for our main study on flow and transport, along with their creation process. This includes the dataset of unsaturated images matching the micromodel size for statistical analysis of short-time dispersion, and the dataset of long images for studying long-time dispersion;
- Characterization of the effect of saturation on flow properties, particularly how it decreases permeability, enhances flow heterogeneity and alters the spatial characteristics of flow;
- Statistical study of short-time dispersion, including an analysis of the nature of dispersion on short images and how the non-Fickian behavior evolves with saturation. Additionally, the effect of the Peclet number on dispersion is examined to determine its role in the non-Fickian behavior of short-time dispersion;
- Examination of long-time dispersion on long images for a selection of saturations to assess if the non-Fickian behavior persists over time. The effect of the Peclet number is further investigated;
- Investigation of the effect of borders on dispersion, evaluating the impact of medium width on flow properties on short and long images.

7.2 Data set

In this chapter, our focus is on conducting Lattice Boltzmann Method (LBM) simulations using the MPS workflow outlined in the previous chapter 6. In this section, we provide further clarification on the dataset we utilize to generate these images and the process of creating a representative dataset of MPS-generated images for studying dispersion.

7.2.1 Experimental Dataset: training images

Through our experimental study, we acquire phase distributions resulting from co-injection across a saturation range of 0.55 to 1. The experimental dataset comprises 25 images that capture the configuration of phases within the micromodel. From this dataset, we extract training images (TI).

We aim to create training images statistically representative of the various saturations and phase distributions that can be observed in the micromodel. We cannot take a whole experimental image as a training image, because of a memory limitation of the MPS algorithm we use. However, from a same experimental image, we can extract different training images with different configurations. Each training image is not necessarily representative

of the whole experimental image. Indeed, the REV for phases configurations might be superior to the TI size or even the micromodel size for the lower saturations. However, it allows us to explore a large set of saturations and configurations. Our TI dataset contains 20 training images. For a sufficiently large number of TI, it allows to create a training image dataset fully representative of the phases configurations in the micromodel and their variability.

7.2.2 Generated images: two data sets

The Multiple-Point Statistics (MPS) approach allows us to generate images of desired sizes and various configurations using a training image (TI). By leveraging the MPS technique, we can create datasets suitable for conducting Lattice Boltzmann Method (LBM) simulations to study flow and transport phenomena. However, conducting simulations on long images can be computationally intensive and time-consuming.

To address this challenge, we employ two parallel strategies in our approach. Indeed, our main datasets for LBM flow and transport computations consist of two distinct sets:

- The short dispersion dataset: this dataset comprises images that are approximately the same size as the micromodel ($L_y^* = 1980$, $L_x^* = 3780$ pixels¹ or $L_y = 0.90$, $L_x = 1.73$ cm). To ensure statistical significance and capture the variability in the system, we generate multiple realizations for each training image using different random seeds. This dataset allows us to study short-time dispersion phenomena within a reasonable computational time.
- The long time dispersion dataset: in contrast to the short dispersion dataset, the images in this dataset are four times longer ($L_y^* = 1980$, $L_x^* = 18000$ pixels, or $L_y = 0.90$ and $L_x = 8.3$ cm). However, due to the increased size, the computational cost for simulating flow and transport becomes significantly higher. Therefore, we carefully select a limited number of long images to investigate dispersion over longer time periods. These longer images enable us to gain insights into the behavior of solute transport over extended durations, albeit at a higher computational expense.

Table 7.1 presents a summary of the properties associated with the two datasets. Fig.7.1 illustrates how the MPS generated dataset was created.

By leveraging these two datasets, we can comprehensively analyze both short-time and long-time dispersion phenomena, balancing computational efficiency and capturing the relevant aspects of flow and transport processes.

	Short-time dispersion dataset	Long-time dispersion dataset
Numbers of TI	20	5
L_x^* (pixels)	3780	18000
Number of processors	180	9000

Table 7.1 – Properties of the two different datasets

1. The notations L_x^* and L_y^* concerns Lattice-Boltzmann units

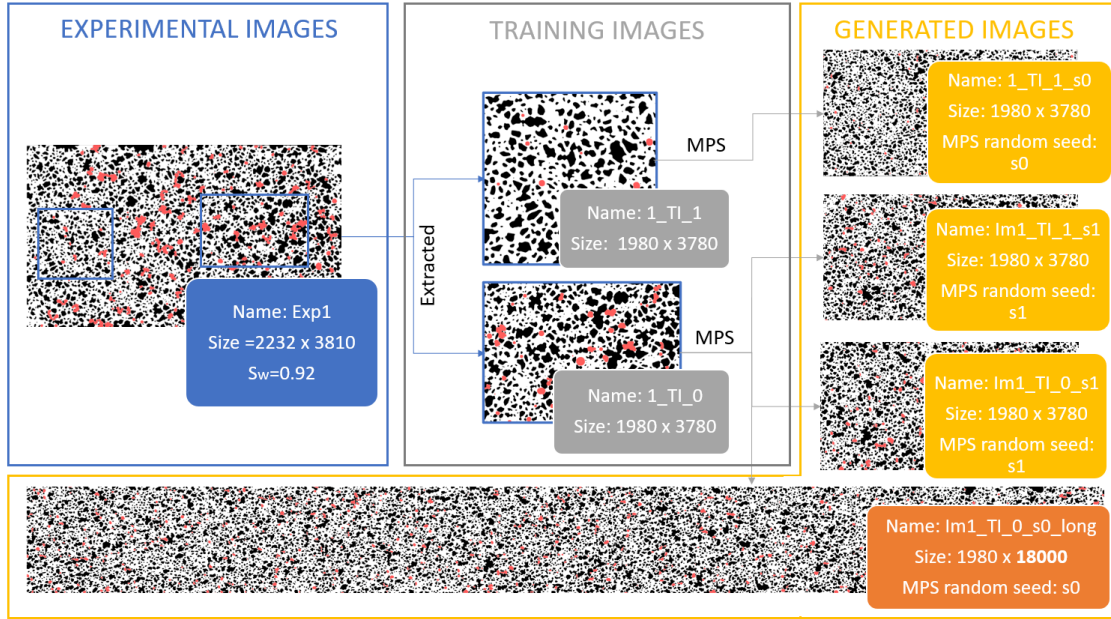


Figure 7.1 – Creation of the MPS generated images from experimental images, illustration with an experimental image of the micromodel.

7.3 Effect of saturation on the flow

7.3.1 Introduction

In this section, we examine the evolution of different characteristics (permeability, tortuosity, heterogeneity) of the flow with saturation across the entire range of saturation values, $S_w \in [0.5 - 1]^2$. To have a large number of data points, we use the dataset with small size realizations.

In the initial stage of our analysis, we concentrate on the evolution of permeability as it relates to water saturation. It has been observed that as the saturation decreases, the permeability of the medium also diminishes [112]. Our objective is to quantitatively measure this effect and determine if our data aligns with existing models or theories. Secondly, we delve into the evolution of velocity fields in relation to saturation. Our transport experiments have revealed the presence of dead ends within the medium, which are characterized by areas of low velocity, as well as preferential flowpaths exhibiting high velocities. We aim to quantify how saturation influences the occurrence of low-velocity dead ends and examine the heterogeneity of flow through the standard deviation of velocity. Lastly, we observed that dispersion patterns undergo alterations with varying saturation levels. There is a spatial reorganization of the flow that demands characterization. Specifically, we analyze the spatial correlation of the flow with saturation and also explore tortuosity, which highlights the increased significance of transverse flow at low saturations.

7.3.2 Apparent permeability

Permeability is an essential characteristic of porous media. Understanding the permeability of a porous medium is crucial for predicting fluid flow patterns and transport of

2. The saturation range is slightly larger than in the experiments, as training images selected in unsaturated experimental images can have a smaller saturation than the whole medium.

contaminants. In our medium, the gas phase consists of immobile air clusters, which we have treated as an additional solid matrix in our simulation. This allows us to calculate the apparent permeability of the flow as a function of saturation.

By analyzing the velocity fields, we can determine the mean Darcy velocity of the medium, denoted as U_{Darcy} .

$$U_{Darcy} = \frac{1}{L_x L_y} \sum_{i=0}^{L_x} \sum_{j=0}^{L_y} u_x(x_i, y_j) \quad (7.3.1)$$

with $L_x L_y$ the number of pixels in the image (width and length of the image)³. The apparent permeability K_{app} in the x-direction can then be computed using the equation

$$K_{app} = -\frac{U_{Darcy} \nu \rho L_x}{\Delta P}, \quad (7.3.2)$$

where ν , ρ , L_x , and ΔP represent constant parameters in our simulations, given in the numerical methods section 4.3.1.

Since many permeability models incorporate porosity as a key parameter, we introduce the concept of apparent porosity to facilitate comparisons. The apparent porosity of the medium can be calculated using the equation

$$\phi_{app} = \phi S_w, \quad (7.3.3)$$

where ϕ represents the saturated medium porosity, which equals 0.69 in our case.

Fig. 7.2 illustrates the relationship between the apparent permeability and the apparent porosity of the medium. Our observations reveal a clear trend where the permeability decreases as the apparent porosity, or saturation, decreases. In the fully saturated medium (represented by $S_w = 1$ and $\phi_{app} = \phi = 0.69$), the apparent permeability is measured at approximately 20 Darcy⁴. As the saturation decreases to its lowest point ($S_w = 0.5$ and $\phi_{app} = 0.40$), the apparent permeability approaches zero.

Numerous experimental and numerical studies have extensively explored the relationship between porosity and permeability, including well-known models like the Kozeny-Carmann model and its derivatives [152]. Several authors have proposed power-law relations, summarized by Equation 7.3.4, where permeability (K) is expressed as a function of porosity (ϕ), with R representing a function of the pore radius and c denoting the power-law index.

$$K = R\phi^c. \quad (7.3.4)$$

We can fit our data using a power-law function of the form $K_{app} = R\phi_{app}^c$, considering the apparent porosity, to determine the values of R and c that provide a good fit.

In our experimental observations, we found that we were unable to achieve saturation values lower than approximately $S_{w0} \sim 0.5$, which corresponded to the point where water phase percolation occurred. As a result, the permeability approached zero for saturation values close to this limit. We introduced the concept of percolation apparent porosity $\phi_0 = \phi S_{w0}$, representing the porosity below which there is no longer percolation of the water phase.

3. $U_{Darcy} = \phi \langle u_x \rangle$ with $\langle u_x \rangle$ the interstitial longitudinal velocity.

4. It is superior to the value of the experimental micromodel set-up permeability (4.7 Darcy), as we measure not only the micromodel but also all the connectors permeability in the experimental case.

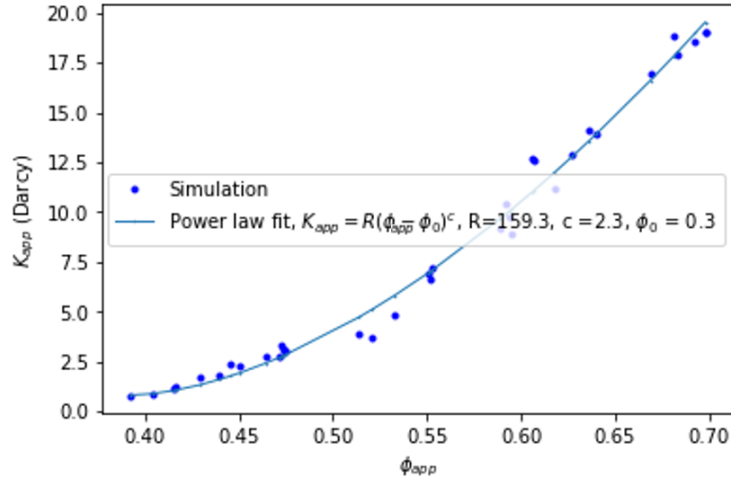


Figure 7.2 – Apparent permeability as a function of the apparent saturation $\phi_{app} = \phi S_w$. A power law fit is shown in the figure.

To better represent the trend of permeability approaching zero as the saturation approaches the lower limit of our saturation range, we employed a fitting approach with the equation $K_{app} = R(\phi_{app} - \phi_0)^c$. As seen in Fig 7.2, the model reasonably fits our data, yielding the following parameters $R = 153$, $c = 2.2$, and $\phi_0 = 0.3$. Consequently, the permeability can be described by the equation

$$K_{app} = R\phi^c(S_w - S_{w0})^c. \quad (7.3.5)$$

Overall, the evolution of the apparent permeability of the medium aligns with certain classical models that establish the relationship between permeability and porosity in experimental systems. We ignored the two-phase nature of our system by considering the apparent porosity, however it still gave satisfying matches with existing theories. This is rather surprising, as the structure of the gas phase is quite different from the porous structure. It would be relevant to extend this analysis to different media with varying porosity values to assess the general applicability of this model in describing the evolution of permeability with saturation.

7.3.3 Velocity field distributions

Velocity distributions

The velocity field in a porous medium provides valuable information about how fluids flow within the material. It reveals how the flow velocity varies spatially across the porous medium. Notably, it gives insights into the heterogeneity of the flow, heterogeneous velocity fields can include preferential flow or localized stagnation zones, influencing the overall transport and mixing behavior. This section describes the velocity field changes with saturation in the porous medium. The aim is to understand how low and high velocities are affected by different saturation levels.

Due to the wide range of velocities, we consider the distribution of the logarithmic velocities $p(\log |u|)$. We consider interstitial velocity, i.e. velocities in the flow section of the porous medium (taking the gas phase as solid). Only strictly positive velocities are

taken into account. Moreover, to facilitate comparison, the velocities are normalized by the mean velocity. This normalization accounts for variations in mean velocity caused by changes in permeability with saturation, as we applied the same pressure drop in all simulations. The normalized velocity is given by

$$u_{norm}(x,y) = \frac{\|u\|(x,y)}{\langle \|\mathbf{u}\| \rangle}. \quad (7.3.6)$$

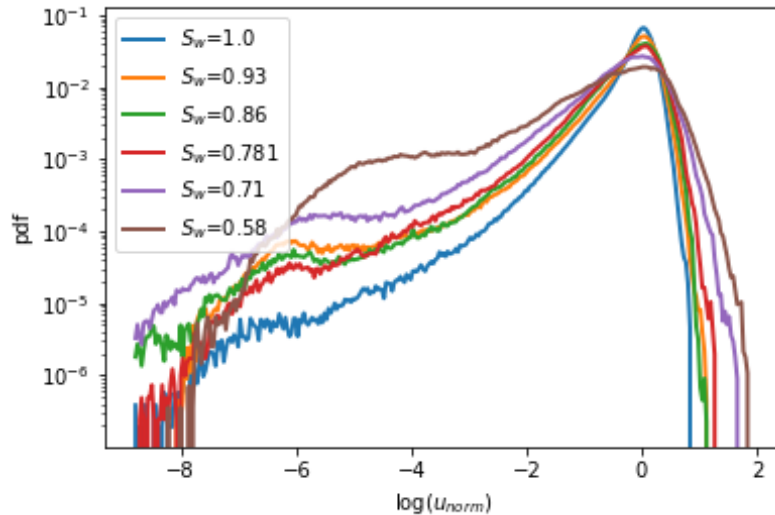


Figure 7.3 – For different saturations, distributions of $\log(u_{norm})$ are shown. The number of bins for the distribution computation is given by $N_{bin}=300$.

In Figure 7.3, the velocity distribution is plotted for various saturation values. It is observed that as the saturation decreases, the velocity distribution becomes wider, and the tail of the distribution extends towards lower velocities. This widening suggests the formation and expansion of dead-end regions within the medium. Notably, at lower saturation levels, a second peak emerges at very low velocities, indicating the presence of nearly stagnant zones in the flow.

Additionally, there is a spreading towards high velocities with saturation especially below $S_w = 0.70$. These high velocities arise due to the formation of preferential paths as the saturation decreases. The maximal velocity increases with decreasing saturation implying a stronger flow along these preferential paths.

The transition between the velocity distributions of saturated and unsaturated conditions is observed to be rather gradual in our study, which contrasts with findings from other similar studies such as Velasquez et al. (2021) [122]. One possible explanation for this difference is that the system under investigation in our study does not involve a model system with regular pillars. Instead, it consists of an intrinsic heterogeneous medium derived from a rock section. The inherent heterogeneity of the medium could contribute to the progressive nature of the transition between saturated and unsaturated velocity distributions, as compared to the more abrupt transitions observed in studies involving regular pillar structures.

In summary, the velocity distribution analysis reveals that as saturation decreases, the velocity field undergoes changes characterized by a wider distribution, spreading towards lower velocities, as well as the appearance of nearly stagnant zones and the development of preferential flow paths with higher velocities.

Heterogeneity of the flow: velocity standard deviation

The characterization of flow heterogeneity is performed by considering the normalized standard deviation of the velocity field, denoted as σ_u . We consider the interstitial velocity, therefore σ_u is defined considering the ensemble of points where the liquid is present within the medium, denoted as L . The size of L is given by $\phi_{app}n_xn_y$ and therefore

$$\sigma_u^2 = \frac{1}{\phi_{app}} \frac{1}{L_x L_y \langle \|\mathbf{u}\| \rangle^2} \sum_{(x_i, y_j) \in L} (\|u\|(x_i, y_j) - \langle \|\mathbf{u}\| \rangle)^2. \quad (7.3.7)$$

Figure 7.4 displays σ_u as a function of saturation, revealing that the standard deviation increases as the saturation decreases. This indicates that the flow becomes more heterogeneous in unsaturated conditions. Notably, for the lowest saturation values, the standard deviation is approximately three times higher than that in saturated conditions.

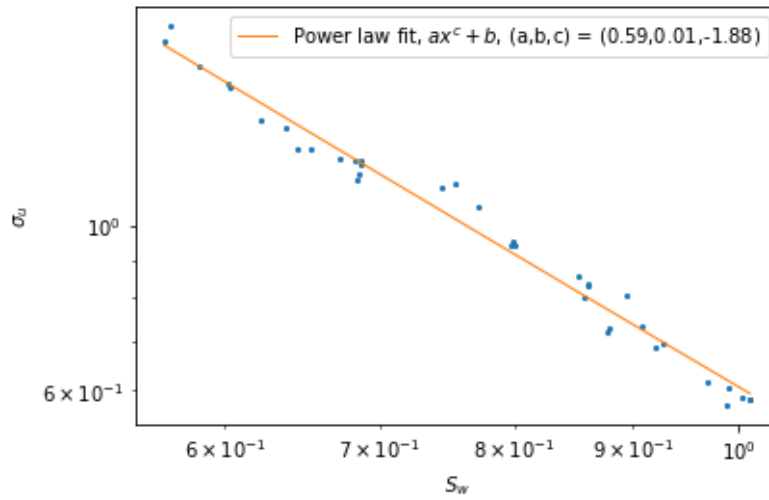


Figure 7.4 – Normalized velocity standard deviation σ_u as a function of saturation

Moreover, when plotted on a logarithmic scale, a linear relationship is observed between σ_u and the saturation. This linear behavior suggests a power law relationship between the two variables. Fitting the data with a power law yields a satisfactory agreement, with a power coefficient of -1.9, giving the following relation

$$\sigma_u \simeq \sigma_{u, S_w=1} S_w^{-1.9}. \quad (7.3.8)$$

7.3.4 Spatial evolution of the flow

The velocity distribution helps to identify the existence of pathways through which fluids preferentially flow within the porous medium. It indicates the presence of regions of higher or lower flow velocities, revealing the network of interconnected pores or channels that contribute to fluid transport.

Qualitative observations

Fig. 7.5 presents velocity fields for 5 different saturations covering the whole range of saturation. As saturation decreases, we observe that certain flow paths become predominant, leaving zones with almost no flow that grow in size. For the lower values of

saturation, particularly near the percolation limit ($S_w \sim 0.5$), there are only a few velocity paths and the dead ends are nearly as large as the medium width.

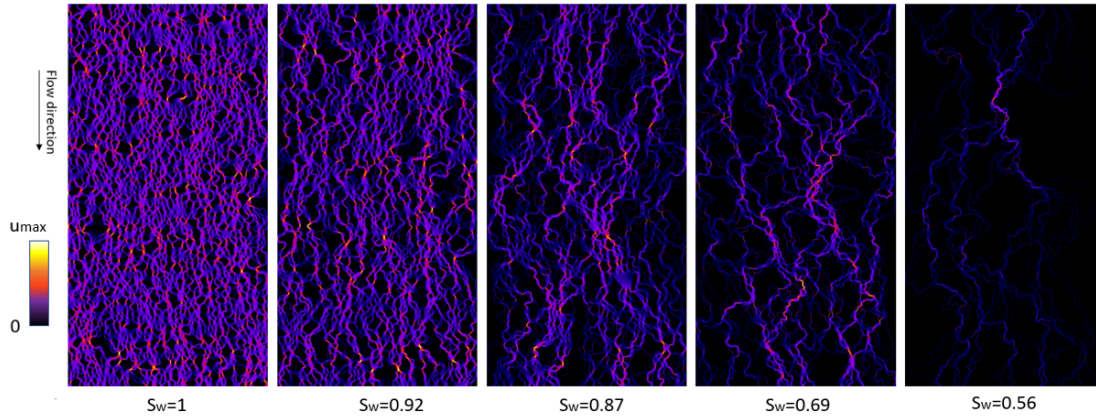


Figure 7.5 – Example of velocity fields for 5 saturation values. (MPS generated porous media).

Dead-ends

As we discussed, the velocity distributions show the presence of low velocity zones of increasing importance when the saturation decreases, corresponding to dead ends in the flow. To characterize these dead-ends, we compute for all saturations the area where velocity is under a certain velocity threshold (excluding the solids and air clusters). We try different thresholds to ensure that the main tendency is for the dead ends does not depend on the threshold.

This velocity ratio threshold is chosen between $r_{u,threshold} = \frac{u_{threshold}}{\langle \|\mathbf{u}\| \rangle} = 1.6.10e^{-4}$ and $r_{u,threshold} = \frac{u_{threshold}}{\langle \|\mathbf{u}\| \rangle} = 1.6.10e^{-6}$, the lowest range of velocities in the saturated porous medium (cf Fig. 7.3). Again, the threshold is normalized by the mean velocity in the medium for all saturations.

Fig. 7.6 shows the area of dead ends according to the saturation. It decreases exponentially with saturation, reaching maxima for the lower saturations. The tendency does not depend on the velocity threshold chosen, as we find a similar exponential factor.

Tortuosity

Tortuosity provides valuable information on the geometric complexity and the path lengths of fluid flow within the material. It quantifies the degree to which fluid pathways deviate from straight lines due to the tortuous nature of the porous structure. As the saturation decreases in our medium, the level of heterogeneity increases, resulting in greater tortuosity. This can be attributed to the growth of obstacles within the medium, which causes the paths reaching the end of the medium to become more convoluted and tortuous.

Tortuosity is typically defined as the ratio of the average pore length (L_e) to the length of the porous medium (L) along the major flow or diffusion axis

$$\tau = \frac{L_e}{L}. \quad (7.3.9)$$

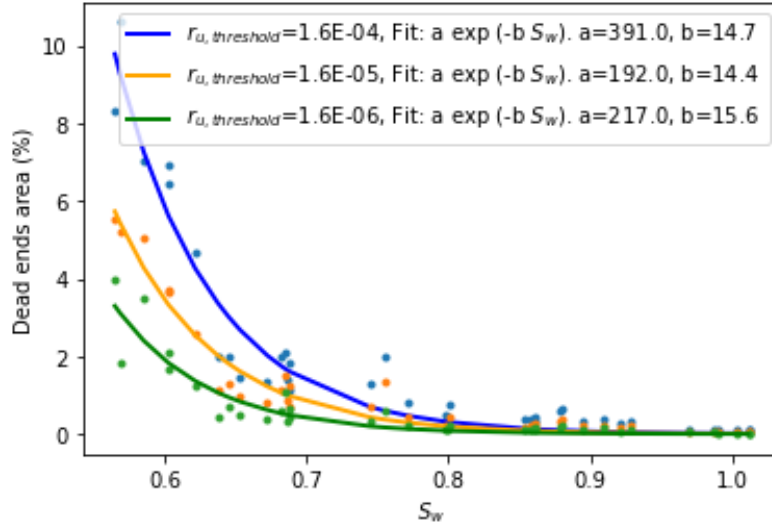


Figure 7.6 – Area of dead ends as a function of saturation for different velocity thresholds. Exponential fits are shown.

Alternatively, another straightforward approach to compute tortuosity is by calculating the ratio of the average magnitude of the velocity over the entire flow (solid zones where there is no flow are not considered) to the average magnitude of its component along the macroscopic flow direction (x) using the latter equation:

$$\tau = \frac{\langle \|\mathbf{u}\| \rangle}{\langle |u_x| \rangle}. \quad (7.3.10)$$

We compute the tortuosity for the entire dataset. While most tortuosity models consider the relationship with porosity, there is a lack of consistency in models that incorporate the relationship between tortuosity and saturation, which likely depends on the specific characteristics of the medium and flow. As a result, we choose to represent the tortuosity as a function of the apparent porosity in Figure 7.7. Our findings demonstrate that tortuosity increases as saturation decreases, indicating that the flow paths become more convoluted. At lower saturations (or apparent porosities), the tortuosity reaches a value of 1.4, indicating that transverse velocity contributes nearly as much as longitudinal velocity.

There are several models available to explain the connection between tortuosity and porosity. Among them, the logarithmic model proposed by Koponen *et al.* [98] is frequently mentioned. Koponen *et al* utilized the Lattice Gas Automata (LGA) technique to solve flow equations within a two-dimensional porous medium composed of randomly positioned rectangles. They investigated the porosity range of $\phi \in [0.5, 1]$ and arrived at the following findings

$$\tau = 1 - p \ln \phi. \quad (7.3.11)$$

Barrande *et al.* (2007) [9] developed a correlation based on experimental measurements on glass sphere pack in 3D with $p = 0.49$.

We fitted our data with the logarithmic model and obtained a satisfactory fit, with $p = 0.42$, which is surprisingly close to the coefficient (p) obtained by Barrande *et. al* [9] ($p = 0.49$).

Overall, the evolution of flow tortuosity aligns with classical models that describe the relationship between tortuosity and porosity in experimental model systems. It is worth

noting that our study accounts for apparent porosity variations resulting from changes in saturation. The two-phase (air/water) nature of our system is ignored when defining the apparent porosity, but as we found that the tortuosity still aligns with classical models considering tortuosity change over porosity, it may then not significantly impact the tortuosity.

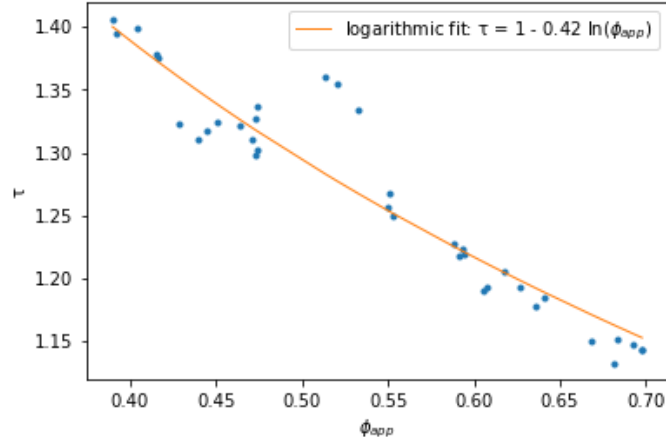


Figure 7.7 – Tortuosity τ as a function of the apparent porosity ϕ_{app} .

Spatial correlation of the flow

As mentioned earlier, the flow exhibits distinct patterns, including zones of low velocity and preferential flow paths with high velocities. These patterns become more prominent as the saturation decreases. Specifically, the low velocity zones tend to expand, and the preferential flow paths become fewer in number. This behavior is particularly noticeable in the growth of dead ends and the reduction of available preferential paths. Consequently, the spatial heterogeneity of the flow experiences a significant increase.

To quantify the spatial heterogeneity of the flow and determine its characteristic length, we employ the autocorrelation function, denoted as $\zeta(x, y)$. This function is defined as follows

$$\zeta(\vec{r}_0) = \frac{1}{L_x L_y} \int \int v(\vec{r}) v(\vec{r}_0 - \vec{r}) d\vec{r} \quad (7.3.12)$$

with $v(x, y) = \frac{\|\mathbf{u}(x, y)\| - \phi_{app} \langle \|\mathbf{u}\| \rangle}{\phi_{app} \langle \|\mathbf{u}\| \rangle}$ the normalized and centralised velocity. The mean velocity is computed for the entire medium, including solid components where there is no flow.

As discussed later, the flow might decrease close to the boundaries. To mitigate these boundary effects and ensure accurate computation of the autocorrelation function, we focus on the central region of the medium, excluding the boundaries. Specifically, we consider the spatial domain defined by $0.05L_x < x < 0.95L_x$ and $0.15L_y < y < 0.85L_y$. It is particularly important to account for the boundary effects in the transverse flow, especially at low saturation levels, as we will see in a following section.

Furthermore, due to the presence of flow directionality along the x axis, the x and y directions are not equivalent in the velocity field. Consequently, we cannot compute the correlation function using the norm of the distance $\langle \|\mathbf{r}\| \rangle$. Instead, we separately analyze the correlation in two directions. We calculate $\zeta(x = 0, y) = \zeta_{x=0}(y)$ to examine the correlation in the direction transverse to the flow, and $\zeta(x, y = 0) = \zeta_{y=0}(x)$ to analyze the correlation in the direction of the flow. This approach allows us to capture and

differentiate the spatial correlation characteristics in each direction, accounting for the anisotropy of the velocity field.

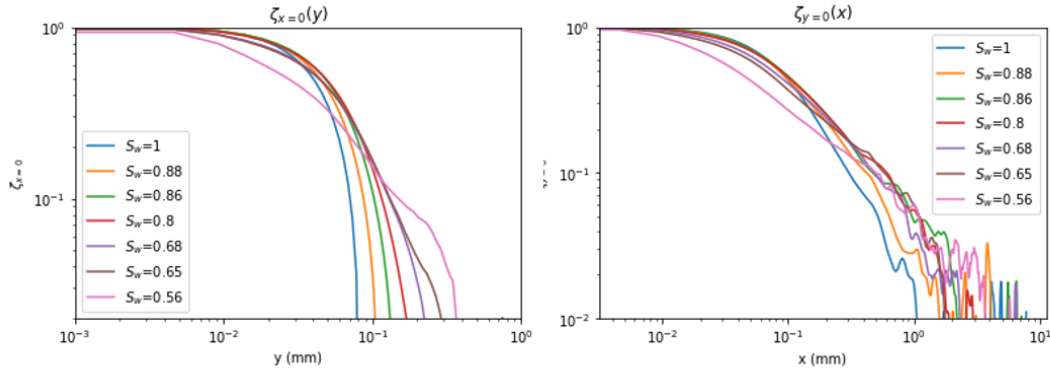


Figure 7.8 – Correlation function in the transverse direction $\zeta_{x=0}(y)$ (Left) and in the longitudinal direction $\zeta_{y=0}(x)$ (Right) for a selection of saturation values.

In Figure 7.8, we present the transversal and longitudinal correlation functions of the flow. The left side of the figure displays the transversal correlation function, while the right side shows the longitudinal correlation function. These functions are plotted for various saturation levels.

An important observation is that as the saturation decreases, the correlation function exhibits a slower decrease, indicating a longer-range spatial dependence. In other words, the correlation persists over greater distances at lower saturation levels. Comparing the transversal and longitudinal correlation functions, we notice a significant difference in correlation lengths. The correlation length in the longitudinal flow direction is greater compared to the transverse flow direction by approximately an order of magnitude. This indicates that the flow exhibits stronger spatial correlation along the direction of the flow compared to the transverse direction.

To quantify the characteristic correlation length, we introduce a threshold approach. We define a threshold value r_ζ such that the correlation function falls below these thresholds at specific distances ξ_x and ξ_y . We select a threshold value of $r_\zeta = 0.05$. Several methods, including exponential fitting and integral computation, were tested for length quantification, and the threshold method yielded the best results.

In Fig. 7.9, we present the evolution of the computed correlation length with saturation. The figure shows the characteristic correlation length for the transversal direction $\zeta_{x=0}(y)$ and the longitudinal direction $\zeta_{y=0}(x)$. In saturated conditions, the correlation length in the transverse direction is of the same order of magnitude than the pore size (0.1 mm). The correlation length globally increases as the saturation decreases, indicating that the spatial structures of the flow become more extended and exhibit larger characteristic lengths at lower saturation levels.

7.3.5 Conclusion

In this section, we examined various properties of flow in unsaturated porous media using our dataset of MPS-generated images with micromodel size. Here is a summary of our findings.

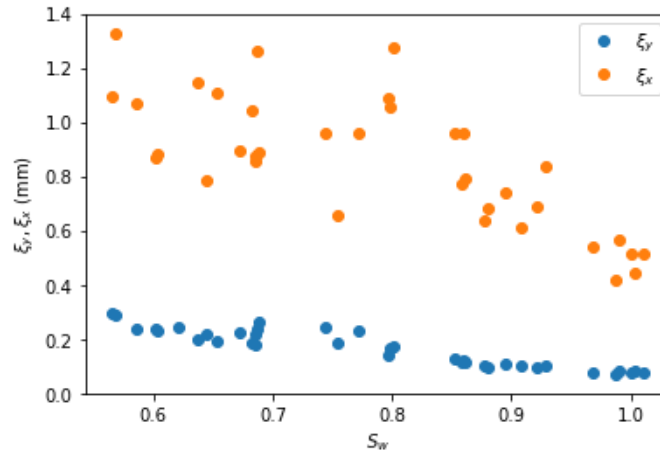


Figure 7.9 – Correlation characteristic length as a function of saturation in the transverse direction ξ_y for and in the longitudinal direction ξ_x for a threshold $r_\zeta = 0.05$.

Average Flow Properties We calculated the apparent permeability of the flow by considering air clusters as an additional solid phase, as they do not percolate or move in the flow. We related the apparent permeability to the apparent porosity, which is proportional to the saturation. The results showed that the apparent permeability decreases with decreasing saturation following a power law relationship $K_{app} = R\phi^{2.2}(S_w - S_{w,perc})^{2.2}$. This finding is consistent with existing models and experimental studies relating porosity and permeability.

Velocity Distribution We analyzed the velocity field distributions and observed that as the saturation decreases, the distribution widens significantly for low velocities, indicating the presence of dead ends in the medium. Additionally, high velocities are more prevalent in low-saturated media, indicating the emergence of preferential flow paths. The maximum velocities also increase with decreasing saturation, indicating that as the number of preferential paths decreases, the velocity within them increases by one order of magnitude compared to saturated conditions. Overall the flow heterogeneity increases, as quantified by the standard deviation of velocities, which increases threefold in low saturation compared to saturated conditions, and follows a power law $\sigma_u \propto S_w^{-1.9}$.

Tortuosity The heterogeneity of the flow is also spatial, as the pathways become more and more tortuous as the saturation decreases. We aimed to characterize the evolution of flow tortuosity with saturation. As mentioned in the experimental chapter, dead ends grow in size as saturation decreases, resulting in tortuous flow paths. We found that the tortuosity increases with decreasing saturation and could be described using apparent porosity. Our data fitted well with the logarithmic model commonly used in numerical and experimental studies.

Dead-ends and spatial correlation of the flow We investigated the emergence of dead ends by considering the cumulative area covered by regions with velocities below the lowest velocities observed in saturated conditions. We observed an exponential increase in the dead-end area with decreasing saturation. Furthermore, we examined the spatial

correlation of the flow to understand how it evolves with saturation. The transverse correlation length, which is perpendicular to the flow direction, was found to be of the order of the pore size in saturated conditions and increased as saturation decreased. In contrast, the longitudinal correlation length, aligned with the flow direction, was greater. These findings highlight the considerable evolution of spatial heterogeneity in the flow with saturation, including an exponential increase in the area occupied by dead ends, increased flow tortuosity, and enhanced spatial correlation of the velocity field.

In summary, our study reveals that as saturation decreases in unsaturated porous media, the flow exhibits widening velocity distributions, increased flow heterogeneity, higher flow tortuosity, and the emergence of dead ends and preferential flow paths. These changes are accompanied by a decrease in apparent permeability and an increase in the spatial correlation length of the flow. Overall, the flow properties undergo significant transformations with decreasing saturation, leading to more complex and heterogeneous flow patterns.

7.4 Dispersion in unsaturated porous media

7.4.1 Introduction

In this section, we investigate the effect of saturation on dispersion in porous media with numerical simulations. We perform Lattice-Boltzmann simulation for transport in the flow fields previously determined. The LBM method in unsaturated conditions, considering the second phase as solid, has been validated with experiments in the micromodel in saturated and unsaturated conditions. The flow fields have been computed beforehand and the properties of the flow, such as the velocity distribution, permeability and emergence of dead ends, have been studied in the previous section. We perform continuous tracer injections simulation in unsaturated porous media generated with the MPS method described in a previous chapter. Numerical simulations offer distinct advantages over the previously described transport experiments. They provide a completely neat initial concentration front, minimal noise⁵, and allow greater flexibility in parameter adjustments, such as the Peclet number. As a result, numerical transport simulations enable a more precise quantification of the evolution of the second moment and the nature of dispersion, whether it is Fickian or non-Fickian. Additionally, employing Lattice Boltzmann simulations in the MPS-generated images offers the advantage of generating a substantial number of different realizations. Furthermore, it provides flexibility in terms of the size of the porous medium being simulated. By utilizing numerical simulations, we gain the flexibility to explore a wider range of scenarios and parameters, providing a deeper understanding of dispersion phenomena in unsaturated porous media. This approach bridges the gap between experimental observations and theoretical analysis, allowing for more accurate insights into the complex dynamics of dispersion in porous media.

The first part of our study focuses on analyzing short-term dispersion by conducting simulations on a large number of realizations to ensure statistical relevance. We investigate dispersion patterns, such as dead ends and preferential paths. Additionally, we delve into the quantitative aspects by examining concentration profiles and the temporal evolution of the second moment. In our study, we examine the nature of dispersion in unsaturated porous media, specifically investigating whether the second moment exhibits a linear relationship with time or not, through a power law index. Furthermore, we conduct transport simulations for different values of the Peclet number (Pe) to understand its impact on

5. except for high Peclets for which numerical errors increase significantly

dispersion. Specifically, we explore whether higher Peclet numbers tend to lead to more non-Fickian dispersion due to increased advection.

In the second part of our study, we focus on investigating long-term dispersion using a selected set of MPS-generated images with larger dimensions. Similar to the short-term dispersion simulations, we perform simulations for different saturations and Peclet numbers. However, due to the computational cost associated with Lattice Boltzmann simulations in longer media, the number of realizations is limited. Nonetheless, this allows us to examine whether the results obtained for short dispersion are indicative of a short transient regime or if they are representative of longer dispersion behavior.

By analyzing these results, we aim to gain deeper insights into the nature of dispersion in unsaturated porous media, particularly characterizing the dependence of dispersion on saturation. This understanding contributes to a better characterization of transport processes in such porous media environments.

7.4.2 Methodology

Parameter range

We conducted Lattice Boltzmann Method (LBM) simulations on Multi-Point Statistics (MPS) generated images, encompassing the entire saturation range of $[0.5, 1]$. Additionally, we explored a range of achievable Peclet numbers, with high values limited by numerical stability and low values limited by computation time. The Peclet number is computed as

$$Pe = \frac{\langle \|\mathbf{u}\| \rangle d_{\text{pore}}}{D_m} \quad (7.4.1)$$

with $\langle \|\mathbf{u}\| \rangle$ the mean interstitial velocity, d_{pore} the mean pore diameter of the saturated medium and D_m the diffusion coefficient. In order to control the Peclet number, we adjusted both the mean velocity $\langle \|\mathbf{u}\| \rangle$ and the molecular diffusion coefficient D_m . Indeed, due to numerical constraints, we were unable to maintain the same flow velocity while varying only D_m across all simulations. As a result, both the diffusion coefficient and flow velocity had to be modified for the LBM simulations to function properly. We perform LBM simulation on MPS generated images, covering the range of saturation $[0.5, 1]$, and we also explore a range of Peclet number that could be achieved $Pe \in [0.01, 1000]$, but limited in high values by simulation errors and in low values by computation time.

Transport analysis

In our simulations, we obtain concentration fields over time. We analyze these fields by calculating longitudinal concentration profiles and computing spatial moments of the concentration profile at different time points. The moments analysis is described thoroughly in the Chapter 3, section 3.2.2.

The evolution of the first moment over time provides information on the mean position of the front in the micromodel. To determine the velocity of the front, we perform linear regression on the first moment data to calculate its slope. The second moments indicate the spreading of the front. To account for potential non-Fickian dispersion, we examine the slope of the second moment evolution over time using a logarithmic scale. By considering a power law relationship for the second moment, denoted by $\sigma^2(t) \propto t^\alpha$, we can assess the nature of dispersion. If the power law index α is close to one, the dispersion can be considered Fickian; otherwise, it is non-Fickian. It is worth noting that computing a

dispersion coefficient becomes problematic when the second moment exhibits a power law behavior with $\alpha \neq 1$ as it would be time dependent. Therefore, we introduce a fractional dispersion coefficient D_α^{frac} that allows us to represent the best fit of the second moment using a power law with a power law index of α .

$$\sigma_{fit}^2(t) = D_\alpha^{\text{frac}} t^\alpha \quad (7.4.2)$$

However, fractional dispersion coefficients are difficult to compare if the value of α is not constant (the unit, in $\text{cm}^2 \cdot \text{s}^{-\alpha}$ depends on α). Therefore, α has to be fixed to allow a comparison. Furthermore, note that the fractional dispersion coefficient coincides with the dispersion coefficient for $\alpha = 1$, $D = \frac{1}{2} D_{\alpha=1}^{\text{frac}}$. In some cases, notably when considering different Peclet numbers, fractional dispersion coefficients are not longer suited for the analysis, as they cannot be compared to existing literature, and the fractional unit hinders simple normalization. In these cases, we rather compute dispersion coefficients instead.

7.4.3 Qualitative observations

To begin, in order to understand the impact of saturation on dispersion, we examine the concentration fields for various saturation values. Fig. 7.10 displays the simulation results for four chosen saturation levels. The figure illustrates the concentration fields at three consecutive positions of the concentration front.

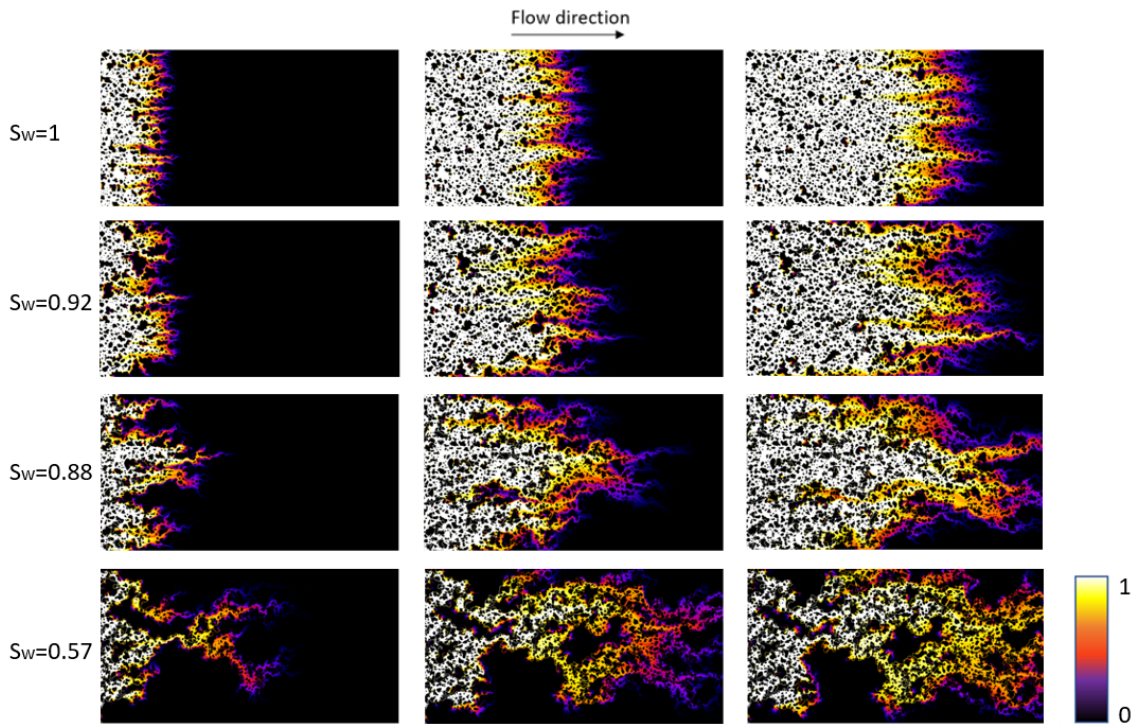


Figure 7.10 – Effect of saturation on transport. Concentration fields for 4 saturations values and three mean positions of the concentration front ($\mu_0 = 0.18L_x$, $\mu_1 = 0.43L_x$, $\mu_2 = 0.65L_x$).

Similar to the findings from experimental results, the concentration front appears relatively homogeneous in the case of highest saturation. However, as the saturation diminishes, the concentration front spreads out and the dispersion patterns undergo a change.

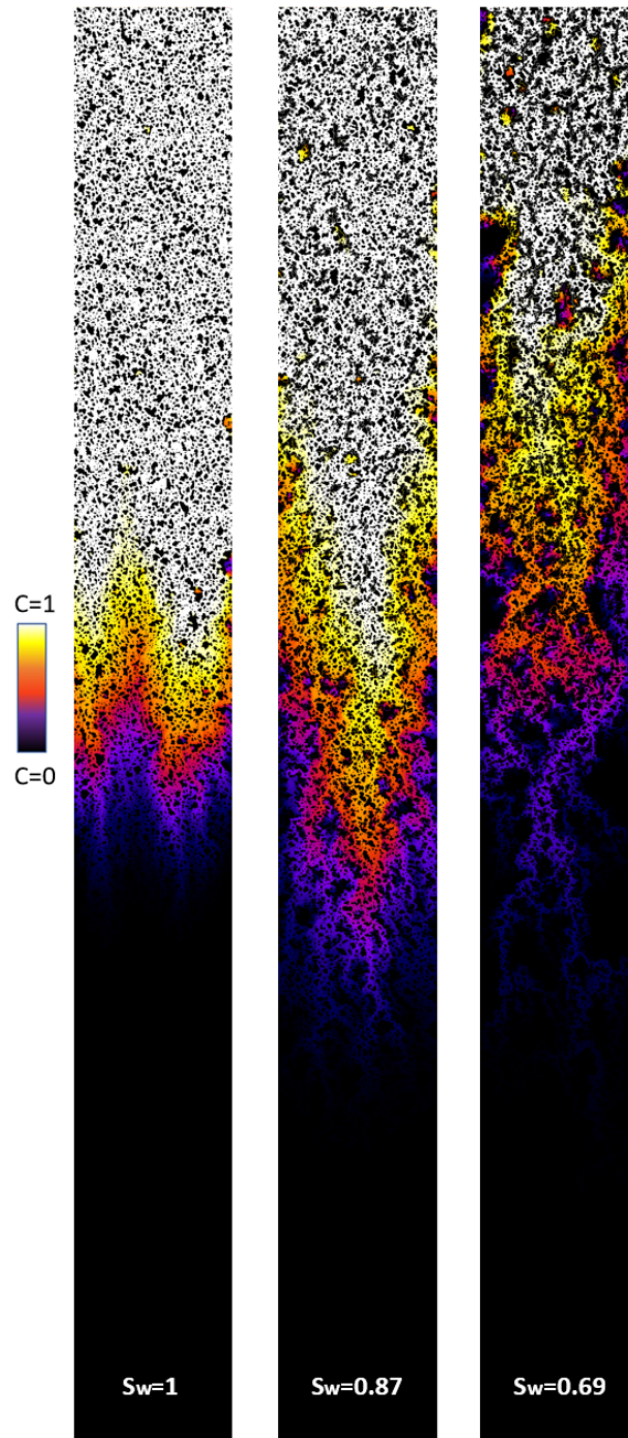


Figure 7.11 – Effect of saturation on long time dispersion. Concentration fields for 3 saturations values, the concentration has been normalized by the tracer concentration.

Specifically, we observe distinct preferential paths that gain prominence in intensity while decreasing in number as saturation decreases. In the saturated case, there are no dead ends, as the concentration rapidly reaches the tracer concentration after the passage of the front. Nevertheless, as saturation decreases, dead ends start to emerge, growing in

size with further reductions in saturation. In the case of minimal saturation, dead ends become a substantial portion of the concentration field. Even after the front has passed, there remain extensive areas with a concentration close to zero. Overall, the dispersion patterns, including both preferential paths and dead ends, significantly expand in size as saturation decreases.

Fig. 7.11 displays the concentration fields for three different saturations in the context of long time dispersion. Similar observations to those in the case of short time dispersion can be made. Notably, in the low saturated scenario, the dead ends remain unfilled with concentration even for long time dispersion. However, the influence of the lateral borders becomes more pronounced in the long images, particularly for low saturations. We will delve into quantifying this border effect on dispersion in a later section.

7.4.4 Short time dispersion: spatial moments of the dispersion

Concentration profiles

To quantify the dispersion properties, we aim to compute spatial moments, specifically by examining the longitudinal profiles of the concentration profiles across our entire dataset. Fig. 7.12 displays the concentration front at successive times for selected saturation values. Here and in the following, for a same Peclet number, the time is multiplied by a corrective term so that the longitudinal interstitial velocity would be the same when comparing different simulations⁶.

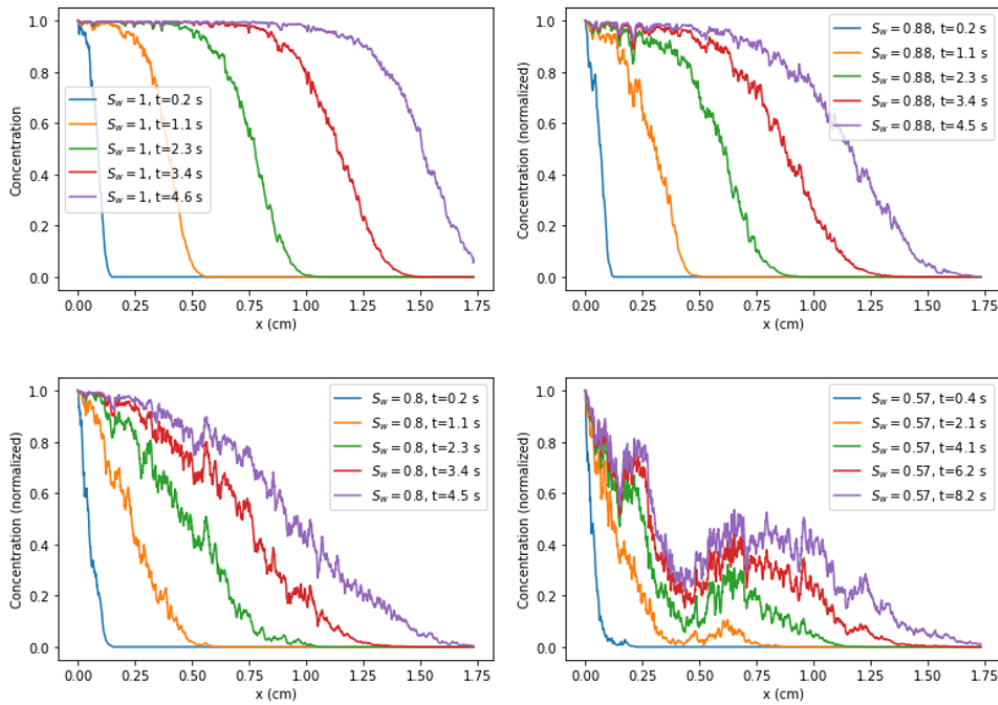


Figure 7.12 – Concentration profiles for different time and saturation values.

6. For a given Peclet, the simulation were computed so that the Darcy velocities would be equal. With the change of saturation and tortuosity, the longitudinal interstitial velocity (ruling the transport velocity) is not the exactly the same. Therefore, to able a comparison, we correct the time such that $t_{si} = t_{si}^{num} \frac{\langle u_x \rangle}{\langle u_{x,ref} \rangle}$. $u_{x,ref}$ is a selected reference velocity from a simulation conducted under saturated conditions at the given Peclet.

As the saturation decreases, we observe that the concentration profiles become more spread out, and they exhibit higher levels of noise. Additionally, in certain cases, the concentration profiles may not be on average monotonous. This occurs when there are large dead ends at specific positions in the image, as shown in Fig. 7.12. In such instances, the local concentration can be smaller than the concentration further ahead.

It is important to note that differentiating the concentration profiles to study transport properties, particularly for moments computation, becomes impractical at low saturation levels. Consequently, it is necessary to compute moments through integration by parts to overcome this limitation (cf Chapter 3, section 3.2.2).

First moment of the concentration: front velocity

Firstly, we compute the first moment as a function of time. Fig 7.13 (Left) presents the evolution of the first moment over time for different saturations. It is evident that the first moment exhibits a linear relationship with time across all cases. The slope of the first moment remains the same for the different saturations. To quantify this observation, we perform linear regression analysis on the first moment for all our dataset. For each fit, we obtain a regression coefficient greater than 0.9999. The slope of the regression line indicates the velocity of the front.

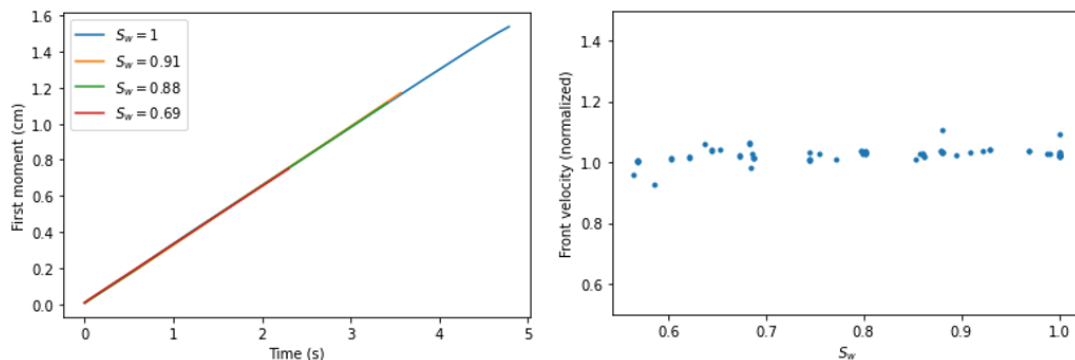


Figure 7.13 – Influence of saturation on the front velocity. (Left) First moment as a function of time for different saturations values. (Right) Normalized front velocity (slope of the first moment normalized by the longitudinal interstitial velocity $\langle u_x \rangle$) as a function of saturation S_w for all the Peclet number range $Pe \in [0.1, 1000]$.

In Fig. 7.13 (Right), we display the velocity of the front normalized by the interstitial velocity $\langle u_x \rangle$. Since no significant effect was observed with respect to the Peclet number, we represent all the data collectively, without distinguishing the different Peclet numbers. As it could be expected, the front velocity matches with the interstitial velocity, and there is no significant effect of the saturation. In a sense, this result could be surprising for low saturations and high Peclet number, for which large dead ends are observed in the velocity field. Indeed, in the MIM model (cf Chapter 2, section 2.2), which takes into account the presence of dead-ends in the flow, the front velocity depends on the percentage of dead ends in the flow field.

Influence of saturation on the second moment

We consider the evolution of the second moment with time for different water saturation. Fig. 7.14 (Left) illustrates the second moment for a selection of saturations. Firstly, it is evident that the amplitude of the second moment increases as the saturation

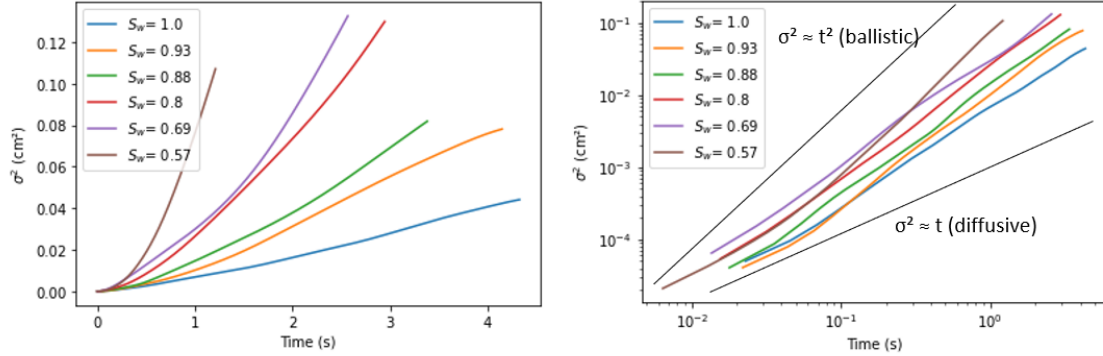


Figure 7.14 – Influence of saturation on dispersion: second moment as a function of time for different saturation values, $Pe=100$. (Left) Linear scale. (Right) Logarithmic scale.

decreases. This indicates a significant increase in dispersion with decreasing saturation. Furthermore, the second moment does not exhibit a linear relationship with time, particularly noticeable for low saturation values. Fig. 7.14 (Right) presents the second moments on a logarithmic scale. After a transient time, they are represented by rather straight lines indicating a power law behavior. The slope is greater than one, emphasizing that the second moment is not proportional to time. This observation holds true even for fully saturated conditions. The slope ranges between 1 (diffusive behavior) and 2 (ballistic behavior). Additionally, the slope seems to be closer to 2 in low saturation conditions.

Therefore, dispersion exhibits non-Fickian behavior under these conditions. Dispersion is increased in unsaturated conditions, and the non-Fickian character (reflected in the power-law index) may depend on the saturation level.

Non-Fickian dispersion: Computation of the power law index

To quantify the non-Fickian behavior, we measure the slope of the second moment on a logarithmic scale. Fig. 7.15 provides an example (for $S_w = 0.8$) of a second moment plot and the linear regression performed on a logarithmic scale. We optimize the fit by considering the appropriate time range for the regression, ensuring an regression coefficient above 0.9985 for the entire dataset. The value of $\alpha = 1.49$ in this example confirms non-Fickian dispersion.

Power law index as a function of saturation

Fig. 7.16 shows the power law index α as a function of saturation. The values of α range between 1 and 2 across the dataset. The mean value of α is 1.49 with a standard deviation of 0.21. This indicates a statistical dispersion in the data. However, there is a slight decreasing trend when the saturation increases. We fit a linear trend of $\alpha = -0.9S_w + 2.7$, with a regression coefficient of $r^2 = 0.59$. We observe that dispersion is non-Fickian even in saturated conditions. To determine if this trend is statistically significant, we calculate the

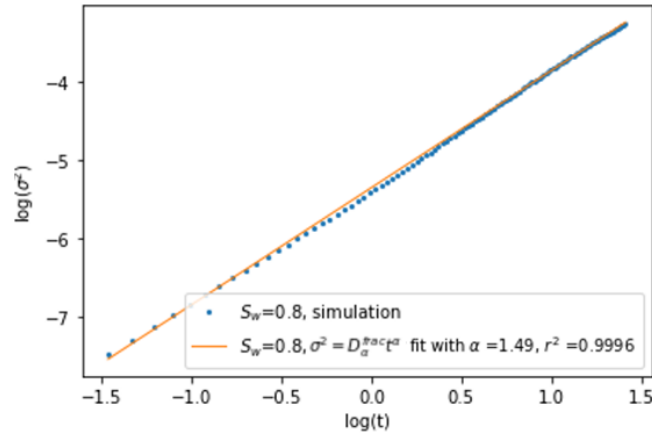


Figure 7.15 – Example of fit used to determine the power law index α , $S_w = 0.8$, and $Pe=100$.

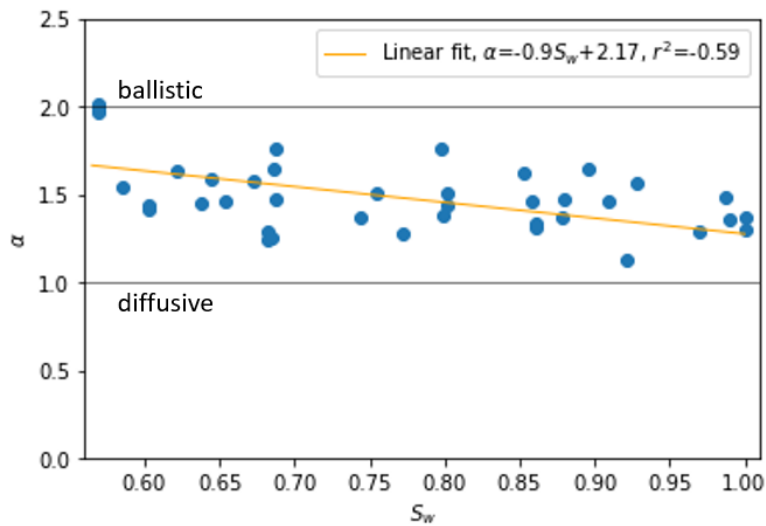


Figure 7.16 – Power law index as a function of saturation S_w . $Pe=100$.

Pearson correlation coefficient⁷. The correlation coefficient is found to be 0.47, indicating a moderate correlation between the data (where 0 represents no correlation and 1 represents complete correlation). The p-value (0.0025) is significantly smaller than 0.05. Therefore, the trend indicating a dependence of α on saturation is statistically relevant, despite the weak correlation due to the strong statistical dispersion in the data.

In conclusion, the dispersion behavior observed for $Pe=100$ in the study is predominantly non-Fickian, with a mean power law index α of 1.5. The dispersion exhibits a range of behaviors, including diffusive (α close to 1) and ballistic (α close to 2) in the most extreme cases. Additionally, as the saturation decreases, there is a trend for α to increase, indicating a stronger departure from Fickian behavior and a more pronounced non-Fickian character of dispersion in unsaturated conditions.

7. The Pearson correlation coefficient is a correlation coefficient measuring linear correlation between two sets of data. It is the ratio between the covariance of two variables and the product of their standard deviations.

In 2D regular structures, they observed a transition from Fickian to non-Fickian with decreasing water saturation ([163]). 3D transport experiments using RMN imaging in homogeneous rock with various degrees of saturation ([73]) show non-Fickian dispersion even in saturated conditions, with a non-Fickian character enhanced by lower saturations. Our results are therefore representative of a general tendency and most likely not constraint to the geometry of the porous media.

Fractional dispersion coefficient

Here, the objective is to quantify the amplitude of dispersion. However, we observed non-Fickian dispersion ($\sigma^2 \propto t^\alpha$, with $\alpha \neq 1$), therefore computing dispersion coefficients is not judicious and we compute fractional dispersion coefficients. Nonetheless, the power law index is not constant for the whole dataset, and fractional dispersion coefficients cannot be compared for different α values. Thus, to able a comparison, we take the medium value $\alpha = 1.5$ for computing a comparable fractional dispersion coefficients $D_{1.5}^{\text{frac}}$. We perform a power law fit such that

$$\alpha_{fit} = D_{1.5}^{\text{frac}} t^{1.5} \tag{7.4.3}$$

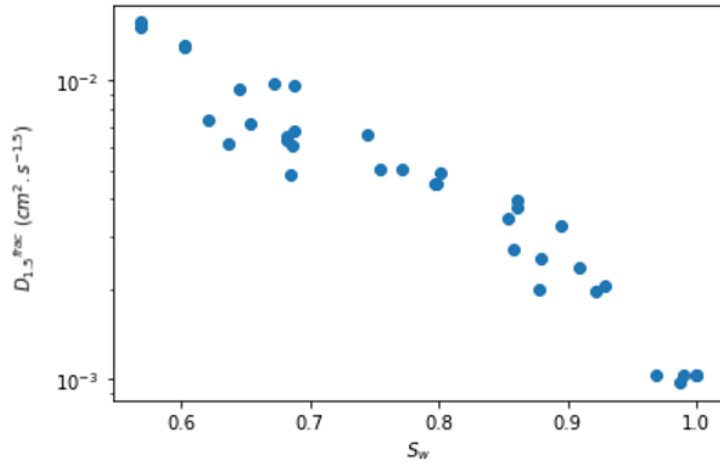


Figure 7.17 – Fractional dispersion coefficient as a function of saturation S_w ($Pe=100$), $\alpha = 1.5$.

Fig.7.17 illustrates the fractional dispersion coefficient as a function of saturation. It is observed that the fractional dispersion coefficient increases significantly as the saturation decreases, reaching more than ten times the value observed in saturated conditions. There is more statistical fluctuation in the data for low saturations. This can be attributed to two factors: first, the real power law index (α) tends to be higher than the average value of 1.5 in these cases, indicating a stronger departure from Fickian behavior; second, the representative elementary volume (REV) may increase with heterogeneity and may approach the size of the medium, leading to greater statistical variability in the data.

In summary, the dispersion exhibits non-Fickian behavior for this Pe in both saturated and unsaturated conditions for the considered parameters. Therefore, we are very likely characterizing a transient. Furthermore, the non-Fickian character, as represented by the power law index (α), tends to increase as the saturation decreases. Dispersion is

significantly enhanced in unsaturated conditions, with the fractional dispersion coefficient reaching up to ten times the value observed in saturated conditions.

7.4.5 Short time dispersion: Effect of the Peclet number

We also examined the influence of Peclet number on the dispersion properties, which represents the interplay between diffusion and advection. In this section, we explore the impact of Peclet numbers on dispersion characteristics at various saturations. Specifically, we examine the changes in second moments for different saturations and Peclet numbers, calculating the power law index α and dispersion coefficient.

Qualitative observations

Fig. 7.18 illustrates concentration fields at the same position of the front for various saturations as the Peclet number increases.

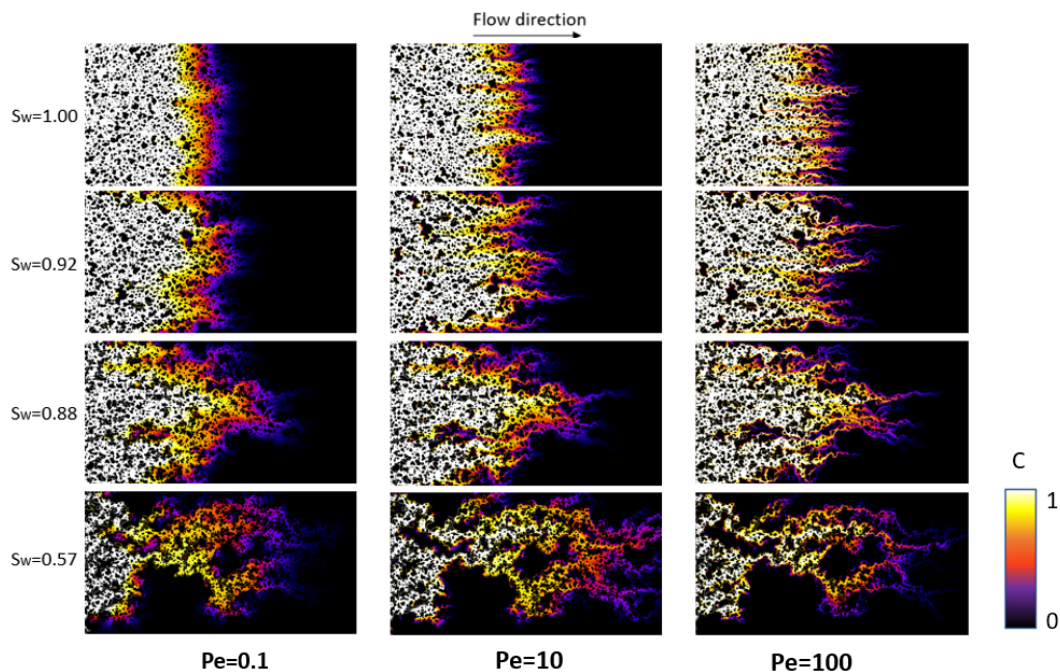


Figure 7.18 – Effect of Peclet number on transport for different saturation. Concentration fields for 4 saturation values. For each saturation, a concentration field for three Pe values is shown.

In the case of saturation being at its highest, we observe that the concentration front spreads further with increasing Peclet number. Additionally, there is a notable appearance of channeling patterns, which are less present at low Pe values. Even for saturation values close to 1, the channeling effect and front spreading are evident at high Peclet numbers.

However, as the saturation decreases, the impact of Peclet number becomes less distinct. The diffusion is not able to smooth the distortion of the front caused by the heterogeneity. For medium and low saturation levels, the Peclet number mainly accentuates the contrast between preferential paths and dead ends.

In highly saturated case, two distinct preferential paths observed at high Pe can coalesce and become one at low Pe due to greater diffusion. However, at low saturation, the typical distance between the preferential paths is too large to result on mixing at low Peclet numbers and the main shape of the concentration front remains similar.

Saturated case

While the dispersion may not be Fickian, we consider dispersion coefficient in the following, and not fractional dispersion coefficient. This decision was made to facilitate a straightforward comparison of our results with classical findings from the literature. Moreover, comparing fractional dispersion coefficients with different Pe values can prove to be quite challenging and may introduce complexities in the analysis⁸. First, we examine the impact of the Peclet number in a saturated medium. Fig. 7.19 illustrates how the Peclet number influences the power law index α . α , which indicates the Fickian or non-

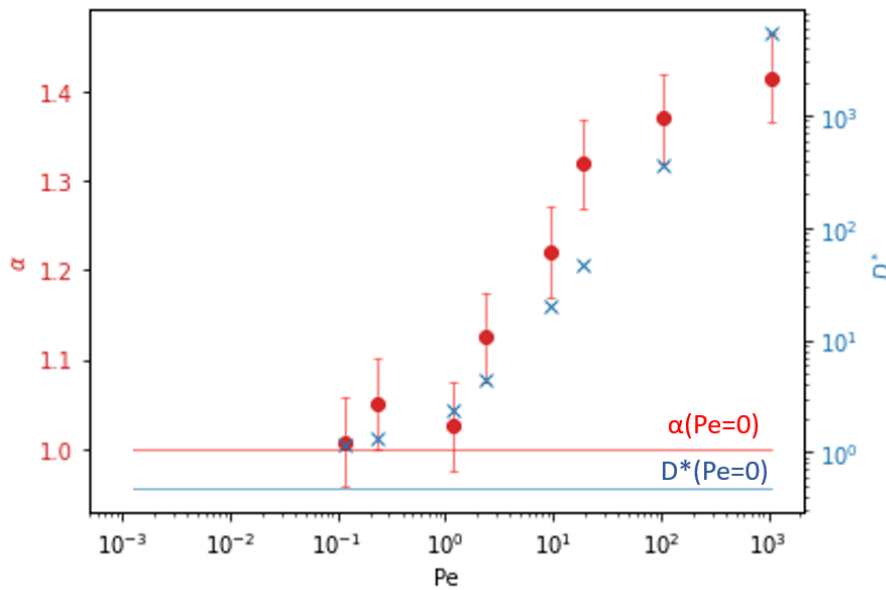


Figure 7.19 – Evolution of the power law index α and the normalized dispersion coefficient D^* with the Peclet number, $S_w = 1$. The red and blue lines indicate the value for the simulation realized at $Pe=0$, for α (red) and D^* (blue).

Fickian nature of dispersion, is greater than 1 at high Pe values ($\alpha \sim 1.4$) and decreases as the Peclet number decreases. Remarkably, it approaches 1 when the Peclet number is less than 1. In other words, dispersion exhibits non-Fickian behavior at high Peclet numbers and becomes more Fickian as the Peclet number decreases.

Literature thoroughly studied the effect of Peclet number on the dispersion coefficient, as detailed in the bibliography Chapter 2, section 2.1.3. To able a comparison with results from the literature, we computed the normalized dispersion coefficient $D^* = \frac{D_{disp}}{D_m}$ as a function of the Peclet number. It implies that we impose $\alpha = 1$ when fitting the second moment (D^* is computed by linear regression of the second moment). In Fig. 7.19, for

8. When varying the Pe , we change the value of D_m . To quantify dispersion we need to normalize the dispersion coefficient by D_m ($cm^2.s^{-1}$). However, in the case of the fractional dispersion coefficient, the unit is fractional ($cm^2.s^{-\alpha}$) and depends on α , normalization proves to be quite complex, preventing an accurate comparison of the results.

high Peclet values, the dispersion coefficient is approximately proportional to the Peclet number. As the Peclet number decreases, the normalized dispersion coefficient slowly converges to a constant value close to 1.

This relationship with the Peclet number has been observed in saturated condition by several authors [124] [55] [115]. The regime in which the dispersion coefficient is not Peclet dependant is commonly referred to as the diffusive regime. On the other hand, the regime where the normalized dispersion coefficient D^* is proportional to the Peclet number is dominated by advection.

The simultaneous dependence of α and D^* on the Peclet number suggests that dispersion in a saturated medium is Fickian in the diffusive regime as it would be expected. For high Peclet numbers, the dispersion is completely dominated by advection and the transport is non-Fickian. The non-Fickian character slowly decreases with decreasing the Peclet number as diffusion becomes more effective (but dispersion is still dominated by advection; ($Pe > 10, D^* > 100$)). When diffusion and advection have the same order of magnitude ($Pe \in [1,10]$ and $D^* \in [1,10]$), α sharply decreases towards 1 (Fickian transport). It is worth noting that the value of the normalized dispersion coefficient provides an indication of the diffusive tortuosity in the saturated medium, given by the relationship $D_{disp} = \frac{D_m}{\tau_d}$ for low Peclet numbers. For instance, it yields a diffusive tortuosity value of $\tau_{d,S_w=1} = 2.15$.

The Influence of Saturation on the Peclet Number's Effect

We now examine the influence of the Peclet number for different saturations. Fig. 7.20 (Left) displays how the exponent α changes as the Peclet number varies.

For all saturations, we observe a similar trend with the Peclet number as in the saturated case. Namely, there is a transition from Fickian behaviour at low Pe ($\alpha = 1$) to non-Fickian behaviour at higher Pe ($\alpha \approx 1.5$ in this case). However, we note that the Pe value of the transition depends on the saturation, with the transition occurring at lower Pe when the saturation is lower. For example, the transition in the saturated case happens for a Peclet value around 5, whereas the transition occurs at $Pe \approx 0.05$ for the lower saturation ($S_w = 0.69$).

Now, we examine the normalized dispersion coefficient D^* as a function of the Peclet number, shown in Fig. 7.20 (Right). Similarly to the saturated case, the dispersion coefficient increases with saturation. However, as the saturation decreases, the dispersion coefficient begins to increase at lower values of the Peclet number. For a given Pe , the dispersion coefficient is therefore higher at lower saturation. Furthermore, the regime for which the dispersion coefficient is rather constant with the Peclet; known as the diffusive regime; occurs at lower Peclet for lower saturations. Typically, it becomes rather constant for $Pe \approx 1$ in saturated conditions and $Pe \approx 0.01$ for the lower saturation ($S_w = 0.69$). Interestingly, the transition between the diffusion regime and a regime for which advection becomes effective in the dispersion (i.e. D^* depends on the Peclet) occurs at a Peclet of the same order of magnitude (slightly smaller) than for the transition between Fickian and not Fickian observed for the power law index α .

Note that the value of D^* in purely diffusive conditions ($Pe = 0$, straight line in Fig. 7.20 (Right)) decreases with reducing saturation: the diffusive tortuosity of the medium thus rises with saturation.

For all saturation cases, D^* increases with the Peclet number. For the low and medium saturations, it increases proportionally with the Peclet indicating an advective regime. For a saturation close to 1 (e.g $S_w = 0.88$), it starts decreasing more slowly as Pe decreases,

indicating the transition towards a diffusive regime for lower Peclet values. Therefore, as saturation decreases, dispersion is more dominated by advection which leads to non-Fickian dispersion for a larger range of Peclet $[Pe_{S_w}, +\infty]$.

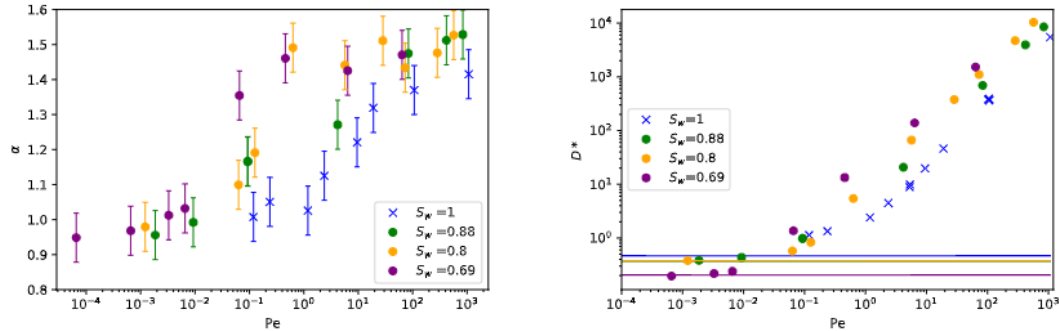


Figure 7.20 – (Left) For different saturations, evolution of the power law index α with the Peclet number. (Right) For different saturations, evolution of the normalized dispersion coefficient D^* with the Peclet number. The continuous lines show values of $D^*(Pe = 0)$ obtained from simulations with no flow.

Fig. 7.21 shows the evolution of α with saturation values for a larger number of realizations. It confirms the results given by the Fig. 7.20. For high values of Peclet number (e.g $Pe = 1000$), advection dominates transport and dispersion is non-Fickian, even for the saturated case, which leads to a power law index α being relatively constant with saturation. For low Peclet number values (e.g $Pe=1$), we observe that α increases as saturation decreases. Indeed, the dispersion is still dominated by advection and is non Fickian for low saturations; but for high saturation values, diffusion is more effective, and therefore dispersion is closer to Fickian. In other words, the correlation between α and S_w depends on the Peclet number.

For our statistical study with a large number of realizations on the influence of α with saturation, we used an intermediate Peclet number value ($Pe = 100$). Therefore, a moderate correlation is observed, as dispersion in low saturation is completely advective and non Fickian, whereas dispersion in both the saturated and moderately unsaturated cases is only weakly influenced by diffusion and also exhibit a non-Fickian character, although in average weaker than for the low saturations values. In hindsight, conducting this study with a smaller Peclet number value would have been more relevant.

Overall, we can describe the dependency of α as

$$\begin{cases} \alpha(Pe, Pe_{S_w}) \rightarrow 1 \text{ for } Pe \ll Pe_{S_w}, \\ \alpha(Pe, Pe_{S_w}) \rightarrow \alpha_{\text{advection}} \text{ for } Pe \gg Pe_{S_w}. \end{cases} \quad (7.4.4)$$

with Pe_{S_w} the threshold Peclet number separating the diffusion and advection regime, that decreases with decreasing saturation. For the saturated case, this threshold can be estimated to $Pe_{S_w=1} = 5$, whereas it is inferior in unsaturated conditions. It can be estimated to $Pe_{S_w=0.88} = 0.5$, $Pe_{S_w=0.8} = 0.1$, and $Pe_{S_w=0.69} = 0.05$.

7.4.6 Long time dispersion

To characterize long time dispersion, we extended our analysis to include larger images. This approach was particularly important for low saturations, where analyzing dispersion

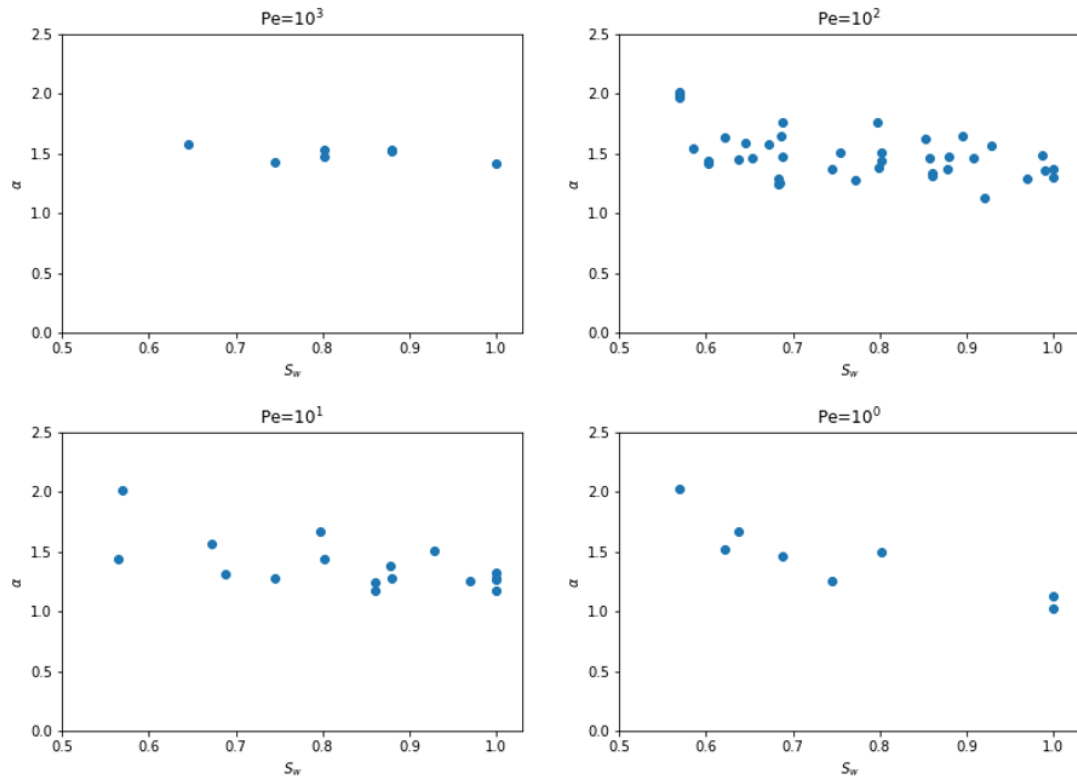


Figure 7.21 – Evolution of the power law index α with the saturation for different Peclet numbers.

in images of the micromodel size is limited due to the highly heterogeneous front and rapid tracer movement, resulting in a short transient observation. By observing long time dispersion, we can confirm whether the tendencies observed for short-time dispersion are comparable and not solely dependent on initial properties. This enables us to gain a more comprehensive understanding of the overall dispersion behavior.

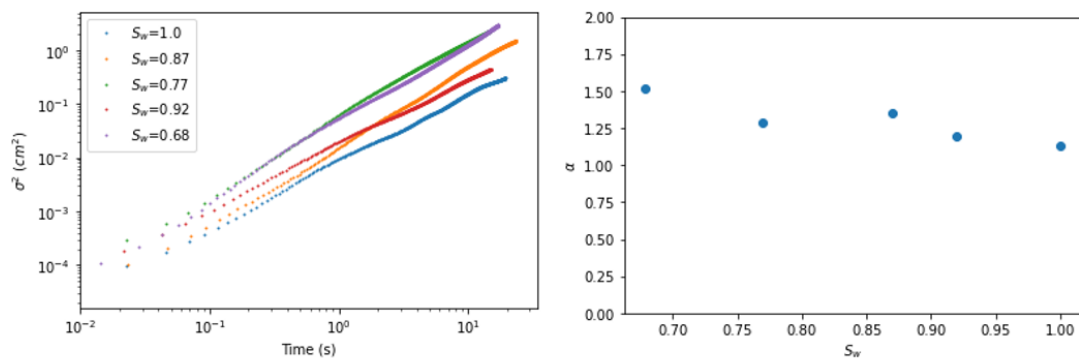


Figure 7.22 – (Left) Evolution of the second moment with time for different saturations. (Right) Power law index α as a function of the saturation S_w . $Pe=5$.

Fig. 7.22 (Left) shows the evolution of the second moment as a function of time for different saturation. As observed for short time dispersion, the second moments exhibit a

power law behavior. The slope is different from 1, proving non Fickian behavior, especially for low saturations. Indeed, as Fig. 7.22 (Right) shows, the power law index α tends to increase when the saturation decreases, as it was observed for short time dispersion.

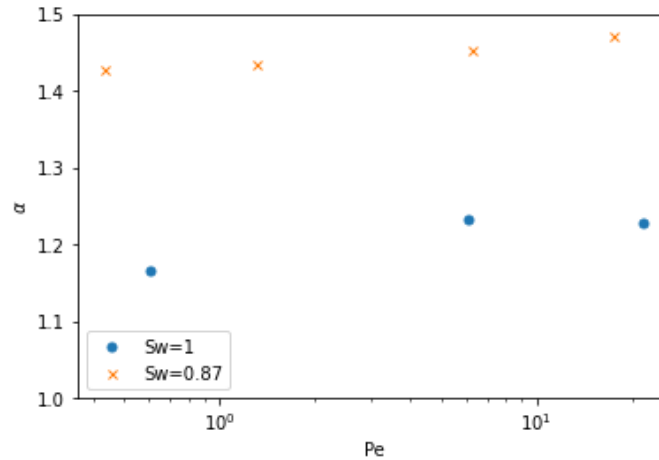


Figure 7.23 – Evolution of the power law index with the Peclet number in the saturated case and for $S_w = 0.87$.

Fig. 7.23 depicts the variation of the power law index as a function of the Peclet number. The range of Peclet number values we could explore was severely restricted due to extremely long computation times for low Peclet numbers and numerical stability issues for high Peclet numbers.

Nonetheless, we observed a consistent decrease in the power law coefficient α with increasing Peclet numbers, reaffirming the findings from our previous analysis. Despite the limitations in the Peclet number range studied, this trend reinforces our earlier observations regarding the relationship between dispersion behavior and the Peclet number.

To conclude, the long-time simulations we performed do not allow to observe a transition to an asymptotic Fickian regime. The transient, i.e. non Fickian dispersion, could be extremely long, and the medium is still too short to observe it. The computational cost for longer media is too high to consider this method to observe asymptotic dispersion.

7.4.7 Conclusion

This study, conducted on a large number of realizations, has provided valuable insights into short-time dispersion in unsaturated porous media. The key findings can be summarized as follows:

- Firstly, the evolution of the second moments over time indicates that transport is non-Fickian over a wide range of Peclet number values, in both saturated and unsaturated conditions. Therefore, we are characterizing a transient. The mean value of the power law index α is found to be close to 1.5, but with a substantial statistical variance among the data.
- The dispersion, characterized by the fractional dispersion coefficient D_α^{frac} associated with $\alpha = 1.5$, reveals a significant increase in dispersion as the saturation decreases.
- For saturated and moderately unsaturated porous media, dispersion becomes Fickian as the Peclet number decreases. Interestingly, the transition between Fickian and

non-Fickian is rather sharp, with a threshold Peclet number that depends on the saturation Pe_{S_w} .

- The dependence of the normalized dispersion coefficient with the Peclet number shows that the transition between non-Fickian and Fickian regime happens when diffusion is more effective in the dispersion.
- Moreover, the Peclet number Pe_{S_w} at which dispersion becomes Fickian decreases with decreasing saturation. The advective regime covers a broader range of Peclet numbers in the unsaturated case. In situations of low saturation, the diffusion regime is not observed within the range of Peclet number values considered, and transport remains non-Fickian, with α values relatively constant over the considered Peclet number range.

Thus, the dependence of the Fickian regime with Peclet number depends on the saturation, and the power law index α increases as the saturation decreases for low Peclet number values. This is because transport at low saturation is predominantly advective, while at high saturation diffusion is more effective. Conversely, for high Peclet number values, transport remains advective even in the saturated case, and no correlation is observed between the power law index α and the saturation.

7.5 Quantification of the boundary effect on flow and transport

7.5.1 Motivation

When looking at the concentration fields Fig. 7.10, it seems that the concentration fronts are not perfectly flat with a slight curvature near the borders. When examining dispersion in a medium with a finite width, we should observe both inherent dispersion resulting from the medium's properties, as well as an additional dispersion caused by the borders of the medium. The existence of boundaries or borders within a medium introduces additional resistance and modifies the complexity of the flow path, resulting in decreased velocities at the outer edges of the medium. This is because the presence of borders creates obstructions and constrains the movement of fluid, causing the flow to take a more convoluted and elongated route, known as tortuosity. As a result, the overall velocities near the lateral extremities of the medium are reduced compared to the velocities within the central regions. A lateral gradient of the velocity could change the dispersion, as it is observed in Taylor dispersion in a channel. In our simulation, we implemented a no-slip condition for the grains, meaning that the fluid velocity at the surface of the grains is assumed to be zero. However, we employed free-slip conditions for the borders or boundaries of the system. This choice was made to minimize the boundary effect.

Our objective is to evaluate the impact of boundaries on flow and transport phenomena and determine whether the width of the micromodel is sufficient to represent and study transport accurately. Additionally, we aim to quantify the distance from the wall at which the effects of the boundaries become negligible.

To conduct our study, we employ the following method: firstly, we utilize the MPS algorithm to generate a large unsaturated porous medium using a training image obtained from our experimental data set. For this purpose, we select a saturation value of $S_w = 0.82$. The size of the generated medium is set to $L_y = L_x = 3780$ pixels (1.73 cm). From the newly created image, we extract five additional images with increasing widths: $L_{y1} = 360$,

$L_{y2} = 900$, $L_{y3} = 1800$, $L_{y4} = 2700$, and $L_{y5} = 3780$ pixels. These images have the same length of $L_x = 3780$ pixels. Fig. 7.24 illustrates the original generated image and the set of images with different widths extracted from it. Next, we perform Lattice Boltzmann

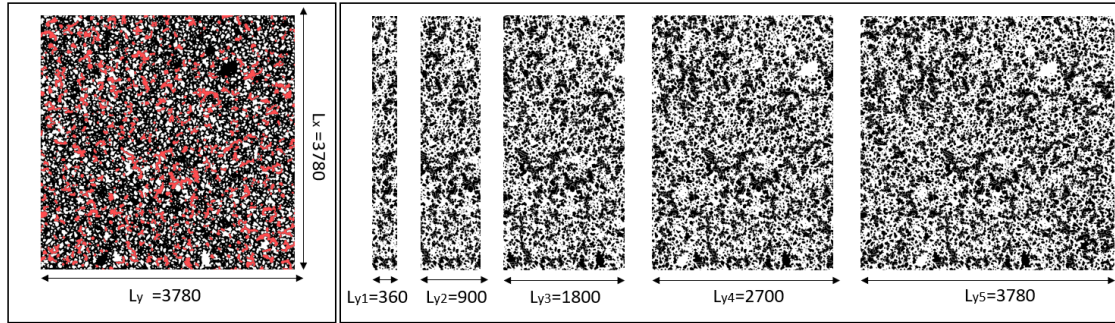


Figure 7.24 – Set of images created to study the effect of the width. (Left) Unsaturated image generated with the MPS algorithm. White: grains. Red: gas. Black: water. (Right) Images extracted from the MPS generated image with different widths L_y , indicated in pixels. Images have been binarized to compute the flow with LBM. Black: solid. White: Void.

Method (LBM) simulations for flow and transport in each of the five extracted images. By simulating the flow and transport processes, we obtain steady-state velocity fields as well as concentration fields over time.

7.5.2 Effect of the medium width on the flow properties

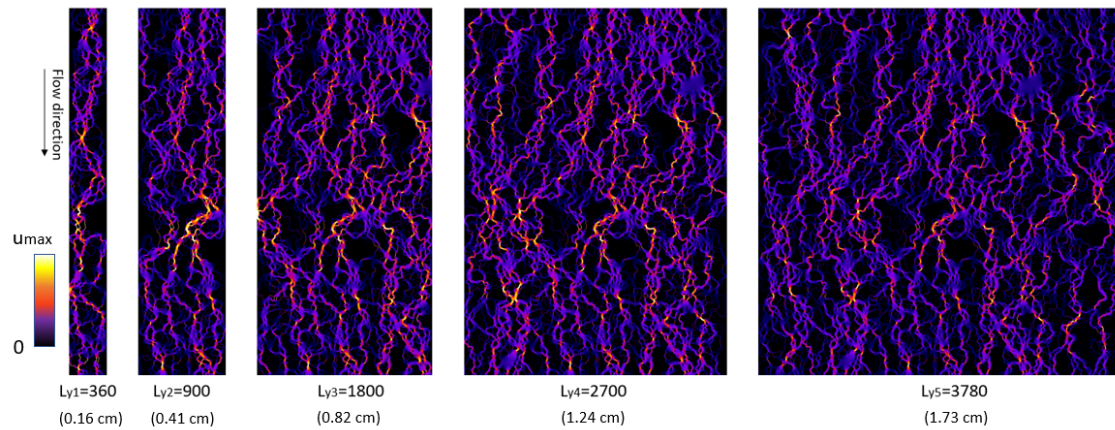


Figure 7.25 – Velocity fields for different widths obtained with LBM.

Fig. 7.25 displays the velocity fields corresponding to the five different widths investigated in this study. It is important to note that the same pressure boundary conditions were applied to all simulations. Upon observing the velocity fields, we notice that the movement of the fluid in the lateral direction is constrained by the presence of walls, leading to an enhanced channeling effect. This effect is particularly pronounced in cases with smaller widths, where a single dominant channel is observed along the length of the

medium. In order to further analyze the flow characteristics, we compute velocity profiles in the transverse direction of the flow, normalized by the mean velocity, defined as

$$\tilde{u}^*(y) = \frac{1}{L_x \langle \|\mathbf{u}\| \rangle} \int_0^{L_x} \|\mathbf{u}(x,y)\| dx. \quad (7.5.1)$$

For the flow simulations, pressure conditions are applied at the boundaries, resulting in different mean velocities for each medium width. To assess the permeability change of the medium, we compute the ratio between the permeability of each width (K_{L_y}) and the permeability of the widest medium width ($K_{L_{y5}}$). This normalized velocity is denoted as $K_{L_y}^* = \frac{K_{L_y}}{K_{L_{y5}}}$.

In Fig. 7.26 (Left), the permeability and the normalized velocity standard deviation are presented. Notably, the permeability exhibits a significant decrease as the medium width decreases. When the width increases, after reaching a certain threshold (around 0.8 cm), the permeability reaches a plateau, indicating a typical width where further increase has limited impact on permeability. Similar observations can be made for the velocity standard deviation. It increases when the width decreases, the boundaries adding heterogeneity to the flow. As the medium width increases, the flow becomes more statistically representative, leading to the velocity deviation reaching a plateau. The permeability and velocity variations are low for widths greater than $L_{y3} = 0.8$ cm, suggesting that beyond this point, the medium captures more adequately the flow dynamics.

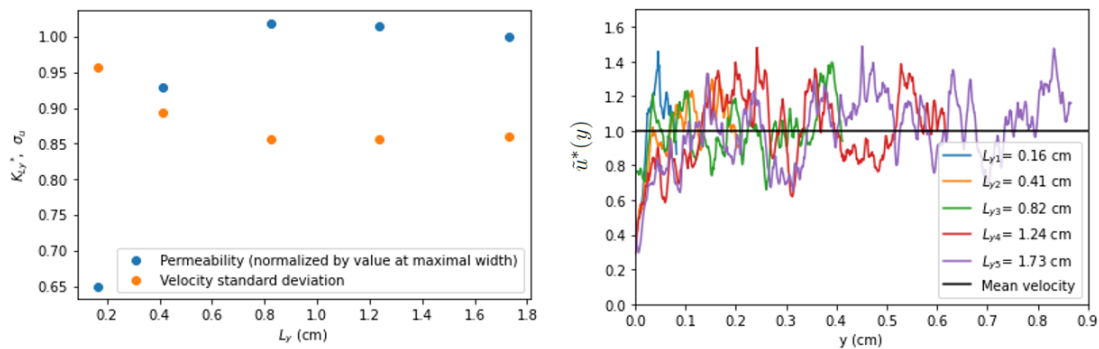


Figure 7.26 – Effect of width on the velocity profiles. (Left) Permeability and velocity standard deviation evolution with the medium width. (Right) Velocity profiles along the y axis (transverse to the flow) averaged along the x axis (direction of the flow). Velocities have been normalized for each profile by the mean velocity of the widest image $\langle \|\mathbf{u}\| \rangle_{L_{y5}}$.

In Fig. 7.26 (Right), the transverse velocity profiles for the five different widths are presented. Despite significant fluctuations in the profiles, the presence of boundary effects is evident. On average, the velocity decreases near the walls, indicating the impact of the boundaries on the flow. Specifically, there is a zone adjacent to the wall where the velocity remains consistently below the mean velocity. However, due to the implementation of a free-slip condition (to minimize boundary effects), the velocity does not reach zero in close proximity to the wall. Quantifying the precise length of the boundary effect proves challenging; however, it can be approximated to be around 0.05 – 0.1 cm. This range represents approximately 10% of the micromodel width, signifying that the boundary effect on the flow is spatially significant within the system.

The observed boundary effects highlight the importance of considering the impact of boundaries when analyzing flow properties. It is indeed critical to select an appropri-

ate medium width for studying flow properties, as excessively narrow widths may not accurately represent the flow properties of the porous media.

7.5.3 Effect of the medium width on transport properties

Having examined the influence of width on flow, we now focus on the impact of boundaries on dispersion. It is important to note that the mean velocities differ across the media of different widths. To facilitate a meaningful comparison of transport properties, we normalize the time by the mean velocity of each respective medium. This normalization is achieved by

$$t'_{L_y} = t \frac{\langle \|\mathbf{u}\| \rangle_{L_{y5}}}{\langle \|\mathbf{u}\| \rangle_{L_y}}, \quad (7.5.2)$$

where t'_{L_y} represents the normalized time for a specific medium width L_y , and $\langle \|\mathbf{u}\| \rangle_{L_{y5}}$ and $\langle \|\mathbf{u}\| \rangle_{L_y}$ denote the mean velocities for the widest and considered width, respectively. By normalizing the time in this manner, we account for the variations in mean velocities and establish a consistent reference for comparing transport properties across the different samples.

In Fig. 7.27, the concentration fields for the five different medium widths are presented at a specific normalized time. Notably, we observe that the concentration near the walls tends to be lower compared to the bulk of the medium. Additionally, in the case of smaller media widths, a notable observation is the presence of only one or two dominant preferential paths for the transport of the solute. This characteristic limits the statistical relevance of the medium in terms of the dispersion pattern.

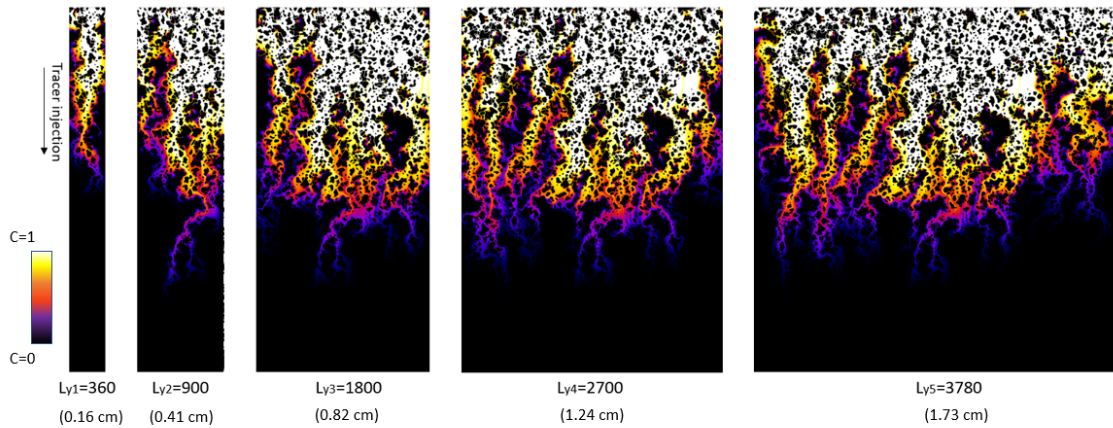


Figure 7.27 – Effect of width on the transport. Concentration fields as a function of the position x at $t' = 100000(\text{LBM units}) = 2.3s$ for 5 different widths.

Fig. 7.28 provides concentration profiles for the various medium widths at a normalized time of $t' = 100000 = 2.3s$. There is a noticeable difference in the concentration profiles, particularly for the smaller values of L_y . However, as the medium width, L_y , increases, the disparity between the concentration profiles diminishes rapidly. This observation suggests that the influence of the boundaries on the concentration distribution becomes less pronounced as the width of the medium expands.

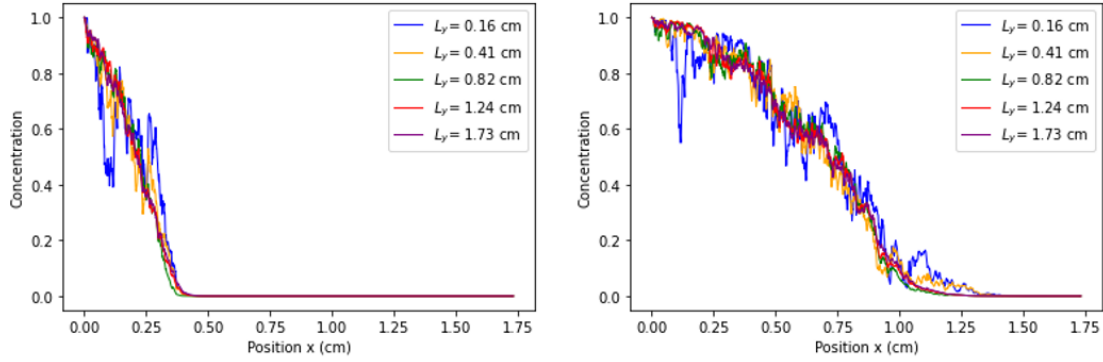


Figure 7.28 – Effect of width on the concentration profiles. Concentration profiles for 5 medium widths at $t' = 30000$ (LBM units) = $0.7s$ (Left) and $t' = 100000$ (LBM units) = $2.3 s$ (Right). $S_w = 0.82$.

For a more quantitative comparison of transport properties, we calculate the second moment as a function of time for each medium width L_y . In Fig. 7.29 (Left), we present the evolution of the second moments with time on a logarithmic scale. Remarkably, all the curves display a similar slope of $\alpha = 1.5$.

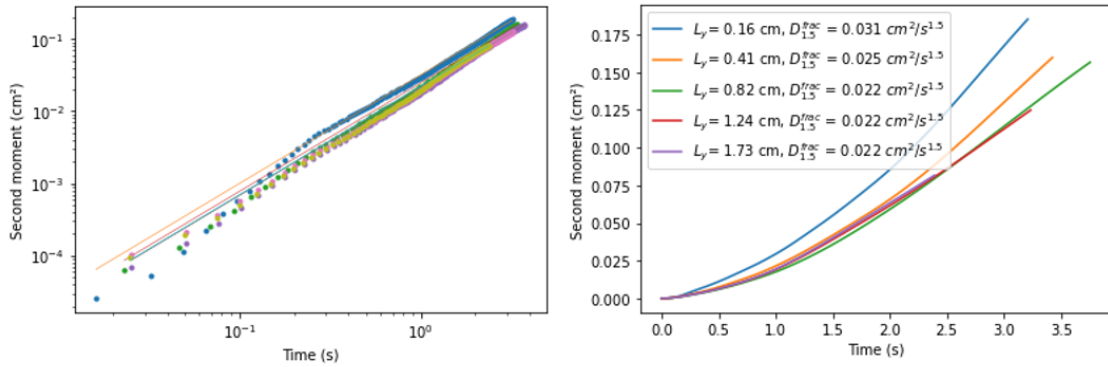


Figure 7.29 – Second moments evolution with time for different medium widths. (Left) Second moment in logarithmic scale (dashed lines) and fit (solid lines) of the second moments. The slopes indicate non-Fickian behavior i.e., a power law coefficient $\alpha = 1.5$ different than one. The moments curves are fitted with a power law $\sigma^2 = D_{1.5}^{frac} t^{1.5}$. (Right) Second moment in linear scale to highlight the different fractional dispersion coefficients. $D_{1.5}^{frac}$ estimated with the power law fit is indicated.

Fig. 7.29 (Right) accentuates the distinct slopes through the utilization of a linear scale. The fractional dispersion coefficient decreases when the medium width L_y increases. However, as the width L_y reaches a value of L_{y3} (0.82 cm/1800 pixels in this case), the tendencies for the second moments become remarkably similar and the fractional dispersion coefficient reaches a constant. This finding indicates that the influence of the boundaries is not significantly impacting the transport dynamics for widths larger than 0.82 cm in this specific configuration.

Overall, this quantitative analysis suggests that for widths greater than 0.82 cm, boundaries have a relatively minor impact on the transport behavior. The similarities in the fractional dispersion coefficients above this width imply that the dispersion mecha-

nisms in these larger widths exhibit consistent and comparable characteristics, independent of the specific width. Based on the findings and analysis presented, conducting transport studies within images with the micromodel width ($L_y = 0.90$ cm) appears to be a reasonable choice.

Nonetheless, we focused on investigating the impact of medium width on dispersion for a specific saturation value, without considering the entire saturation range. However, given that the system's heterogeneity increases as saturation decreases, it becomes important to explore the effect of saturation on the boundary effect. Specifically, it would be valuable to determine if saturation influences the length of the boundary region within the medium.

7.5.4 Influence of saturation on the boundary effect

Our objective is to investigate the influence of medium heterogeneity on the boundary effect, particularly considering the effect of saturation. In particular, we aim to quantify the length of the boundary region for different saturation values. To accomplish this, we conduct flow simulations in MPS-generated images of the same size as the micromodel for varying saturation levels. We analyze the velocity profiles to assess the impact of saturation on the boundary effect. As we observed significant fluctuations in the velocity profiles in the previous section, we also compute velocity fields for longer media with a length of $L_x = 8.2$ cm ($L_y = 0.90$ cm) to decrease the noise. By examining the velocity profiles for different saturation values, we can determine if there are notable differences in the length of the boundary region.

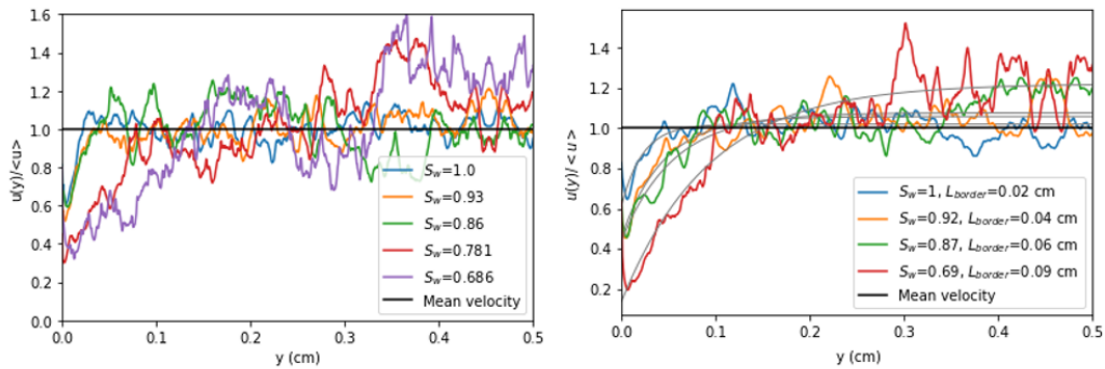


Figure 7.30 – Effect of saturation on the boundary border. Velocity profiles $\tilde{u}^*(y)$ along the y direction (transverse to the flow) for different saturation values and medium lengths. (Left) $L_x = 1.73$ cm (Right) $L_x = 8.3$ cm, an exponential fit ($\tilde{u}^*(y) = b - ae^{-\frac{y}{L_{border}}}$) is used to compute the border length L_{border} .

In Fig. 7.30 (Left), the transverse velocity profiles for different saturation levels in short media ($L_x = 1.73$, $L_y = 0.90$ cm) are presented. It is observed that saturation appears to have an influence on the boundary effect, with indications of increased lengths of the boundary effect at lower saturation levels. However, due to the presence of statistical noise, conducting a precise quantitative analysis becomes challenging.

In Fig. 7.30 (Right), the transverse velocity profiles for different saturation levels in longer media are shown. The increased length of the media allows for clearer observations of the boundary effect, as the profiles exhibit reduced noise. It is clear that as saturation decreases, the characteristic length of the boundary effect L_{border} (i.e. the length for

which the profile becomes constant) increases significantly. To quantify the extent of the boundary effect, we conduct an exponential fit to determine the characteristic length L_{border} over which it influences the system.

$$\tilde{u}_{L_y}^*(y) = b - ae^{-\frac{y}{L_{border}}}, \quad (7.5.3)$$

a , b and L_{border} are estimated with a fit and given in Fig. 7.30. It appears that L_{border} for the least saturated case is approximately four times longer than that for the saturated conditions. Interestingly, the boundary length observed for the saturated medium is of the same order of magnitude than the average diameter of a grain, which measures around 0.016 cm in the porous medium.

As expected, the analysis of transverse velocity profiles in media with different saturations reveals that decreasing water saturation intensifies the boundary effect, leading to increased significance of the borders effect in the overall dispersion behavior. To extend the findings to a broader context, as the heterogeneity of the medium increases, the impact of the boundary effect becomes more prominent.

7.5.5 Conclusion

In this section, we conducted a quantitative analysis of the boundary effect on flow and transport in porous media. We performed simulations for media with varying widths, focusing on a saturation value within our range ($S_w = 0.82$). Our findings revealed several key insights. Regarding flow properties, we observed that the average flow characteristics, such as mean velocity and velocity standard deviation, were influenced by the medium width up to a certain size. Beyond this threshold, the flow properties become independent of the system size. In terms of spatial variability, the transverse velocity profiles exhibited a clear boundary effect, with lower velocities near the lateral boundaries. We estimated a characteristic length of the boundary effect of approximately 0.05 cm for a saturation $S_w = 0.87$, representing around 10% of the micromodel size, within which the boundary effect was still perceptible. Turning to transport properties, we investigated them for all medium widths. Our results indicated that the width of the medium had a significant impact on transport properties for widths below $L_y = 0.82$ cm. This suggests that in our configuration, the borders do not play a major role in the transport behavior when studying dispersion in media of our micromodel size for this saturation.

However, it is important to note that our analysis focused on a specific saturation value. The boundary effect on dispersion behavior could vary with different saturation or with different porous media properties. Therefore, we quantified the border length for different saturation values. Note that the value of the border length found for $S_w = 0.87$ matches the one estimated in the short images $L_{border} = 0.05$ cm. We found that the border length increased as saturation decreased. In fact, the border length for the lowest saturation value was up to three times longer than in the saturated case. This implies that when considering lower saturations, the width needed to neglect the impact of the borders might need to be larger than our micromodel size. Additionally, dispersion patterns such as preferential flow paths and dead ends are more prominent with decreasing saturation, as noted in the experimental results, necessitating a larger medium width to capture the dispersion behavior with statistical relevance.

Despite these observations, we maintained a consistent width equal to the micromodel size for all saturations in our LBM simulations. This decision was made considering the computational time, as LBM simulation time increases at least quadratically with the image size. However, it is essential to keep in mind the potential influence of saturation and

medium heterogeneity on the boundary effect and dispersion behavior when considering flow and transport in confined porous media systems.

Chapter 8

Conclusion

The vadose zone, located above water tables and partially saturated with water, plays a crucial role in hydrogeology, particularly in water table recharge. Human activities, including agricultural practices, contribute to pollution sources affecting the vadose zone. With different saturation levels, the vadose zone is expected to experience a significant increase in saturation variability, especially in the southern region of France due to climate change. Consequently, comprehending contaminant transport in unsaturated porous media becomes essential for effectively assessing and managing water resources

Nonetheless, the understanding of dispersion in unsaturated porous media remains incomplete. In the existing literature, there is a significant disparity concerning the impact of saturation on dispersion. As the saturation decreases and the porous medium becomes more heterogeneous, the transport process becomes increasingly intricate. Consequently, conventional models of dispersion, such as the Advection-Diffusion Equation, often fail to accurately capture the dispersion phenomenon in such conditions.

Through this study, our objective is to gain insights into dispersion in unsaturated porous media by investigating transport at the pore scale. By doing so, we aim to assess properties at a larger scale and, particularly, understand how dispersion can be characterized and modeled in unsaturated porous media. Despite a substantial number of studies on this subject, a consensus regarding the impact of saturation on dispersion remains elusive. Specifically, the relationship between the dispersion coefficient and saturation exhibits considerable discrepancies. While a majority of studies suggest an increasing dispersion coefficient with decreasing water saturation, some show a non-monotonic relation, and a few even propose a decreasing dispersion coefficient with decreasing saturation. To unravel the origins of these disparities, we must delve into the fundamental mechanisms of dispersion and the intricate interplay between phase flow and the characteristics of the porous medium.

In the classical model, Fick's empiric law states that the flux is directly proportional to the concentration gradient, giving rise to the Advection-Diffusion Equation (ADE). The coefficient of dispersion is the constant of proportionality between the concentration variance (σ^2) and time in the asymptotic regime $D = \frac{1}{2} \lim_{t \rightarrow \infty} \frac{d\sigma^2}{dt}$. When the dispersion follows Fick's law, it is termed Fickian dispersion. To derive the ADE theoretically, one considers Brownian motion, where molecules undergo random walks, eventually leading to the ADE with a diffusion coefficient equal to the molecular diffusion coefficient. In porous media, dispersion is influenced not only by molecular diffusion but also by advection due to flow heterogeneity, resulting in a dispersion coefficient expressed as the sum of a diffusion and advection components.

To achieve convergence toward Fickian motion, the variance of displacements must be finite. A higher variance leads to slower convergence towards Fickian dispersion. Since real porous media have finite width, the variance of displacements should also be finite. Therefore, asymptotic dispersion should be Fickian theoretically. As a result, non-Fickian dispersion characterizes a transient behavior. However, the convergence toward Fickian dispersion can be extremely slow, and in some cases, the Fickian regime might never be observed. In fact, non-Fickian dispersion is rather the norm than the exception in porous media.

In the context of unsaturated porous media, the presence of a second phase introduces additional heterogeneity, which often results in increased dispersion. A fundamental question addressed in this thesis was to comprehend the impact of saturation on the nature of dispersion, whether it exhibits Fickian or non-Fickian behavior. Properly characterizing and modeling dispersion is of utmost importance in this regard. To understand dispersion in unsaturated porous media, it was essential to investigate the interactions between the multiphase flow and the porous medium. Specifically, the study focused on how the structural properties of the porous media change with saturation. For instance, the investigation aimed to understand how the heterogeneity of the porous medium varies with saturation levels.

In order to understand dispersion in unsaturated porous media, we performed a pore scale study, to identify flow and dispersion mechanisms at the microscopic scale in order to better characterize dispersion at a greater scale. This was done through two main axes, an experimental study, and numerical work to complement experimental findings. For our study, we utilized a micromodel, a transparent 2D porous network that enables visualization at the pore scale, commonly employed for multiphase flow and transport investigations. The micromodel was created based on a 2D slice of a rock. To conduct our experiments, we designed a specific experimental set-up to carry out air-water multiphase flow experiments followed by transport experiments.

Our focus was on studying transport in unsaturated porous media with a trapped phase, meaning that bubbles were trapped within the medium, and we deliberately did not examine transport during bubble movement, as this would introduce significant complexity to the study. We devised an experimental set-up to create an unsaturated porous medium with uniform and repeatable bubble distributions. To achieve this, we employed a co-injection system, where both water and air were injected simultaneously, and we stopped the injection once a steady state was achieved. The resulting multiphase flow led to a porous medium with trapped bubbles, which we utilized for our transport experiments.

One challenge in conducting transport experiments in a micromodel is to establish a clear inlet condition. With a simple inlet system, the tracer becomes dispersed in the medium even before entering the porous medium, making it difficult to accurately quantify dispersion. To address this issue, we improved the transport experiment by developing a device with a well-defined inlet injection system. In addition, we developed specific data processing techniques for our experimental data. We designed methods to analyze the phase distribution resulting from co-injection, to perform phases segmentation, retrieve porosity and saturation values, as well as grains and pores size distributions.

Furthermore, to quantitatively analyze how dispersion changes with saturation, we adopted spatial moments of the concentration as our approach. One advantage of this method is that it does not require making any assumptions about the nature of dispersion, such as whether it is Fickian or non-Fickian. Instead, by examining the evolution

of the second moment with time, we can differentiate between Fickian and non-Fickian dispersion. In specific terms, if the second moment σ^2 is proportional to t^α , and α equals 1, it indicates Fickian dispersion. Conversely, if α differs from 1, it points to non-Fickian dispersion. To compute the spatial moments, we employed integration by parts, a technique that enables us to calculate moments even for distributions affected by noise, which is common in unsaturated conditions.

The entire experimental set-up provided valuable experimental results, offering insights into dispersion in unsaturated porous media. Initially, we characterized the interaction between the multiphase flow and the porous medium and identified the properties of the resulting unsaturated porous medium. Specifically, we observed that saturation increases with the Capillary number (Ca), defined based on the dynamic viscosity μ , flow velocity (v), and surface tension (γ) as $Ca = \frac{\mu v}{\gamma}$. This relationship follows a power law, and saturation approaches 1 for sufficiently high Ca values. However, we were unable to explore the entire range of saturation since, below $S_w = 0.5$, the water phase does not percolate. Consequently, our dispersion study was restricted to the range of $[0.5 - 1]$ for saturation. The distribution of bubbles primarily depended on the maximal Ca number imposed in the system. Our results align closely with previous findings in the literature, particularly concerning the distribution of bubble sizes. At larger sizes, bubble size distributions followed a power-law decay with a cut-off that depended on the Ca number. As flow rates increase, larger bubbles are chased away, leading to a decrease in the maximum bubble size. Notably, below the pore size, the Ca had little impact on the distribution of bubbles. Furthermore, at the pore scale under unsaturated conditions, we observed that pores were either almost completely filled with air, hosting only a thin water film with local water saturation ($S_{w,local}$) of approximately 0.2, or completely saturated with water. As saturation decreased, the number of pores filled with air increased, and large pores were preferentially occupied by bubbles compared to more saturated conditions.

Having characterized the unsaturated porous medium, we then investigated the effect of saturation on dispersion. Our findings revealed a global increase in dispersion as saturation decreased. In saturated conditions, the concentration front appeared relatively flat and uniform. However, as saturation decreased, the concentration front exhibited more distortion, with the emergence of preferential paths and dead ends. Consequently, the heterogeneity in the dispersion process significantly increased. To quantify dispersion, we computed spatial moments. Overall, we observed an increase in dispersivity¹ as saturation decreased. Nevertheless, characterizing the nature of dispersion, whether Fickian or non-Fickian, proved challenging, particularly in unsaturated conditions. Several factors contributed to this difficulty. First, the limited size of the micromodel constrained our study to short time periods, especially in unsaturated conditions where the tracer rapidly exited the micromodel. Second, experimental noise and uncertainty made it challenging to precisely quantify spatial moments, especially for the lowest saturations. As a result, it was not possible to observe long time dispersion. Moreover, our study was limited in terms of flow rates, which prevented us from analyzing dispersion over a wide range of Peclet numbers experimentally.

To overcome the experimental limitations of the micromodel setup, we turned to numerical simulations as a powerful alternative. Specifically, we utilized Lattice-Boltzmann simulations, a widely adopted method for simulating flow and transport in complex porous media. LBM offers high accuracy and can be efficiently parallelized, leading to relatively

1. Ratio of the dispersion coefficient and the mean flow velocity

short computation times. In our numerical simulations, we conducted separate calculations for flow in the unsaturated medium and subsequently for transport. This approach has several advantages. Notably, it gives access to the velocity fields which is difficult experimentally. For transport simulation, it enables us to achieve perfectly neat inlet conditions for tracer injections, which is challenging to achieve in experimental setups. As a result, the data generated through numerical simulations are less noisy and easier to quantify. This is particularly beneficial when computing the second spatial moment, which plays a crucial role in determining the nature of dispersion.

Currently, simulating the result of an immiscible multiphase flow in a complex porous medium using numerical methods, such as Lattice-Boltzmann simulations, remains challenging. As a result, we rely on experimental phase distributions as inputs for LBM simulations to study flow and transport in such media. However, this approach requires making several strong assumptions and simplifications compared to the actual experimental conditions. Reproducing accurately the complex conditions at the interface between the air meniscus and water is not feasible in LBM simulations. Therefore, we had to consider the gas phase as an additive solid phase and impose a no-slip condition for all obstacles in the simulation. Additionally, due to computational constraints, LBM simulations are typically conducted in 2D, while the micromodel has a depth (L_z). To account for the depth of the Hele-Shaw cell, we incorporate the Darcy-Brinkmann model (or depth-integrated) model for flow. However, this approach neglects the depth profile of bubbles, which is present in the actual experimental setup. To validate the accuracy of the LBM workflow in simulating transport in unsaturated conditions in the micromodel, we compare the results of transport simulations with experimental data for three different saturation values. Remarkably, the LBM simulations yield results that are close to the experimental transport data, indicating that the LBM approach successfully captures the physics of flow and transport in the unsaturated micromodel, despite the assumptions and simplifications made. This validation process provides confidence in the use of LBM simulations to study transport phenomena in unsaturated porous media, compensating for the limitations of experimental setups and providing valuable insights into transport dynamics under these conditions.

Given that the LBM method still requires experimental phase distributions as inputs, the study is inherently limited to the size of the micromodel images. As saturation decreases and heterogeneity increases, the micromodel size becomes increasingly smaller compared to the Representative Elementary Volume (REV) of the unsaturated porous medium. Consequently, to ensure the relevance of our dispersion study, we require either longer images of the micromodel to consider longer time dispersion or a large number of two-phase configurations. Unfortunately, obtaining such experimental data can be challenging and may come with significant limitations.

To address these constraints and broaden the scope of our study, we are exploring the use of machine learning techniques. By employing machine learning algorithms, we aim to create unsaturated porous media models from our experimental data. This approach holds the promise of overcoming size and sample number limitations. We employed the Multiple Point Statistics (MPS) algorithm, originally developed for statistical applications but increasingly utilized in porous media studies, particularly by Jimenez-Martinez [90] for generating unsaturated porous media. In their work, they simulated the trapped phase using experimental data with a regular grid as the porous medium. Our approach is similar, but we go a step further by generating both a new porous medium and the associated phase distribution for a given saturation. To validate the MPS method's efficacy, we com-

pared the structural properties of the generated media with the experimental images used as training data. Notably, we compared porosity and saturation values, as well as the distributions of bubbles and grains. The comparison showed that the structural properties were highly comparable between the generated media and the experimental images. To further validate the method, we conducted flow and transport simulations in both the experimental and generated images using the Lattice-Boltzmann method. The results demonstrated that the MPS-generated porous media effectively replicated the flow and transport properties observed in the experimental images. The velocity distributions of the flow were accurately reproduced, and the transport properties showed good agreement between the experimental and generated images.

Overall, we successfully validated the MPS method for generating unsaturated porous media from experimental images and for studying flow and transport with similar properties. The strength of this approach lies in its generality, making it applicable to any 2D unsaturated two-phase distribution. By employing the MPS algorithm, we can overcome the limitations of experimental size and sample numbers, enabling us to explore dispersion and transport phenomena in unsaturated porous media at a greater scale and with increased accuracy.

Once the entire workflow was developed, we pursued two different strategies to study dispersion in unsaturated porous media. The first strategy involved generating long images to investigate long-time dispersion behavior. However, there was a significant computation cost associated with Lattice-Boltzmann simulations, as it is quadratic with the image size. Furthermore, the range of Peclet we could explore was limited due to numerical stability or computational constraints. To address this limitation, we adopted a second strategy, which involved generating a large dataset of MPS-generated porous media images at the micromodel size. This dataset covered the entire range of saturation values, enabling a statistical study of dispersion in unsaturated porous media. Unlike the long images, the short images in this dataset allowed us to explore a wide range of Peclet values. By employing these two strategies, we were able to gain insights into both long-time dispersion behavior through the long images and statistical trends in dispersion with varying saturation and Peclet values through the large dataset of short images.

Firstly, concerning flow properties, we focused on the apparent permeability, tortuosity, and heterogeneity under saturated conditions for the small realizations. The apparent permeability showed a significant decrease as saturation decreased, approaching zero near the residual gas saturation. As the gas acted as an additional solid matrix in our system, we compared our results with permeability-porosity relations using the concept of apparent porosity $\phi_{app} = \phi S_w$. The permeability data aligned well with the power-law relation commonly found in the literature, following the form $K_{app} \propto (\phi_{app} - \phi_0)^c$. Similarly, the tortuosity increased considerably with decreasing saturation. We again compared our results with tortuosity-porosity relations, incorporating the concept of apparent porosity, and found a good fit with a logarithmic function, $\tau = 1 - p \ln \phi_{app}$ commonly used in literature. This suggested that the apparent porosity accurately represented flow characteristics, indicating that the gas nature of the trapped phase might not significantly impact flow properties.

Additionally, we quantified flow heterogeneity by examining the normalized velocity standard deviation σ_u . This parameter exhibited a significant increase as saturation decreased, driven by the emergence of dead ends and preferential flow paths. As saturation

decreased, the number of dead ends expanded exponentially, leading to very low velocities, while preferential flow paths resulted in regions of very high velocities.

Based on our analysis of small realizations, we found that the evolution of the second moments over time indicated non-Fickian transport behavior over a wide range of Peclet values, both in saturated and unsaturated conditions. Therefore, we would not observe asymptotic dispersion for the medium length and Pe considered, and we characterized a transient regime. The mean value of the power law index α in the second moment was estimated to be 1.5, but there was a considerable statistical variance among the data. Since transport was non-Fickian, we quantitatively characterized dispersion using the fractional dispersion coefficient D_α^{frac} associated with $\alpha = 1.5$. This analysis revealed a significant increase in dispersion as saturation decreased, which confirmed the experimental findings.

Interestingly, for saturated and moderately unsaturated porous media, dispersion became Fickian as the Peclet number decreased. Moreover, the transition from non-Fickian to Fickian behavior was rather sharp. The normalized dispersion coefficient's dependence on the Peclet number indicated that the transition occurred when diffusion became more effective in the dispersion process. Furthermore, we observed that the range of Peclet numbers for which dispersion was non-Fickian increased with decreasing saturation. In other words, at low saturation, transport was predominantly advective, leading to a more pronounced non-Fickian dispersion. On the other hand, at high saturation, diffusion became more dominant, resulting in a transition towards Fickian dispersion.

In the long time realizations, we observed that the power law index α increased as saturation decreased, which confirmed the findings from the small realizations. This trend suggested that as saturation decreased, the non-Fickian behavior became more pronounced, with stronger dispersion effects. Moreover, despite the limited range of Peclet values that we could explore in the long simulations, we still observed the same effect of Peclet as found in the short images. This consistency across both short and long simulations provided strong support for the validity and robustness of our findings.

To summarize, this work provided valuable insights into the study of transport in unsaturated porous media. We developed an experimental set-up that allowed us to investigate both multiphase flow and transport in a micromodel, along with the development of appropriate data processing techniques. Through these experiments, we characterized the interaction between the multiphase flow and the porous medium and derived the structural properties of the unsaturated porous medium. Transport experiments indicated an increase in dispersion with decreasing saturation, although quantitative analysis was limited due to experimental constraints. To overcome these limitations, we utilized Lattice-Boltzmann (LBM) simulations after validating their suitability for modeling flow and transport in unsaturated conditions within the micromodel. Furthermore, we developed a machine learning-based method using the Multiple Point Statistics (MPS) algorithm to generate images with experimental data, enabling large-scale sample productions without size limitations. Employing LBM simulations in the MPS-generated images provided powerful insights into flow properties and dispersion. Notably, we found that as flow heterogeneity increased, and flow paths became more tortuous, with an increased presence of dead ends, dispersion in unsaturated porous media exhibited a more advective behavior. Consequently, we found that non-Fickian dispersion became more pronounced in unsaturated conditions. In contrast, in saturated conditions, dispersion tended to be Fickian as the Peclet number decreased, as diffusion became more effective in the dispersion process. Overall, this comprehensive approach combining experiments, machine learning-based image generation, and LBM simulations significantly advanced our under-

standing of transport phenomena in unsaturated porous media. The findings shed light on the complex interplay between flow and dispersion, which has implications for a wide range of applications, including groundwater management, environmental remediation, and the transport of contaminants in porous media.

This work lays the foundation for potential future advancements, including the modeling of non-Fickian dispersion in unsaturated porous media. For instance, it would be interesting to apply the Continuous Time Random Walk (CTRW) approach in unsaturated media to predict transport behaviors over longer time frames in unsaturated conditions. Furthermore, it's worth noting that our present study focused on dispersion in unsaturated media with an immobile trapped phase. Expanding our investigation to encompass transport involving two mobile immiscible phases would provide a more comprehensive understanding of transport dynamics in unsaturated conditions. Looking ahead, there's potential to extend this workflow to three-dimensional conditions, which would allow for a closer representation of real-world porous media. However, it's important to acknowledge that such numerical applications would demand substantial computational resources due to the increased complexity and computational demands associated with 3D simulations.

Chapter 9

Appendices

9.1 Bibliography appendix: Non Fickian dispersion modelling

9.1.1 Modeling with the Mobile-Immobile concept

MRMT (Multi-Rate Mass Transfer) model

The Multi-Rate Mass Transfer model is a generalization of the MIM model, with N immobile zones, hence N transfer coefficients α_i . The mobile zone is connected to the N immobile zones and there is a diffusive transfer associated to each of these zones. Hence, the MRMT model can be considered as a matrix formulation of the MIM model. The following illustration explains the model for $N=5$, the arrow symbolizes the mobile zone, and the squares of different size the immobile zones characterized by their respective transfer coefficient to the mobile region [8] [139].

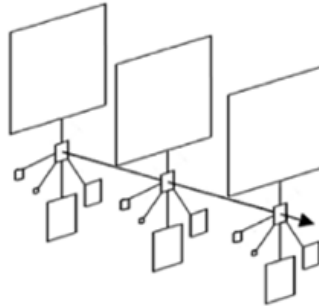


Figure 9.1 – Illustration of the MRMT model for $N=5$, from Babey 2014

The domain is assumed to consist of a mobile continuum, and several overlapping immobile continua, each of them is characterized by its state variable, the concentration in the zone. The governing equations of the MRMT models are given by

$$\beta \frac{\partial c_m}{\partial t} + \sum_{j=1}^N \beta_j \frac{\partial c_{im,j}}{\partial t} = L_u(c_m), \quad (9.1.1)$$

and

$$\frac{\partial c_{im}}{\partial t} = \alpha_j (u_m - u_{im,j}); \quad j = 1, \dots, N, \quad (9.1.2)$$

with L_u the transport operator such that $L_u(c_m) = \nabla \cdot (D_m \nabla c_m)$ and $\beta = R_m \phi_m$ with ϕ_m the mobile porosity and R_m the retardation factor for the mobile phase; $\beta_i = R_{im,j} \phi_{im,j}$ with $\phi_{im,j}$ the porosity and $R_{im,j}$ the retardation factor of the immobile region i .

F the total exchange between mobile and immobile regions is the sum of all mass transfer

$$F = \sum_{j=1}^N F_j = \sum_{j=1}^N \beta_j \alpha_j (c_m - c_{im,j}). \quad (9.1.3)$$

The physical meaning of the parameters is that N immobile zones are considered, that they are characterized by their concentration $c_{im,j}$ and they exchange mass with the mobile zone proportionally to the difference of concentration. The parameters can be related to a memory function, which encodes mass transfer between the mobile and the immobile regions, such as in the CTRW model or fractional ADE model [139] [155]. We will develop in another section the equivalences between those different models. The model parameters are adjusted to fit the dispersion behavior, for example in a field experiment.

Applications of the MRMT models, limitations

The MRMT allows more flexibility than the MIM model because more exchange terms are allowed. The more immobile regions are considered, the closer from real transport the model becomes, according to Babey, 2015 [8], especially for transport at long times. Particularly, MRMT models have been successfully applied to multi-phase transport [155], even though it is not commonly used by experimenters at the moment. The MRMT model can be quite general, as it can be equivalent to the CTRW and fractional ADE under some restrictions (cf section Equivalence between models). A limitation of the MRMT is the number of parameters needed, which increases linearly with the number of immobile zones considered. Hence, the MRMT formulation is not a parsimonious model (i.e a model that requires a minimal number of parameters to describe a phenomenon).

9.1.2 Modelling with random walk concepts: Continuous Time Random Walk

CTRW formulation

The probability by unity of time for a walker to just arrive in s at the time t $R(s,t)$ is given by the sum at all discrete positions s' of the probability to be at the position s' and to perform the transition from s' to s for any given time. Then, the continuous nature in time distribution of the CTRW is expressed through the time integral and the probability function $\psi(\delta s, \delta t)$, which gives the probability rate for the walker to realize a jump of δs after a time δt . $R(s,t)$, the probability for a walker to just arrive in s at the time t is given by

$$R(s,t) = \sum_{s'} \int_0^t \psi(s - s', t - t') R(s', t') dt'. \quad (9.1.4)$$

To understand this formula, let's take a particle in s which just arrived from a position s' , and arrived at the time t' in s' . The probability for this event equals to the probability to just arrive in s' at the time t' $R(s', t')$ multiplied by the probability to realize a jump from s' to s between t' and t , $\psi(s - s', t - t')$. To get the probability $R(s,t)$, we sum the probabilities on all positions s' , for all lapses of time $t - t'$.

The probability for the walker to be in s at the time t $P(s,t)$ is the probability for a particle to arrive in s at a time t' , and to stay in s between t and t' , summed for all times t' . Therefore, it is a function of $R(s,t)$ given by

$$P(s,t) = \int_0^t \Psi(t-t')R(s,t')dt', \quad (9.1.5)$$

with $\Psi(\delta t)$ the probability to stay in site during the time lapse δt . It is given by

$$\Psi(t) = 1 - \int_0^t \psi(t')dt', \quad (9.1.6)$$

with $\psi(t')$ is the probability to leave the site after a time t' , for all possible jumps.

For a walker to be on site at the time t , it would have arrived at time inferior or equal to t , or stayed in site at the time t . Consequently, the sum of probability for all times t' to arrive in site at a time $t' < t$ plus the probability to stay in site at the time t equals to 1, which give the expression of $\Psi(t)$. $\psi(t')$ is given by

$$\psi(t') = \sum_s \psi(s,t')dt'. \quad (9.1.7)$$

The whole concept resides in the choice of the probability $\psi(s,t)$ to adequately describe the physical process of the particle motion. Typically, for anomalous transport to occur, large time behavior of $\psi(s,t)$ are needed, in other words, the transitions times must be able to take really high values, and the variance of the transition time distribution must be infinite. This is the case when $\psi(s,t)$ is power tailed,

$$\psi(s,t) \rightarrow_{t \rightarrow \infty} t^{-1-\beta}, \quad 0 < \beta < \infty. \quad (9.1.8)$$

Usually, the dependence of the mean position $l(t)$ and the standard deviation $\sigma(t)$ of the probability $P(s,t)$ (or the concentration distribution) depends essentially of the form of $\psi(s,t)$ at larger times. In the special case of a power tailed probability distribution, it can be shown [17] that

$$l(t) \propto t^\beta, \quad (9.1.9)$$

and

$$\sigma(t) \propto t^\beta. \quad (9.1.10)$$

This demonstrates the non-Gaussian behavior of the process of propagation of $P(s,t)$, a Gaussian behavior would have been characterized by $l(t) \propto t$ and $\sigma(t) \propto t^{\frac{1}{2}}$.

To get back to what was said about the Central Limit Theorem and the conditions for a random walk to converge toward Brownian motion, this is typically a case where $\psi(s,t)$ does not fulfill the conditions for the central limit theorem, which is why it does not converge toward a Gaussian behavior.

Analytical analysis

Resolution of the $R(s,t)$ equation and analytical expressions

The equation of $R(s,t)$ is a convolution in space and time, that could be resolved through Laplace or Fourier transform. With inverse Laplace transform, we can theoretically get the analytical expression of $P(s,t)$ the concentration distribution for a given $\psi(s,t)$. However, given the difficulty to compute accurately inverse Laplace transform, they are not calculated. Nonetheless, some calculation in Laplace space give essential information, notably for First Time Passage distributions (probability to arrive in s at the

time t for the first time). They are equivalent in tracer test measurement to breakthrough curves for a pulse input. Breakthrough curves for a step input are described by Cumulative FPTD (CFPTD).

In the same example of power tailed distribution, characterized with a β parameter such that $\psi(s,t) \propto t^{-1-\beta}$, we get analytical expression for the CFPTD for large values of x [18]:

$$CFPTD(x) = \frac{\exp(-\frac{1-\beta}{\beta}(\beta x)^{\frac{1}{1-\beta}})}{\sqrt{2\pi(1-\beta)(\beta x)^{\frac{1}{1-\beta}}}} \quad (9.1.11)$$

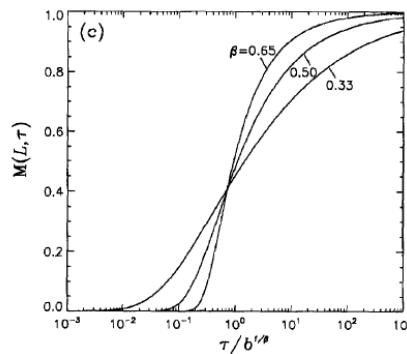


Figure 9.2 – Illustration of CFPTD (or BTC curves) with different values of β , with L the distance between the inlet and the outlet, and τ a dimensionless time. The axis are normalized to allow a comparison of the curves.

From the CFPTD curves Fig. 9.2, we can see that low values of β involve greater dispersion and long tails in the distributions, with greater standard deviation.

9.1.3 Generalization of the Fokker-Planck equation: fractional advection-diffusion equations

Introduction

The concept behind fractional ADE is actually quite similar to the CTRW concept, it resides in a generalization of the random walk, but goes further in the analogy of Brownian motion with a generalized version of the Fokker-Planck equation, which is a fractional ADE. The conditions to obtain these equations are a bit more restrictive than the Continuous Random Walk, which is why fractional ADE are less general than continuous Random Walk models.

The fractional ADE commonly found in the literature are fractional in space [15], which means that the random walk is continuous in space. They are a special case of Levy flight. In this section, we will describe the principle of fractional ADE and how they can be used to model dispersion behavior or fit experimental data.

Fractional calculus

Before we can explain in detail the principle of fractional ADE, it is needed to introduce a few notions of fractional calculus. In order to define fractional derivation, a generalization

of the integration operator I is introduced. The iterative integration formula for an integer n is given by the Cauchy Formula [30]

$$(I^n f)(x) = \frac{1}{(n-1)!} \int_0^x (x-t)^{n-1} f(t) dt. \tag{9.1.12}$$

This formula can be generalized to a positive number α thanks to the Gamma function. The gamma function is given by $\Gamma(\alpha) = \int_0^\infty t^{-\alpha-1} e^{-t} dt$ and for any integer n $\Gamma(n+1) = n!$. Hence, we can define I^α given by

$$(I^\alpha f)(x) = \frac{1}{\Gamma(\alpha)} \int_0^x (x-t)^{\alpha-1} f(t) dt. \tag{9.1.13}$$

Then, to define a fractional derivative, we can use a little trick by combining the classical derivation operator D and the generalized integration operator. Indeed, for a positive number α , we can define an integer n such that $n = \text{int}(\alpha) + 1$. Then, a derivation of order α is equivalent to an integration of order n_α times and a derivation of order n.

Then, we can write [83]

$$D_{a+}^\alpha f(x) = \frac{d^n}{dx^n} D_{a+}^{-(n-\alpha)} f(x) = \frac{d^n}{dx^n} I_{a+}^{n-\alpha}; \quad x > a, \tag{9.1.14}$$

$$D_b^\alpha f(x) = \left(-\frac{d}{dx}\right)^n D_b^{-(n-\alpha)} f(x) = \left(-\frac{d}{dx}\right)^n I_b^{n-\alpha}; \quad x < b. \tag{9.1.15}$$

This is the Riemann-Liouville fractional derivative. Fractional derivative can be a real practical tool, especially since the properties of the usual derivation are conserved in Fourier space (the Fourier transform of the α derivative of a function f(x) will be given by $TF(D^\alpha f(x))(k) = (ik)^\alpha f(\hat{k})$).

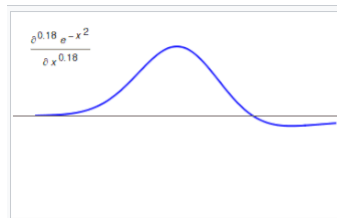


Figure 9.3 – Fractional derivative of a Gaussian function, $\alpha = 0.18$

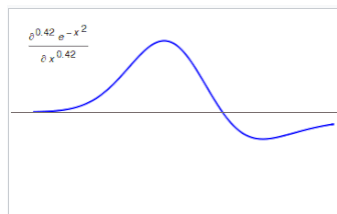


Figure 9.4 – Fractional derivative of a Gaussian function, $\alpha = 0.42$

NB: This is the simplest way to introduce fractional derivation, however some generalized definitions of fractional derivation have been introduced, that allow a more uniform definition but we won't discuss it further, the aim was just to introduce the concept to be able to understand the following section.

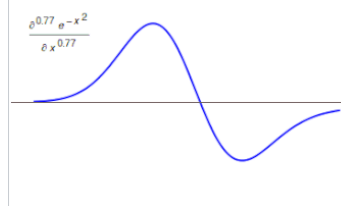


Figure 9.5 – Fractional derivative of a Gaussian function, $\alpha = 0.74$

Principle of space fractional ADE

The fractional ADE is a consequence of the random walk. We will see here how we can obtain a generalized Fokker-Plank equation from a random walk continuous in time, and under which hypotheses (from [15]). If the distribution of displacement of the random walk has an infinite variance, the Central Limit Theorem can not be applied. However, the sum of displacements can converge toward an α -stable Levy density which is a generalization of the CLT mentioned in the section Random walk and dispersion.

Typically, for a long tailed distribution such as $P(Y > y) \approx W y^\alpha$, if $\alpha < 2$, the variance $\int y^2 (y^{-\alpha-1})$ diverges. Therefore, the Central Limit Theorem can not be applied anymore, but the random walk converges toward Levy motion, characterized by Levy density $f(y)$, and the Fourier transform of $f(y)$ is given by

$$\hat{f}(k) = \int_{-\infty}^{\infty} e^{-iky} f(y) dy = \exp[-|k|^\alpha \sigma^\alpha (1 + i \beta \operatorname{sign}(k) \tan(\frac{\pi\alpha}{2})) - \mu ik], \quad (9.1.16)$$

with α the stability index, μ the mean of the distribution, β the skewness and σ the spreading. Then, the concentration distribution for a large number of particles is given by

$$\begin{aligned} \hat{C}(k,t) &= \exp[-\sigma(t) |k|^\alpha \sigma^\alpha (1 + i \beta \operatorname{sign}(k) \tan(\frac{\pi\alpha}{2})) - \mu ik] \\ &= \exp[-Dt |\cos(\frac{\pi}{\alpha/2})| |k|^\alpha (1 + i \beta \operatorname{sign}(k) \tan(\frac{\pi\alpha}{2})) - \mu ik], \end{aligned} \quad (9.1.17)$$

with the spreading σ

$$\sigma = (Dt |\cos(\frac{\pi}{\alpha/2})|)^\alpha. \quad (9.1.18)$$

This is equivalent to

$$\hat{C}(k,t) = \exp[q Dt (-ik)^\alpha + p Dt (ik)^\alpha - ik vt], \quad (9.1.19)$$

with p and q characterizing the skewness, $p+q=1$, $\mu = v$ and D a constant coefficient (D is not the dispersion coefficient). Then, it can be easily verified that the equation governing this distribution is

$$\frac{\partial C}{\partial t} = -v \frac{\partial C}{\partial x} + p D \frac{\partial^\alpha C}{\partial x^\alpha} + q D \frac{\partial^\alpha C}{\partial (-x)^\alpha}, \quad (9.1.20)$$

or

$$\frac{\partial C}{\partial t} = -v \frac{\partial C}{\partial x} + (\frac{1}{2} + \frac{\beta}{2}) D \frac{\partial^\alpha C}{\partial x^\alpha} + (\frac{1}{2} - \frac{\beta}{2}) D \frac{\partial^\alpha C}{\partial (-x)^\alpha}, \quad (9.1.21)$$

with the α derivative defined with the fractional calculus concept detailed in the previous section. For a symmetric distribution ($p = q = \frac{1}{2}$) or $\beta = 0$ we have

$$\frac{\partial C}{\partial t} = -v \frac{\partial C}{\partial x} + D \Delta_\alpha C, \quad (9.1.22)$$

with $\Delta_\alpha = \frac{\partial^\alpha}{\partial (-x)^\alpha} + \frac{\partial^\alpha}{\partial x^\alpha}$.

We can see the close analogy with the ADE equation. Furthermore, for $\alpha = 2$, the equation becomes identical to the ADE. However, the coefficient D can be qualified of dispersion coefficient only if $\alpha = 2$ (Gaussian regime). Indeed, for a given α density, a dispersion coefficient can not be defined, plus the coefficient D has the unity of m^α/s , its physical interpretation cannot be similar to the fickian regime as the variance of the plume grows as $(Dt)^\alpha$.

By analogy to the ADE solutions for a step of concentration, we can derive similar semi-analytical expressions for fractional ADE symmetric solutions

$$C(x,t) = \frac{C_0}{2} (1 - \text{serf}_\alpha(\frac{x-vt}{Dt^\alpha})), \quad (9.1.23)$$

with

$$\text{serf}_\alpha(z) = 2 \int_0^z f_\alpha(x) dx, \quad (9.1.24)$$

and f_α the α -stable density.

Few remarks on α -stable densities

α -stable densities are invariant when shifted by vt and scaled by $t^{\frac{1}{\alpha}}$. Plus, the variance of the plume is scaled as $\frac{2}{\alpha}$. Once again, if $\alpha = 2$, the results coincide with the solution of the ADE equation (for a pulse input), i.e a Gaussian distribution. From the figure of the α -stable densities for different values of α (9.6), we can see that α -stable densities, or in other words the fractional ADE model allows long tailed distributions, which is not the case of the Gaussian model. This is particularly remarkable in the graph (b) (Fig 9.6), with the logarithmic scale.

Application of fractional ADE

Fractional ADE (fADE) can adequately fit and predict dispersion in porous media that exhibits patterns of non-fickian dispersion. According to the work of Zhou (2003) [184], it becomes interesting to use fractional ADE instead of the ADE if the order of the fADE is significantly inferior to 2. In other words, the dispersion needs to show clear signs of non linearity to use fADE.

Benson *et al.* have applied the fADE to predict dispersion successfully in a field experiment (MADE tests, [15] [14]) with heterogeneous porous media. In Moradi (2018) [113], they show that space fADE adequately capture the non-fickian nature of the dispersion for heterogeneous soil, but the comparison of ADE and fADE in homogeneous soils gave similar results, even though the dispersion in the homogeneous media tests shows patterns of non-fickian dispersion. The non-fickian nature of the dispersion needs to be significant to properly use the space fADE.

Efforts have been made to develop the fractional ADE tools and extend the link with other models such as CTRW and MRMT. The extension to time fractional ADE has been pursued, but it is not widely used in modelling yet due to the computational burden of the solution of time fADE [109].

Nonetheless, Meerschaert *et al.* [109] have developed the time fractional ADE and applied space fADE and time fADE to field experiments and numerical simulations to assess the adequacy of the fractional ADE. Their analysis highlights that natural porous media with highly contrasting permeability may form mobile and relatively immobile zones, which results in a wide time distribution for solute waiting time. They conclude that transport process can be characterized efficiently by time-non local model, including the time fADE, the MRMT model, and the CTRW framework with mobile/immobile distinction and appropriate memory function.

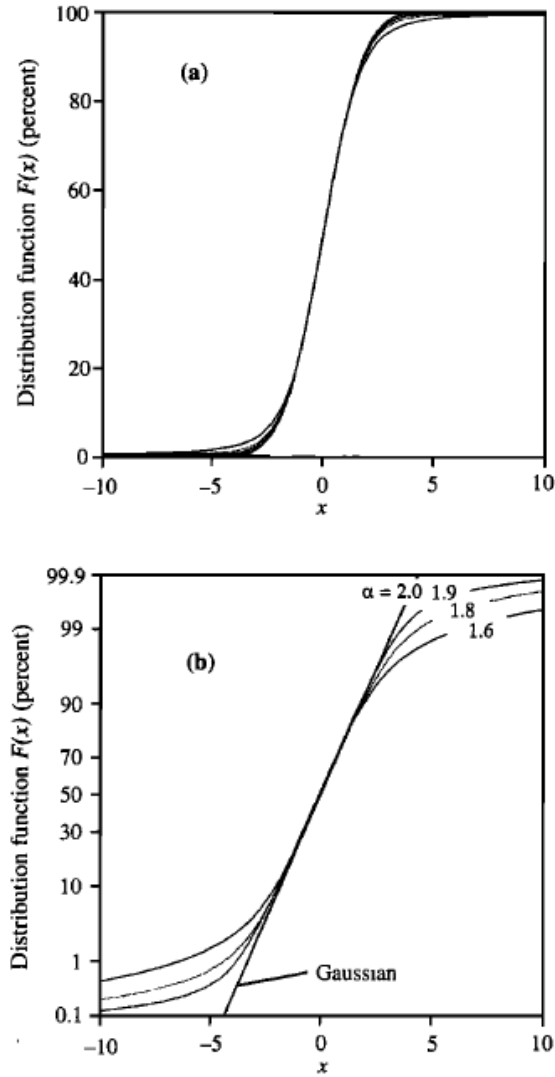


Figure 9.6 – Symmetric α -stable densities for different values of α , with a linear scale (a) and logarithmic scale (b), from Benson, 2001 [15].

Space fADE can also adequately describe the transport if the porous media tends to form preferential flow paths. Spatio-temporal ADE might be the more adequate way to model the dispersion in cases with sub-diffusion (retention of solute in dead-ends) and super-diffusion (particle jumps due to preferential paths).

Remarks

Although fractional ADE implies to understand, at least superficially, rather complex mathematical concepts such as fractional calculus, the fractional ADE formulation is very general, and can model adequately non-fickian dispersion. Gaussian dispersion is just a particular case of the fractional ADE.

Furthermore, the main advantage of the fractional ADE is to give a rather simple equation to describe the transport, as well as an analytical solution in Fourier space. The model is parsimonious, a few parameters only are needed to define the model entirely

(v, α, D and eventually β for space fADE asymmetric distributions).

Plus, in the case of space fADE, the parameters of the model can be directly linked with physical parameters of the concentration distribution. Indeed, if we have access to the concentration profile, v and β are given by the first and third moment of the distribution, and α and D can be computed from the maximum concentration as a function of time and the second moment as a function of time. Nonetheless, the fractional ADE is not as general as the CTRW, as it assumes that the random walk converges toward an α -stable distribution.

9.1.4 Comparison of dispersion models

Formulation or phenomena	α_j	β_j	Description of parameters
Solute transport with mass exchange	$\frac{D_{m,j}}{R_{m,j} L_{m,j}^2}$	$R_{m,j} \phi_{m,j}$	$D_{m,j} [L^2 T^{-1}]$ is a molecular diffusion coefficient in the j th immobile region; $R_{m,j} [-]$ is the retardation factor of the j th immobile zone; $L_{m,j} [L]$ is the distance from the mobile zone to the j th immobile zone; $\phi_{m,j} [L^3 L^{-3}]$ is the porosity of the j th immobile zone.
Flow with delayed storage (e.g., Boulton, 1955)	$\frac{\sigma_{m,j} K_{m,j}}{S_{m,j} L_{m,j}}$	$S_{m,j}$	$\sigma_{m,j} [L^2 L^{-2}]$ is the specific surface of the j th immobile region; $K_{m,j} [L T^{-1}]$ is the hydraulic conductivity in the j th immobile region; $S_{m,j} [L^{-1}]$ is the specific storage coefficient of the j th immobile zone; $L_{m,j} [L]$ is the distance from the mobile zone to the j th immobile zone.
MRMT (Haggerty and Gorelick, 1995)	$\alpha_{\beta HG}$	$\beta_{\beta HG} \beta$	$\beta_{\beta HG}$ and $\alpha_{\beta HG}$ are the capacity and first-order mass transfer coefficients used by Haggerty and Gorelick (1995); β is the mobile capacity.
Integro-differential (e.g., Carrera et al., 1998)	$\gamma_j^2 \frac{D_m}{R_m T_m^2}$	$\frac{a_j}{\gamma_j} R_m \phi_m$	$\phi_m [L^3 L^{-3}]$, $R_m [-]$, $D_m [L^2 T^{-1}]$ and $L_m [L]$ are characteristic parameters of the entire immobile domain with the same meaning as in solute transport; coefficients a_j and γ_j are shape factors for diffusion into different geometries.
CTRW (e.g., Dentz and Berkowitz, 2003)	α_j	$a_k = \left[\sum_{j=1}^{\infty} \alpha_j^{-k} \beta_j \right] \quad k=1 \dots \infty$	a_k are the expansion coefficients of the Laplace transform of the memory function g^* .
Fractional derivatives (e.g., Willmann et al., 2008)	$\alpha_1 = t_N^{-1}, \alpha_N = t_1^{-1}$ $\alpha_j = \alpha_1 + (j-1) \frac{(\alpha_N - \alpha_1)}{N-1}$ $j = 2 \dots N-1$	β_N $\beta_j = \frac{\sum_{i=1}^N \beta_i \alpha_i}{\alpha_j} \left[\left(\frac{\alpha_j}{\alpha_{j+1}} \right)^{m_0} - 1 \right]$ $j = 1 \dots N-1$	m_0 is the slope of the memory function in log-log scale; $[t_1, t_N]$ is the interval of time on which this function displays a power-law behavior.
Solute transport in rivers (e.g., Lees et al., 2000)	$\alpha_1 = \alpha_s A/A_s$	$\beta_1 = A_s$	$\alpha_s [T^{-1}]$ is the storage zone exchange coefficient; $A [L^2]$ is the stream channel cross-sectional area; and $A_s [L^2]$ is the storage zone cross-sectional area.
Low permeability blocks (e.g., Warren and Root, 1963)	$\alpha_1 = \frac{a k_{im}}{\mu \phi_m C_{im}}$	$\beta_1 = \phi_m C_{im}$	$a [L^{-2}]$ is a geometry factor of the matrix blocks; $k_{im} [L^2]$ is the absolute permeability of this region; $\mu [M L^{-1} T^{-1}]$ is the fluid viscosity; $\phi_m [L^3 L^{-3}]$ is the porosity of the matrix blocks; $C_{im} [L T^2 M^{-1}]$ is the total compressibility of matrix blocks.

Figure 9.7 – Equivalence between models based on MRMT formulation, from Silva *et al.* 2009 [140]

Overview of non-Fickian dispersion models

Tab. 9.8 summarizes some essential traits of the different models.

9.1.5 Micromodels bibliography appendix

Micromodels fabrication methods

Additive manufacturing: shaping

The other shaping method is additive manufacturing, the main method is stereolithography. It is a kind of 3D printing, based on the solidification of a liquid resin by photo-polymerisation, the resin is added layer by layer. There are other kind of additive manufacturing, such as fused deposition, electron beam melting, laser sintering. However, additive manufacturing is still in its early stage for the fabrication of micromodels [1].

Models	ADE	ADE coefficients non constant	MIM (Mobile Immobile Model)	MRMT (MultiRate Mass Transfer)	ADE fractionnaire spatiale (Levy Motion)	CTRW
Principe	Consequence of Brownian motion. Fick's law.	Dispersion coefficient space dependant.	Diffusive mass transfer between the mobile region and the immobile region.	MIM generalization with N immobile zones.	Generalization of the random walk with a displacement distribution that converges toward an Levy, according to the generalized Central limit theorem.	Generalization of the random walk for which transition times follow any given probability distribution
Modeling of anomalous dispersion?	No	Not well	Transient anomalous dispersion only	Yes	Yes	Yes
Local/non local	Local	Local	Non local	Non local	Non local	Non local
Parsimonie (Number of parameters to define the model)	*** Np=1;2	*** Np=1;2	*** Np=2	* Np=N+1	*** Np=2;3	***
Generality	*	*	**	***	****	*****
Mathematical concepts	Classical algebra	Classical algebra	Classical algebra	Matrical calculus	Fractional calculus Advanced probability Fourier transform	Advanced probability Laplace transform
Equivalence between models	Particular case of all other models		-Equivalent to the ADE when the proportion of immobile zones or the transfer coefficient to these zones is equal to zero.	-When N tends to infinity, there is possible equivalence with fADE and CTRW models, gwith adequate choice of tranfer coefficients	-Equivalence with CTRW when the probability of transition times is power tailed. -Generalization of the ADE -Possible equivalence with MRMT	-Most general formulation, with the propoer choice of transition time probability function, it can describe any other model
Remarks		Ambiguity in the definition of the dispersion coefficient, can be misleading for data interpretation	-Unique transfer coefficient. -process with finite variance: non-fickian behavior corresponds to a transient	-the generality of the model increaseswith N (choice of transition times) but the number of parameters needed increases as well.	-Analytical solutions in Fourier space. -Access to model parameters directly fromconcentration distribution	-essence of the model in the choice of the probability of transition function

Figure 9.8 – Modeling non-Fickian dispersion, overview

Table 1. Micromodel fabrication methods along with their advantages and disadvantages.

Fabrication method	Advantages	Disadvantages	Major references
Hele–Shaw and glass beads	easy to make, choice of wetting properties, cheap to make, no mask needed	fixed or random network geometry cannot be used under dynamic conditions because the lower half of the model cannot be visualized	Corapcioglu et al. (1997), Corapcioglu and Fedirchuk (1999), Chatenever and Calhoun (1952)
Optical lithography	accurate, can reproduce any network pattern, cheap to make	not suitable for making elongated models due to the manufacturing procedure, fixed wetting properties, cannot be exposed to regular light, requires a clean room to manufacture, mask needed	Thompson et al. (1983, 1994), Cheng et al. (2004)
Wet etching	relatively easy, choice of wetting properties depending on the chosen material, can reproduce any network pattern	curvature on the walls makes back-light illumination impossible, limited ratio between pore width and depth, mask needed	Wegner and Christie (1983), Johnston (1962), Sagar and Castanier (1998)
Deep reactive ion etching, laser etching, ion etching	highly accurate, can reproduce any network pattern	limitation on the depth of the model, maximum ratio between width and depth, very expensive	Yeom et al. (2003), Ohara et al. (2010)
Stereo lithography	three-dimensional structures	low resolution, very expensive	Hull (1986), Melchels et al. (2010)
Soft lithography	highly accurate, easy to make, can reproduce any network pattern, cheap to make	needs treatment to fix wettability issues, needs clean room to prepare the silicon wafer	Xia and Whitesides (1998), Kim et al. (1996, 1997)

Figure 9.9 – Micromodels fabrication methods, from Kadamitriou, 2012 [92]

Micromodels visualization methods

Table 2. The visualization methods along with their limitations and their applicability.

Visualization method	Suitability	Limitations
Microscope and camera	any transparent (partially) two-dimensional micromodel, high-resolution optical image	not suitable for three-dimensional models, limited in resolution ($>1 \mu\text{m}$)
Direct visualization with a camera	relaxed needs in resolution, high acquisition rate	not suitable for three-dimensional models, very low resolution
Photo-luminescent volumetric imaging	three-dimensional porous media, high resolution	refractive index matching is necessary, relatively slow effects, relatively expensive
Confocal microscopy	very high resolution (submicron), quasi-static or very low speed effects	effective for depths up to 250 μm , relatively expensive, very low acquisition rate, not suitable for dynamic effects

Figure 9.10 – Visualisation techniques, from Anbari, 2018 [1]

9.2 Method appendix

9.2.1 Taylor dispersion in the tubing

The Taylor dispersion coefficient in a tube is given by

$$D_{Taylor} = D_0 \left(1 + \frac{P_e^2}{48}\right). \quad (9.2.1)$$

Thus, the spreading of the concentration in the tubing is given by

$$\langle x^2 \rangle = D_0 \left(1 + \frac{P_e^2}{48}\right) \frac{L}{u}, \quad (9.2.2)$$

with $P_e = \frac{uL}{D_0}$.

$$\langle x^2 \rangle = D_0 \frac{L}{u} + \frac{u^2}{LD_0 48} \quad (9.2.3)$$

Hence, there is a competition between the diffusive term of the dispersion and the convective term. The optimal flow rate is given by $Q_{opt} = D_0 \pi a^2 \sqrt{48}$.

9.3 Experimental results appendix

9.3.1 Phase distribution resulting from a two-phase flow

Position of the bubbles in the porous medium: deterministic or probabilistic?

A question arises when considering the interaction between the multiphase flow and the porous medium. Is the position of the bubbles random in the porous medium or are there more probable sites for bubbles to be trapped in? We repeated three experiments of co-injection for two different Ca values (6.4×10^{-5} and 6.4×10^{-4}). The position of the bubbles have been determined in each case, and the images have been superposed. Fig. 9.12 shows the superposition of images for the highest Ca . Solid is blue and the dark spots highlight the presence of areas in the porous medium where bubbles are most likely

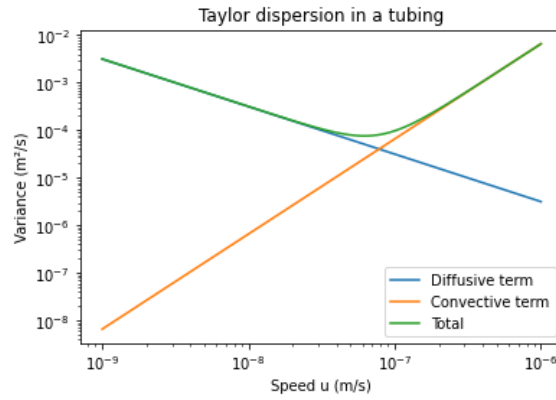


Figure 9.11 – Taylor dispersion

to be trapped in and the white color shows areas where it is very unlikely for bubbles to get trapped in.

Remark This is done with only three experiment repetitions, but a superposition of a large number of images would give us a good estimation of the probability for a bubble to be trapped in the porous medium for a given flow rate.

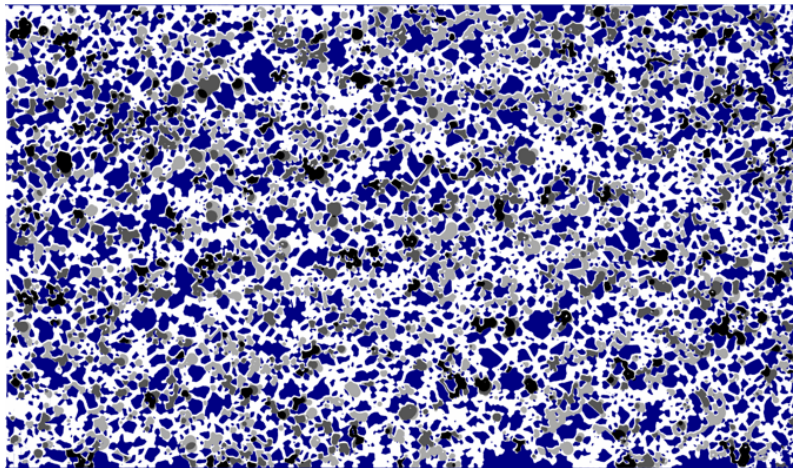


Figure 9.12 – Superposition of the bubbles positions for three co-injection experiments, $Ca = 6.4 \times 10^{-5}$. Blue: Solid. Dark: presence of bubble for each repetition. Dark grey: Presence of bubble for two out of three repetition. Light grey: Presence of bubble for only one repetition. White: Absence of bubble

Fig. 9.13 gives the comparison of bubbles positions superposition for two flow rates. For readability and to ease the comparison, the solid phase is shown in white. We can see that the image for the highest Ca (right) is more contrasted than the low Ca (left): the area where bubbles are likely to be trapped (grey or dark spots) decreases greatly. The position of bubbles is restricted to a smaller portion of the porous media hence the position of the bubbles is more deterministic. This is consistent with the work of Chevalier [35], in which they computed the presence probability over a large number of realisations, and for different values of Ca values. They observed that with increasing Ca , the images would get more contrasted, which highlights that the phase distribution patterns becomes more

deterministic.

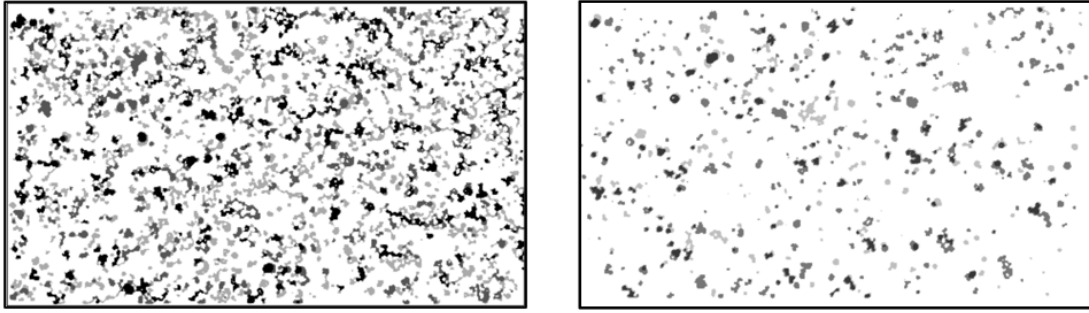


Figure 9.13 – Comparison of the bubble positions probabilities p for two Ca . (Left) $Ca = 6.4 \times 10^{-5}$. (Right) $Ca = 6.4 \times 10^{-4}$. Dark: presence of bubble for each repetition. Dark grey: $p=1$ Dark grey: $p=0.66$ Light grey: $p=0.33$. White: $p=0$.

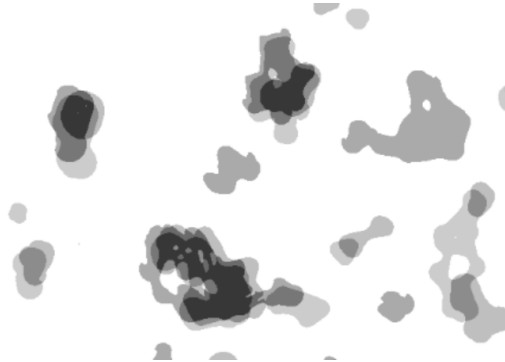


Figure 9.14 – Illustration of trapping site. Superposition of three occurrences for $Ca = 6.4 \times 10^{-4}$.

At the pore scale, we observe that there are favorable sites of trapping for which the probability to find a bubble is high (dark spots), but the bubble shape around a trapping site changes from one experience to another. Typically, for the highest Ca number, 31% of the ganglia on average share a trapping site (dark spot), when the dark spots only represent 7% of the total area occupied by bubbles. The trapping around a site is illustrated Fig. 9.14.

9.3.2 Structural properties of the unsaturated porous medium

Ratio of saturated pores We define the ratio of saturated pores as the number of pores saturated over the total number of pores.

$$r_{pores} = \frac{n_{pores/S_w=1}}{n_{pores}} \quad (9.3.1)$$

In Fig. 9.15, the ratio of saturated pores decreases progressively when the water saturation decreases. Plus, there is an important variability for low water saturation values. Plus, at the lower mean saturation value, around 40% of the pores are still fully saturated in water. The observed tendency indicates that pores are filled with air selectively.

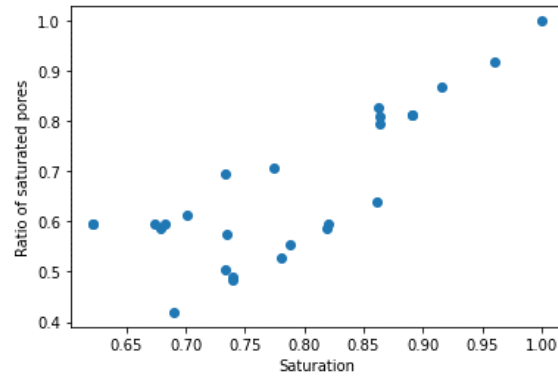


Figure 9.15 – Ratio of saturated pore as a function of water saturation

Evolution of the porous network with saturation

Assuming air clusters at rest, we consider a new porous medium where the air cluster are replaced by solid. For a given saturation, a new porous medium is defined, with its pores and throats. Here, we aim to analyze the evolution of the pores and throats properties of this new network with saturation.

Pores and throats identification: watershed operation Air clusters are assimilated as solid. We create a binary image of the unsaturated porous medium. Then, we apply a watershed operation to create the pore and throats network. This is illustrated in the Fig. 9.16. Then, we can analyse the pores and throats size by using the particle analysis tool (ImageJ).

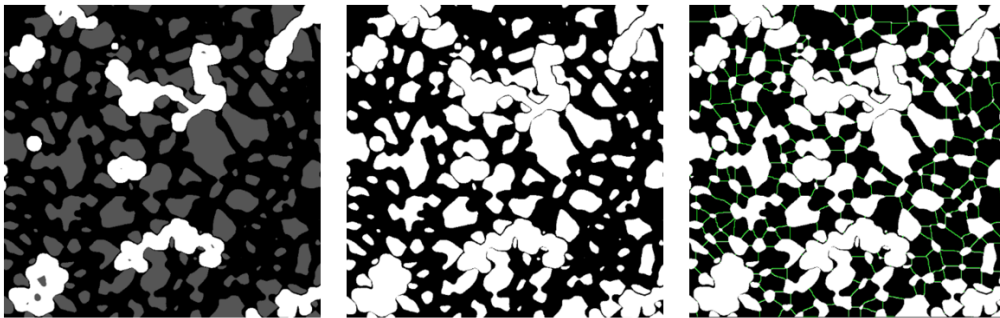


Figure 9.16 – Unsaturated pore network identification. From left to right: unsaturated image, binarized unsaturated image (new pore network), pores and throats identification with watershed.

Pores size analysis Fig. 9.17 shows that the mean pore size in the modified porous network decreases with a decreasing water saturation, as bubbles occupy a fraction of the pores. Mean pore size and saturation are almost proportional: the pore size in the modified network is directly related to the local saturation of a pore in the porous network. The creation of smaller pores when the saturation decreases can also be seen Fig. 9.17 (Bottom left), as pores distribution spreads towards small pore sizes. Pores of really small size (100 times smaller than the mean pore size in the saturated medium) corresponds

to water films around the bubbles. Plus, the pore size variance increases when the water saturation decreases, which means the heterogeneity of the medium gets wider.

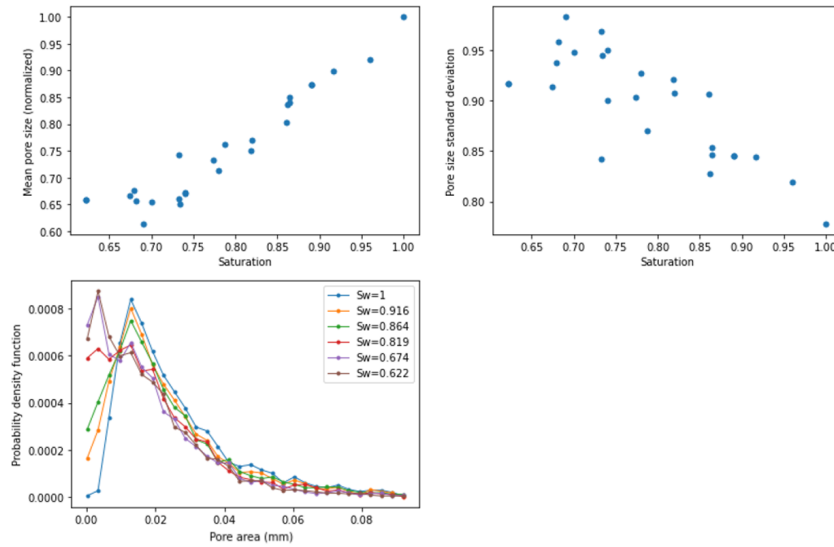


Figure 9.17 – Pore area analysis of the unsaturated networks. [Top] Mean pore size and standard variation of the unsaturated network normalized by the mean pore size in the saturated medium. [Bottom left] Distributions of the pore areas for different saturation values.

Bibliography

- [1] Alimohammad Anbari, Hung-Ta Chien, Sujit S. Datta, Wen Deng, David A. Weitz, and Jing Fan. Microfluidic model porous media: Fabrication and applications. *Small*, 14(18):1703575, March 2018.
- [2] G Burc Arpat and Jef Caers. Conditional simulation with patterns. *Mathematical Geology*, 39:177–203, 2007.
- [3] Pietro Asinari. Generalized local equilibrium in the cascaded lattice boltzmann method. *Phys. Rev. E*, 78:016701, Jul 2008.
- [4] M. Auset and A. Keller. Pore-scale visualization of colloid straining and filtration in saturated porous media using micromodels. *Water Resour Res*, 42, 10 2006.
- [5] Maria Auset and Arturo A. Keller. Pore-scale processes that control dispersion of colloids in saturated porous media. *Water Resources Research*, 40(3), March 2004.
- [6] R. Aziz, V. Joekar-Niasar, and P. Martinez-Ferrer. Pore-scale insights into transport and mixing in steady-state two-phase flow in porous media. *Int. J. Multiph. Flow*, 109:51–62, 2018.
- [7] Chopard B., Falcone J. L., and Latt J. The lattice boltzmann advection-diffusion model revisited. *The European Physical Journal Special Topics*, 171(1):245–249, 2009.
- [8] Tristan Babey, Jean-Raynald de Dreuzy, and Céline Casenave. Multi-rate mass transfer (MRMT) models for general diffusive porosity structures. *Advances in Water Resources*, 76:146–156, February 2015.
- [9] M Barrande, R Bouchet, and R Denoyel. Tortuosity of porous particles. *Analytical chemistry*, 79(23):9115–9121, 2007.
- [10] G. Batôt, L. Talon, Y. Peysson, M. Fleury, and D. Bauer. Analytical and numerical investigation of the advective and dispersive transport in herschel–bulkley fluids by means of a lattice–boltzmann two-relaxation-time scheme. *Chemical Engineering Science*, 141:271–281, 2016.
- [11] Martin Bauer, Sebastian Eibl, Christian Godenschwager, Nils Kohl, Michael Kuron, Christoph Rettinger, Florian Schornbaum, Christoph Schwarzmeier, Dominik Thönnies, Harald Köstler, et al. walberla: A block-structured high-performance framework for multiphysics simulations. *Computers & Mathematics with Applications*, 81:478–501, 2021.
- [12] F. Bauget and M. Fourar. Non-fickian dispersion in a single fracture. *Journal of Contaminant Hydrology*, 100(3-4):137–148, September 2008.

- [13] P. Bedrikovetsky. Upscaling of stochastic micro model for suspension transport in porous media. *Transport in Porous Media*, 75(3):335–369, April 2008.
- [14] David A. Benson and Mark M. Meerschaert. A simple and efficient random walk solution of multi-rate mobile/immobile mass transport equations. *Advances in Water Resources*, 32(4):532–539, April 2009.
- [15] David A. Benson, Rina Schumer, Mark M. Meerschaert, and Stephen W. Wheatcraft. Fractional dispersion, lévy motion, and the made tracer tests. *Transport in Porous Media*, 42(1/2):211–240, 2001.
- [16] Brian Berkowitz, Joseph Klafter, Ralf Metzler, and Harvey Scher. Physical pictures of transport in heterogeneous media: Advection-dispersion, random-walk, and fractional derivative formulations. *Water Resources Research*, 38(10):9–1–9–12, October 2002.
- [17] Brian Berkowitz, Georg Kosakowski, Gennady Margolin, and Harvey Scher. Application of continuous time random walk theory to tracer test measurements in fractured and heterogeneous porous media. *Ground Water*, 39(4):593–604, July 2001.
- [18] Brian Berkowitz, Harvey Scher, and Stephen E. Silliman. Anomalous transport in laboratory-scale, heterogeneous porous media. *Water Resources Research*, 36(1):149–158, January 2000.
- [19] Prabhu Lal Bhatnagar, Eugene P Gross, and Max Krook. A model for collision processes in gases. i. small amplitude processes in charged and neutral one-component systems. *Physical review*, 94(3):511, 1954.
- [20] Patrick Billingsley. *Probability and Measure*. John Wiley and Sons, second edition, 1986.
- [21] J. Birkholzer and C.-F. Tsang. Solute channeling in unsaturated heterogeneous porous media. *Water Resour Res*, 33(10):2221–2238, October 1997.
- [22] Gianluca Blois, Julio M. Barros, and Kenneth T. Christensen. A microscopic particle image velocimetry method for studying the dynamics of immiscible liquid–liquid interactions in a porous micromodel. *Microfluidics and Nanofluidics*, 18(5-6):1391–1406, January 2015.
- [23] Tanguy Le Borgne, Marco Dentz, Diogo Bolster, Jesus Carrera, Jean-Raynald de Dreuzy, and Philippe Davy. Non-fickian mixing: Temporal evolution of the scalar dissipation rate in heterogeneous porous media. *Advances in Water Resources*, 33(12):1468–1475, December 2010.
- [24] H. C. Brinkman. A calculation of the viscous force exerted by a flowing fluid on a dense swarm of particles. *Flow, Turbulence and Combustion*, 1(1), December 1949.
- [25] H.C. Brinkman. A calculation of the viscous forces exerted by a flowing fluid on a dense swarm of particles. *Appl. Sci. Res.*, sect A1:27–39, 1947.
- [26] M. Bromly and C. Hinz. Non-fickian transport in homogeneous unsaturated repacked sand. *Water Resour Res*, 40(7), July 2004.
- [27] Hans-Jürgen Butt, Karlheinz Graf, and Michael Kappl. *Physics and chemistry of interfaces*. John Wiley & Sons, 2013.

- [28] Francisco J Carrillo, Ian C Bourg, and Cyprien Soulaine. Multiphase flow modeling in multiscale porous media: An open-source micro-continuum approach. *Journal of Computational Physics: X*, 8:100073, 2020.
- [29] Edwin Earl Catmull. *A subdivision algorithm for computer display of curved surfaces*. The University of Utah, 1974.
- [30] Louis Auguste Cauchy. *Résumé des leçons données à l'École royale polytechnique sur le calcul infinitésimal*. Imprimerie Royale, Paris, 1823.
- [31] Zhenhua Chai and T. S. Zhao. Nonequilibrium scheme for computing the flux of the convection-diffusion equation in the framework of the lattice boltzmann method. *Phys. Rev. E*, 90:013305, Jul 2014.
- [32] S. Chapman and T.G. Cowling. *The Mathematical Theory of Non-uniform Gases: An Account of the Kinetic Theory of Viscosity, Thermal Conduction, and Diffusion in Gases*. Cambridge University Press, 1958.
- [33] E. Charlaix, J. P. Hulin, and T. J. Plona. Experimental study of tracer dispersion in sintered glass porous materials of variable compaction. *Physics of Fluids*, 30(6):1690, 1987.
- [34] Shiyi Chen and Gary D Doolen. Lattice boltzmann method for fluid flows. *Annual review of fluid mechanics*, 30(1):329–364, 1998.
- [35] T. Chevalier, D. Salin, L. Talon, and A.G. Yiotis. History effects on nonwetting fluid residuals during desaturation flow through disordered porous media. *Phys. Rev. E*, 91(4), April 2015.
- [36] MA Christie. Flow in porous media—scale up of multiphase flow. *Current Opinion in Colloid & Interface Science*, 6(3):236–241, 2001.
- [37] Charles A. Conn, Kun Ma, George J. Hirasaki, and Sibani Lisa Biswal. Visualizing oil displacement with foam in a microfluidic device with permeability contrast. *Lab Chip*, 14(20):3968–3977, 2014.
- [38] Yavuz M. Corapcioglu, Sabina Chowdhury, and Sharon E. Roosevelt. Micromodel visualization and quantification of solute transport in porous media. *Water Resources Research*, 33(11):2547–2558, November 1997.
- [39] Molly S Costanza-Robinson, Benjamin D Estabrook, and David F Fouhey. Representative elementary volume estimation for porosity, moisture saturation, and air-water interfacial areas in unsaturated porous media: Data quality implications. *Water Resources Research*, 47(7), 2011.
- [40] John Crank. *The mathematics of diffusion*. Oxford university press, 1979.
- [41] J-F Daian, CP Fernandes, PC Philippi, and JA Bellini da Cunha Neto. 3d reconstitution of porous media from image processing data using a multiscale percolation system. *Journal of Petroleum Science and Engineering*, 42(1):15–28, 2004.
- [42] Paul J. Dellar. Bulk and shear viscosities in lattice boltzmann equations. *Phys. Rev. E*, 64:031203, Aug 2001.

- [43] Paul J. Dellar. Incompressible limits of lattice boltzmann equations using multiple relaxation times. *Journal of Computational Physics*, 190(2):351–370, 2003.
- [44] B. Doligez, M. Le Ravalec, S. Bouquet, and M. Adelinet. A review of three geostatistical techniques for realistic geological reservoir modeling integrating multi-scale data. *Bulletin of Canadian Petroleum Geology*, 63(4):277–286, 2015.
- [45] G. Dongmo, B. Braconnier, C. Preux, Q. Tran, and C. Berthon. Glimm and finite volume schemes for polymer flooding model with and without inaccessible pore volume law. *ECMOR XVII*, 2020(1):1–21, 2020.
- [46] Z. Dou, X. Zhang, C. Zhuang, Y. Yang, J. Wang, and Z. Zhou. Saturation dependence of mass transfer for solute transport through residual unsaturated porous media. *Int J Heat Mass Tran*, 188:122595, 2022.
- [47] François Dubois and Pierre Lallemand. Quartic parameters for acoustic applications of lattice boltzmann scheme. *Computers & Mathematics with Applications*, 61(12):3404–3416, 2011. Mesoscopic Methods for Engineering and Science — Proceedings of ICMES-09.
- [48] D. D’Humières. Generalized lattice boltzmann equations, rarefied gas dynamics: Theory and simulations. *Progress in Astronautics and Aeronautics*, 159:450–458, 1992.
- [49] Alexei A Efros and Thomas K Leung. Texture synthesis by non-parametric sampling. In *Proceedings of the seventh IEEE international conference on computer vision*, volume 2, pages 1033–1038. IEEE, 1999.
- [50] CL Farmer. Upscaling: a review. *International journal for numerical methods in fluids*, 40(1-2):63–78, 2002.
- [51] I Fatt and H Dykstra. Relative permeability studies. *Journal of Petroleum Technology*, 3(09):249–256, 1951.
- [52] Junxi Feng, Qizhi Teng, Xiaohai He, and Xiaohong Wu. Accelerating multi-point statistics reconstruction method for porous media via deep learning. *Acta Materialia*, 159:296–308, 2018.
- [53] Andrea Ferrari, Joaquin Jimenez-Martinez, Tanguy Le Borgne, Yves Méheust, and Ivan Lunati. Challenges in modeling unstable two-phase flow experiments in porous micromodels. *Water Resources Research*, 51(3):1381–1400, March 2015.
- [54] E. G. Flekkøy. Lattice bhatnagar-gross-krook models for miscible fluids. *Phys. Rev. E*, 47:4247–4257, Jun 1993.
- [55] JJ Fried and MA Combarous. Dispersion in porous media. In *Advances in hydro-science*, volume 7, pages 169–282. Elsevier, 1971.
- [56] Christophe C Frippiat and Alain E Holeyman. A comparative review of upscaling methods for solute transport in heterogeneous porous media. *Journal of Hydrology*, 362(1-2):150–176, 2008.
- [57] U Frisch and B Hasslacher. Y. pomeau, “lattice-gas automata for the navier-stokes equation,”. *Phys. Rev. Lett*, 56(14):1505–1508, 1986.

- [58] C. Gardet. *Modélisation multi-échelles de réservoir et calage d'historique de production*. PhD thesis, Université Pierre et marie Curie, 2014.
- [59] C. Gardet, . Le Ravalec, and E. Gloaguen. Pattern-based conditional simulation with a raster path: a few techniques to make it more efficient. *Stoch Env Res Risk A*, 30(2):429–446, January 2016.
- [60] C. Gardet and M. Le Ravalec. Multiscale multiple point simulation based on texture synthesis. 09 2014.
- [61] Martin Geier, Andreas Greiner, and Jan G. Korvink. Cascaded digital lattice boltzmann automata for high reynolds number flow. *Phys. Rev. E*, 73:066705, Jun 2006.
- [62] Martin Geier, Martin Schönherr, Andrea Pasquali, and Manfred Krafczyk. The cumulant lattice boltzmann equation in three dimensions: Theory and validation. *Computers & Mathematics with Applications*, 70(4):507–547, 2015.
- [63] I. Ginzburg, D. d’Humières, and A. Kuzmin. Optimal stability of advection-diffusion lattice boltzmann models with two relaxation times for positive/negative equilibrium. *J. Stat. Phys.*, 139(6):1090–1143, 2010.
- [64] I. Ginzburg, G. Silva, and L.Talon. Analysis and improvement of Brinkman lattice Boltzmann schemes: Bulk, boundary, interface. similarity and distinctness with finite elements in heterogeneous porous media. *Phys. Rev. E: Stat. Phys. Plasmas Fluids Relat. Interdisciplin. Top.*, 91:023307, February 2015.
- [65] I. Ginzburg, F. Verhaeghe, and D. d’Humières. Two-Relaxation-Time Lattice Boltzmann scheme: About parametrization, velocity, pressure and mixed boundary conditions. *Commun. Comput. Phys.*, 3:427–478, 2008.
- [66] Irina Ginzburg. Multiple anisotropic collisions for advection–diffusion lattice boltzmann schemes. *Advances in Water Resources*, 51:381–404, 2013. 35th Year Anniversary Issue.
- [67] BV Gnedenko, AN Kolmogorov, BV Gnedenko, and AN Kolmogorov. Limit distributions for sums of independent. *Am. J. Math*, 105, 1954.
- [68] Christian Godenschwager, Florian Schornbaum, Martin Bauer, Harald Köstler, and Ulrich Rüde. A framework for hybrid parallel flow simulations with a trillion cells in complex geometries. In *Proceedings of the International Conference on High Performance Computing, Networking, Storage and Analysis*, pages 1–12, 2013.
- [69] T.I. Gombosi. *Gaskinetic Theory*. Cambridge Atmospheric and Space Science Series. Cambridge University Press, 1994.
- [70] Ian J Goodfellow, Oriol Vinyals, and Andrew M Saxe. Qualitatively characterizing neural network optimization problems. *arXiv preprint arXiv:1412.6544*, 2014.
- [71] P. Gouze, T. Le Borgne, R. Leprovost, G. Lods, T. Poidras, and P. Pezard. Non-fickian dispersion in porous media: 1. multiscale measurements using single-well injection withdrawal tracer tests. *Water Resources Research*, 44(6), June 2008.
- [72] Felipe B Guardiano and R Mohan Srivastava. Multivariate geostatistics: beyond bivariate moments. *Geostatistics Tróia’92: Volume 1*, pages 133–144, 1993.

- [73] V Guillon, M Fleury, D Bauer, and Marie-Christine Néel. Superdispersion in homogeneous unsaturated porous media using nmr propagators. *Physical Review E*, 87(4):043007, 2013.
- [74] Zhaoli Guo and T. S. Zhao. Lattice boltzmann model for incompressible flows through porous media. *Phys. Rev. E*, 66:036304, Sep 2002.
- [75] Zhaoli Guo, Chuguang Zheng, and Baochang Shi. Discrete lattice effects on the forcing term in the lattice boltzmann method. *Phys. Rev. E*, 65:046308, Apr 2002.
- [76] D. Haga, Y. Niibori, and T. Chida. Hydrodynamic dispersion and mass transfer in unsaturated flow. *Water Resour Res*, 35(4):1065–1077, April 1999.
- [77] Roy Haggerty, Sean A. McKenna, and Lucy C. Meigs. On the late-time behavior of tracer test breakthrough curves. *Water Resources Research*, 36(12):3467–3479, December 2000.
- [78] Ryan Haggerty, Dong Zhang, Jongwan Eun, and Yusong Li. Characterization of bubble transport in porous media using a microfluidic channel. *Water*, 15(6):1033, March 2023.
- [79] N. Haque, A. Singh, and U.K. Saha. Experimental visualization and analysis of multiphase immiscible flow in fractured micromodels using micro-particle image velocimetry. *J. Energy Res. Technol.*, 144(2), May 2021.
- [80] J Hardy, Yves Pomeau, and O De Pazzis. Time evolution of a two-dimensional classical lattice system. *Physical Review Letters*, 31(5):276, 1973.
- [81] S. Hasan, V. Joekar-Niasar, N.K. Karadimitriou, and M. Sahimi. Saturation dependence of non-fickian transport in porous media. *Water Resour Res*, 55(2):1153–1166, February 2019.
- [82] David J Heeger and James R Bergen. Pyramid-based texture analysis/synthesis. In *Proceedings of the 22nd annual conference on Computer graphics and interactive techniques*, pages 229–238, 1995.
- [83] Richard Herrmann. *Fractional Calculus*. WORLD SCIENTIFIC, March 2014.
- [84] M Honarpour and SM Mahmood. Relative-permeability measurements: An overview. *Journal of petroleum technology*, 40(08):963–966, 1988.
- [85] Rongzong Huang and Huiying Wu. A modified multiple-relaxation-time lattice boltzmann model for convection–diffusion equation. *Journal of Computational Physics*, 274:50–63, 2014.
- [86] Henk Huinink. Unsaturated flow. In *Fluids in Porous Media Transport and phase changes*. IOP Publishing, 2016.
- [87] N. Jarrige, I. Bou Malham, J. Martin, N. Rakotomalala, D. Salin, and L. Talon. Numerical simulations of a buoyant autocatalytic reaction front in tilted hele-shaw cells. *Phys. Rev. E: Stat. Phys. Plasmas Fluids Relat. Interdisciplin. Top.*, 81:066311, 2010.

- [88] F. Javadpour and D. Fisher. Nanotechnology-based micromodels and new image analysis to study transport in porous media. *Journal of Canadian Petroleum Technology*, 47(02), February 2008.
- [89] Miroslav Tuma Jennifer Scott. *Algorithms for Sparse Linear Systems*. Birkhauser, Cham, 2023.
- [90] J. Jiménez-Martínez, A. Alcolea, J.A. Straubhaar, and P. Renard. Impact of phases distribution on mixing and reactions in unsaturated porous media. *Adv Water Resour*, 144:103697, October 2020.
- [91] J. Jiménez-Martínez, T. Le Borgne, H. Tabuteau, and Y. Méheust. Impact of saturation on dispersion and mixing in porous media: Photobleaching pulse injection experiments and shear-enhanced mixing model. *Water Resour Res*, 53(2):1457–1472, February 2017.
- [92] N. K. Karadimitriou and S. M. Hassanizadeh. A review of micromodels and their use in two-phase flow studies. *Vadose Zone Journal*, 11(3):vzj2011.0072, August 2012.
- [93] N.K. Karadimitriou, V. Joekar-Niasar, M. Babaei, and C. A. Shore. Critical role of the immobile zone in non-fickian two-phase transport: A new paradigm. *Environmental Science & Technology*, 50(8):4384–4392, April 2016.
- [94] F. Kazemifar, G. Blois, D.C. Kyritsis, and K.T. Christensen. A methodology for velocity field measurement in multiphase high-pressure flow of CO₂ and water in micromodels. *Water Resour Res*, 51(4):3017–3029, April 2015.
- [95] Farzan Kazemifar, Gianluca Blois, Dimitrios C. Kyritsis, and Kenneth T. Christensen. Quantifying the flow dynamics of supercritical CO₂–water displacement in a 2d porous micromodel using fluorescent microscopy and microscopic PIV. *Advances in Water Resources*, 95:352–368, September 2016.
- [96] Arturo A. Keller and Maria Auset. A review of visualization techniques of biocolloid transport processes at the pore scale under saturated and unsaturated conditions. *Advances in Water Resources*, 30(6-7):1392–1407, June 2007.
- [97] Donald L. Koch and John F. Brady. Anomalous diffusion in heterogeneous porous media. *Physics of Fluids*, 31(5):965, 1988.
- [98] A. Koponen, M. Kataja, and J. Timonen. Tortuous flow in porous media. *Physical Review E*, 54(1):406–410, July 1996.
- [99] T. Krüger, H. Kusumaatmaja, A. Kuzmin, O. Shardt, G. Silva, and E.M. Viggien. *The Lattice Boltzmann Method: Principles and Practice*. Graduate Texts in Physics. Springer International Publishing, 2016.
- [100] A. Kuzmin, I. Ginzburg, and A.A. Mohamad. The role of the kinetic parameter in the stability of two-relaxation-time advection–diffusion lattice boltzmann schemes. *Computers & Mathematics with Applications*, 61(12):3417–3442, 2011. Mesoscopic Methods for Engineering and Science — Proceedings of ICMMS-09.
- [101] A.J.C. Ladd. Numerical simulations of particulate suspensions via a discretized boltzmann equation. part 1. theoretical foundation. *Journal of Fluid Mechanics*, 271:285–309, 1994.

- [102] Pierre Lallemand and Li-Shi Luo. Theory of the lattice boltzmann method: Dispersion, dissipation, isotropy, galilean invariance, and stability. *Phys. Rev. E*, 61:6546–6562, Jun 2000.
- [103] Karine Laurent, Éric Flauraud, Christophe Preux, Quang Huy Tran, and Christophe Berthon. Design of coupled finite volume schemes minimizing the grid orientation effect in reservoir simulation. *Journal of Computational Physics*, 425:109923, 2021.
- [104] V. Leontidis, S. Youssef, and D. Bauer. New insights into tracer propagation in partially saturated porous media. *Oil & Gas Science and Technology – Revue d’IFP Energies nouvelles*, 75:29, 2020.
- [105] Melissa Levy and Brian Berkowitz. Measurement and analysis of non-fickian dispersion in heterogeneous porous media. *Journal of Contaminant Hydrology*, 64(3-4):203–226, July 2003.
- [106] Mojtaba G. Mahmoodlu, Amir Raoof, Tom Bultreys, Jeroen Van Stappen, and Veerle Cnudde. Large-scale pore network and continuum simulations of solute longitudinal dispersivity of a saturated sand column. *Advances in Water Resources*, 144:103713, October 2020.
- [107] M.A. Maraqa, R.B. Wallace, and T.C. Voice. Effects of degree of water saturation on dispersivity and immobile water in sandy soil columns. *J. Contam. Hydrol.*, 25(3-4):199–218, March 1997.
- [108] G. Matheron and G. De Marsily. Is transport in porous media always diffusive? a counterexample. *Water Resources Research*, 16(5):901–917, October 1980.
- [109] Mark M. Meerschaert, Jeff Mortensen, and Stephen W. Wheatcraft. Fractional vector calculus for fractional advection–dispersion. *Physica A: Statistical Mechanics and its Applications*, 367:181–190, July 2006.
- [110] Yashar Mehmani. *Modeling single-phase flow and solute transport across scales*. PhD thesis, University of Texas at Austin, 2014.
- [111] Henk G Merkus. *Particle size measurements*. Particle Technology Series. Springer, Dordrecht, Netherlands, 2009 edition, January 2009.
- [112] R. J. MILLINGTON and J. P. QUIRK. Permeability of porous media. *Nature*, 183(4658):387–388, February 1959.
- [113] G. Moradi and B. Mehdinejadani. Modelling solute transport in homogeneous and heterogeneous porous media using spatial fractional advection-dispersion equation. *Soil and Water Research*, 13(No. 1):18–28, January 2018.
- [114] Lukas Mosser, Olivier Dubrule, and Martin J Blunt. Reconstruction of three-dimensional porous media using generative adversarial neural networks. *Physical Review E*, 96(4):043309, 2017.
- [115] Peyman Mostaghimi, Branko Bijeljic, and Martin J. Blunt. Simulation of flow and dispersion on pore-space images. In *All Days*. SPE, September 2010.
- [116] Alon Nissan and Brian Berkowitz. Anomalous transport dependence on pécelet number, porous medium heterogeneity, and a temporally varying velocity field. *Physical Review E*, 99(3), March 2019.

- [117] Yufu Niu, Peyman Mostaghimi, Mehdi Shabaninejad, Pawel Swietojanski, and Ryan T Armstrong. Digital rock segmentation for petrophysical analysis with reduced user bias using convolutional neural networks. *Water Resources Research*, 56(2):e2019WR026597, 2020.
- [118] G. Nützmann, S. Maciejewski, and K. Joswig. Estimation of water saturation dependence of dispersion in unsaturated porous media: experiments and modelling analysis. *Adv Water Resour*, 25(5):565–576, May 2002.
- [119] Hiroshi Okabe and Martin J Blunt. Prediction of permeability for porous media reconstructed using multiple-point statistics. *Physical Review E*, 70(6):066135, 2004.
- [120] Rezki Oughanem, Souhail Youssef, Daniela Bauer, Yannick Peysson, Eric Maire, and Olga Vizika. A multi-scale investigation of pore structure impact on the mobilization of trapped oil by surfactant injection. *Transport in Porous Media*, 109(3):673–692, July 2015.
- [121] I.Y. Padilla, T.-C.J. Yeh, and M.H. Conklin. The effect of water content on solute transport in unsaturated porous media. *Water Resour Res*, 35(11):3303–3313, November 1999.
- [122] Andrés Vélasquez Parra, Tomas Aquino, Mathias Willman, Tanguy Le Borgne, Yves Méheust, and Joaquin Jimenez-Martinez. Sharp transition to strongly anomalous transport in unsaturated porous media. *Water Resources Research*, March 2021.
- [123] Mathis Pasquier, Stéphane Jay, Jérôme Jacob, and Pierre Sagaut. A lattice-boltzmann-based modelling chain for traffic-related atmospheric pollutant dispersion at the local urban scale. *Building and Environment*, 242:110562, 2023.
- [124] T.K. Perkins and O.C. Johnston. A review of diffusion and dispersion in porous media. *Society of Petroleum Engineers Journal*, 3(01):70–84, March 1963.
- [125] Steve Plimpton. Fast parallel algorithms for short-range molecular dynamics. *Journal of Computational Physics*, 117(1):1–19, 1995.
- [126] Swain N. R., Latu K., Christensen S. D., Jones N. L., Nelson E. J., Ames D. P., and Williams G. P. A review of open source software solutions for developing water resources web applications. *Environmental Modelling & Software*, 67:108–117, 2015.
- [127] TC Ransohoff and CJ Radke. Mechanisms of foam generation in glass-bead packs. *SPE reservoir engineering*, 3(02):573–585, 1988.
- [128] A. Raoof, H. Nick, S.M. Hassanizadeh, and C.J. Spiers. Poreflow: A complex pore-network model for simulation of reactive transport in variably saturated porous media. *Computers & Geosciences*, 61:160–174, 2013.
- [129] Roland Masson Robert Eymard, Cindy Guichard. Grid orientation effect in coupled finite volume schemes. *IMA Journal of Numerical Analysis*, 2012.
- [130] JG Roof. Snap-off of oil droplets in water-wet pores. *Society of Petroleum Engineers Journal*, 10(01):85–90, 1970.
- [131] M Sahimi and A O Imdakm. The effect of morphological disorder on hydrodynamic dispersion in flow through porous media. *Journal of Physics A: Mathematical and General*, 21(19):3833–3870, October 1988.

- [132] Muhammad Sahimi. Fractal and superdiffusive transport and hydrodynamic dispersion in heterogeneous porous media. *Transport in Porous Media*, 13(1):3–40, October 1993.
- [133] James E. Saiers and John J. Lenhart. Colloid mobilization and transport within unsaturated porous media under transient-flow conditions. *Water Resources Research*, 39(1), January 2003.
- [134] J. Schindelin, I. Arganda-Carreras, E. Frise, V. Kaynig, M. Longair, T. Pietzsch, S. Preibisch, C. Rueden, S. Saalfeld, B. Schmid, J. Tinevez, D. J. White, V. Hartenstein, K. Eliceiri, P. Tomancak, and A. Cardona. Fiji: an open-source platform for biological-image analysis. *Nature Methods*, 9(7):676–682, June 2012.
- [135] James J Sheng. *Enhanced oil recovery field case studies*. Gulf Professional Publishing, 2013.
- [136] N. Shokri, P. Lehmann, and D. Or. Critical evaluation of enhancement factors for vapor transport through unsaturated porous media. *Water Resources Research*, 45(10), October 2009.
- [137] Siemens Digital Industries Software. Simcenter STAR-CCM+, version 2021.1, Siemens 2021.
- [138] S. E. Silliman and E. S. Simpson. Laboratory evidence of the scale effect in dispersion of solutes in porous media. *Water Resources Research*, 23(8):1667–1673, August 1987.
- [139] Orlando Silva, Jesus Carrera, Marco Dentz, S. Kumar, Andrés Alcolea, and Matthias Willmann. A general real-time formulation for multi-rate mass transfer problems. 2009.
- [140] Orlando Silva, Jesus Carrera, Marco Dentz, S. Kumar, Andrés Alcolea, and Matthias Willmann. A general real-time formulation for multi-rate mass transfer problems. *Hydrology and Earth Sciences*, 2009.
- [141] F. De Smedt and P. J. Wierenga. Solute transfer through columns of glass beads. *Water Resources Research*, 20(2):225–232, February 1984.
- [142] Yoshio Sone and Y Sone. *Kinetic theory and fluid dynamics*. Springer, 2002.
- [143] C. Soullaine, J. Maes, and S. Roman. Computational microfluidics for geosciences. *Frontiers in Water*, 3, March 2021.
- [144] J. Straubhaar, P. Renard, and T. Chugunova. Multiple-point statistics using multi-resolution images. *Stochastic Environmental Research and Risk Assessment*, 34(2):251–273, February 2020.
- [145] Sebastien Bruno Strebelle. *Sequential simulation drawing structures from training images*. Stanford University, 2000.
- [146] Shinsuke Suga. Stability and accuracy of lattice boltzmann schemes for anisotropic advection-diffusion equations. *International Journal of Modern Physics C*, 20(04):633–650, 2009.

- [147] Shinsuke Suga. An accurate multi-level finite difference scheme for 1d diffusion equations derived from the lattice boltzmann method. *Journal of Statistical Physics*, 140:494–503, 2010.
- [148] Pejman Tahmasebi. Multiple point statistics: a review. *Handbook of mathematical geosciences: Fifty years of IAMG*, pages 613–643, 2018.
- [149] Pejman Tahmasebi. *Multiple Point Statistics: A Review*, pages 613–643. Springer International Publishing, Cham, 2018.
- [150] Ken Tore Tallakstad, Grunde Løvoll, Henning Arendt Knudsen, Thomas Ramstad, Eirik Grude Flekkøy, and Knut Jørgen Måløy. Steady-state, simultaneous two-phase flow in porous media: An experimental study. *Physical Review E*, 80(3), September 2009.
- [151] Laurent Talon, Emma Ollivier-Triquet, Marco Dentz, and Daniela Bauer. Transient dispersion regimes in heterogeneous porous media: On the impact of spatial heterogeneity in permeability and exchange kinetics in mobile-immobile transport. *Advances in Water Resources*, 174:104425, 2023.
- [152] Xiao-Hua Tan, Li Jiang, Xiao-Ping Li, Yue-Yang Li, and Kai Zhang. A complex model for the permeability and porosity of porous media. *Chemical Engineering Science*, 172:230–238, November 2017.
- [153] Y. B. Tang, M. Li, Y. Bernabé, and J. Z. Zhao. Viscous fingering and preferential flow paths in heterogeneous porous media. *Journal of Geophysical Research: Solid Earth*, 125(3), March 2020.
- [154] Sir Geoffrey Taylor. On the dispersion of a solute in a fluid flowing through a tube. *Proceedings of the Royal Society of London. Series A. Mathematical and Physical Sciences*, 235(1200):67–77, April 1956.
- [155] Jan Tecklenburg, Insa Neuweiler, Jesus Carrera, and Marco Dentz. Multi-rate mass transfer modeling of two-phase flow in highly heterogeneous fractured and porous media. *Advances in Water Resources*, 91:63–77, May 2016.
- [156] Nathaniel Trask, Martin Maxey, Kyungjoo Kim, Mauro Perego, Michael L. Parks, Kai Yang, and Jinchao Xu. A scalable consistent second-order sph solver for unsteady low reynolds number flows. *Computer Methods in Applied Mechanics and Engineering*, 289:155–178, 2015.
- [157] Dimetre Triadis, Fei Jiang, and Diogo Bolster. Anomalous dispersion in pore-scale simulations of two-phase flow. *Transport in Porous Media*, 126(2):337–353, October 2018.
- [158] Alina Tyukhova, Marco Dentz, Wolfgang Kinzelbach, and Matthias Willmann. Mechanisms of anomalous dispersion in flow through heterogeneous porous media. *Physical Review Fluids*, 1(7), November 2016.
- [159] S. Ubertini, P. Asinari, and S. Succi. Three ways to lattice boltzmann: A unified time-marching picture. *Phys. Rev. E*, 81:016311, Jan 2010.
- [160] Bram van Leer. Towards the ultimate conservative difference scheme. v. a second-order sequel to godunov’s method. *Journal of Computational Physics*, 32(1):101–136, 1979.

- [161] J. Vanderborght and H. Vereecken. Review of dispersivities for transport modeling in soils. *Vadose Zone J*, 6(1):29–52, February 2007.
- [162] Igor Varfolomeev, Ivan Yakimchuk, and Ilia Safonov. An application of deep neural networks for segmentation of microtomographic images of rock samples. *Computers*, 8(4):72, 2019.
- [163] A. Velásquez-Parra, T. Aquino, M. Willmann, Y. Méheust, T. Le Borgne, and J. Jiménez-Martínez. Sharp transition to strongly anomalous transport in unsaturated porous media. *Geophys Res Lett*, 49(3):e2021GL096280, 2022.
- [164] D. Violeau. *Fluid Mechanics and the SPH Method: Theory and Applications*. University Press, Oxford, 2012.
- [165] J. Wan and J.L. Wilson. Colloid transport in unsaturated porous media. *Water Resour Res*, 30(4):857–864, April 1994.
- [166] Jiamin Wan, John L. Wilson, and Thomas L. Kieft. Influence of the gas-water interface on transport of microorganisms through unsaturated porous media, February 1994.
- [167] Ying Da Wang, Martin Blunt, Ryan Armstrong, and Peyman Mostaghimi. Deep learning in pore scale imaging and modeling. *Earth-Science Reviews*, 215, 02 2021.
- [168] Stephen Whitaker. Flow in porous media i: A theoretical derivation of darcy's law. *Transport in Porous Media*, 1(1):3–25, 1986.
- [169] Mark D. Wilkins, Linda M. Abriola, and Kurt D. Pennell. An experimental investigation of rate-limited nonaqueous phase liquid volatilization in unsaturated porous media: Steady state mass transfer. *Water Resources Research*, 31(9):2159–2172, September 1995.
- [170] Dieter Wolf-Gladrow. A lattice boltzmann equation for diffusion. *Journal of Statistical Physics*, 79:1023–1032, 1995.
- [171] Yuqi Wu, Chengyan Lin, Lihua Ren, Weichao Yan, Senyou An, Bingyi Chen, Yang Wang, Xianguo Zhang, Chunmei You, and Yimin Zhang. Reconstruction of 3d porous media using multiple-point statistics based on a 3d training image. *Journal of Natural Gas Science and Engineering*, 51:129–140, 2018.
- [172] Ke Xu, Tianbo Liang, Peixi Zhu, Pengpeng Qi, Jun Lu, Chun Huh, and Matthew Balhoff. A 2.5-d glass micromodel for investigation of multi-phase flow in porous media. *Lab on a Chip*, 17(4):640–646, 2017.
- [173] Liang Xue, Xiaozhe Guo, and Hao Chen. *Fluid Flow in Porous Media*. WORLD SCIENTIFIC, February 2020.
- [174] Xiaofan Yang, Yashar Mehmani, William A. Perkins, Andrea Pasquali, Martin Schönherr, Kyungjoo Kim, Mauro Perego, Michael L. Parks, Nathaniel Trask, Matthew T. Balhoff, Marshall C. Richmond, Martin Geier, Manfred Krafczyk, Li-Shi Luo, Alexandre M. Tartakovsky, and Timothy D. Scheibe. Intercomparison of 3d pore-scale flow and solute transport simulation methods. *Advances in Water Resources*, 95:176–189, 2016. Pore scale modeling and experiments.

-
- [175] Christopher Yeates. *Multi-Scale Study of Foam Flow Dynamics in Porous Media*. PhD thesis, Sorbonne Université, 2019.
- [176] Hiroaki Yoshida and Makoto Nagaoka. Multiple-relaxation-time lattice boltzmann model for the convection and anisotropic diffusion equation. *J. Comput. Phys.*, 229(20):7774–7795, oct 2010.
- [177] Wonjin Yun, Cynthia M. Ross, Sophie Roman, and Anthony R. Kovscek. Creation of a dual-porosity and dual-depth micromodel for the study of multiphase flow in complex porous media. *Lab on a Chip*, 17(8):1462–1474, 2017.
- [178] J. Zeng, Y.C. Yortsos, and D. Salin. On the Brinkman correction in unidirectional Hele-Shaw flows. *Phys. Fluids*, 15:3829–3836, 2003.
- [179] Jie Zeng, Yannis C Yortsos, and Dominique Salin. On the brinkman correction in unidirectional hele-shaw flows. *Physics of Fluids*, 15(12):3829–3836, 2003.
- [180] D. Zhang, R. Zhang, S. Chen, and W.E. Soll. Pore scale study of flow in porous media: Scale dependency, REV, and statistical REV. *Geophys Res Lett*, 27(8):1195–1198, April 2000.
- [181] Ting Zhang and Yi Du. Reconstructing porous media using mps. In *Multimedia and Signal Processing: Second International Conference, CMSP 2012, Shanghai, China, December 7-9, 2012. Proceedings*, pages 341–348. Springer, 2012.
- [182] Ting Zhang, Yi Du, Tao Huang, and Xue Li. Reconstruction of porous media using multiple-point statistics with data conditioning. *Stochastic environmental research and risk assessment*, 29:727–738, 2015.
- [183] Xiaoxian Zhang and Mouchao Lv. Persistence of anomalous dispersion in uniform porous media demonstrated by pore-scale simulations. *Water Resources Research*, 43(7), July 2007.
- [184] Liuzong Zhou and H. M. Selim. Application of the fractional advection-dispersion equation in porous media. *Soil Science Society of America Journal*, 67(4):1079–1084, July 2003.